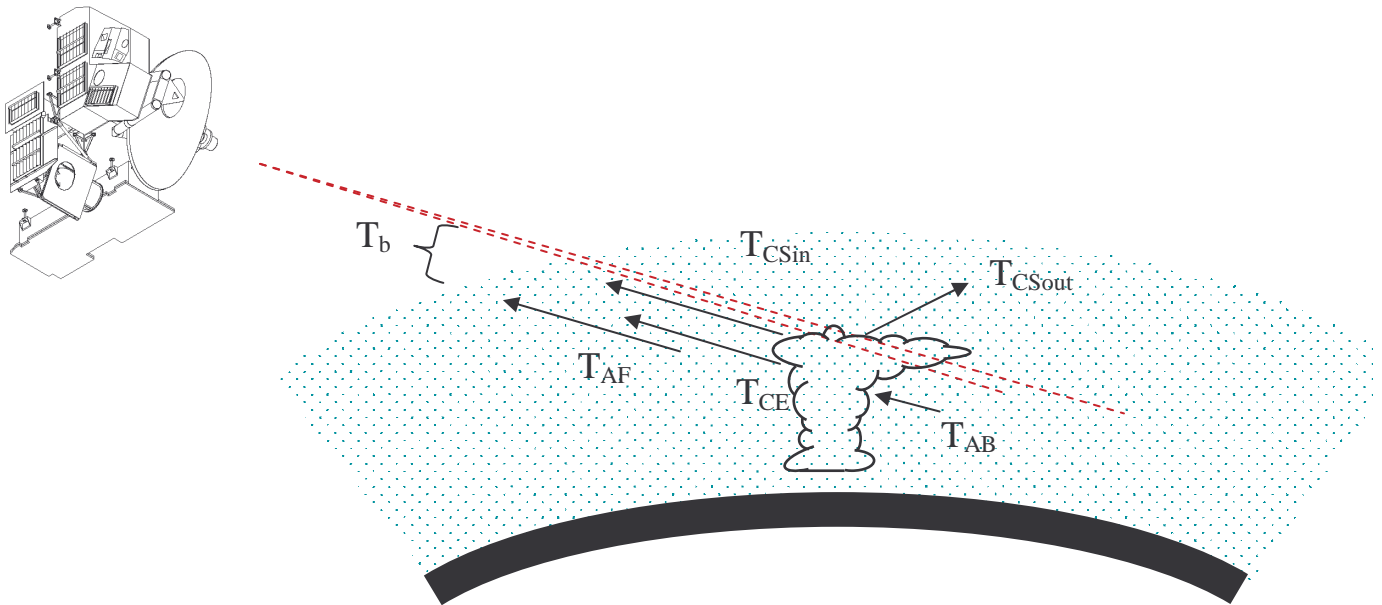


JPL D-19299/CL#04-2160  
EOS MLS DRL 601 (part 6)  
ATBD-MLS-06

Earth Observing System (EOS)

Microwave Limb Sounder (MLS)

## EOS MLS Algorithm Theoretical Basis for Cloud Measurements



Dong L. Wu  
Jonathan H. Jiang

Version 1.0  
June 4, 2004

**JPL**

Jet Propulsion Laboratory  
California Institute of Technology  
Pasadena, CA 91109-8099

<b>Version</b>	<b>Date released</b>	<b>comments</b>
<b>1.0</b>	<b>June 4, 2004</b>	<b>Initial version</b>

## Table of Content

<b>1</b>	<b><i>Introduction</i></b> .....	<b>1</b>
<b>2</b>	<b><i>Overview</i></b> .....	<b>2</b>
<b>2.1</b>	<b>Scope and Purpose</b> .....	<b>2</b>
<b>2.2</b>	<b>The Aura MLS Experiment</b> .....	<b>3</b>
<b>2.3</b>	<b>MLS Cloud Flag</b> .....	<b>4</b>
<b>2.4</b>	<b>MLS Cloud Products</b> .....	<b>4</b>
2.4.1	Standard Products .....	4
2.4.2	Diagnostic Products .....	4
<b>3</b>	<b><i>Cloud Flag Algorithms</i></b> .....	<b>8</b>
<b>3.1</b>	<b>Cloud Effects</b> .....	<b>8</b>
<b>3.2</b>	<b>Cloud-Induced Radiances</b> .....	<b>9</b>
<b>3.3</b>	<b>Empirical Methods</b> .....	<b>10</b>
3.3.1	Clear-sky statistics approach .....	10
3.3.2	Horizontal differential approach .....	11
<b>3.4</b>	<b>Model Methods</b> .....	<b>12</b>
3.4.1	Single-frequency methods .....	12
3.4.1.1	Assuming RHi=110% .....	12
3.4.1.2	Using the retrieved profiles .....	13
3.4.2	Multi-channel methods .....	13
<b>3.5</b>	<b>False Cloud Detection</b> .....	<b>14</b>
<b>4</b>	<b><i>Radiative Transfer Model for Cloudy Atmospheres</i></b> .....	<b>15</b>
<b>4.1</b>	<b>Geometry and Radiative Transfer Equation</b> .....	<b>15</b>
4.1.1	Limb-Viewing Geometry and Model Configuration .....	15
4.1.2	The Generalized Radiative Transfer Equation .....	16
<b>4.2</b>	<b>Numerical Method</b> .....	<b>17</b>
4.2.1	Basic Assumptions.....	17
4.2.2	General Definitions.....	18
4.2.3	The Discrete Equation .....	18
4.2.4	Iterative Calculations for the Scattering Source Function .....	20
4.2.5	Final Radiative Transfer Calculation at Limb.....	21
4.2.6	Flow Diagram of the Cloudy Sky Radiance Model .....	22
<b>4.3</b>	<b>Clear-Sky Radiation (<math>\beta_{\text{gas}_a}</math>)</b> .....	<b>25</b>
4.3.1	Dry air continuum ( $\beta_{\text{dry}}$ ).....	25
4.3.2	Water vapor continuum ( $\beta_{\text{wet}}$ ) .....	26
4.3.3	Line emissions ( $\beta_{\text{ul}}$ ) .....	26
<b>4.4</b>	<b>Cloudy-Sky Radiation [<math>\beta_{\text{c}_s}</math>, <math>\beta_{\text{c}_a}</math>, <math>\mathbf{P}(\theta)</math>]</b> .....	<b>28</b>
4.4.1	Important Cloud Parameters .....	29
4.4.1.1	Efficiency Factors .....	29
4.4.1.2	Phase Function .....	29
4.4.1.3	Particle Size Parameter .....	30
4.4.2	The Mie Solution .....	30
4.4.2.1	Mie Efficiencies .....	30
4.4.2.2	Phase function .....	32

4.4.3	Polydispersion of Particles.....	36
4.4.3.1	The Volume Scattering and Extinction Coefficients.....	36
4.4.3.2	The Integrated Phase Function.....	37
4.4.4	Scattering Calculations.....	38
4.4.4.1	Scattering Geometry.....	38
4.4.4.2	Angle Interpolation.....	39
4.4.4.3	Iterative Method and Multiple Scattering among Cloud Layers.....	40
4.4.4.4	Single Scattering Assumption within a Cloud Layer.....	41
<b>5</b>	<b>Model Atmosphere.....</b>	<b>42</b>
<b>5.1</b>	<b>Clear-Sky Atmosphere.....</b>	<b>42</b>
<b>5.2</b>	<b>A Review of General Cloud Properties.....</b>	<b>42</b>
5.2.1	Cloud Classification and Distribution.....	42
5.2.2	Physical Properties of High Clouds.....	43
5.2.2.1	Mixed-phase Clouds.....	43
<b>5.3</b>	<b>Cloud Models.....</b>	<b>45</b>
5.3.1	Vertical Profiles of Cloud Water Contents.....	45
5.3.2	Particle Size Distributions.....	45
5.3.2.1	Ice Particle Size Distributions.....	46
5.3.2.2	Water Droplet Size Distribution.....	47
5.3.2.3	Cloud Radiative Properties.....	48
5.3.2.4	Particle Size Dependence of Volume Extinction/Scattering Coefficients.....	50
<b>6</b>	<b>Cloud Radiance Simulations and Fast Models.....</b>	<b>54</b>
<b>6.1</b>	<b>Cloud-Induced Limb Radiance (<math>\Delta T_{\text{CIR}}</math>) and its Sensitivity to IWC.....</b>	<b>54</b>
6.1.1	High-ht Radiances.....	55
6.1.2	Low-ht Radiances.....	56
<b>6.2</b>	<b>Effective Ice Water Path (<math>h\text{IWP}</math>).....</b>	<b>56</b>
<b>6.3</b>	<b>Effective Cloud Optical Depth (<math>\tau_{\text{eff}}</math>).....</b>	<b>59</b>
<b>6.4</b>	<b>Cloud Radiance Sensitivity.....</b>	<b>60</b>
<b>6.5</b>	<b>Low-<math>h_t</math> <math>\Delta T_{\text{cir}}</math> - <math>\tau_{\text{eff}}</math> Relations.....</b>	<b>61</b>
6.5.1	Effects of Cloud Height.....	61
6.5.2	Effects of Cloud Profile Type.....	61
6.5.3	Effects of Tangent Height.....	62
6.5.4	Effects of Frequency.....	62
6.5.5	Effects of Temperature Profile.....	63
6.5.6	Effects of Ice PSD and Habit.....	64
6.5.7	Effects of Liquid Clouds.....	65
<b>6.6</b>	<b>High-<math>h_t</math> <math>\Delta T_{\text{cir}}</math> - <math>\tau_{\text{eff}}</math> Relations.....</b>	<b>65</b>
<b>6.7</b>	<b>The Fast Model.....</b>	<b>66</b>
6.7.1	The $\Delta T_{\text{cir}}$ - $\tau_{\text{eff}}$ Relation at Low- $h_t$ .....	66
6.7.2	The $\Delta T_{\text{cir}}$ - $\tau_{\text{eff}}$ Relation at High- $h_t$ .....	67
<b>7</b>	<b>Cloud Retrievals.....</b>	<b>68</b>
<b>7.1</b>	<b>Overview of Cloud Retrieval Algorithm.....</b>	<b>68</b>
<b>7.2</b>	<b>Determination of Cloud-Induced Radiances.....</b>	<b>70</b>
7.2.1	The $f^{\text{th}}$ Approximation for Splitting Double Sideband $\Delta T_{\text{cir}}$ .....	70
<b>7.3</b>	<b>Cloud Extinction Retrieval.....</b>	<b>71</b>

7.3.1	Cloud Extinction Retrieval from Low-ht Radiances.....	72
7.3.2	Cloud Ice Retrieval from High-ht Radiances.....	73
<b>7.4</b>	<b>Retrieval of IWC from Baseline .....</b>	<b>75</b>
<b>7.5</b>	<b>Convective and Cirrus Cloud Classification.....</b>	<b>75</b>
<b>7.6</b>	<b>Error in <math>\Delta T_{cir}</math>-to-IWC or <math>\Delta T_{cir}</math>-to-IWP conversion .....</b>	<b>76</b>
<b>8</b>	<b><i>Implementation and Future Work</i>.....</b>	<b>78</b>
<b>8.1</b>	<b>The V1.4 Implement for Cloudy Radiance Handling .....</b>	<b>78</b>
8.1.1	Cloud flag thresholds.....	78
8.1.2	The $\Delta T_{cir}$ -IWC conversion coefficients.....	80
<b>8.2</b>	<b>Performance of V1.4 on Simulated Data .....</b>	<b>80</b>
8.2.1	$\Delta T_{cir}$ calculations.....	80
8.2.2	IWC Retrievals .....	82
<b>8.3</b>	<b>Plans for Future Algorithm Improvements.....</b>	<b>84</b>
8.3.1	Refine Post-Launch $\Delta T_{cir}$ Calculations .....	84
8.3.2	Implement and Improve the <i>IWC</i> and <i>hIWP</i> Retrievals .....	84
8.3.3	Enhance MLS RT Model for 2D Cloudy-Sky Atmospheres .....	84
8.3.4	Develop a Physical Retrieval for Cloud-Induced <i>Baseline</i> .....	84
8.3.5	Algorithms to Infer Ice Microphysical Properties .....	85
<b><i>Appendices (A-F)</i> .....</b>		<b>86</b>
<b>Appendix A : Determining Upper/Lower Sideband Radiances.....</b>		<b>86</b>
<b>Appendix B : Cloud-Induced Radiances in Emission-Dominated Situations .....</b>		<b>88</b>
<b>Appendix C : Refractive Indices and Dielectric Constants of Ice and Water .....</b>		<b>90</b>
C1	The LH formulae.....	90
C2	Modified LH formula.....	91
C3	Comparisons with measurements.....	92
C4	Summary .....	96
<b>Appendix D : A Conceptual Cloud Radiance Model.....</b>		<b>97</b>
D1	Simple Radiative Transfer (RT) Equation .....	97
<b>Appendix E : Ice Particle Size Distributions .....</b>		<b>100</b>
E1	Modeled Size Distributions.....	100
	McFarquhar-Heymsfield (MH) Distribution .....	100
	Gamma Size Distribution .....	101
	Liu-Curry Distribution.....	102
	Knollenberg Distributions .....	103
E2	Discussions.....	103
<b>Appendix F : Dry Continuum Absorption.....</b>		<b>107</b>
F1	What is the dry continuum absorption?.....	107
F2	The N <sub>2</sub> -N <sub>2</sub> collision-induced absorption .....	107
F3	Atmosphere dry-air continuum.....	108
F4	Comparisons to experimental data .....	109
<b><i>Acronyms</i>.....</b>		<b>113</b>
<b><i>References</i> .....</b>		<b>114</b>

## List of Figures

Figure 2.1 Level 2 data processing diagram and data flow. The shaded modules are cloud-related algorithms and files to be described in this document. Dashed lines indicate alternatives for the Level 2 routine processing and might be run, if affordable, for some selected cloudy cases. ....	2
Figure 3.1 UARS MLS 204 GHz radiances measured on 1 March 1992. The general radiance increase with tangent pressure is due to dry and water vapor continua, and the radiance variability is roughly bounded by water vapor variation between 0% and 100% saturation. The outliers are indicative of clouds (see text). ....	8
Figure 3.2 Schematic to show the impact of cloud scattering on the clear-sky gas lineshapes in a limb observation. Scattered light can differ significantly from clear-sky radiances and make them difficult to use for the gas retrievals in the presence of clouds. ....	9
Figure 3.3 Flow Diagram of cloud flag algorithms. Dashed lines indicate the alternative approach. ....	10
Figure 3.4 UARS MLS limb-tracking radiances (top panel) measured on 26 March 1996 when the pointing was kept at $h_t = -10$ km. Clear and cloudy-sky radiances are separated according to slowly (middle) and rapidly (bottom) varying components. ....	11
Figure 3.5 Differences between the observed and the modeled clear-sky limit for UARS MLS 203 GHz. Above $\sim 300$ hPa most differences are close to or less than 0 K except for those affected by clouds. The radiance differences below $\sim 300$ hPa cannot be used to detect clouds because of complicated behaviors of the dry and wet profiles. ....	12
Figure 3.6 Differences between the measured radiances and modeled clear-sky minimums. The negative values with $\Delta T_{cir} < -10$ K are flagged as clouds. The threshold of $-10$ K accounts for model uncertainties. ....	13
Figure 3.7 <i>A histogram of the UARS MLS 203-GHz <math>\Delta T_{cir}</math> at 100 hPa. Symbols represent the number of <math>\Delta T_{cir}</math> measurements in 1-K bins from six months of data in early 1992 at latitudes between 25°S and 25°N. A Gaussian distribution is fitted to the clear-sky variability with the bias and standard deviation indicated in the plot. The number of cloudy-sky measurements drops off exponentially at large <math>+\Delta T_{cir}</math>. The 3 K cloud flag threshold is indicated by the dashed line. False cloud detection is described by the portion of the Gaussian distribution with <math>\Delta T_{cir} &gt; 3</math> K and causes a bias of 0.03 K in <math>\Delta T_{cir}</math> and 0.9% in cloud occurrence frequency at 100 hPa.</i> ....	14
Figure 4.1 MLS limb viewing geometry. ....	15
Figure 4.2 An example of multiple layer cloud. Three cloud layers are illustrated here by boxes. ....	16
Figure 4.3 Diagram showing relationship between cosine of zenith $\mu_n$ , tangent height $h_t$ , Earth radius $R_e$ , and the layer thickness $\Delta z = z_{n+1} - z_n$ . ....	20
Figure 4.4 Radiative transfer in local cloud scattering calculations under a plane-parallel atmosphere. ....	21
Figure 4.5 Geometry of limb viewing radiative transfer. ....	22
Figure 4.6 Schematic flow of cloud model module where IPSD is the index assigned for each PSD. ....	23
Figure 4.7 Flow-Chart of the <i>Cloudy-Sky Radiance Model</i> . ....	24
Figure 4.8 Calculated clear-sky limb radiances for 3 tangent pressures in the CIRA86 July tropical atmosphere [Fleming et al., 1988]. The atmosphere includes dry/wet continua, O <sub>2</sub> and H <sub>2</sub> O. ....	27
Figure 4.9 Examples of calculated clear-sky limb-radiances for EOS MLS spectral regions (with O <sub>2</sub> , H <sub>2</sub> O, O <sub>3</sub> , O <sup>18</sup> O and dry-wet continua in the atmosphere). ....	28
Figure 4.10 Mie extinction (solid) and scattering (dashed) efficiencies. The complex refractive indices are computed at $-60^\circ\text{C}$ for ice (blue) and $-15^\circ\text{C}$ for liquid water (red). ....	33
Figure 4.11 Phase function for single ice particles with different size parameters (left-plots). The dielectric constant and single scattering albedo are computed at temperature of $-30^\circ\text{C}$ . The right-plots are to show that the phase function is normalized when integrated over all directions. ....	34

Figure 4.12 Phase function for single liquid water droplets with different size parameters (left-plots). The dielectric constant and single scattering albedo are computed at temperature of $-10^{\circ}\text{C}$ . The right-plots are to show that the phase function is normalized when integrated over all directions. ....	35
Figure 4.13 Integrated phase functions for ice and water Clouds.....	37
Figure 4.14 Definition of angle integrations in the scattering calculation.....	38
Figure 4.15 Angular distribution of incident and scattered radiances at 6, 10, 12 and 16km altitudes as a function of viewing angle. The radiance brightness for both clear-sky (solid lines) and cloudy-sky (dashed lines) near the horizon can differ by more than 200K within $\sim 10^{\circ}$ of incident angle. The red lines show that the angular gradient is greatly reduced in the scattering radiance, $T_{scat}$ , near the horizon because of the smoothing of the phase function integration. An important implication of this property is that one should always interpolate $T_{scat}$ and not $T_b$ .....	39
Figure 4.16 Illustration of multiple-scattering processes.....	40
Figure 5.1 Doppler radar imagery of deep convective cloud system in Hurricane George (September, 1998). Note that the melting layer is stable at $\sim 4$ to 5 km in regions outside the core, but goes upto $\sim 10$ km inside the central core region. Adopted from Geerts et al (2000). ....	44
Figure 5.2 Four ideal cloud models with different liquid and ice water profiles.....	45
Figure 5.3 Characteristics of MH size distributions. <b>(a)</b> Temperature (altitude) dependence for $\text{IWC} = 0.1\text{g/m}^3$ . Curves from light to dark show the MH size-distribution at temperatures $-15^{\circ}\text{C}$ , $-30^{\circ}\text{C}$ , $-45^{\circ}\text{C}$ , $-60^{\circ}\text{C}$ and $-75^{\circ}\text{C}$ . The mass-mean-diameters are respectively 230, 203, 181, 162, and $147\mu\text{m}$ for these temperatures. <b>(b)</b> IWC dependence for $T = -45^{\circ}\text{C}$ . Curves from light to dark show the MH distribution for IWC equal to 0.01, 0.02, 0.04, 0.08, and $0.16\text{g/m}^3$ . The mass-mean-diameters at these IWCs are 118, 135, 153, 173, and $196\mu\text{m}$ , respectively.....	47
Figure 5.4 Modeled ice particle and water droplet size-distributions for a water cloud layer (cumulus-like) at 4 km and an ice-cloud layer at 8 km. Curves from light to dark indicate the IWC for ice cloud or LWC for water cloud to be: 0.01, 0.05, 0.25, and $0.75\text{g/m}^3$ . ....	48
Figure 5.5 Single scattering albedos as a function of (a) IWC and (b) mass-mean-diameter $D_m$ at 203 GHz. The MH size distributions are used to compute these relations and the cloud variability is given for different cloud types. Curves with different thickness indicate size distributions at different altitudes (measured by temperature). Note that the single scattering albedos with/without air are substantially different, and it is misleading to evaluate the relative importance of scattering when using the one without air. Generally speaking, for thin-layer cirrus the scattering process can be neglected in the radiative transfer at this frequency whereas in the case of frontal/convective clouds both emission and scattering processes are important. ....	49
Figure 5.6 Cloud volume extinction coefficients $\beta_{c,e}$ versus (a) IWC and (b) mass-mean-diameter $D_m$ at 203 GHz for the MH size-distributions. ....	50
Figure 5.7 Weighted volume extinction (solid) and scattering (dashed) coefficients for two ice cloud conditions, ( $\text{IWC}=0.01\text{g/m}^3$ , $-60^{\circ}\text{C}$ ) and ( $\text{IWC}=0.1\text{g/m}^3$ , $-30^{\circ}\text{C}$ ), and three MLS frequencies, 203, 640 and 2500 GHz. The area under each curve is normalized to unity. ....	52
Figure 5.8 Weighted IWC for MH size distributions using $\text{IWC}=0.01\text{g/m}^3$ , $-60^{\circ}\text{C}$ or $\text{IWC}=0.1\text{g/m}^3$ , $-30^{\circ}\text{C}$ , at 203 and 640 GH.....	53
Figure 6.1 Calculated 203-GHz limb radiance profiles for a thin-layer cloud. The cloud layer is centered at 16.5 km with a constant IWC at 16-17 km that tails off linearly to zero in 0.5 km at top and bottom. The radiance profiles from different cloud IWCs are shown. For small IWCs, the cloudy radiance has a peak at 16.5 km and the $\Delta T_{cir}$ is nearly linearly proportional to IWC (in $\text{g/m}^3$ ). The $\Delta T_{cir}$ at low tangent height decreases with IWC but become saturated to $\sim 120\text{-}140\text{K}$ for large ( $>0.5\text{g/m}^3$ ) IWC. In the saturated cases, the clouds are so opaque that radiation comes only from the uppermost cloud layer.....	54
Figure 6.2 Calculated 203-GHz cloud limb radiances for a thin (1 km) layer cirrus centered at 16.5km versus IWC ( $\text{g/m}^3$ ) at (a) high $h_t$ and (b) low $h_t$ .....	55

Figure 6.3 The  $\Delta T_{cir}$ -hIWP relation for 203 GHz. For the MH distribution, the maximum retrievable hIWP is  $\sim 4.5 \text{ Kkg}^{-1}\text{m}^2$ , limited by cloud self extinction. The deviation from the linearity near  $4.5 \text{ Kkg}^{-1}\text{m}^2$  (or thick clouds) is likely an artifact of numerical error in evaluating the integration. ....57

Figure 6.4 Weighting functions of cloud radiances on (a) IWC and (b) cloud optical depth  $\tau_{cext}$  at a low  $h_t$ , where  $d\tau_{cext} = \beta_{c,e} \bullet dz$ . The frequencies 203.5, 186.5, and 184.5 GHz are used to show the effect of atmospheric opacity differences on cloud radiance sensitivity. The channel farther away from the 183.3 GHz H<sub>2</sub>O emission, which can see deeper into the atmosphere, has better sensitivity at lower altitudes. The sensitivities to IWC are altitude dependent since the MH particle size distributions used in the simulation depends on altitude. On the other hand, the sensitivities to cloud optical depth do not depend on size distribution, and therefore have a uniform shape that reflects clear-sky transmission profiles at these frequencies. ....60

Figure 6.5 Sensitivity for different cloud heights. In these calculations a 1-km cloud layer is placed at various altitudes. As indicated by the legend, each line represents the sensitivity when the cloud height is used. Only clouds with IWC less than  $0.5 \text{ g/m}^3$  are shown .....61

Figure 6.6 Sensitivities for different cloud profiles as described in chapter 5. The largest IWC in these calculations are 0.1, 0.5, 0.25, and  $0.15 \text{ g/m}^3$ , respectively, for the four cloud types in chapter 5. ....62

Figure 6.7 Sensitivity at different  $h_t$ . Convective cloud type is used in these calculations. The dotted line indicates the slope of  $-106 \text{ K}$ . ....62

Figure 6.8 Sensitivity for different frequencies near 183.3 GHz. The cloud profile is the convective type and only calculations with  $\text{IWC} < 0.5 \text{ g/m}^3$  are shown. ....63

Figure 6.9 Strong latitude dependence of air temperature profiles. These are from the CIRA December climatology in the Northern Hemisphere. ....63

Figure 6.10 Latitude dependence of the sensitivity calculated from the temperature profiles in Figure 6.9. A convective cloud type is used with the same cloud top pressure, surface model, and relative humidity profile. The relative humidity within and below the cloud is set to 100%. ....63

Figure 6.11 Sensitivity changes from different PSD. Five Knollenberg-like PSDs [see examples in Appendix E] are used for the extended calculations where their mass mean diameters are indicated with symbols. The MH and Liu-Curry PSDs are compared to the Knollenberg-like PSD calculations. The Liu-Curry PSD results are very similar to  $D_m=80 \mu\text{m}$  with the Knollenberg case, which is not surprising since for the  $D_m$  in the former distributions mostly fall between 50 and  $100 \mu\text{m}$ . In these calculations, the convective cloud type is used with a vertical range between 5 and 16 km, and only results with  $\text{IWC} < 0.5 \text{ g/m}^3$  are shown. The dotted line is the slope of  $-102 \text{ K}$ . ....64

Figure 6.12 Relative error of the sensitivity due to liquid clouds. For the frontal and anvil cloud models described in chapter 5, liquid cloud impacts are negligible since they reside mostly at low altitudes. In convective clouds, liquid droplets may be brought up to a higher altitude and significantly reduce the scattering-based sensitivity. ....65

Figure 6.13 High- $h_t$  cloud-induced radiances (203 GHz) simulated for the convective clouds (Chapter 5) with the 5-km  $\text{IWC} < 0.2 \text{ g/m}^3$ . Symbols denote the RT results whereas lines are the fits from the generalized form in Eq.6.10. ....66

Figure 7.1 Data flow and components of cloud ice retrieval algorithm. ....69

Figure 7.2 Comparisons of the  $f^4$  approximation and calculated volume scattering coefficients for the upper and lower sideband frequencies relative to the LO frequency. The solid lines are the  $f^4$  ratios of upper (lower) sideband frequency over the LO frequency, whereas symbols are the calculated ratios of corresponding volume scattering coefficients assuming the MH97 PSDs. The volume scattering is determined by modes of PSDs, and thus comparisons are made for different mass mean diameters. The MH PSDs used in the calculations cover a wide range of temperature ( $-15^\circ\text{C}$ ,  $-30^\circ\text{C}$ ,  $-45^\circ\text{C}$ ,  $-60^\circ\text{C}$  and  $-75^\circ\text{C}$ ) and  $\text{IWC}$  ( $0.004 - 1 \text{ g/m}^3$ ) values. The frequencies from four MLS double-sideband radiometers are studied and validation of the  $f^4$  law depends strongly on frequency. ....71

Figure 7.3 Transmission functions for Aura MLS frequency channels. Channels with matched penetration depths are useful for particles size studies. For the 640 GHz (Band10.C1) and 2.5 THz (Band15.C1) calculations, the transmission functions of the upper and lower sidebands are plotted.....	76
Figure 8.1 V1.4 Processing flow with cloud flag and ice retrieval.....	79
Figure 8.2 Retrieved cloud-induced R1-R5 radiances at 100 hPa. ....	81
Figure 8.3 Retrieved cloud-induced R1-R5 radiances at 1000 hPa. ....	81
Figure 8.4 Error of R1-R5 $\Delta T_{cir}$ retrievals estimated from the simulated data. Scattered points are the $\Delta T_{cir}$ residuals (retrieved – truth) in the simulated data. Vertical solid and dashed lines represent bias and the $3\sigma$ standard deviation around the bias, respectively. About 3400 profiles are simulated, including many clear and cloudy (5-10%) situations. ....	82
Figure 8.5 (a) Examples of 100-hPa IWC retrieval from simulated radiances where cloudy-induced radiances are calculated using the 1D cloudy-sky radiance model and added to selected clear-sky profiles. Since V1.4 retrieves 2D baseline profiles along orbital track [Livesey 2004], the IWCs converted from the 2D baselines are not expected to exactly match the truth (1D) profiles. As shown in the time series, the quality of these IWC retrievals depends directly on how well the baselines are retrieved. The R2 baseline seems to have the largest error. (b) Retrieved 100-hPa R4 IWC. Blue (red) points are cloud-free (cloudy) profiles in the truth file. In the IWC-Latitude plot, the clear-sky floor is mostly below 0.5 mg/m <sup>3</sup> except in the tropics where some positive blue points are likely due to the 1D-2D mismatches in the simulations. Also shown is that the blue points are bound tightly within ~1 mg/m <sup>3</sup> , suggesting good reliability of the baseline retrieval scheme in the 2D retrieval. ....	83
Fig A-1 Calculated MLS radiances for (a) lower sideband (183.3 GHz), (b) upper sideband (186.2 GHz), and (c) double sideband as would be measured by the radiometer. Although the lower sideband radiance is saturated below ~50km, it still has weak dependence on tangent height due to slight differences in path length. Such dependence is nearly linear at heights below ~50km and can be modeled relatively easily. A realistic sideband ratio ( $L/U=1.22$ ) is used to calculate the double sideband radiances. There are a quite number of samples between 50km and 20km which is a good height range to estimate the lower-sideband contribution. After the lower-sideband radiance is determined at this height, one may extrapolate it to lower $h_t$ , and remove it from the double-sideband radiance to obtain the upper-sideband radiance.....	86
Fig C-1 Computed and measured imaginary part of ice dielectric constants. The solid lines are $\epsilon''$ computed using the modified LH formula (C-6), the dash lines using the original LH formula (C-3).....	94
Fig C-2 Computed and measured real part of dielectric constants for ice (black-line) and liquid water (colored-lines). The measured data for ice are listed in Table. C-3, and the measured data for liquid water are given in Table. C-4.....	95
Fig C-3 Computed and measured imaginary part of dielectric constants for pure liquid water. The measured data are listed in Table. C-4. ....	96
Fig D-1 Schematic to show the radiative components of MLS optically-thick radiances at low $h_t$ . The important radiation components are indicated by arrows: clear-sky radiation in the front/back of clouds ( $T_{AF}/T_{AB}$ ), radiation of cloud emission ( $T_{CE}$ ), and radiation scattered into/out of FOV by clouds ( $T_{CSin}/T_{CSout}$ ). ....	97
Fig E-1 Observations of cloud particle number density $n(D)$ as a function of the long dimension of the particles at the temperature range of -25°C and -30°C [from Platt, 1997]. It shows a bimodal structure in the ice crystal distribution with the second peak at ~500 $\mu\text{m}$ . The bimodal distribution of ice particle spectra is not fully understood although it has been speculated as a result of balancing between the nucleation of ice particles and the removal of ice particles by aggregation and enhanced diffusion growth via ventilation [Mitchell, 1994]. .	100
Fig E-2 Gamma size distributions for IWC=0.01g/m <sup>3</sup> and $\alpha=0.5$ (solid lines) and $\alpha=1.5$ (dashed lines). Thickness of the lines represents different $D_m$ at 20, 70, 120, 170, 220, and 270 $\mu\text{m}$ (from thin to thick).....	102
Fig E-3 Liu-Curry size distributions for IWC=0.01g/m <sup>3</sup> and temperature -15°C, -30°C, -45°C, -60°C, and -75°C (from thick to thin). ....	102

Fig E-4 Knollenberg-like size distributions for IWC=0.01g/m <sup>3</sup> and $\alpha = 0.005, 0.01, 0.02, 0.04, 0.08, \text{ and } 0.16$ (from thick to thin). .....	103
Fig E-5 Volume extinction coefficient $\beta_{c,e}$ vs. (a) IWC and (b) mass mean diameter. In (a), for the MH and Liu-Curry distributions, the line thickness represents temperature of -15°C, -30°C, -45°C, -60°C, and -75°C (from thin to thick); for the Gamma distribution ( $\alpha=1$ ), the lower/upper line is respectively for $D_m = 30 \mu m$ at -75°C and $D_m = 300 \mu m$ at -15°C; for the Knollenberg-like distribution, the lower/upper line is respectively for $\alpha=0.1$ at -75°C and $\alpha=0.01$ at -15°C. In (b), the same ranges are applied for these distributions but only IWC=0.001 (the lower set), 0.1 (the middle set), 0.6 (the upper set) g/m <sup>3</sup> are plotted. ....	104
Fig E-6 As in Fig E-5 but for volume scattering coefficients. ....	105
Fig E-7 As in Fig E-5 but for volume absorption coefficients. ....	106
Fig E-8 Cloud single scattering albedo without air $\omega_0'$ vs. mass mean diameter $D_m$ for different size distributions. ....	106
Fig F-1 The components of the N <sub>2</sub> collision-induced absorption spectrum. (a) The translational spectrum. (b) The rotational spectrum. (c) The resulting profile is the convolution of (a) and (b). ....	108
Fig F-2 Comparisons between the calculations from the empirical function and the experimental data. (a) The relative error vs. temperature. (b) The calculated lineshape function at different temperatures. ....	110
Fig F-3 Comparisons of dry continuum absorption calculated from different models. The Debye term, important at low frequencies, is included in the calculations. ....	111

## List of Tables

Table 2-1 FOV and polarization of Aura MLS radiometers. Both vertical and horizontal FOVs are estimated at $h_t=0$ . .....	3
Table 2-2 Aura MLS spectral channels selected for cloud measurements .....	5
Table 2-3 Level 2 standard cloud products.....	6
Table 2-4 Level 2 cloud diagnostic files.....	6
Table 3-1 Statistics of UARS MLS 203-GHz radiances near the equator.....	11
Table 4-1 Two examples of $n_{\text{cut}}$ for $-30^\circ\text{C}$ ice at different size parameters .....	31
Table 4-2 Error in calculated $T_b$ due to angular and vertical resolutions.....	40
Table 5-1 Typical cloud water content ( $WC$ ), water path ( $WP$ ) from Blanchet et al (1987).....	42
Table 6-1 The $\Delta T_{\text{cir-to-hIWP}}$ conversion coefficients near 118 GHz.....	57
Table 6-2 The $\Delta T_{\text{cir-to-hIWP}}$ conversion coefficients near 190 GHz.....	58
Table 6-3 The $\Delta T_{\text{cir-to-hIWP}}$ conversion coefficients near 240 GHz.....	58
Table 6-4 The $\Delta T_{\text{cir-to-hIWP}}$ conversion coefficients near 640 GHz and 2.5 THz .....	59
Table 6-5 The $\Delta T_{\text{cir-to-hIWP}}$ conversion coefficients for UARS MLS 183 and 204 GHz channels .....	59
Table 7-1 100-hPa $IWC$ converted from the same $\Delta T_{\text{cir}}$ at 203 GHz using different PSDs. The differences reflect uncertainties caused by assumptions about PSDs in the upper troposphere. $D_{\text{mm}}$ is mass-mean diameter associated with each PSD. ....	77
Table 8-1 V1.4 cloud flag thresholds, ranges and actions .....	78
Table 8-2 The $\Delta T_{\text{cir}}-IWC$ conversion coefficients ( $\text{g/m}^3/\text{K}$ ) .....	80
Table 8-3 Estimated IWC biases and precisions.....	83
Table. C-1 Complex dielectric constants at different temperatures computed using the modified LH Formulae. ....	91
Table. C-2 The measured imaginary refractive indices or dielectric constants for pure water ice** .....	93
Table. C-3 The measured real part of dielectric constants for pure-water ice. ....	94
Table. C-4 Refractive indices and dielectric constants for pure liquid water. ....	95
Table. F-1 Comparisons to some laboratory measurements. Measured and calculated $\text{N}_2\text{-N}_2$ absorption has a unit of $\text{cm}^{-1}/\text{cm}^2/\text{amagat}^2$ .....	110
Table. F-2 Dry continuum absorption estimated from different models for $f=203\text{GHz}$ , $P_{\text{air}} = 200 \text{ hPa}$ and $T=220\text{K}$ .....	111

## 1 Introduction

Clouds play an important role in the Earth's weather and climate [Ramanathan et al., 1989; Stephen et al., 1990; Wylie et al., 1994]. Understanding of cloud properties and distributions remains poor and limited, which is a major obstacle for reliable predictions.

Passive millimeter and sub-millimeter wave radiometers can potentially obtain ice content and particle size information by penetrating clouds in the upper troposphere. Unlike visible/IR techniques, which are only sensitive to the uppermost cloud layer, microwave radiation can penetrate dense clouds and provide information on ice mass and microphysical properties. At microwave frequencies cloud-induced radiances are nearly linearly proportional to cloud optical depth within the instrument field of view, and are not limited by cloud inhomogeneity, skin temperature, surface emission and multiple scattering that often cause problems in other remote sensing techniques.

Remote sensing of ice clouds with passive microwave radiometers is a new research area. A number of groups have attempted to retrieve cloud liquid/ice contents from emission/scattering signatures in the radiances of nadir-viewing sensors [e.g., Vivekanandan et al., 1991; Gasiewski, 1992; Evans and Stephens, 1995b; Liu and Curry, 1998; Weng and Grody, 2000; Skofronick-Jackson and Wang, 2000]. Radiative transfer models can simulate most of the observed cloud-induced radiances, but accuracy of these calculations remains fairly poor - due to complexities of cloud micro- and macro-physics, such as:

- Large variations in particle size and shape distributions,
- Uncertainty in effective ice density,
- Mixture of ice and water layers, and
- Cloud inhomogeneity.

Thus, accurate modeling of real cloud effects remains as a challenging research for the future.

Compared to nadir sounding, microwave limb sounding has some advantages: (1) appreciable vertical resolution (1-3 km) that can measure high clouds near the tropopause, and (2) simple background radiation (mainly from the atmosphere or from cold space at high tangent heights) such that complex surface emission/reflection can be neglected. The Aura MLS 118, 190, 240, 640 GHz, and 2.5 THz measurements together offer a wide range of sensitivity to cloud ice content and particle size in the upper troposphere. Measurements from UARS (Upper Atmosphere Research Satellite) MLS show that at 203 GHz ice clouds can induce radiances at 14-18 km tangent heights ( $h_t$ ) that are 60 K warmer than the normal clear-sky background, and radiances at  $h_t < \sim 5$  km that are up to 150 K colder than the normal background.

MLS has unique ability to make global observations of cloud ice in the upper troposphere. As part of NASA "A-Train" concept, the MLS measurements will be in line with Aqua (since 2002) and CloudSat 94-GHz Cloud Profiling Radar (CPR) (due for launch in 2005) measurements with the footprints only 7 min apart. The synergy of radar-radiometer observations is expected to offer a unique opportunity for accurate measurements of ice water content and effective particle size in the upper troposphere.

## 2 Overview

### 2.1 Scope and Purpose

This document describes the theoretical basis of Aura MLS algorithms for cloud ice measurements, and includes

1. algorithms to determine cloud-induced radiances ( $\Delta T_{\text{cir}}$ ) and produce cloud flags (Chapter 3),
2. radiative transfer models for cloud-sky limb radiances (Chapters 4-6), and
3. algorithms for cloud ice retrievals (Chapter 7).

Chapter 3 describes the  $\Delta T_{\text{cir}}$  calculation methods and their pros/cons. Chapter 4 gives a detailed description of the radiative transfer (RT) model and calculation of MLS radiances in cloudy-sky atmospheres. Chapter 5 summarizes atmospheric and cloud parameters used for MLS RT model. Chapter 6 presents a set of simulated radiances and their sensitivities to various cloud parameters. Chapter 7 outlines the concepts of cloud ice retrieval from MLS  $\Delta T_{\text{cir}}$ . Finally, the actual implementation in MLS V1.4 software is given in Chapter 8.

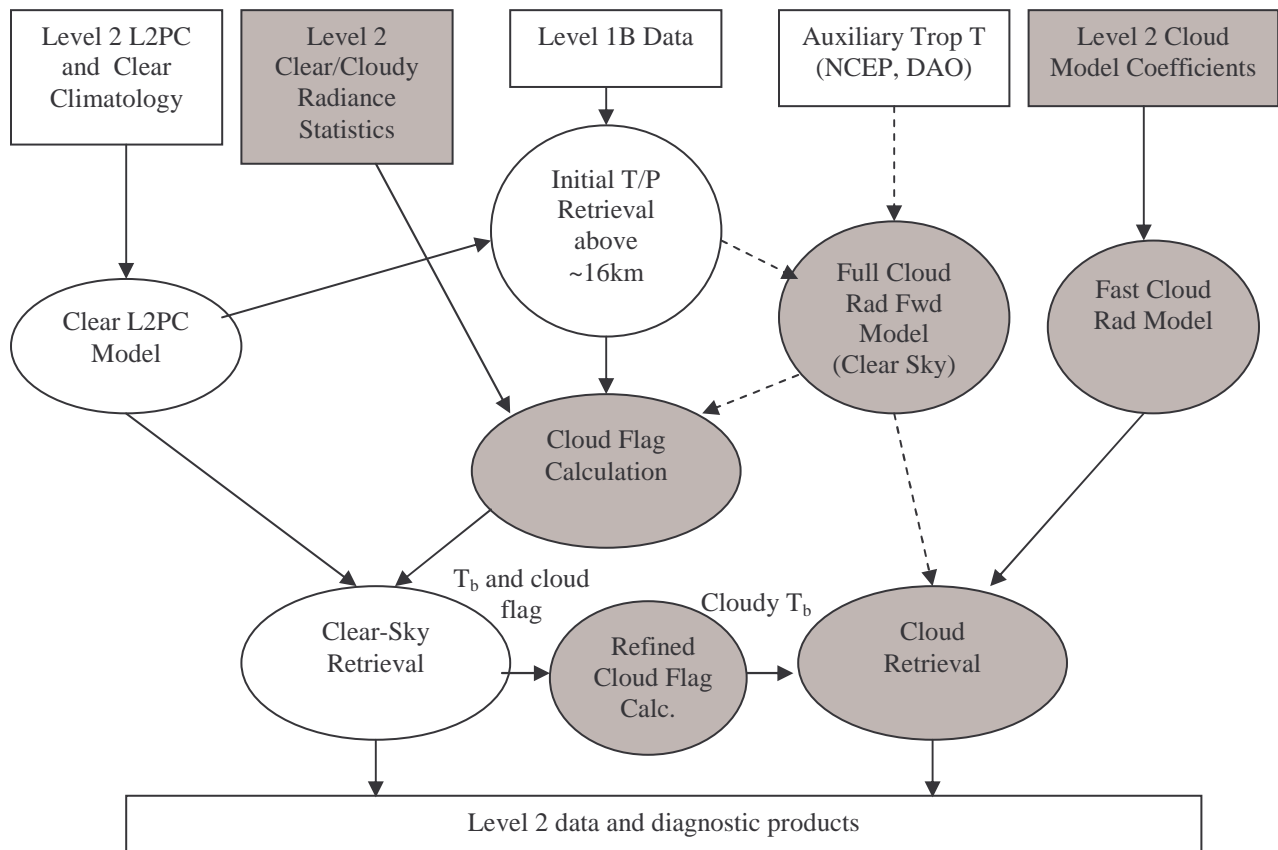


Figure 2.1 Level 2 data processing diagram and data flow. The shaded modules are cloud-related algorithms and files to be described in this document. Dashed lines indicate alternatives for the Level 2 routine processing and might be run, if affordable, for some selected cloudy cases.

These algorithms are integrated as part of MLS Level 2 software [Livesey, 2004], as illustrated in Figure 2.1, where the shaded modules are the cloud-related algorithms to be described in this document.

## 2.2 The Aura MLS Experiment

Aura MLS is a passive instrument with radiometers centered at frequencies near 118, 190, 240, 640 GHz, and 2.5 THz [Waters, 2004]. Several kinds of spectral filters are used to resolve spectral features of interest, including 19 25-channel filter bank spectrometers, 5 11-channel mid-band filter bank spectrometers, 12 wide-band filters, and 4 digital autocorrelator spectrometers [Jarnot et al., 2004]. The 1.6-m primary reflector of MLS antenna provides a vertical field-of-view (FOV) of  $\sim 3$  km at tangent point for 190 and 240 GHz, and  $\sim 1.5$  km for 640 GHz. The THz system has a separate antenna with a 2.5 km beamwidth at tangent point.

Table 2-1 FOV and polarization of Aura MLS radiometers. Both vertical and horizontal FOVs are estimated at  $h_t=0$ .

MLS Radiometer (LO frequency)	Polarization $0^\circ = \text{V pol}$ $90^\circ = \text{H pol}$	Vertical FOV	Cross-Track FOV
R1A (126.8 GHz)	$0^\circ \pm 0.5^\circ$	6.5 km	13 km
R1B (126.8 GHz)	$90^\circ \pm 0.5^\circ$	6.5 km	13 km
R2 (191.9 GHz)	$0^\circ \pm 0.5^\circ$	4.5 km	9 km
R3 (239.66 GHz)	$90^\circ \pm 0.5^\circ$	3.5 km	7 km
R4 (642.87 GHz)	$90^\circ \pm 0.5^\circ$	1.5 km	3 km
R5H (2522.7816 GHz)	$\sim 23^\circ$	2.5 km	2.5 km
R5V (2522.7816 GHz)	$\sim 113^\circ$	2.5 km	2.5 km

The Aura MLS is viewing forward toward the satellite flying direction and cross-track FOV width is frequency-dependent [Table 2-1]. The satellite has a sun-synchronous ( $\sim 1:40$  p.m. ascending crossing time) orbit at 705 km altitude with  $98^\circ$  inclination, and MLS covers latitudes between  $82^\circ\text{S}$  and  $82^\circ\text{N}$ . MLS limb scans are synchronized to the orbital period such that nominal operation will have 240 limb scans (called the major frames or MAFs) per orbit. Unlike step-wise scans in UARS MLS [Waters, 1993], Aura MLS scans are continuous in tangent height from the surface to the mesopause ( $\sim 90$  km) in 24.7s. The integration time for each measurement is 1/6 second, called a minor frame (MIF). The GHz and THz modules have separate scan sequences but are synchronized with the same scan period of 24.7 s. A GHz scan has 40-50 MIFs dedicated to tropospheric measurements, whereas a THz scan has only  $\sim 7$  MIFs at  $h_t < 18$  km. These low- $h_t$  measurements are particularly useful for cloud observations, and there is a sizable data gap in horizontal sampling between scans. More on the MLS nominal operation can be found in Jarnot et al. [2004].

The Aura MLS filters are chosen to cover spectral line features from atmospheric gases ( $\text{O}_2$ ,  $\text{O}_3$ ,  $\text{H}_2\text{O}$ ,  $\text{N}_2\text{O}$ ,  $\text{HNO}_3$ ,  $\text{ClO}$ , etc.). However, the channels useful for cloud measurements need to be away from these lines so that radiance clear-sky variability is small and cloud-induced radiances can be better extracted. Table 2-2 lists the 108 channels selected for cloud studies.

The estimated noises for 1/2-s and 1/6-s integration are given in Table 2-2 where the 1/2-s integration corresponds to the average of three MIFs or  $\sim 1$  km sampling in tangent height. This averaging may be needed if the instrument noise is considerably large. In addition, spectral

averaging (combining radiances from different channels) is also useful to reduce instrument noise and is discussed in the table comments.

### **2.3 MLS Cloud Flag**

MLS cloud flag is determined from cloud-induced radiances and prescribed thresholds in the configuration file. The cloud flag is generated for each radiometer as a function of MIF pressure.

### **2.4 MLS Cloud Products**

MLS provides measurements of cloud ice water content (IWC) at pressures  $< 215$  hPa and ice water path (hIWP) at various depths and frequencies. The IWC is a quantity averaged over MLS FOV, a volume of  $\sim 250$ -km in length with width and height listed in Table 2-1 as a function of frequency. The hIWP represents a column along MLS LOS (line-of-sight) in which the bottom pressure is frequency dependent and determined by the penetration depth.

#### **2.4.1 Standard Products**

IWC is the standard cloud product from MLS Level 2 processing. We report cloud IWC at the standard Level 2 pressure surfaces between 200 and 46 hPa at 12-per-decade resolution. The horizontal resolution is determined by the Level 2 retrieval, normally 240 profiles per orbit.

Table 2-3 summarizes the vertical range and data volume of these cloud products. These files will contain the following ancillary data for each profile: time, latitude, longitude, local solar time, local solar zenith angle, tangent line-of-sight angle with respect to north, and data quality flag.

#### **2.4.2 Diagnostic Products**

Table 2-4 gives the diagnostic products to be produced by the cloud algorithms on a daily basis and their vertical range and data volume. The data volumes are estimated assuming that the cloud profiles are produced at 4-times of the standard ( $1.5^\circ$ ) horizontal resolution, or 960 profiles per orbit.

The cloud extinction files are produced on the standard pressure surfaces. The effective optical depth and cloud-induced radiances are MIF-dependent quantities, and tangent height is vertical coordinate. There will be a slight overhead in these files to register measurements to universal time (UT), latitude, and longitude.

Table 2-2 Aura MLS spectral channels selected for cloud measurements

Radiometer (Polarization)	Channels	Frequency (GHz)	$\Delta I - 1/2s\Delta I - 1/6s$		Comments		
			(K)	(K)			
R1A (V)	R1A:118.B32W:PT.C1	115.3	0.12	0.2	R1A wideband channels and wing channels will be used to measure high-altitude clouds. R1A can be used, jointly with R1B (when it is on), to study cloud ice crystal shape.		
	R1A:118.B32W:PT.C2	117	0.12	0.2			
	R1A:118.B32W:PT.C3	120.5	0.12	0.2			
	R1A:118.B32W:PT.C4	122	0.12	0.2			
	R1A:118.B1F:PT.C1	118.178	0.23	0.4			
	R1A:118.B1F:PT.C2	118.274	0.23	0.4			
	R1A:118.B1F:PT.C24	119.328	0.23	0.4			
	R1A:118.B1F:PT.C25	119.232	0.23	0.4			
R1B (H)	Same as in R1A(V)				R1B is 'backup' radiometer, and will be turned on only occasionally.		
R2 (V)	R2:190.B2F:H2O C13 (C12-C1) (C25-C14)	200.49 183.31 - 183.88 182.74 - 183.31	2.3 0.6-2 2-0.6	4 1-3.5 3.5-1	R2 radiances will be used to profile cloud ice from different absorption near 183.3-GHz H <sub>2</sub> O line (Chapter 7). The 200.49-GHz radiance is upper sideband radiance that can be derived from C12-C14 of B2F when their lower sideband radiance is nearly saturated. The channels C22-C25 (177.15 GHz) in B6F can be averaged together to provide baseline radiance of the lower sideband. The largest frequency differences from the H <sub>2</sub> O line center are ~6.2 GHz in the lower sideband and ~17.2 GHz in the upper sideband.		
	R2:190.B3F:N2O (C25-C10)	182.24 - 183.38	0.6-2	1-3.5			
	R2:190.B4F:HNO3 (C1-C2) (C24-C25)	182.09 181.09	0.5 0.5	0.7 0.7			
	R2:190.B5F:ClO (C1-C2) (C24-C25)	179.94 178.94	0.5 0.5	0.7 0.7			
	R2:190.B6F:O3 (C1-C2) (C22-C25)	178.15 177.15	0.5 0.3	0.7 0.5			
	R3 (H)	R3:240.B33W:O3.C1	239.66 ± 3.0	0.3		0.4	The channels C25-C14 in B9F will be averaged together to provide baseline radiance for the lower sideband. The largest frequency differences from the O <sup>18</sup> O line center are ~4.9 GHz in the lower sideband and ~11.4 GHz in the upper sideband. R3 has a different polarization to R2 and the baseline radiances can be used to study potential polarization differences caused by ice crystal shapes.
		R3:240.B33W:O3.C2	239.66 ± 4.8	0.3		0.4	
		R3:240.B33W:O3.C3	239.66 ± 7.2	0.3		0.4	
		R3:240.B33W:O3.C4	239.66 ± 7.8	0.3		0.4	
		R3:240.B8F:PT C13 (C12-C1) (C25-C14)	245.37 233.95-234.52 233.38-233.95	2.3 0.6-2 2-0.6		4 1-3.5 3.5-1	
		R3:240.B9F:CO (C25-C14)	229.1-230.5	0.2		0.4	
	R4 (H)	R4:640.B10F:ClO R4:640.B11F:BRO (C1-C11) R4:640.B28M R4:640.B29M	643 ± 6.5	0.4		0.6	All listed channels and bands are averaged together, a bandwidth of ~2.2 GHz, to reduce radiance noise at 643 ± 6.5. R4 has better sensitivity to cloud ice and is used primarily for IWC measurements at 100 hPa.
R5V (V)	R5V.B18F:OH (C1-9, C17-22) R5V.B19F:OH (C20-C25)	~2523	0.6	1.0	All listed channels and bands are averaged together, a bandwidth of ~1.7 GHz, to provide baseline radiances at 2.5 THz. T <sub>sys</sub> =17000K for B18 T <sub>sys</sub> =12000K for B19 are assumed for noise estimation.		
R5H (H)	R5V.B15F:OH (C1-11, C15-22) R5V.B16F:OH (C20-C25)	~2523	0.6	1.0	Same as R5V but for horizontal polarization		

Table 2-3 Level 2 standard cloud products

Products*	Unit	Vertical Range				No. of pressure levels	Data Volume (Mb/day)
		Pressure (hPa)		Height (km)			
		Max	Min	Max	Min		
IWC1	g/m <sup>3</sup>	1000	46	20	0	17	0.5
IWC4	g/m <sup>3</sup>	1000	46	20	0	17	0.5x4**
Total							2.5

\* Two IWC files are produced from the retrieval: IWC1 and IWC4, respectively from high-  $h_t$  and low-  $h_t$  radiances.

\*\* Retrievals from low  $h_t$  radiances may yield better horizontal resolution than the standard 1.5° spacing. The suffix of IWC product name is used to reflect the multiple of the standard horizontal resolution.

Table 2-4 Level 2 cloud diagnostic files

Product	Unit	Vertical Range (hPa)		No. of Vertical Levels	Daily Vol. (Mb)	Comments
		Max	Min			
<b>Baseline</b>						
baselineR1A	K	1000	46	50	1.5	These baselines are produced from the clear-sky retrieval algorithm, which account for all spectrally-flat contributions unexplained by the clear-sky forward model.
baselineR1B	K	1000	46	50	1.5	
baselineR2	K	1000	46	50	1.5	
baselineR3	K	1000	46	50	1.5	
baselineR4	K	1000	46	50	1.5	
baselineR5V	K	1000	46	50	1.5	
baselineR5H	K	1000	46	50	1.5	
<b>Effect Cld Opt Depth</b>						As a MIF quantity, $\tau_{eff}$ is the cloud effective optical depth defined in §6.3. It is computed from cloud radiance observations. Only Ce <sub>eff</sub> obtained from the window channel of each radiometer are saved for diagnosis.
$\tau_{eff\_118V}$	-	1000	46	50	1.5	
$\tau_{eff\_118H}$	-	1000	46	50	1.5	
$\tau_{eff\_190}$	-	1000	46	50	1.5	
$\tau_{eff\_240}$	-	1000	46	50	1.5	
$\tau_{eff\_640}$	-	1000	46	50	1.5	
$\tau_{eff\_2T5V}$	-	1000	20	~10	0.3	
$\tau_{eff\_2T5H}$	-	1000	20	~10	0.3	
<b>Cloud Extinction</b>						$\tau_{cext}$ is cloud ice extinction retrieved (Chapter 7). L and H stand for low and high $h_t$ . The H-extinction profiles are retrieved from the window channel using the 2D tomographic method. The L-extinction profiles are retrieved from multiple channels in a wide band on a MIF basis.
$\tau_{cext\_L\_118}$	km <sup>-1</sup>	1000	46	17x4	2.0	
$\tau_{cext\_L\_200}$	km <sup>-1</sup>	1000	46	17x4	2.0	
$\tau_{cext\_H\_190}$	km <sup>-1</sup>	1000	46	17	0.5	
$\tau_{cext\_H\_240}$	km <sup>-1</sup>	1000	46	17	0.5	
$\tau_{cext\_H\_640}$	km <sup>-1</sup>	1000	46	17	0.5	
$\tau_{cext\_H\_2T5}$	km <sup>-1</sup>	1000	46	17	0.5	
<b>Size Distribution</b>						Particle size distribution (PSD) file contains distribution indices as a function of pressure and interacts with the full cloud forward model to test/constrain MLS sensitivity to ice particle size distributions. Mass mean diameter ( $D_m$ ) file contains estimated mean ice particle size as a function of pressure.
PSD	-	1000	46	17	0.5	
$D_m$	-	1000	46	17	0.5	
<b>Cloud Radiance</b>						These are upper-sideband radiances estimated from the measurements at ~200 and 245 GHz for each MIF (Appendix A).
R2:190.B2UF:H2O.C13	K	1000	46	~60	2.0	
R3:240.B8UF:PT.C13	K	1000	46	~60	2.0	
Total					~31	

Table 2-4 Level 2 cloud diagnostic files (continued)

Product	Unit	Vertical Range (hPa)		No. of Vertical Levels	Daily Vol. (Mb)	Comments
		Max	Min			
Subtotal from above					~31	
<b>Cloud Radiances</b>	K	1000	46	~20	70	<p>This file contain GHz cloud radiances for every 1/2 second at tangent pressures greater than 46 hPa, which yields about 20 MIFs for each MAF and 100 frequency channels.</p> <p>The THz cloud radiances have about 7 MIFs in each MAF but with two polarizations.</p>
R1A:118.B32W:PT.C1	:	:	:	:		
R1A:118.B32W:PT.C2	:	:	:	:		
R1A:118.B32W:PT.C3	:	:	:	:		
R1A:118.B32W:PT.C4	:	:	:	:		
R1A:118.B22F:PT.C1	:	:	:	:		
R1A:118.B22F:PT.C2	:	:	:	:		
R1A:118.B22F:PT.C24	:	:	:	:		
R1A:118.B22F:PT.C25	:	:	:	:		
R2:190.B2LF:H2O	:	:	:	:		
C13, (C12-C1), (C25-C14)	:	:	:	:		
R2:190.B3LF:N2O	:	:	:	:		
(C25-C10)	:	:	:	:		
R2:190.B4LF:H2O	:	:	:	:		
(C1-C2), (C24-C25)	:	:	:	:		
R2:190.B5LF:CIO	:	:	:	:		
(C1-C2), (C24-C25)	:	:	:	:		
R2:190.B6LF:O3	:	:	:	:		
(C1-C2), (C22-C25)	:	:	:	:		
R3:240.B33W:O3.C1	:	:	:	:		
R3:240.B33W:O3.C2	:	:	:	:		
R3:240.B33W:O3.C3	:	:	:	:		
R3:240.B33W:O3.C4	:	:	:	:		
R3:240.B8LF:PT	:	:	:	:		
C13,(C12-C1),(C25-C14)	:	:	:	:		
R3:240.B9F:CO.(C25-C14)	:	:	:	:		
R4:640	K	1000	46	~20	0.7	
R5V, R5H	K	1000	46	~7	0.3	
Subtotal					71	
Total					~102	

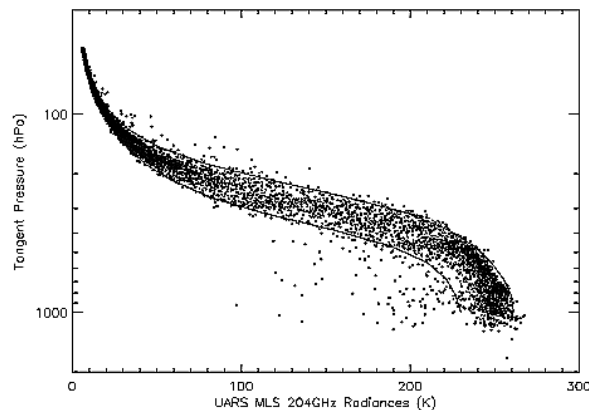
### 3 Cloud Flag Algorithms

The basic quantity for cloud detection is the so-called cloud-induced radiances ( $\Delta T_{\text{cir}}$ ). Usually, the  $\Delta T_{\text{cir}}$  needs to be determined before tropospheric retrievals can be processed to prevent the retrieval from becoming unstable. The clear-sky retrieval can cope with some cloud contaminations by including a so-called “baseline” variable in the state vector. The “baseline” can absorb most of the spectrally-flat radiance induced by clouds, but strong cloud scattering may still cause serious problems in gas retrievals. Hence, we develop a cloud flag algorithm to signal that such serious situations are happening. This cloud flag algorithm also provides  $\Delta T_{\text{cir}}$  to the cloud ice retrieval algorithm.  $\Delta T_{\text{cir}}$  may be re-calculated for better accuracy as gas retrievals are improved in retrieval phases.

#### 3.1 Cloud Effects

Clouds can affect MLS radiances at  $h_t < \text{cloud top}$  but the cloud effects can vary substantially with frequency and tangent height. Figure 3.1 shows UARS MLS radiance measurements at  $\sim 203$  GHz during limb-scan operations. In this case, clear-sky radiance profiles are mostly clustered in a narrow band with clear upper and lower bounds. Water vapor variabilities cause most of the radiance spread within the band. A few measurements outside the clear-sky band are indicative of clouds where the cloud-induced radiance  $\Delta T_{\text{cir}}$  (the difference from the clear-sky limit) can be as high as 30 K at a tangent pressure of  $\sim 150$  hPa or -130 K at  $> 700$  hPa. The instrument noise ( $\sim 0.09$  K) is generally negligible compared to these cloud effects. Lacking contrasts to clear-sky radiances (see Appendix D), clouds become difficult to detect at 250-700 hPa. Thus, for the best cloud detection, we have to rely on limb radiances in optically thin (at high  $h_t$ ) or optically thick (at low  $h_t$ ) situations.

Figure 3.1 UARS MLS 204 GHz radiances measured on 1 March 1992. The general radiance increase with tangent pressure is due to dry and water vapor continua, and the radiance variability is roughly bounded by water vapor variation between 0% and 100% saturation. The outliers are indicative of clouds (see text).



The limb  $\Delta T_{\text{cir}}$  at high  $h_t$  could arise from narrow thick-and-dense towers (e.g., deep convective core) or from extensive cirrus outflows. Because UARS MLS limb measurements are separated by 15 km horizontally, the correlation between the adjacent  $\Delta T_{\text{cir}}$  measurements could be used to infer the sizes of cloud systems. Poor point-to-point correlation suggests that the clouds be likely of deep convective type since their sizes are typically 10-50 km, whereas extensive cirrus anvils would produce a better point-to-point correlation. The limb-tracking data from UARS MLS suggest that clouds sensed by 203 GHz at tropopause heights are mostly of convective type with a few cases blended with broad warmer-than-normal features in the brightness temperature. Long-lived, extensive thin cirrus do not contribute significantly to the

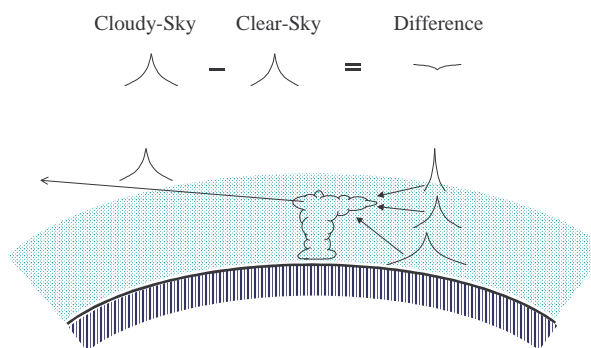
MLS  $\Delta T_{cir}$  because of low  $IWC$ s and small ice particles. These UARS MLS measurements provide valuable cloud statistics for Aura MLS cloud algorithm development.

In principle ice emission and scattering can both cause the excess radiances at  $h_t > 12$  km where scattering directs the radiation from below and above into the LOS. At these heights, the total scattered radiances from below are always positive and thus bring in brightness temperature radiation higher than the normal background whereas the scattered radiance from above brings in colder radiation (cosmic background + downward radiation). In addition to scattering, cloud ice emission itself adds radiation to the normal background. If  $\Delta T_{cir}$  is dominated by ice emission, ice emission would behave like a gas species and the  $\Delta T_{cir}$  is directly proportional to cloud ice mass [Appendix B]. In this case, the  $\Delta T_{cir}$ - $IWC$  relation is independent of particle size distributions (PSD). If the process is dominated by scattering, where the number of large particles becomes significant, the retrieval requires accurate knowledge of PSD, shape and ice density, as well as surface emission and cloud distribution. According to in-situ PSD measurements [references in Appendix E], cloud-induced radiances at frequencies  $> 200$  GHz are mostly due to ice scattering rather than emission.

At tangent heights  $< 8$  km, high clouds tend to scatter more radiance out of than into the LOS, causing a negative effect in the total radiance. Cloud emission is generally negligible compared to scattering effects in these cases. Cloud scattering, self-extinction (e.g., opaque clouds), and atmospheric absorption are most important radiative transfer processes in this case. At high latitudes surface emission and reflection may become non-negligible as the surface pressure is low. In mixed-phase clouds, emission and scattering from liquid clouds (normally below  $\sim 5$  km) need also to be taken in consideration.

Cloud scattering can create serious side effects on clear-sky gas retrievals and need to be treated carefully in modeling and in the attempts to correct them. As shown in Figure 3.2, the differences between cloudy and clear radiances are not spectrally flat near a spectral line. The distortion to the line shape can be caused by several processes in the radiative transfer. Among them, two mechanisms are most important: (a) attenuation between clouds and the instrument and (b) scattered radiation from clouds. In a strong attenuation situation (like one due to stratospheric  $O_3$ ), cloud-induced radiances would not be spectrally flat even though scattered radiances were spectrally flat.

Figure 3.2 Schematic to show the impact of cloud scattering on the clear-sky gas lineshapes in a limb observation. Scattered light can differ significantly from clear-sky radiances and make them difficult to use for the gas retrievals in the presence of clouds.



### 3.2 Cloud-Induced Radiances

As outlined in Figure 3.3, the  $\Delta T_{cir}$  calculation requires information on temperature and tangent pressure, which comes initially from a preliminary T/P retrieval that uses only the radiances above  $\sim 16$  km (namely, cloud-free altitudes). The tangent pressures below  $\sim 16$  km are

extrapolated using the retrieved stratospheric T, P and auxiliary tropospheric temperatures. Once the pointing is established,  $\Delta T_{\text{cir}}$  can be computed with various methods.

The methods for cloud detection generally fall into two categories: (i) empirical approaches based on clear-cloudy sky contrasts between adjacent measurements, and (ii) radiative-transfer (RT) model approaches to calculate expected clear-sky radiance limits for every given atmospheric condition. In either case, the algorithm needs to be robust and reliable enough for exception handling, such as missing data, unknown atmospheric background, and instrument pointing uncertainties.

### 3.3 Empirical Methods

Two empirical approaches have been used to determine clear-sky radiances with some success when applied to UARS MLS 203-GHz data. The first method determines the clear-sky radiances based on the statistics at each latitude bin and attributes outliers as cloudy radiances. The second method finds the clear-sky radiances from nearby measurements (at the same tangent height) based on different spatial scales of cloudy and clear radiance variabilities. These methods are detailed in the following.

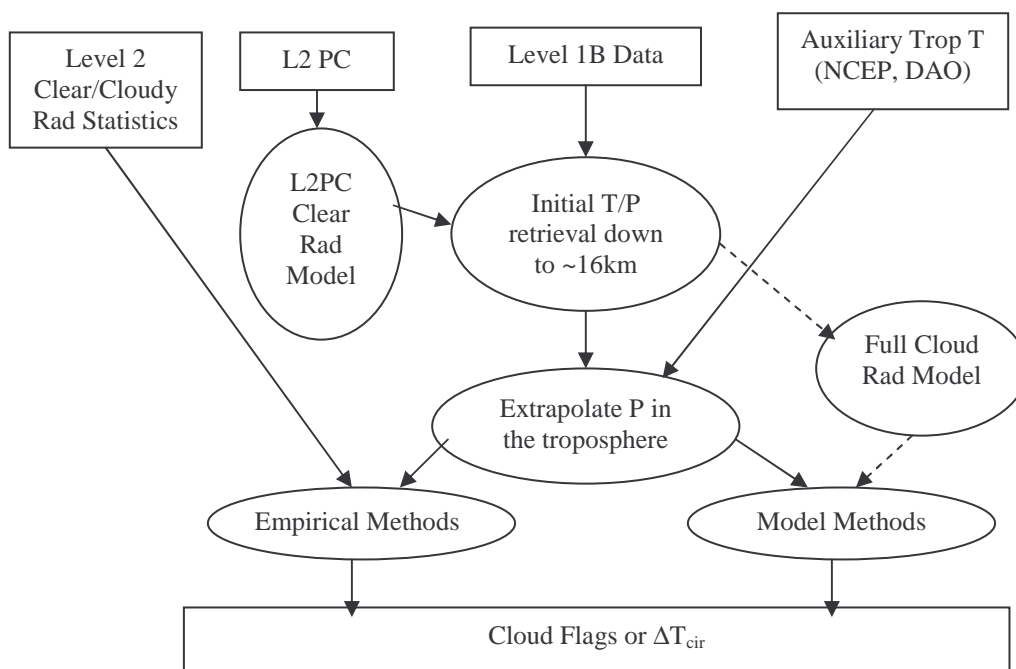


Figure 3.3 Flow Diagram of cloud flag algorithms. Dashed lines indicate the alternative approach.

#### 3.3.1 Clear-sky statistics approach

As shown in Figure 3.1, clear-sky radiance variability is bounded tightly at high and low tangent heights, and good statistics can be obtained with a few days of data. For each latitude bin, the clear-sky variability normally exhibits a Gaussian-like distribution. Thus, we assume that this variability is bounded by the upper and lower limits in terms of the mean and the standard deviation (accordingly,  $3\sigma$  could reduce false detection to  $< 0.1\%$ ). This approach can be readily

implemented for any channel and tangent pressure, a useful alternative during early operation periods when the MLS forward model is under tuning.

Table 3-1 shows typical values of the mean and 2-sigma standard deviation (5% false detection) of the UARS 203GHz radiance near the equator. The empirical method has been attractive at  $h_t > 14$  km or  $z < 5$  km, showing  $\sim 3$  K and  $\sim 10$  K with the 2-sigma criteria. The standard deviations are larger at the transition altitudes due to greater water vapor variability, making cloudy radiance difficult to detect.

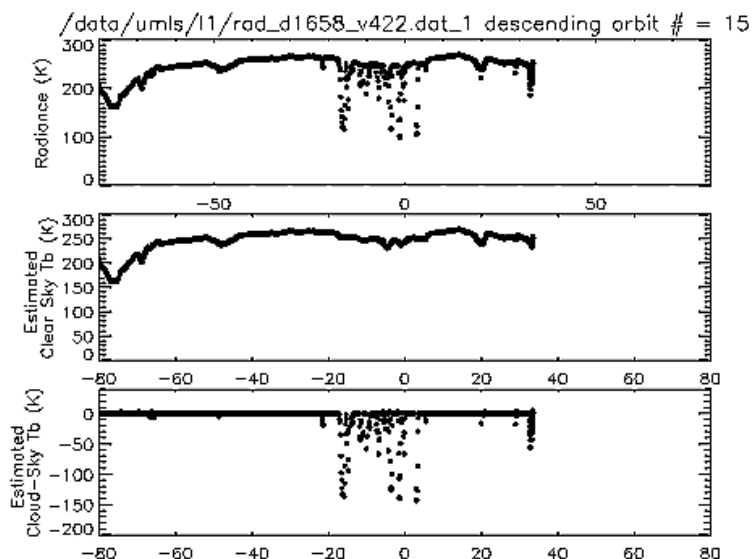
Table 3-1 Statistics of UARS MLS 203-GHz radiances near the equator.

$Z = -\log_{10}(P/1\text{hPa})$	Mean $T_b$	2 sigma
-3.00	247.0	9.4
-2.92	247.0	8.2
-2.83	242.5	7.2
-2.75	236.5	6.7
-2.67	227.5	9.0
-2.58	214.0	8.3
-2.50	186.0	9.0
-2.42	146.5	12.1
-2.33	88.5	16.0
-2.25	61.0	12.0
-2.17	41.5	13.1
-2.08	30.5	3.3
-2.00	22.0	2.3

### 3.3.2 Horizontal differential approach

Another empirical approach is to make use of different horizontal scales associated with cloudy and clear radiance variations. Figure 3.4 illustrates this method with the UARS MLS measurements during limb tracking observations when the instrument is viewing perpendicularly from the flight direction and measurements are separated by  $\sim 15$  km in along-track distance. The top panel shows the raw radiances with smoothly-varying components (due to clear-sky variability) and scattered components (due to clouds). Using the 7-point smoothing along track iteratively, the smooth (middle) and scattered (bottom) components can be separated as in Figure 3.4 (b,c). This method works particularly well for UARS MLS sampling, where clear and cloudy radiances exhibit large differences in horizontal variability, but needs to be tested for the Aura case where MLS viewing is in the same direction as the satellite velocity.

Figure 3.4 UARS MLS limb-tracking radiances (top panel) measured on 26 March 1996 when the pointing was kept at  $h_t = -10$  km. Clear and cloudy-sky radiances are separated according to slowly (middle) and rapidly (bottom) varying components.



### 3.4 Model Methods

RT models have been better than the empirical methods for handling atmospheric variability, missing data and scan anomalies. Especially in the transition altitudes where empirical approaches are likely to fail, RT models may still be able to provide a reliable estimate on clear-sky radiances so that cloud-induced components can be detected.

#### 3.4.1 Single-frequency methods

##### 3.4.1.1 Assuming $RH_i=110\%$

Once initial tangent pressure and temperature are retrieved, we estimate clear-sky radiance limits by assuming  $RH_i=110\%$  and  $RH_i=0\%$  for tropospheric  $H_2O$  limits. The condition  $RH_i=110\%$  accounts for a half of supersaturation cases according to the exponential power law deduced from aircraft data (Sprichtinger et al., 2002). The radiances corresponding to these limits are represented by  $T_{b0}$  and  $T_{b110}$ , respectively. **Error! Reference source not found.** illustrates the single-channel method using the RT model [Read et al., 2001] for UARS 203-GHz measurements at high  $h_t$ . For  $p < p_l$  (which is  $\sim 300$  hPa in the UARS case),  $\Delta T_{\text{cir}}$  is defined as:

$$\Delta T_{\text{cir}} = T_b - T_{b110} \quad (\text{Eq 3.1})$$

Cloud radiances must satisfy the criteria as follows,

$$\Delta T_{\text{cir}} > \sigma_l \quad \text{for} \quad p < p_l \quad (\text{Eq 3.2})$$

where the threshold  $\sigma_l$  is introduced to embrace potential modeling uncertainty (3 K in the UARS case based on the statistics) and  $p_l$  is the cutoff pressure for high  $h_t$  radiances.

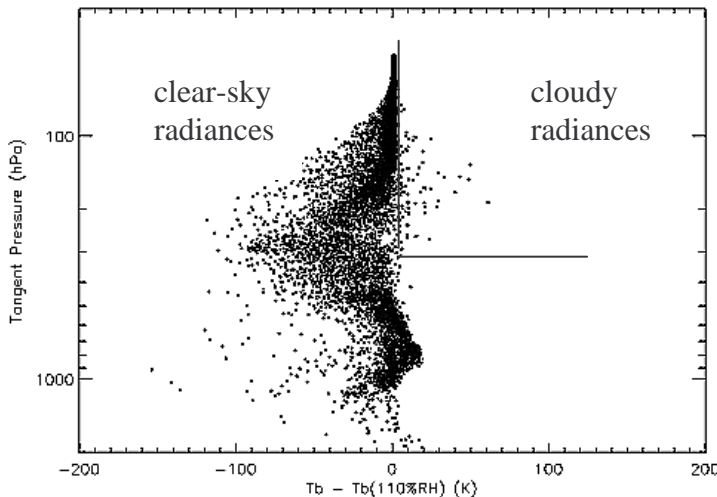


Figure 3.5 Differences between the observed and the modeled clear-sky limit for UARS MLS 203 GHz. Above  $\sim 300$  hPa most differences are close to or less than 0 K except for those affected by clouds. The radiance differences below  $\sim 300$  hPa cannot be used to detect clouds because of complicated behaviors of the dry and wet profiles.

At low  $h_t$  [Figure 3.6], the  $\Delta T_{\text{cir}}$  is defined as:

$$\Delta T_{\text{cir}} = T_b - \min(T_{b0}, T_{b110}) \quad (\text{Eq 3.3})$$

and we flag MIF radiances if:

$$\Delta T_{\text{cir}} < \sigma_2 \quad \text{for} \quad p > p_2 \quad (\text{Eq 3.4})$$

where  $p_2$  is the cutoff pressure for defining low- $h_t$  radiances (which is  $\sim 300$  hPa in the UARS case). The threshold  $\sigma_2$  is dependent on model error, which is usually higher than  $\sigma_1$  due to temperature and H<sub>2</sub>O uncertainties ( $\sim 10$  K in the UARS case based on statistics in the tropics). These radiance thresholds,  $\sigma_1$  and  $\sigma_2$ , can be frequency and pressure dependent, and will be provided as user input parameters.

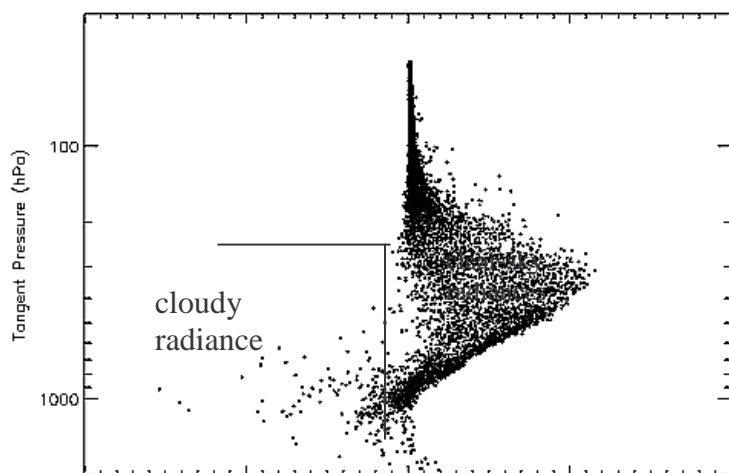


Figure 3.6 Differences between the measured radiances and modeled clear-sky minimums. The negative values with  $\Delta T_{\text{cir}} < -10\text{K}$  are flagged as clouds. The threshold of  $-10\text{K}$  accounts for model uncertainties.

### 3.4.1.2 Using the retrieved profiles

The method based on the assumption of  $\text{RH}_i=110\%$  works well in the tropics where the tropospheric temperature decreases rapidly ( $\sim -6^\circ\text{C}/\text{km}$ ) and nearly uniformly. However, it does not work well at high latitudes where the temperature lapse rate can be altered largely by planetary waves. As a result, high false alarms and misses are associated with the above method when applied to radiance measurements at latitudes  $50^\circ$  poleward.

An improvement on the single-frequency method is to take the retrieved constituents (e.g. H<sub>2</sub>O, O<sub>3</sub>) as the model inputs and use the radiance difference between measured and modeled for cloud detection. Since MLS can retrieve or know constituent profiles relatively well after some initial treatments of cloud effects, this modified single-frequency method is particularly useful to further improve the  $\Delta T_{\text{cir}}$  calculation in the situations where cloud was poorly detected. The disadvantage of this method is its strong dependence on model biases such as those due to incorrect wet and dry continuum coefficients.

### 3.4.2 Multi-channel methods

The single-channel methods generally suffer from inability to detect clouds at the transition tangent heights (say 8-12 km for 203 GHz). Most sophisticated and likely better methods can be implemented by using radiances from channels over a broad bandwidth (say, over 7 GHz with R2 channels).

Rough speaking, cloud effects induce mostly an offset to the limb radiance over a broad spectral range. Such offset can be handled by the MLS L2 retrieval with a quantity called *baseline*. Currently, the L2 baseline represents only the spectrally-flat component and is retrieved

independently for each MLS radiometer. The retrieved baseline can absorb most of the  $\Delta T_{cir}$ , and therefore is a useful proxy for  $\Delta T_{cir}$ . Similar to the above ones, this method has a disadvantage of being affected strongly by model biases.

A more advanced method for the  $\Delta T_{cir}$  calculation is to retrieve cloud volume scattering and absorption coefficients in conjunction with other gas species. This requires generalization of MLS forward model such that cloud-induced radiances are adequately modeled. This approach, along with modifications of MLS retrieval algorithm, is currently under investigation.

### 3.5 False Cloud Detection

The  $\Delta T_{cir}$  uncertainty depends on how well the clear-sky radiances can be modeled. For the model method using a single-frequency channel, the model accuracy is affected largely by pointing, temperature, and uncounted gas abundances. As discussed in Read et al. (2001), the dry and wet continuum coefficients can be modeled empirically to 5%, which absorbs most of the systematic biases in the temperature. As shown in Figure 3.5, the deduced  $\Delta T_{cir}$  show two distinct distributions in a histogram where the clear-sky measurements exhibit a Gaussian-like distribution narrowly around  $\Delta T_{cir}=0$  and the cloudy radiances tail off exponentially for the positive values.

Figure 3.7 A histogram of the UARS MLS 203-GHz  $\Delta T_{cir}$  at 100 hPa. Symbols represent the number of  $\Delta T_{cir}$  measurements in 1-K bins from six months of data in early 1992 at latitudes between 25°S and 25°N. A Gaussian distribution is fitted to the clear-sky variability with the bias and standard deviation indicated in the plot. The number of cloudy-sky measurements drops off exponentially at large  $+\Delta T_{cir}$ . The 3 K cloud flag threshold is indicated by the dashed line. False cloud detection is described by the portion of the Gaussian distribution with  $\Delta T_{cir} > 3$  K and causes a bias of 0.03 K in  $\Delta T_{cir}$  and 0.9% in cloud occurrence frequency at 100 hPa.

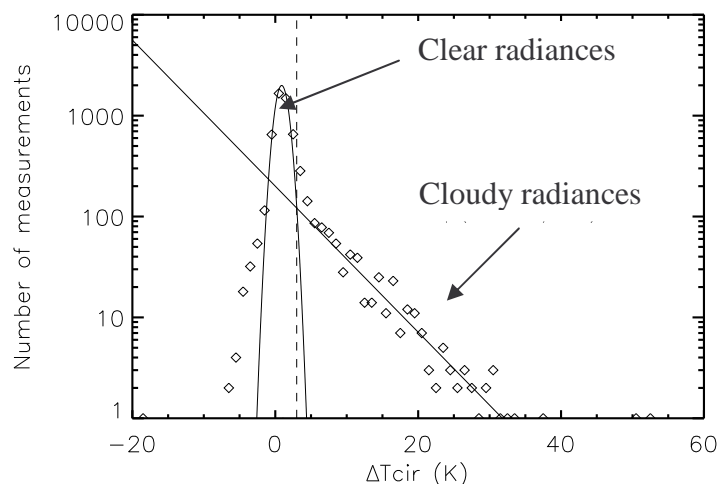


Figure 3.7 shows that the 100-hPa clear-sky  $\Delta T_{cir}$ , fitted well to a Gaussian distribution, and has a bias of 0.9 K and a standard deviation of 0.9 K at 100 hPa, due to a combination of error in  $P_{tan}$  and  $T$  and other uncertainties in  $H_2O$ ,  $O_3$  and  $HNO_3$ . Error in  $P_{tan}$  and  $T$  may be latitude-dependent. Consequently, false detection may increase at winter high latitudes where wave activity is strong. False detection could introduce a bias to  $\Delta T_{cir}$ . In the 100hPa case it can be determined by the portion of the Gaussian distribution with  $\Delta T_{cir} > 3$  K. If a 3-K threshold is used, false detection can cause biases of 0.03 K in  $\Delta T_{cir}$  and 0.9% in cloud occurrence frequency. The errors drop sharply to 0.001 K and 0.025%, respectively, when the 4-K threshold is used.

For the 640-GHz (R4) and THz (R5) radiances, additional spectral averaging is needed to reduce large random error of radiance measurements. The single-channel noise of Band10.C1 (1.5 K) and Band15.C1 (~4 K) is perhaps too high for cloud detection.

## 4 Radiative Transfer Model for Cloudy Atmospheres

### 4.1 Geometry and Radiative Transfer Equation

This chapter describes the theoretical basis and mathematical algorithms for microwave radiation propagation through cloudy atmospheres. The radiant energy, or radiance measured by MLS, is governed by the radiative transfer equation that needs to be solved numerically, and the numerical methods we use are also described in the chapter.

#### 4.1.1 Limb-Viewing Geometry and Model Configuration

The geometry of the MLS observation is sketched in Figure 4.1, where the model atmosphere is divided into spherical-shells, showing MLS line-of-sight (LOS) direction along limb path  $s$ . MLS radiance ( $I$ ) represents the radiation at  $s=0$ , above most of the atmosphere.

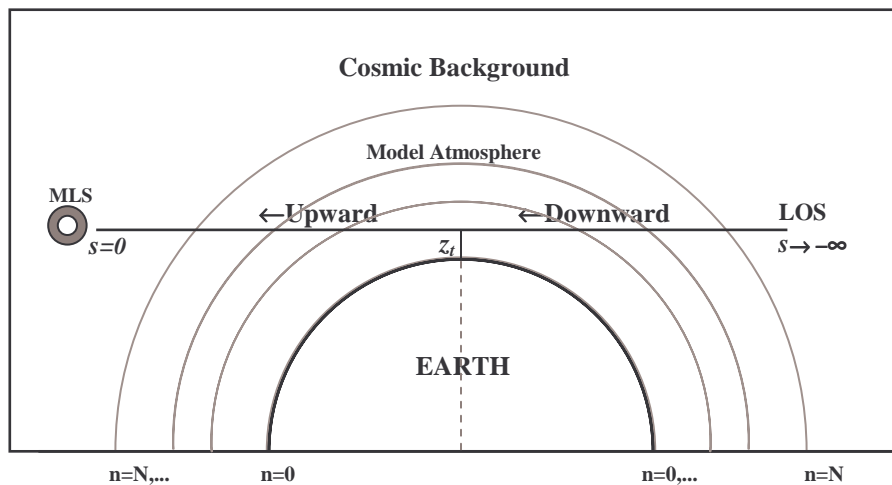


Figure 4.1 MLS limb viewing geometry.

The atmosphere state includes not only T, P, and gas abundances, but also cloud ice and water profiles and hydrometeor properties. In the 1D case, the model atmosphere, which is detailed in the next chapter, is represented by homogeneous and isothermal spherical layers. The standard model configuration has  $N=640$  layers that are 0.125 km thick and evenly distributed between 0 and 80 km. The number of layers and the model top height are controlled by user input in the MLS Level 2 algorithm.

Cloud layers have the same resolution as in clear-sky atmospheres, and are treated as single or multiple layers of non-zero ice-water-content (IWC) and/or non-zero liquid-water-content (LWC). As illustrated in Figure 4.2, the cloud boxes have all layers parallel to the local surface with the top/base defined by  $H_{CT}$  or  $H_{CB}$ . In the 1D model, the cloud boxes will occupy the entire spherical shell at that altitude. It is important to model cloud-induced radiances in the 2D geometry because of the long path length in MLS case. To understand the multi-frequency

measurements, cloud inhomogeneity along the path must be taken in account as MLS channels all have different penetration depths and sensitivities to cloud ice. In the current configuration only IWC and cloud extinction profiles are in the retrieval vector, while other cloud model parameters are supplied by the user input files in the Level 2 configuration [Livesey, 2004].

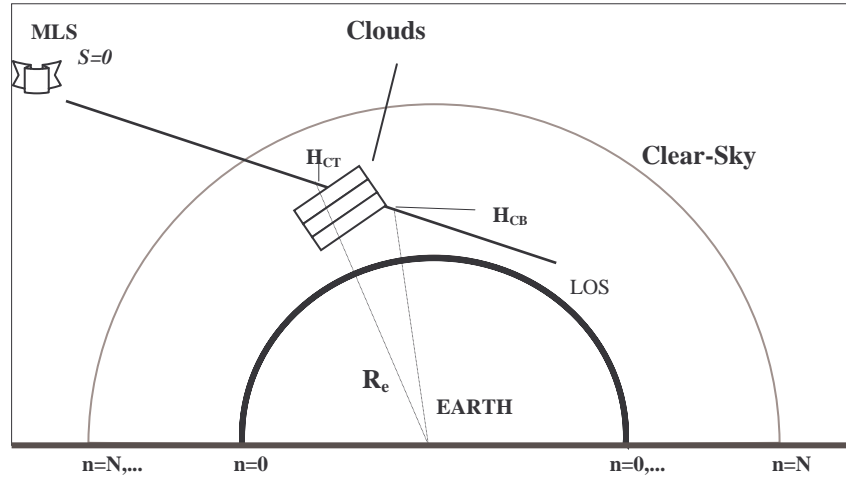


Figure 4.2 An example of multiple layer cloud. Three cloud layers are illustrated here by boxes.

#### 4.1.2 The Generalized Radiative Transfer Equation

The radiative processes across an elemental length ( $ds$ ) along the LOS ( $s$ ), is described by the radiative transfer equation

$$\frac{dI}{ds} = -\beta_e I + \beta_a B + \beta_s J_s \quad (\text{Eq 4.1})$$

where  $I$  is radiance in SI units of  $\text{Wm}^{-2}\text{sr}^{-1}\text{Hz}^{-1}$ , and following coefficients are in unit of  $\text{m}^{-1}$ :

$$\begin{aligned} \beta_e &= \beta_{\text{gas}_a} + \beta_{c_s} + \beta_{c_a} && \text{total volume extinction coefficient,} \\ \beta_{\text{gas}_a} &&& \text{gas volume absorption coefficient,} \\ \beta_{c_s} &&& \text{cloud volume scattering coefficient,} \\ \beta_{c_a} &&& \text{cloud volume absorption coefficient,} \\ \beta_a &= \beta_{\text{gas}_a} + \beta_{c_a} && \text{total volume absorption coefficient.} \\ \beta_s &= \beta_{c_s} && \text{total volume scattering coefficient.} \end{aligned}$$

Here we assume the only scatterers are clouds. The source function  $B$  represent thermal (air + cloud) emission in terms of the Planck function at temperature  $T$ , i.e.,

$$B = \frac{2h\nu}{c^2} \left( \frac{1}{e^{h\nu/kT} - 1} \right). \quad (\text{Eq 4.2})$$

where  $\nu$  is frequency,  $c$  is the speed of light,  $k$  is Boltzmann's constant and  $h$  is Planck's constant.  $B$  has the same units as radiance  $I$ . The second source function  $J_s$  accounts for radiation

scattered from clouds (Ulaby *et al.* 1981), which is an angular integration of radiation from all directions, i.e.,

$$J_s = \frac{1}{4\pi} \oint P(\Omega, \Omega') I(\Omega') d\Omega' \quad (\text{Eq 4.3})$$

where  $\Omega$  is the solid angle in the LOS direction,  $\Omega'$  is the incident solid angle of scattered radiation. The difference between  $\Omega$  and  $\Omega'$  is called scattering angle  $\theta$ .  $P$  is the scattering phase function that will be discussed in §4.4.2.

## 4.2 Numerical Method

This section outlines how the radiative transfer equation can be solved for parameterized radiative fluxes, extinction and augmentation, and what assumptions are made. Parameterizations involved in solving Eq 4.1 are described in §4.3 and §4.4.

The strategy for solving Eq 4.1 in limb-viewing geometry is as follows. First, for each cloud layer we calculate cloud radiative properties, i.e.  $\beta_{c_s}$ ,  $\beta_{c_a}$  and phase functions using Mie theory. Second, we calculate source functions  $B$  and  $J_s$ .  $B$  is simply clear-sky emission whereas  $J_s$  must be solved locally from  $B$ . We choose the commonly-used iterative approach to solve  $J_s$  with Eq 4.1 on plane-parallel geometry [Wilheit *et al.*, 1982]. Once these source functions are calculated, the final RT integration along the limb path is carried out. Detailed steps of radiative transfer modeling are given in 4.2.4.

### 4.2.1 Basic Assumptions

The radiative transfer equation for cloudy-sky MLS radiances is developed with the following key assumptions:

- (1) Polarization differences of cloud scattering are neglected. This eliminates the separation of Equation (4.1) into polarized components like one used in Tsang and Kong [1977].
- (2) Atmospheric emission is considered to be from a perfect blackbody so that the source function can be expressed in terms of Planck's function (Eq. 4.2)

Due to the great complexity of cloud microphysical properties, the following assumptions are made to simplify the calculations of cloud scattering:

- (3) Scattering is independent (or incoherent) among different cloud hydrometeors, which is valid at microwave frequencies since the mean distance between cloud hydrometeors is much larger than their radii (van de Hulst, 1981 and Ulaby *et al.*, 1981).
- (4) Cloud hydrometeors are spherical. Shape differences are neglected. The particle diameter is related to its mass  $M$  by:

$$\frac{4}{3}\pi \cdot \left(\frac{D}{2}\right)^3 \cdot \rho = M$$

or  $D = (6M/\pi\rho)^{1/3}$ , where  $\rho$  is either ice or water density.

- (5) Cloud hydrometeors are composed of pure water. As default, the parameterization in McFarquhar and Heymsfield (1997) is used for ice particle size distributions (PSD).

Effect of other PSDs is discussed later in Appendix E. Liquid water droplets follow a Gamma size distribution. Effects of impurities on the dielectric constants are neglected.

- (6) Single scattering is assumed for phase function and scattering calculations within each cloud layer. Multiple scatterings between cloud layers are effectively taken into account through an iterative approach in solving Eq. 4.1. See further discussions later in this chapter.

### 4.2.2 General Definitions

The following definitions are made to simplify the radiative transfer equation:

- (1) Transform radiance and source functions to measurement-related variables:

$$\hat{T} \equiv \frac{c^2}{2k\nu^2} B \quad (\text{Eq 4.4})$$

$$T_b \equiv \frac{c^2}{2k\nu^2} I \quad (\text{Eq 4.5})$$

where  $\hat{T}$  and  $T_b$  are in K.  $T_b$  is radiance brightness temperature and used throughout this document. Similarly, scattering source function  $J_s$  is defined as *scattered radiance*  $T_{scat}$ , namely,

$$T_{scat} = \frac{1}{4\pi} \oint P(\Omega, \Omega') T_b(\Omega') d\Omega' \quad (\text{Eq 4.6})$$

- (2) The optical depth at height  $z$  is defined by  $\tau = \int_0^z \beta_e(z') dz'$ .

- (3) The *single scattering albedo*  $\omega_0$ , widely used to characterize relative importance of cloud scattering over extinction, is defined as the ratio of cloud volume scattering and total (cloud + air) extinction coefficients, i.e.  $\omega_0 = \beta_{c-s} / \beta_e$ , as used in Stamnes *et al.* [2000]. The term “*single*” means only single scattering is considered in computing the cloud volume scattering coefficient. This is different from the usual definition where no air extinction is considered. Normally, multiple scattering is considered in computing the volume scattering coefficient  $\beta_{c-s}$  and  $\omega_0$  in the radiative transfer is defined as the fraction of incident beam scattered by that volume.

### 4.2.3 The Discrete Equation

With the above assumptions and definitions, Equation (4.1) can be written as:

$$\begin{aligned} \mu \frac{dT_b(\mu, \tau)}{d\tau} + T_b(\mu, \tau) &= (1 - \omega_0) \hat{T}(\tau) + \frac{\omega_0}{4\pi} \oint P(\Omega, \Omega') T_b(\Omega') d\Omega' \\ &= (1 - \omega_0) \hat{T}(\tau) + \omega_0 T_{scat} \end{aligned} \quad (\text{Eq 4.7})$$

where  $\mu$  is cosine of zenith angle and  $d\tau = \beta_e \cdot dz = \beta_e \cdot \mu \cdot ds$  is the layer optical thickness. The form of the equation is identical between limb and nadir applications. For plane-parallel cases, often used in nadir applications,  $\mu$  is independent of altitude; whereas in the spherical geometry,  $\mu$  is a function of  $h_t$  and altitude  $z$ .

Eq 4.7 is further separated into downward and upward components. The discrete forms of the downward and upward radiance calculations are written as follows:

*Downward:*

$$T_b[-\mu_n(h_t), n] = T_b[-\mu_{n+1}(h_t), n+1]e^{-(\tau_{n+1}-\tau_n)/\mu_{n+1}(h_t)} + (1 - e^{-(\tau_{n+1}-\tau_n)/\mu_{n+1}(h_t)}) \left\{ (1 - \omega_0)\hat{T}(n) + \omega_0 T_{scat}[-\mu_{n+1}(h_t), n] \right\} \quad (\text{Eq 4.8})$$

*Upward:*

$$T_b[\mu_n(h_t), n] = T_b[\mu_{n-1}(h_t), n-1]e^{-(\tau_n-\tau_{n-1})/\mu_n(h_t)} + (1 - e^{-(\tau_n-\tau_{n-1})/\mu_n(h_t)}) \left\{ (1 - \omega_0)\hat{T}(n) + \omega_0 T_{scat}[\mu_n(h_t), n] \right\} \quad (\text{Eq 4.9})$$

where  $n = 0, 1, 2, \dots, N$ , is the model layer index and  $\tau_n$  is the optical thickness for model layer  $n$ . Note that for the *Downward* radiation, the calculation is performed from the top of model atmosphere to the tangent point (or the surface); *Upward* radiation is calculated from the tangent point (or the surface) to MLS (or the top of the atmosphere). Normally, the tangent height is the bottom altitude of a model layer. Therefore, a half of the first layer above tangent height uses the *Downward* formulas and the other half uses the *Upward* one.

As mentioned above, Equations 4.8-4.9 have the same form for both plane-parallel and spherical geometry, except in the limb case  $\mu_n(h_t)$  is a function of  $h_t$  and layer altitude. In the plane-parallel models,  $\mu_n(h_t)$  is replaced by  $\mu_k$ , where  $k$  is the stream index. In spherical geometry  $\mu_n(h_t)$  is a function of altitude and tangent height as follows

$$\mu_n(h_t) \equiv \cos \Theta = \frac{\Delta z}{\sqrt{(z_{n+1} + R_e)^2 - (h_t + R_e)^2} - \sqrt{(z_n + R_e)^2 - (h_t + R_e)^2}} \quad (\text{Eq 4.10})$$

where  $R_e$  is the Earth radius and  $\Delta z = z_{n+1} - z_n$  is model layer-thickness. Figure 4.3 shows the spherical geometry of the  $\mu_n(z_t)$  calculation where LOS passes through layers  $n$  and  $n+1$  at altitude  $z_n$  and  $z_{n+1}$ , respectively. Tangent height  $h_t > 0$  if LOS does not intersect with the surface, and  $h_t \leq 0$  if the tangent point is at or below the surface.

The boundary condition of the radiative equation at top of atmosphere ( $n=N$ ) is given by:

$$T_b[-\mu_N(h_t)] = \hat{T}_{2.7} \quad (\text{Eq 4.11})$$

where  $\hat{T}_{2.7} = c^2 B_{2.7} / 2k\nu^2$ , in which  $B_{2.7}$  is the Planck function at cosmic background temperature for  $T = 2.7$  K. When the tangent point is at or below Earth's surface, a surface boundary ( $n=0$ ) condition is used, i.e.,

$$T_b[\mu_0(z_t)] = \varepsilon_s T_s + (1 - \varepsilon_s) T_b[-\mu_0(h_t)] \quad (\text{Eq 4.12})$$

where  $\varepsilon_s$  and  $T_s$  are the surface emissivity and temperature, respectively.

The number of model layers is specified in the user input file, depending on model accuracy required. A recommended specification is given later in this chapter as a trade-off between computing time and model accuracy.

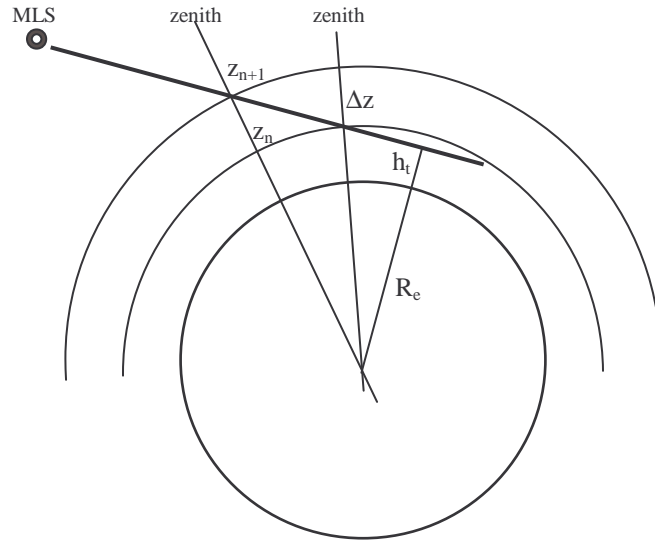


Figure 4.3 Diagram showing relationship between cosine of zenith  $\mu_n$ , tangent height  $h_t$ , Earth radius  $R_e$ , and the layer thickness  $\Delta z = z_{n+1} - z_n$ .

#### 4.2.4 Iterative Calculations for the Scattering Source Function

Cloud scattering source functions  $J_s$  need to be determined for all the cloudy layers before the RT calculation can be carried out for limb paths. The model to compute these source functions is the same RT equation except under plane-parallel geometry, which works well for microwave radiation as shallow angle calculations remain valid. The plane-parallel approximation suffers substantially for IR and visible radiation due to cloud inhomogeneity and large optical depths [Liou and Rao, 1996]. Instead using the doubling-adding method, the source functions at microwave are allowed to solve iteratively as cloud and surrounding radiation interacts with each other through Eq.(4.7). The iteration approach is imposed because initial clear-sky radiation may be changed by the presence of clouds. The final solution must be converged and self-consistent at all model layers such that both clear-sky and cloud scattering radiations satisfy Eq. 4.7. For source function calculations,  $\mu_n$  can be replaced with  $\mu_k$  ( $k=1, \dots, n\_streams$ ) in Eqs 4.8-4.9 for a number of streams, and the iterative calculations are detailed as follows:

##### Step-1 Initialization:

- Select a set of evenly-spaced streams  $\mu_k$ . Let radiance  $T_b(\mu_k, n)$  be a function of altitude (at layer  $n$ ) and angle  $\mu_k$ . Note that for each  $T_b$  ray in Figure 4.4  $\mu_k$  is constant at all the layers.
- Initialize radiance  $T_b(\mu_k, n)$  such that  $T_b(-\mu_k, n)^{down} = \hat{T}_c$  for all *downward* radiances and

$T_b(\mu_k, n)^{up} = 300 \text{ K}$  for all *upward* radiances.

### Step-2 Calculation of scattering source function:

- Identify cloud layers and read in cloud properties (e.g., IWC and particle size).
- Compute  $T_{scat}(\mu_k, n)$  using Eq 4.6 from  $T_b(\mu_k, n)$  for each angle  $\mu_k$  and each layer  $n$  where cloud is present.

### Step-3 Integration to update downward radiances:

- Apply Eq 4.8 for a new set of downward radiances  $T_b'(-\mu_k, n)^{down}$  for all streams  $k$ .

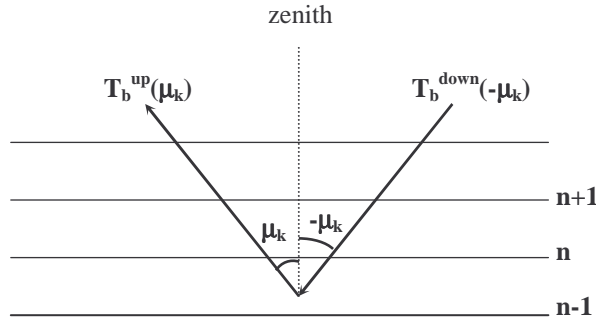


Figure 4.4 Radiative transfer in local cloud scattering calculations under a plane-parallel atmosphere.

### Step-4 Surface emission and reflection:

- For brightness temperature at the surface  $T_b'(\mu_k, 0)$ , a simple model is applied to provide the reflected and emitted radiances from the surface.

### Step-5 Integration to update upward radiances:

- Apply Eq 4.8 to calculate a new set of upward radiances  $T_b'(\mu_k, n)^{up}$  using  $T_{scat}(\mu_k, n)$  wherever applied. At the surface  $T_b'(\mu_k, 0)^{up}$  the surface reflection for  $T_b'(-\mu_k, 0)^{down}$  and surface emission are determined in Step-4.

### Step-6 Check convergence:

- Check if the new upward radiances at the top atmosphere agree with the old ones. If  $|T_b'(N) - T_b(N)| > \epsilon$ , where  $\epsilon$  is a convergence criterion (default  $\epsilon = 0.1 \text{ K}$ ) depending on specified model accuracy, update  $T_b(\mu_k, n)$  with  $T_b'(\mu_k, n)$ , then repeat step-2 to step-6. Once convergence is found,  $T_{scat}(\mu_k, n)$  are output.

## 4.2.5 Final Radiative Transfer Calculation at Limb

### Step-7 Interpolate scattering source function onto LOS:

- Determine  $\mu_n(h_t)$  at each layer along the LOS path for tangent height  $h_t$ . Note, for each  $T_i$  ray, angle  $\mu_n(h_t)$  changes as the ray passes through each model layer  $n$  (Figure 4.5).
- Interpolate  $T_{scat}(\mu_k, n)$  obtained in Step-6 to get  $T_{scat}[\mu_n(h_t), n]$  at each cloud along the LOS.

**Step-8 Perform integration along LOS:**

- Integrate the radiative transfer equation (4.8) to compute limb radiances at MLS. Again, the integration starts with downward calculation from the top atmosphere to the surface for all  $T_t[-\mu_n(h_t), n]^{down}$ , including cloud emission and scattering  $T_{scat}[\mu_n(h_t), n]$  wherever applicable. The boundary condition at the top of the atmosphere ( $n=N$ ) is given by equation (4.11).
- If the tangent height is at or below the surface, determine the reflected and emitted radiances  $T_t[\mu_n(h_t), 0]$  at the surface, otherwise, move directly to the next.
- Integrate the radiative transfer equation (4.9) upward to calculate the upward brightness temperatures  $T_t[\mu_n(h_t), n]^{up}$  for all model layers including cloud emission and scattering  $T_{scat}[\mu_n(h_t), n]$  wherever applicable.

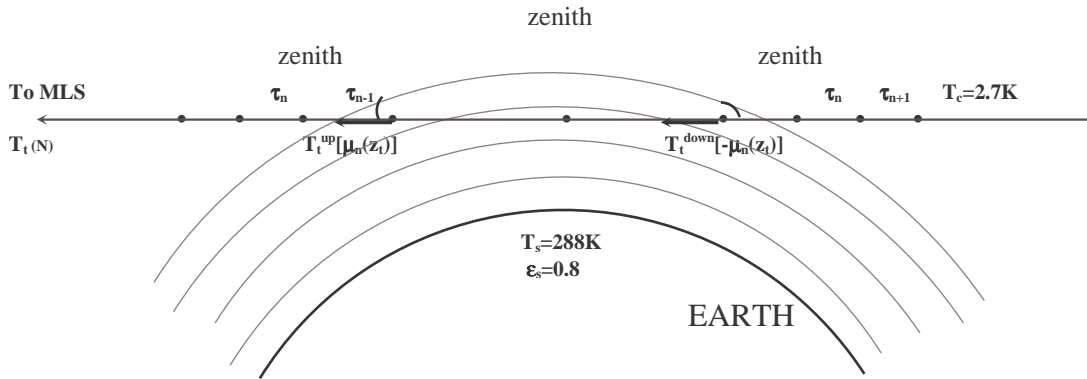


Figure 4.5 Geometry of limb viewing radiative transfer.

**Step-9 Output Results:**

- The limb radiance at the top atmosphere,  $T_t[\mu_n(h_t), N]$ , is the modeled radiance for a single frequency and a single ray. The double sideband summation and FOV averaging, as “observed” by MLS, are carried out in the same way as in the full clear-sky model [Read, 2004]. Spectral averaging over channel filters is not included in the cloudy-sky model.

**4.2.6 Flow Diagram of the Cloudy Sky Radiance Model**

To model MLS radiances, the above calculations (§4.2.4 and §4.2.5) need to be repeated for a set of frequencies and tangent heights. The resultant radiances are then convolved with the instrument filter shape, antenna pattern, and sideband ratio to complete MLS forward model. The convolved radiances are further interpolated onto MLS tangent heights that often vary with orbit. Because of complexities in cloudy-sky RT model, derivatives or sensitivities of MLS radiances to cloud parameters have to be computed using the finite differencing method.

A flow diagram of MLS *Cloudy Sky Radiance Model* is shown in Figure 4.6, containing several key modules, namely, *Model Input*, *Clear-Sky Radiation*, *Cloudy-Sky Radiation*, *Radiative Transfer*, and *Model Output*.

**Model Input** provides radiation frequency, model clear-sky atmosphere, and cloud model, all parameters in which come from user input files. The **cloud model** is a separate program that provides the cloud water content and size distribution profiles with parameters specified by the user (see Chapter 5).

**Clear-Sky Radiation Module** computes clear-sky gas absorption coefficient to be passed to the radiative transfer calculation. The clear-sky model is described briefly in section 4.3, which is a simpler version of the comprehensive one as described in Read [2004].

**Cloudy-Sky Radiation Module** computes cloud scattering and extinction coefficients, and scattering phase function, which are needed in radiative transfer calculation. The cloudy-sky radiation scheme is discussed in section 4.4.

**Radiative Transfer Module** performs radiative transfer calculations described in this section. This module is the core to produce calculated limb radiances.

**Model Output** contains outputs from radiative transfer module, including clear sky radiances, cloud induced radiances, effective cloud optical depths and cloud radiance sensitivity (see Chapter 6). FOV averaging and air refraction correction are carried out in this module, which is essentially same as used in Read [2004].

The *Cloud Forward Model* described in this chapter is generalized for limb, nadir and slant (e.g., 45°) radiance calculations. In addition for simulating cloud-induced radiances, it is also called in MLS retrieval processing to provide radiance sensitivities to cloud parameters. It can be applied to any observing platform (airborne or spaceborne) with various viewing angle, such as the cases where receivers are placed inside clouds looking up or down.

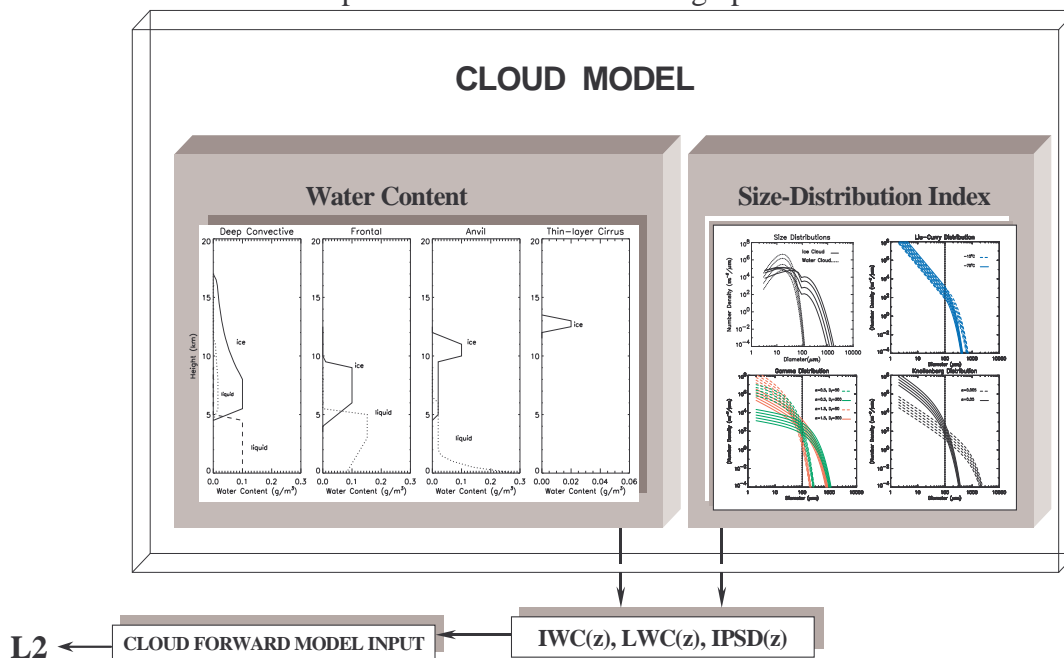


Figure 4.6 Schematic flow of cloud model module where IPSD is the index assigned for each PSD.

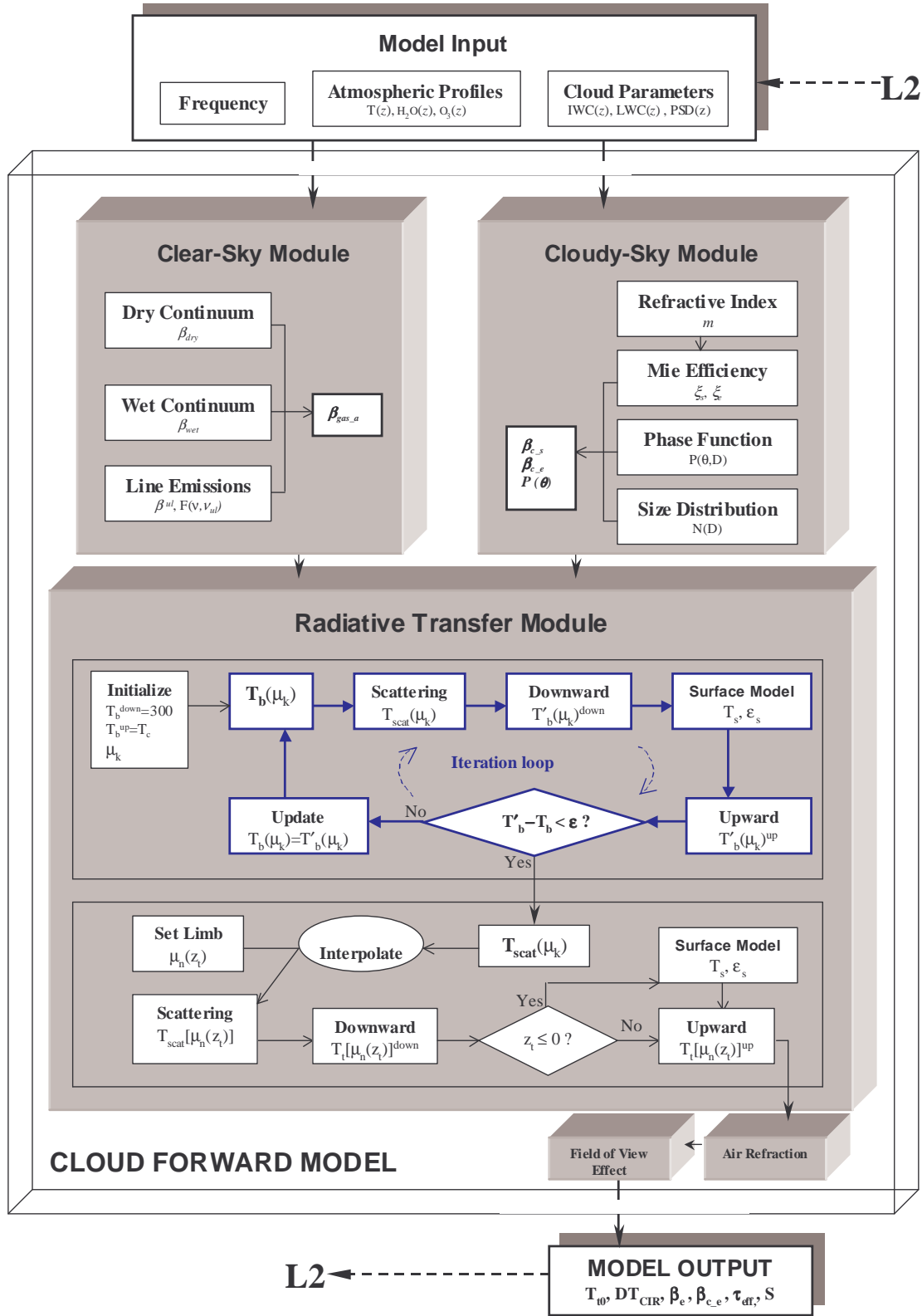


Figure 4.7 Flow-Chart of the Cloudy-Sky Radiance Model.

### 4.3 Clear-Sky Radiation ( $\beta_{gas\_a}$ )

In clear-sky atmospheres, the scattering and absorption terms due to the cloud ice particles and water droplets vanish, i.e.,  $\omega_0=0$ ,  $\beta_e=\beta_a=\beta_{gas\_a}$  and  $d\tau=\beta_{gas\_a}\cdot dz$ . Thus the model needs only to calculate the absorption coefficients from the major atmospheric gas molecules. In current version, we use the line-by-line method to compute emissions ( $\beta^{ul}$ ) from O<sub>2</sub>(44 lines), H<sub>2</sub>O(31 lines), O<sup>18</sup>O (93 lines), and O<sub>3</sub>(722 lines) at 1-1000GHz, and add dry and wet continuum absorption ( $\beta_{dry}$  and  $\beta_{wet}$ ), on the top of those, namely,

$$\beta_{gas\_a} = \beta_{dry} + \beta_{wet} + \beta^{ul} \quad (\text{Eq 4.13})$$

#### 4.3.1 Dry air continuum ( $\beta_{dry}$ )

The contribution from dry air continuum is computed as follows:

$$\beta_{dry} = \frac{0.042S_d\nu}{w_d[1+(\nu/w_d)^2]} + A_{dry}(\nu) \quad (\text{Eq 4.14})$$

where the first term is the Debye spectrum of O<sub>2</sub> which is only important at low frequencies [Liebe, 1982]. The Debye strength  $S_d$  and width  $w_d$  are given by:

$$S_d = 6.14 \cdot 10^{-4} p \theta^2 \quad (\text{Eq 4.15})$$

$$\begin{aligned} w_d &= 5.6 \cdot 10^{-3} (p_d + 1.1e)\theta \\ &\approx 5.6 \cdot 10^{-3} p(1 + 1.1w)\theta \end{aligned} \quad (\text{Eq 4.16})$$

where  $\theta=300/T$ ,  $T$  is air temperature in  $K$ ,  $p_d$  and  $e$  are partial pressures for dry air and water vapor in  $kPa$ ,  $\nu$  is frequency in GHz,  $p$  is the total atmospheric pressure, and  $w$  is the water vapor volume mixing ratio. In our program,  $p$  and  $w$  are used in model calculation (instead of  $p_d$  and  $e$ ).

The second term in Eq 4.14 is the collision-induced absorption valid up to 4 THz and has an empirical form [Appendix F]:

$$A_{dry}(\nu) = 0.65 \times 10^{-2z} \theta^2 \nu^2 \alpha_{N_2-N_2}(\nu) \quad (\text{Eq 4.17})$$

where  $z \equiv -\log_{10}(\text{pressure}/1013hPa)$ , and

$$\alpha_{N_2-N_2}(\nu) = [a_1 e^{-c_1 \theta \nu^2} + a_2 e^{-c_2 \theta \nu^2} (d^2 + \nu^2)] \theta^b \quad (\text{Eq 4.18})$$

and

$$\begin{aligned} A_1 &= 7.7 \times 10^{-10} & A_2 &= 1.0 \times 10^{-13} \\ B &= 1.7 & c_2 &= 1.0 \times 10^{-4} \\ C_1 &= 1.5 \times 10^{-3} & d &= 60 \end{aligned}$$

Both  $\beta_{dry}$  and  $A_{dry}$  have unit of  $km^{-1}$ .

### 4.3.2 Water vapor continuum ( $\beta_{wet}$ )

The water vapor continuum is calculated using a temperature dependent function in Godon et al. [1992] that was obtained from laboratory measurements at 213GHz:

$$\beta_{wet} = 7.53 \times 10^{-16} \left( \frac{300}{T} \right)^{4.2} \nu^2 pe + 1.40 \times 10^{-14} \left( \frac{300}{T} \right)^{6.18} \nu^2 e^2 \quad (\text{Eq 4.19})$$

The first term in Eq 4.19 is the contribution from H<sub>2</sub>O-air collision whereas the second term is due to the H<sub>2</sub>O-H<sub>2</sub>O collision. The coefficients of the two terms are slightly adjusted to give the best fit to other measurements at 239GHz [Bauer et al., 1995], 190GHz [Bauer and Godon, 1991] and 153GHz [Bauer et al., 1993]. We will continue to examine these parameters for EOS MLS frequencies as more laboratory data become available.

### 4.3.3 Line emissions ( $\beta_{ul}$ )

Near each spectrum line, the expression of line absorption coefficient  $\beta^{ul}$  at frequency  $\nu$  is given as:

$$\beta^{ul} = (10^{-12}) n F(\nu, \nu_{ul}) \mathfrak{S}_{ul} \frac{\nu}{\nu_{ul}} \frac{e^{-h\nu_l/kT} (1 - e^{-h\nu_{ul}/kT})}{e^{-h\nu_l/300k} (1 - e^{-h\nu_{ul}/300k})} \frac{Q_{rs}(300)}{Q(T)} \quad (\text{Eq 4.20})$$

where  $\nu_{ul}$  is the line center frequency in MHz,  $\nu_l$  is the ground-state energy in  $cm^{-1}$ ,  $n$  is the total number density of the molecular gas.  $Q = Q_{rs} Q_{ev} \approx Q_{rs}$  is known as the partition function, where  $Q_{rs}$  and  $Q_{ev}$  indicate the partition terms due to rotation-spin and electronic-vibration respectively. Values of  $E_l$  and  $\log Q_{rs}$  are obtained from the JPL catalogue at temperatures of 300 K, 225K and 150K, along with the logarithm of line intensity parameter  $\log \mathfrak{S}_{ul}$  at 300 K which representing the intensity of the energy transition between the upper state  $u$  and the lower state  $l$ . Values of  $Q_{rs}$  for other temperatures are calculated from the catalogued values by logarithmic interpolation.

The line-shape function  $F$  is used to determine the absorption behavior near spectral lines by introducing some line broadening parameters. In the troposphere and lower stratosphere the line shape is mainly controlled by the collision broadening. We choose the Van-Vleck-Weisskopf (VW) line-shape model for O<sub>2</sub> and the Gross kinetic line-shape for other molecules, since the Gross shape is thought to fit the far wings of H<sub>2</sub>O lines better [Gaut and Reifenstein, 1971; Ma and Tipping, 1990]. The VW line shape function is given by

$$F_{VW}(\nu, \nu_{ul}) = \frac{1}{\pi} \frac{\nu}{\nu_{ul}} \left[ \frac{\Delta\nu - Y_k(\nu_{ul} - \nu)}{(\nu_{ul} - \nu)^2 + \Delta\nu^2} + \frac{\Delta\nu - Y_k(\nu_{ul} + \nu)}{(\nu_{ul} + \nu)^2 + \Delta\nu^2} \right] \quad (\text{Eq 4.21})$$

where  $\Delta\nu$  is called *line-width*, the half-width at half-maximum, which is a function of pressure.  $Y_k$  is the interference coefficient, which is only applicable to O<sub>2</sub> lines [Rosenkranz, 1989; Liebe, et al, 1993], given by:

$$Y_k = p \left( \delta_k \left( \frac{300}{T} \right)^{0.8} + \gamma_k \left( \frac{300}{T} \right)^{1.8} \right) \quad (\text{Eq 4.22})$$

where the parameters  $\delta_k$  and  $\gamma_k$  are computed as:

$$\delta_k = a_4 \times 10^{-3} p \left( \frac{300}{T} \right)^{a_5} \quad (\text{Eq 4.23})$$

$$\gamma_k = a_3 \times 10^{-3} \left[ p \left( \frac{300}{T} \right)^{0.8-a_6} + 1.1 e \left( \frac{300}{T} \right) \right] \quad (\text{Eq 4.24})$$

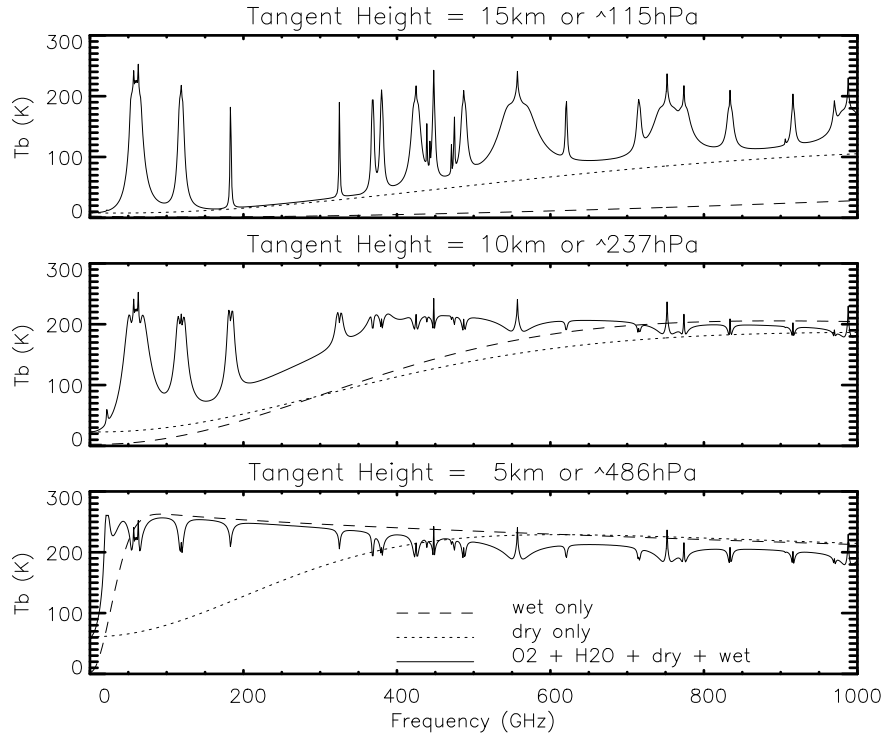


Figure 4.8 Calculated clear-sky limb radiances for 3 tangent pressures in the CIRA86 July tropical atmosphere [Fleming et al., 1988]. The atmosphere includes dry/wet continua,  $\text{O}_2$  and  $\text{H}_2\text{O}$ .

The line parameters for all  $\text{O}_2$  and  $\text{H}_2\text{O}$  are adopted from Liebe et al. [1989]. The line broadening parameters for  $\text{O}^{18}\text{O}$  are estimated based on their quantum numbers similar to  $\text{O}_2$  lines. The broadening parameters for  $\text{O}_3$  lines are same as used in Read [2004]. The  $\text{O}_3$  lines not included therein have a constant width (2.1 MHz/hPa) and constant temperature coefficient (0.75). The Gross line-shape function is defined as:

$$F_{\text{Gross}}(\nu, \nu_{ul}) = \frac{1}{\pi} \frac{4\nu\nu_{ul}\Delta\nu}{(\nu_{ul}^2 - \nu^2)^2 + 4\nu^2\Delta\nu^2}. \quad (\text{Eq 4.25})$$

Figure 4.8 shows the calculated clear-sky limb radiances at 1-1000GHz for three  $h_t$ . Also shown in Figure 4.8 are the radiances due to dry and wet continua without the resonant

emissions. In Figure 4.9 are the calculated clear-sky radiances in the four spectral regions (including the upper and lower sidebands) featured by MLS GHz radiometers.

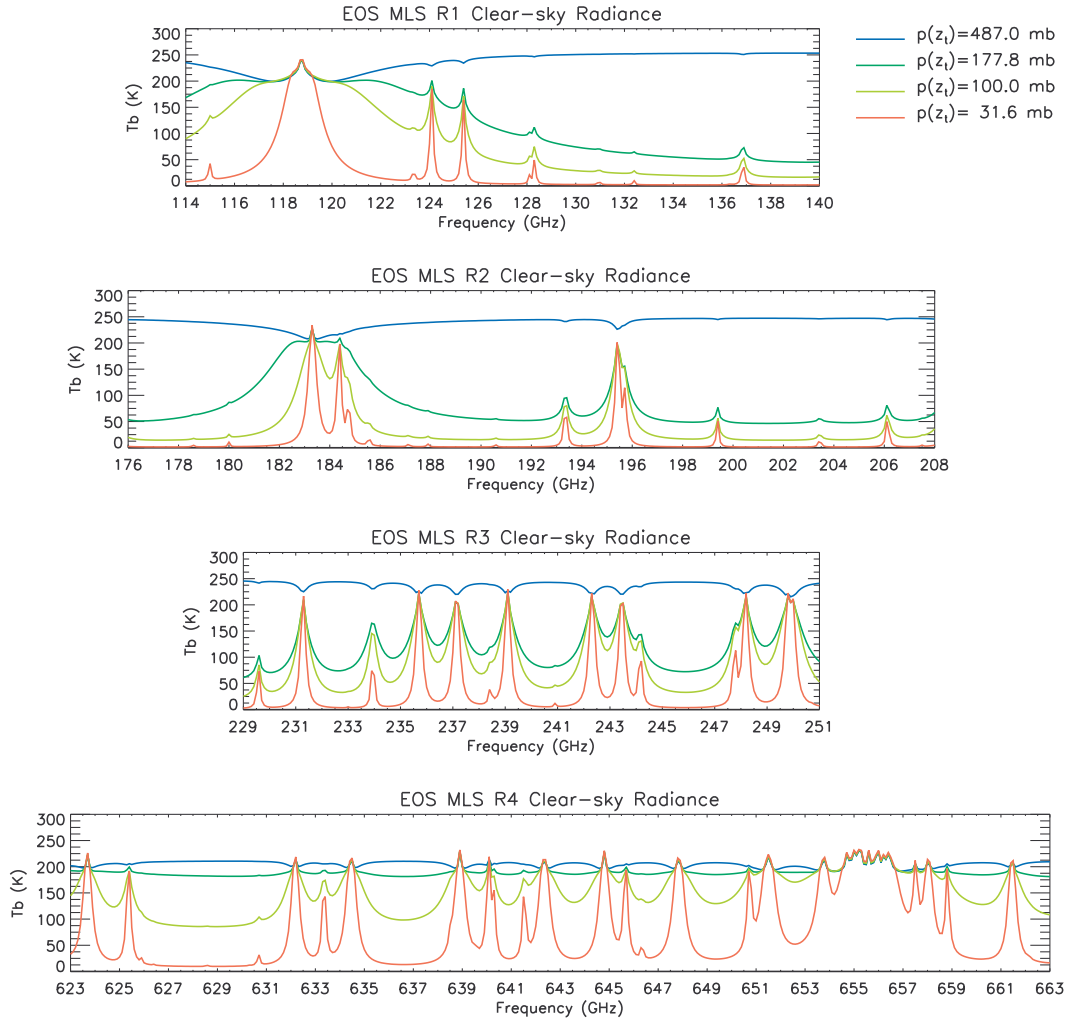


Figure 4.9 Examples of calculated clear-sky limb-radiances for EOS MLS spectral regions (with  $O_2$ ,  $H_2O$ ,  $O_3$ ,  $O^{18}O$  and dry-wet continua in the atmosphere).

#### 4.4 Cloudy-Sky Radiation [ $\beta_{c_s}$ , $\beta_{c_a}$ , $P(\theta)$ ]

In cloudy atmospheres, we compute the cloud scattering and absorption coefficients ( $\beta_{c_s}$ ,  $\beta_{c_a}$ ), the total extinction coefficient ( $\beta_e = \beta_{gas_a} + \beta_{c_s} + \beta_{c_a}$ ) and the scattering phase function ( $P$ ) prior to solving the radiative transfer equation. These are the essential quantities for obtaining the source function of clouds.

To deal with the cloud scattering problem, we describe the nature of the problem in two steps: First, we review the theory of interactions of electromagnetic waves with a single spherical particle. Second, we study the radiative properties for polydispersions of particles where clouds exhibit collective effects from different sizes of particles in terms of scattering and absorption of atmospheric radiation. The assumption of cloud hydrometeors as mass-equivalent spheres allows

us to apply Mie theory for analytical calculations of particle scattering and absorption properties. Non-spherical particle scattering is considered as a secondary effect and its significance in polarimetric observation remains to be seen.

#### 4.4.1 Important Cloud Parameters

##### 4.4.1.1 Efficiency Factors

When electromagnetic radiation having a power density  $\mathbf{I}$  ( $Wm^{-2}$ ) is incident upon a particle with cross-sectional-area  $A$ , a fraction of the incident power is absorbed by the particle, and another fraction is scattered by the particle. The ratio of absorbed power  $P_a$  to the incident power density is defined as the *absorption cross-section*,  $C_a$ . The ratio of  $C_a$  to the particle cross-section-area  $A$  is defined as the *absorption efficiency*  $\xi_a$ . For a spherical particle of radius  $r$ , we have

$$\xi_a = \frac{C_a}{\pi r^2} \quad (\text{Eq 4.26})$$

Similarly, the scattering cross-section,  $C_s$  and corresponding scattering efficiency  $\xi_s$ , are defined as

$$\xi_s = \frac{C_s}{\pi r^2}, \quad (\text{Eq 4.27})$$

The sum of  $\xi_a$  and  $\xi_s$  is the extinction efficiency  $\xi_e$ , i.e.,

$$\xi_e = \xi_a + \xi_s. \quad (\text{Eq 4.28})$$

##### 4.4.1.2 Phase Function

The angular distribution of the scattered light is represented by a dimensionless quantity called the *phase function*  $P(\Omega)$ , where  $\Omega$  is the scattering solid angle—the difference between the solid angle of scattered radiation and incident radiation. The plane in which the scattering angle lies is called the scattering plane. The phase function is normalized such that its integral over all angles is  $4\pi$ , i.e.,

$$\frac{1}{4\pi} \oint P(\Omega, \Omega') d\Omega' = 1. \quad (\text{Eq 4.29})$$

where  $d\Omega'$  is the element of solid angle. For spherical particles, the phase function depends only on polar angle  $\theta$ , which is the difference between the incident angle and the LOS direction in the MLS case, i.e.,

$$\frac{1}{4\pi} \int_{-\pi}^{\pi} \int_0^{\pi} p(\theta) \sin \theta d\theta d\phi = 1. \quad (\text{Eq 4.30})$$

where azimuth angle  $\phi$  lies in the plane perpendicular to the LOS.

#### 4.4.1.3 Particle Size Parameter

The particle size parameter is defined as the ratio of the circumference of a spherical particle to the wavelength, i.e.,

$$\chi = \frac{2\pi r}{\lambda} \quad (\text{Eq 4.31})$$

where  $\lambda$  is the wavelength in vacuum.

### 4.4.2 The Mie Solution

#### 4.4.2.1 Mie Efficiencies

For a single spherical particle, the Mie solution gives the scattering and extinction efficiencies as functions of the complex Mie coefficients  $a_j$  and  $b_j$ :

$$\xi_s = \frac{2}{\chi^2} \sum_{j=1}^{n_{cut}} (2j+1) (|a_j|^2 + |b_j|^2) \quad (\text{Eq 4.32})$$

$$\xi_e = \frac{2}{\chi^2} \sum_{j=1}^{n_{cut}} (2j+1) \text{Re}\{a_j + b_j\} \quad (\text{Eq 4.33})$$

Here  $\text{Re}$  signifies the real part of the complex quantity.  $a_j$  and  $b_j$ , are the Mie coefficients computed using the formula of Deirmendjian (1969), which are functions of relative complex refractive index  $m$  and size parameter  $\chi$ :

$$a_j = \frac{(A_j/m + j/\chi) \text{Re}\{W_j\} - \text{Re}\{W_{j-1}\}}{(A_j/m + j/\chi) W_j - W_{j-1}} \quad (\text{Eq 4.34})$$

$$b_j = \frac{(mA_j + j/\chi) \text{Re}\{W_j\} - \text{Re}\{W_{j-1}\}}{(mA_j + j/\chi) W_j - W_{j-1}} \quad (\text{Eq 4.35})$$

The value  $j$  here is the same as the index of summation in Eqs (4.33-4.34). Intermediate variables  $W_j$  and  $A_j$  are calculated from the recursive expression in the following manner:

$$W_j = \left( \frac{2j-1}{\chi} \right) W_{j-1} - W_{j-2} \quad (\text{Eq 4.36})$$

where

$$W_0 = \sin \chi + i \cos \chi$$

$$W_{-1} = \cos \chi - i \sin \chi$$

and

$$A_j = -\frac{j}{m\chi} + \left( \frac{j}{m\chi} - A_{j-1} \right)^{-1} \quad (\text{Eq 4.37})$$

$$A_0 = \cot m\chi$$

Note that  $m$  is the *complex refractive index*, which is related to the *complex dielectric constant*  $\varepsilon$  by:

$$m = \sqrt{\varepsilon} \quad (\text{Eq 4.38})$$

Values of  $m$  and  $\varepsilon$  at MLS frequencies are discussed in Appendix C.

The number of terms ( $n_{cut}$ ) summed in the Eqs (4.32-4.33) is determined by the convergence of the sums. The summation will continue until the convergence criteria (<0.001%) is reached. The minimum number of terms for the summation is 2. Listed in Table 4-1 are typical values of  $n_{cut}$  for various size parameters where ice dielectric constants of 203 GHz and 640 GHz at  $-30^\circ\text{C}$  are used.

Table 4-1 Two examples of  $n_{cut}$  for  $-30^\circ\text{C}$  ice at different size parameters

203GHz		640GHz	
$\varepsilon=3.15-0.0106i$		$\varepsilon=3.15-0.0335i$	
$n_{cut}$	$\chi$	$n_{cut}$	$\chi$
2	0.1	2	0.1
2	1	2	1
4	3	4	3
7	5	8	5
13	10	13	10
20	15	21	15
		32	27

Here  $n_{cut}$  depends mainly on the size parameter. The larger the size parameter, the more terms are needed in the summation. We tested our calculations for selected dielectric constants, frequencies (between 63 and 640 GHz), and temperatures (between  $+30^\circ\text{C}$  and  $-90^\circ\text{C}$ ), and confirmed that the minimum number of  $n_{cut}=2$  should not cause any arithmetic error in the calculation even for the smallest particles ( $\chi \sim 0.001$  for ice,  $\chi \sim 0.0001$  for water). Rayleigh approximation is often used in some studies to compute the Mie efficiencies for small particles of size parameter  $\chi < 0.1$ . Our studies show that the changeover is not needed since the number of summation terms used for small particles with  $\chi < 0.1$  is already efficient and accurate.

Figure 4.10 shows Mie extinction (solid) and scattering (dashed) efficiencies calculated at 4 selected MLS frequencies for ice particles (blue) and water droplets (red) with sizes from 1-4000  $\mu\text{m}$ . The complex refractive indices for ice and liquid water are computed for temperatures of  $-60^\circ\text{C}$  and  $-15^\circ\text{C}$ , respectively. From this example we see that the Mie extinction and scattering efficiencies of small liquid water particles are much higher than those of small ice particles due to different dielectric constant. Most importantly, for ice particles ( $< 1000 \mu\text{m}$ ), which account for most ice cloud types in the upper atmosphere, scattering occurs mostly in the Rayleigh regime at frequencies  $< 200$  GHz. Thus, for most upper-atmospheric clouds, the more large-size ice

particles the greater the scattering coefficient. This radiative property is key to the scattering-based ice content retrieval with MLS GHz measurements.

#### 4.4.2.2 Phase function

The phase function calculation for a particle of radius  $r$  involves two amplitude functions  $S_1(\theta, r)$  and  $S_2(\theta, r)$  for electric fields perpendicular and parallel to the plane of scattering, respectively. Since the intensity of the scattered radiation is proportional to the sum of the square of these two quantities, the phase function can be written as

$$p(\theta, r) = C \cdot (|S_1(\theta, r)|^2 + |S_2(\theta, r)|^2) \quad (\text{Eq 4.39})$$

where the constant of proportionality  $C$  is obtained from the normalization condition of  $P(\theta, r)$ . The Mie solution for the two amplitude functions is given by Lenoble (1985) as:

$$S_1(\theta, r) = \sum_{j=1}^{\infty} \frac{2j+1}{j(j+1)} \left( a_j \frac{dP_j^1}{d\theta} + b_j \frac{P_j^1}{\sin \theta} \right) \quad (\text{Eq 4.40})$$

$$S_2(\theta, r) = \sum_{j=1}^{\infty} \frac{2j+1}{j(j+1)} \left( a_j \frac{P_j^1}{\sin \theta} + b_j \frac{dP_j^1}{d\theta} \right) \quad (\text{Eq 4.41})$$

where  $a_j$  and  $b_j$  are the Mie coefficients defined by equations (4.35) and (4.36). The truncation numbers used in the summations are the same as used in the scattering and extinction efficiency calculations with convergence criteria of 0.001%. The quantities  $P_j^1$  are the associated Legendre polynomials, which are derived from the recurrence relations provided by Arfken [1985]. That is, given the initial values  $P_1^1 = \sin \theta$  and  $P_2^1 = 3 \cos \theta \sin \theta$ , all the subsequent polynomials and the corresponding derivatives can be found by formula:

$$P_j^1 = \left( \frac{2j-1}{j-1} \right) P_{j-1}^1 \cos \theta - \left( \frac{j}{j-1} \right) P_{j-2}^1 \quad (\text{Eq 4.42})$$

$$\frac{dP_j^1}{d\theta} = \left( \frac{2j-1}{j-1} \right) \left( \cos \theta \frac{dP_{j-1}^1}{d\theta} - P_{j-1}^1 \sin \theta \right) - \left( \frac{j}{j-1} \right) \frac{dP_{j-2}^1}{d\theta} \quad (\text{Eq 4.43})$$

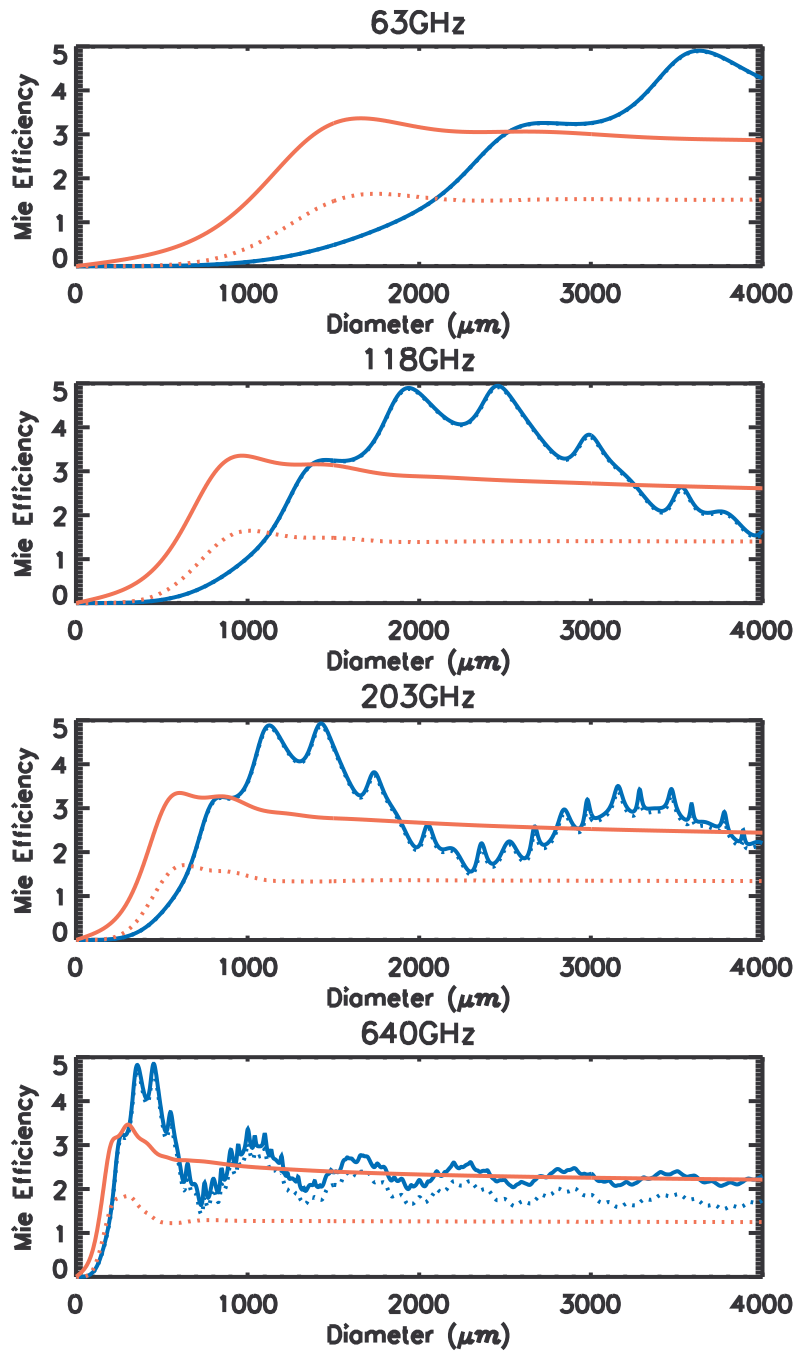


Figure 4.10 Mie extinction (solid) and scattering (dashed) efficiencies. The complex refractive indices are computed at  $-60^{\circ}\text{C}$  for ice (blue) and  $-15^{\circ}\text{C}$  for liquid water (red).

Phase function of single ice particle,  $T = -30^\circ\text{C}$ , Freq=203GHz,  $\epsilon = 3.15 - 0.0106i$

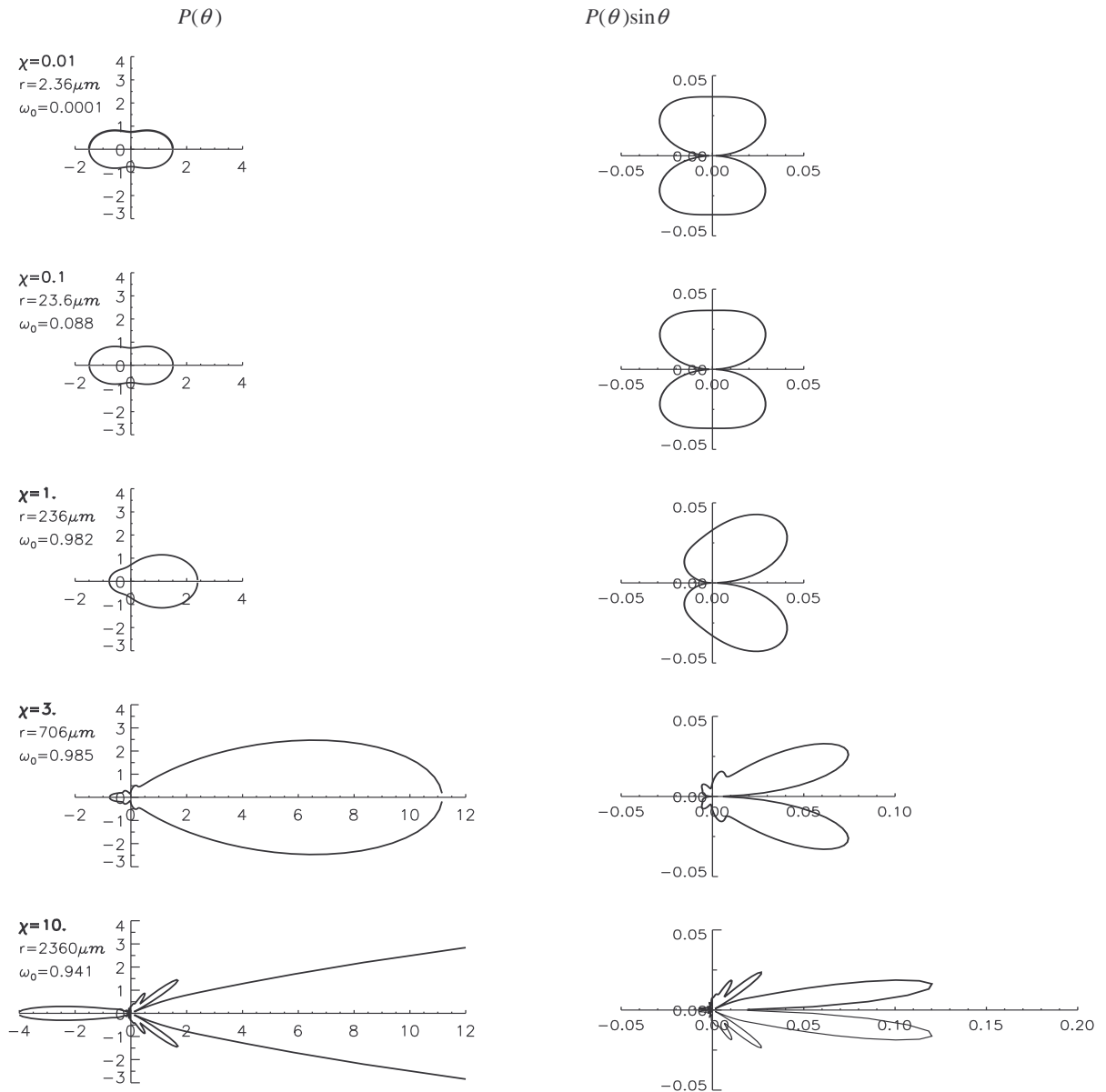


Figure 4.11 Phase function for single ice particles with different size parameters (left-plots). The dielectric constant and single scattering albedo are computed at temperature of  $-30^\circ\text{C}$ . The right-plots are to show that the phase function is normalized when integrated over all directions.

Phase function of single liquid water droplets,  $T = -10^\circ\text{C}$ ,  $\text{Freq} = 203\text{GHz}$ ,  $\epsilon = 5.12 - 3.34i$

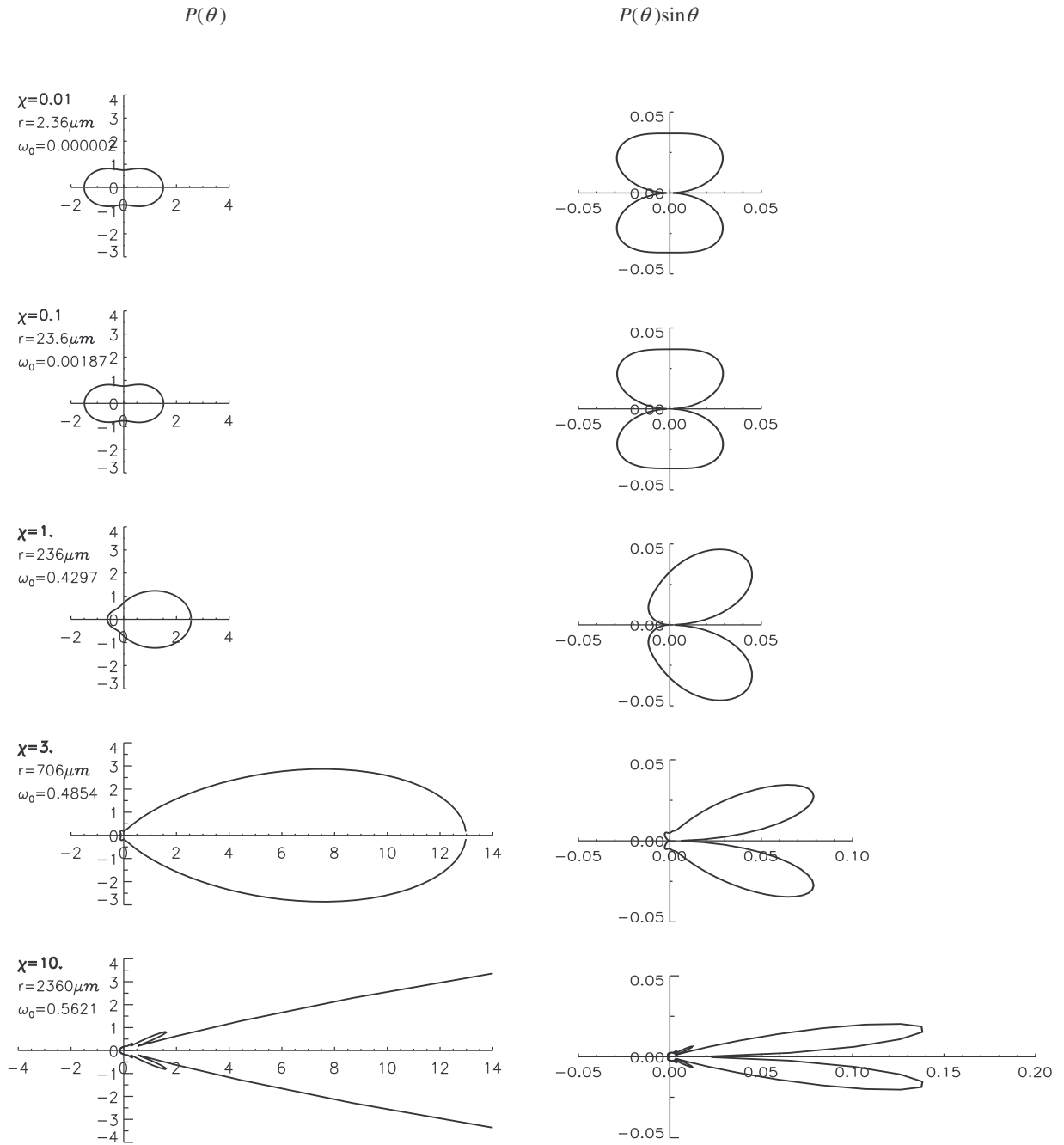


Figure 4.12 Phase function for single liquid water droplets with different size parameters (left-plots). The dielectric constant and single scattering albedo are computed at temperature of  $-10^\circ\text{C}$ . The right-plots are to show that the phase function is normalized when integrated over all directions.

The phase function in the Mie theory depends on size parameter  $\chi$  and complex refractive index  $m$ . Figure 4.11 shows the computed phase functions of single (spherical) ice particles at various particle size parameters, where the dielectric constant is from the LH model in Appendix C for conditions of  $-30^\circ\text{C}$  and 203 GHz. The single scattering albedo ( $\omega_0$ ) is defined as the ratio of scattering to total (clear and cloudy) extinction volume coefficients. For comparison, the phase functions for single (spherical) water droplets with the same set of particle size parameters are shown in Figure 4.12. The dielectric constant for water is also from the LH model at  $-10^\circ\text{C}$ . All the plots are in the same scales. Some important properties to note are:

- (1) For small size parameters (e.g.  $\chi < 0.1$ ), the particle scatters radiation in nearly equal quantities forwards and backwards, the single scattering albedo is small.
- (2) For large size parameters (e.g.  $\chi > 1$ ), the radiation is heavily concentrated in a narrow forward lobe, the single scattering albedo is large (e.g.  $\omega_0 > 0.9$ ).
- (3) At the same size parameter the ice and water phase functions are slightly different, but the single scattering albedo for ice is significant larger than that for water.
- (4) At very large size parameters (e.g.  $\chi = 10$ ), the backward scattering of ice particles is much larger than that of liquid droplets.

### 4.4.3 Polydispersion of Particles

#### 4.4.3.1 The Volume Scattering and Extinction Coefficients

Clouds in the atmosphere are polydispersions of hydrometeors, in other words, made of ice particles or water droplets of different sizes. Cloud scattering properties are the integrated effects of all the contributions from individual particles weighted by their cross sections. The hydrometeor sizes in a cloud are characterized by the function known as *Particle Size Distribution*  $n(r)$ , which is defined as particle concentration in unit volume and in unit radius  $r$ . The total number density  $N$  ( $\text{m}^{-3}$ ) is given by

$$N = \int_0^\infty n(r) dr \quad (\text{Eq 4.44})$$

From the size distribution, cloud ice water content (IWC) can be determined by

$$IWC = \int_0^\infty \frac{4}{3} \pi r^3 \rho_{ice} n(r) dr$$

The volume extinction coefficient, or simply the extinction coefficient, is defined as the extinction cross-section per unit volume. For a single particle with radius  $r$ , it is simply equal to

$$\beta_e = \frac{1}{\text{unit volume}} \cdot \pi r^2 \cdot \xi_e \quad (\text{Eq 4.45})$$

Scattering is assumed to be independent among hydrometeors of different sizes, which means that the total cloud extinction coefficient is a direct summation of all the individual particle contributions, i.e.

$$\beta_{c\_e} = \pi \int_0^{\infty} n(r) r^2 \xi_e(r) dr . \quad (\text{Eq 4.46})$$

Similarly, the total cloud scattering coefficient is given by

$$\beta_{c\_s} = \pi \int_0^{\infty} n(r) r^2 \xi_s(r) dr \quad (\text{Eq 4.47})$$

Their difference yields the total volume absorption coefficient:

$$\beta_{c\_a} = \beta_{c\_e} - \beta_{c\_s} . \quad (\text{Eq 4.48})$$

Particle size distributions can vary substantially from cloud to cloud, which has been a major uncertainty in retrieving cloud microphysical properties. Here we assume the ice size distributions described in McFarquhar and Heymsfield [1997] and water droplet Gamma size distributions as model default, and use other size distributions functions for sensitivity studies.

#### 4.4.3.2 The Integrated Phase Function

The phase function of clouds in polydispersion is the angular distribution of the scattered light integrated over all particle sizes. It is computed by summing up all the individual phase functions from the Mie calculations and weighting each one by its scattering efficiency  $\pi r^2 \xi_s$ :

$$P(\theta) = \frac{\pi}{\beta_{c\_s}} \int_0^{\infty} n(r) r^2 \xi_s(r) p(\theta, r) dr \quad (\text{Eq 4.49})$$

where  $\theta$  is the scattering angle.

For the phase function integration we choose optimal 40 size-bins between 1-4000 $\mu m$  for ice clouds and 0.1-400 $\mu m$  for water clouds. Figure 4.13 plots integrated phase functions for ice and water hydrometeors in polar and standard XY Cartesian layouts. Differences between the integrated and single particle phase functions are significant. The former varies smoothly and gradually with scattering angle.

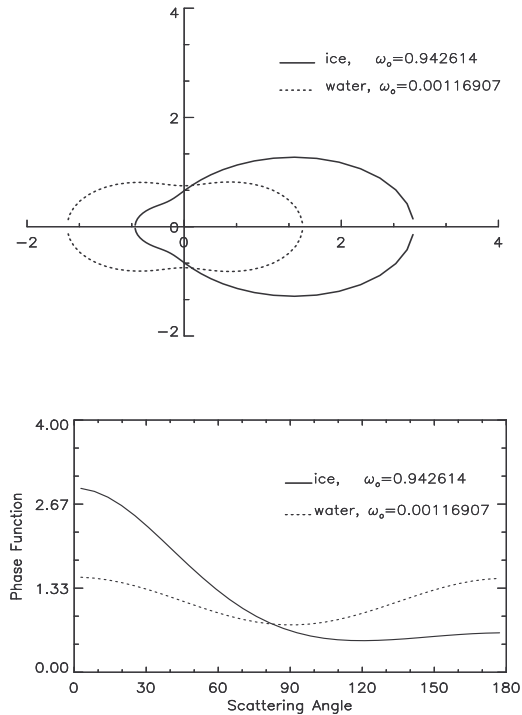


Figure 4.13 Integrated phase functions for ice and water Clouds.

#### 4.4.4 Scattering Calculations

##### 4.4.4.1 Scattering Geometry

Figure 4.14 shows the geometry used in calculating  $T_{scat}$  in Eq 4.5, where the Z-axis points to the zenith. The origin is a scattering volume containing poly-dispersed scattering particles, and the LOS lies in the Y-Z plane with angle  $\Theta$  from zenith and  $\Phi=90^\circ$  from X-axis. The incident radiance  $T_b$  has zenith angle  $\Theta'$  that is a function of  $\theta$ ,  $\phi$  and  $\Theta$ . The  $(\theta, \phi)$  coordinates are relative to the LOS, and the incident  $T_b$  is only a function of  $\Theta'$ . Within this framework, equation (4.6) can be written as

$$T_{scat}(\Theta) = \frac{1}{2} \int_0^\pi P(\theta') \bar{T}_b(\theta') \sin \theta' d\theta' \quad (\text{Eq 4.50})$$

where

$$\begin{aligned} \bar{T}_b(\theta') &= \frac{1}{2\pi} \int_0^{2\pi} T_b(\theta', \phi') d\phi' \\ &= \frac{1}{2\pi} \int_0^{2\pi} T_b(\Theta') d\phi' \end{aligned} \quad (\text{Eq 4.51})$$

where  $\theta'$  is the scattering angle between  $\Theta$  and  $\Theta'$  and  $\phi'$  is the azimuth angle that lies in the plane perpendicular to the LOS. The angle  $\Theta'$  can be expressed in terms of angles  $\theta'$ ,  $\phi'$  and  $\Theta$  by relations:

$$\bar{z} = \bar{j} \sin \Theta + \bar{k} \cos \Theta$$

and

$$\bar{r} = \bar{i} \sin \theta' \cos \phi' + \bar{j} \sin \theta' \sin \phi' + \bar{k} \cos \theta'$$

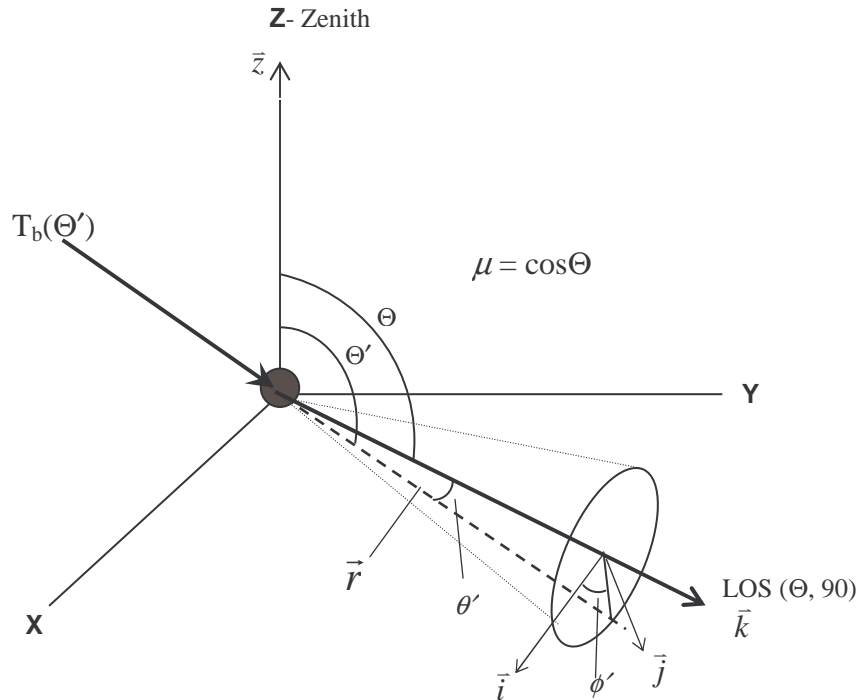


Figure 4.14 Definition of angle integrations in the scattering calculation.

Thus,

$$\cos \Theta' = \vec{r} \cdot \vec{z} = \sin \theta' \sin \Theta \sin \phi' + \cos \theta' \cos \Theta \quad (\text{Eq 4.52})$$

where  $\vec{r}$  and  $\vec{z}$  are the unit vectors of the incident radiance and the zenith, respectively. Therefore  $\bar{T}_b(\theta')$  can be calculated at each layer for all zenith angles  $\Theta'$ . Note, we use  $T_b(\Theta')$  from layer  $n-1$  if  $\Theta' \leq 90^\circ$  (upward radiances), or from layer  $n+1$  if  $\Theta' > 90^\circ$  (downward radiances).

#### 4.4.4.2 Angle Interpolation

For limb radiance calculations, we *first* interpolate  $T_{scat}(\mu_k)$  onto the angles along the LOS, i.e.,  $\mu_n(h_t)$ , and *then* apply the RT integration to compute limb radiance at each  $h_t$ . Because limb radiance varies sharply at a narrow range ( $\sim 1^\circ$ ) of tangent angle and scattering calculations are normally performed on a coarse angular grid (32 streams in our case), the limb radiance interpolated from top atmosphere outputs of plane-parallel calculations will result in large error. This is illustrated in Figure 4.15, where  $T_b$  has a sharp transition at and near the limb whereas  $T_{scat}$  varies gradually cross the horizon. Hence, the interpolation  $T_{scat}$  from calculations with coarse angular resolution will have little effect on the accuracy of  $T_t$  (limb radiances in the stratified atmosphere) calculations.

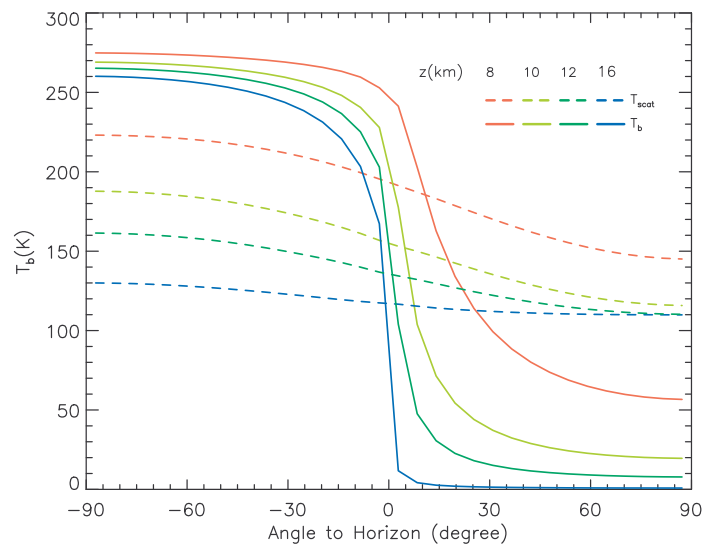


Figure 4.15 Angular distribution of incident and scattered radiances at 6, 10, 12 and 16km altitudes as a function of viewing angle. The radiance brightness for both clear-sky (solid lines) and cloudy-sky (dashed lines) near the horizon can differ by more than 200K within  $\sim 10^\circ$  of incident angle. The red lines show that the angular gradient is greatly reduced in the scattering radiance,  $T_{scat}$ , near the horizon because of the smoothing of the phase function integration. An important implication of this property is that one should always interpolate  $T_{scat}$  and not  $T_b$ .

The angular density used for the scattering calculation (e.g. 32 streams over  $0-\pi$ ) can affect the accuracy of calculated  $T_{scat}$ . Although high angular density is desired, it must be traded off against computing time as the number of cloud layers could make the computation unrealistic. Table 4-2 summarizes the error as functions of angular and vertical resolutions used in the model. These errors are estimated for frequency = 200 GHz and IWC < 1 g/m<sup>3</sup>. Our current

configurations (16  $\theta$ -streams, 8  $\phi$ -streams and  $dz = 0.125$  km) are aimed for 1% accuracy for 200-GHz cloudy-sky radiances.

Table 4-2 Error in calculated  $T_b$  due to angular and vertical resolutions.

$\theta$ -stream = 32 $dz = 0.25$ km		$\phi$ -stream=16 $dz = 0.25$ km		$\phi$ -stream=8 $\theta$ -stream = 16	
$\phi$ -stream	%	$\theta$ -stream	%	$dz$ (km)	%
32	0.04	64	0.16	1.0	8.8
16	0.18	32	0.14	0.5	4.2
8	0.65	16	0.26	0.25	2.2
4	1.6	8	0.60	0.125	0.62

% = relative error  $\equiv \Delta T_b / T_b$   
 $\theta$ -stream = number of angles divided over  $0-\pi$   
 $\phi$ -stream = number of angles divided over  $0-2\pi$   
 $dz$  = vertical resolution

#### 4.4.4.3 Iterative Method and Multiple Scattering among Cloud Layers

Multiple scattering means that the scattered rays may themselves become part of the incident rays upon scatterers. Therefore, the total radiance or intensity of light must include the radiation being scattered once, twice, three times, and so forth. Mathematically, multiple scattering between cloud layers can be effectively modeled by an iterative approach (as used in our model), in which the incident radiation from adjacent layers is updated in each iteration. The radiation scattered from layer  $n$  to layer  $n+1$  may further be scattered into layer  $n+2$  or back to layer  $n$  until the radiative balance is achieved. The chance and impact of secondary scattering is proportional to volume scattering coefficient. The phase function and scattering coefficient are obtained in each layer assuming only single scattering, and remain the same throughout the iteration.

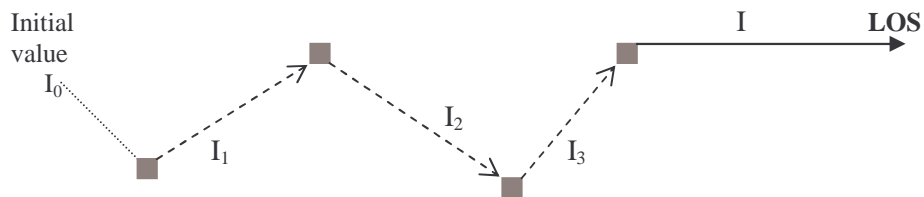


Figure 4.16 Illustration of multiple-scattering processes

As described in §4.2.4, the radiative transfer equation is solved using the iterative method until convergence is reached. Several (3-8) iterations are usually needed to achieve convergence for  $IWC < 0.5 \text{ g/m}^3$  in 205 GHz calculations. More iterations are required in the cases of larger IWCs and/or higher frequencies, which generally means multiple scattering processes are going among cloud layers.

The cloud radiances calculated from the iterative solution undergo multiple scattering among different cloud layers before reaching the top atmosphere. This is illustrated in Figure 4.16. The first iteration after an initial run yields a set of single scattered radiances  $I_1$  which are used later as the incident radiation to the scatterers in the next run. Then the following iteration uses the previous set of radiances  $I_1$  to determine the source function due to augmentation, resulting in a new set of incident rays,  $I_2$ . The new radiances are then used as the incident radiation filed  $I_3$  for the next run. The final result is therefore triple-scattered.

#### ***4.4.4.4 Single Scattering Assumption within a Cloud Layer***

Single scattering assumption is valid as long as cloud optical depth in the model layer is small ( $\ll 1$ ) for all streams. In the case of denser clouds, thinner layers are required to make the assumption valid. More cloud layers may cause more iterations to obtain the solution. For example, let us consider a ray passing through a cloud-layer of optical thickness  $\tau$ . The scattering loss due to cloud is about  $(1 - e^{-\tau/\mu})$ , where  $\mu$  is the cosine of zenith angle of the incident ray. If  $IWC=1 \text{ g/m}^3$  and  $\Delta z=0.0625 \text{ km}$ , we have  $\tau=0.05$  at an altitude of  $\sim 6 \text{ km}$  for 203 GHz. If we use 16  $\theta$ -streams, the shallowest slant path would give  $\mu = 0.1$ , or  $\tau/\mu \sim 0.5$ , which is not good enough for the single scattering assumption. We normally trade off the model resolution required for radiance accuracy against affordable computing time.

For extensive and thick clouds, the 1D plane-parallel scheme is unlikely to model scattering radiation properly in near horizontal directions. Shallow incident angles like limb viewing observations always pose more challenges for RT models than nadir observations. A 2D RT model on the spherical geometry is needed for accurate calculations. Spherical geometry does not allow clouds to be infinitely long. Besides, in reality, clouds always have a finite dimension. Thus, the single scattering requirement may be evaluated using the longest cloud dimension in each model layer, which can always be met by having finer model resolution.

## 5 Model Atmosphere

The clear-sky atmosphere and the cloud model together form the *model atmosphere*. The purpose of this chapter is to describe what clear and cloud parameters are used in the RT model calculations and why.

### 5.1 Clear-Sky Atmosphere

The default configuration of the cloudy-sky RT model assumes a fixed volume mixing ratio for O<sub>2</sub> (0.209476), fixed isotope ratios for O<sup>18</sup>O (0.00409524) and H<sub>2</sub>O<sup>18</sup> (0.00204), and accepts any volume mixing ratio profiles for H<sub>2</sub>O, O<sub>3</sub>, and N<sub>2</sub>O.

The relative humidity (*RH*) is computed from H<sub>2</sub>O volume mixing ratio (*w*) or vapor pressure (*e*),

$$RH = 100 \frac{w}{w_s} \approx 100 \frac{e}{e_s} \quad (\text{Eq 5.1})$$

where  $w_s$  is saturation volume mixing ratio, and  $e_s$  is saturation vapor pressure with respect to ice [List, 1951] and liquid water [Buck, 1981]. For temperature  $T$  (in Kelvin) they are given by

$$e_s^{ice} = 10^{-9.097 \left( \frac{273.16}{T} - 1 \right) - 3.5665 \log_{10} \left( \frac{273.16}{T} \right) + 0.8768 \left( 1 - \frac{T}{273.16} \right) + 0.786} \quad (\text{hPa})$$

$$e_s^{liquid} = 6.1121 \times \exp \left( 17.5 \frac{T - 273.16}{T - 32} \right) \quad (\text{hPa}) \quad (\text{Eq 5.2})$$

### 5.2 A Review of General Cloud Properties

In this section, we review macro- and micro-physical properties of the high clouds that are important to MLS measurements. Then we select several cloud models that are representative for cloud radiance simulations used later on.

#### 5.2.1 Cloud Classification and Distribution

Following London (1957), we divide clouds into 6 classes: cirrus (Ci), alto-stratus (As), nimbostratus (Ns), stratus (St), cumulus (Cu) and cumulonimbus (Cb) with base and top height as a function of latitude and season. For each type, a representative total water content (*WC*), ice and liquid, is listed in Table 5.1.

Table 5-1 Typical cloud water content (*WC*), water path (*WP*) from Blanchet et al (1987).

Cloud Type	WC (g m <sup>-3</sup> )	WP (g m <sup>-2</sup> )
Ci	0.195	19.5
As	0.15	60-200
Ns	0.22	260-620
St	0.51	51
Cu	0.33	80-400
Cb	0.50	600-2500

Because of large water vapor loading at low altitudes (especially in the tropics), only clouds with top above ~5 km can be observed by MLS. We focus on high-altitude cirri-form and

convective-form clouds that are mostly composed of ice particles. The mixed-phase clouds are also important, especially in the cases of cumulus and cumulonimbus.

### 5.2.2 Physical Properties of High Clouds

For Aura MLS, high-altitude clouds, such as, cirrus, cirrostratus, and deep convection, are likely observable. Cirrus is the principal cloud type in the upper troposphere and covers ~20% of the earth's surface on average [Hartman et al., 1992]. Cirrus clouds can have ice particles as large as several *mm* but the number density at these sizes are rather low ( $\sim 0.1 \text{ cm}^{-1}$ ). Thin-layer cirrus are sometimes associated with the jet-stream, forming uniformly along the track of the jets; the cloud band comprises a series of distinct rolls created by the motion in the air current.

Cirrus are often separated from their parent cloud systems and become wispy thin-layer clouds. Typically, separated cirrus anvil or thin-layer clouds have thickness about 1 to 2 *km*, with height ranges between ~7 and ~18 *km* depending on conditions. For example, anvils generated in tropics are usually higher than those of mid-latitudes. The IWC of thin cirrus varies from 0.001 to ~ 0.1  $\text{g/m}^3$ . In the cases where anvils are close to a convective system, they can have larger IWC and be associated with underlying liquid water clouds.

Mid-latitude high cirrostratus and mid-level altostratus are commonly found with a spread of a few hundreds of kilometers in advance of the front. Typical cloud top of frontal cirrus is ~10 *km* with the main concentration around ~7-8 *km*. A mixed-phase layer has been found often at ~5 *km* with a thickness of ~1 *km* [Dowling and Radke, 1990; Stephens et al., 2000; Hogan and Illingworth, 2000]. In the mixed-phase layer, liquid water content is seen generally higher in value than ice water content [Platt, 1997].

Convective clouds (like Cumulus) are usually caused by surface heating that initiates a convective warming in the mid-troposphere, sometimes referred to as shallow convection. Deep convective clouds (like Cumulonimbus) are much larger and more vertically extended than convective clouds. They often exist as a single tower cloud but can develop into a line of towers, known as squall line. Deep convective clouds are often a few kilometer thick with the base near the surface and the top at 10 *km* at mid-latitudes and > 13 *km* in the tropics [e.g., McCormick, 1987; Dowling and Radke, 1990; Lin and Johnson, 1996]. Tops of some vigorous thunderhead storm clouds can reach up to 20 *km* aided by strong vertical updrafts [Jones, 1986; Knollenberg et al., 1993]. The lower part of deep convective clouds contains mostly water droplets while the upper portion primarily made of ice crystals. Most liquid clouds are observed at temperatures > 240 *K* but mixed-phase layers can spread to a higher altitude during strong convective mixing [Geerts et al., 1999]. Cirrus anvils from outflows of deep convective clouds can spread to form cloud layers as large as hundreds of kilometers.

#### 5.2.2.1 Mixed-phase Clouds

Mixed-phase clouds are the regions where both ice particles and water droplets are present. Convective and non-convective clouds exhibit very different characteristics of mixed-phase hydrometeors.

Non-convective mixed-phase clouds have distinct thin layers, usually at altitudes of 4-6 *km*. Table 5.2 lists several observations of mixed-phase layer thickness and base/top temperatures, which show that the layer is usually less than 1 *km* thick. The percentage of ice in mixed-phase clouds depends on the environment air temperature (e.g. Pruppacher and Klett, 1990).

Baumgardt (2000) also found that mixed-phased layers occur where the atmospheric temperature ranges between  $-10^{\circ}\text{C}$  to  $-20^{\circ}$ .

Table 5.2 Observed mixed layer cloud thickness and base/top temperatures [ from Cavazini *et al* (1997)].

Location	Date	Mixed Cloud Thickness (km)	Mixed Cloud Base Temp.	Mixed Cloud Top Temp.
Puget Sound	27/01/78	0.5	-10.5	-15
Puget Sound	09/02/78	0.6	-22	-26
Puget Sound	24/02/78	0.5	-18	-18.5
Puget Sound	10/01/79	1.0	-13	-20
Pacific Ocean	14/02/80	0.8	-14.5	-21.5
Pacific Ocean	07/03/80	0.6	-7	-11.5
Eastern Washington	02/07/80	0.8	-8	-13
Puget Sound	13/05/81	0.4	-11.5	-14
Puget Sound	26/05/82	0.5	-6	-11
Puget Sound	04/03/83	0.5	-4.5	-7.5
Cascade Mountains	25/01/78	0.6	-6	-11
Cascade Mountains	06/02/78	0.4	-13.5	-16.5
Puget Sound	23/01/79	0.4	-15	-16.5

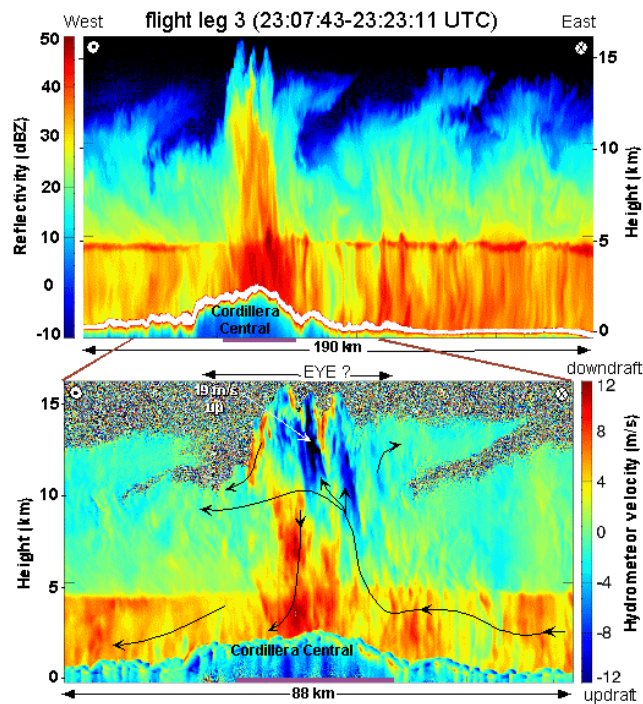


Figure 5.1 Doppler radar imagery of deep convective cloud system in Hurricane George (September, 1998). Note that the melting layer is stable at  $\sim 4$  to  $5$  km in regions outside the core, but goes upto  $\sim 10$  km inside the central core region. Adopted from Geerts *et al* (2000).

Convective mixed-phase cloud layers are well-defined and can extend to a much higher altitude, such as in convective cores or hurricane eyes [Figure 5.1]. An important difference between the convective and non-convective clouds is that the temperature inside non-convective clouds is usually much closer to the temperature of the background atmosphere.

### 5.3 Cloud Models

Based on the cloud characteristics reviewed here, we establish four cloud models for sensitivity studies: convective clouds (topical), frontal clouds (mid-latitude), cirrus anvils (tropical and mid-latitude), and thin-layer cirrus (global). As concluded later in §6.5.2, MLS sensitivity to cloud extinction differs only slightly for these cloud types.

#### 5.3.1 Vertical Profiles of Cloud Water Contents

The ice water content (IWC) and liquid water content (LWC) of the four cloud models are shown in Figure 5.2. These cloud water contents are profiled to represent some observational results (e.g. Hogan and Illingworth, 2000, Skofronick-Jackson and Wang, 2000, Intrieri et al., 1993). The total amount of water content in the model can vary, according to simulation needs, by multiplying the profile with different IWC and LWC (see Chapter 6). Note that for the convective clouds, there is an extended mixing layer embedded in the IWC profile. For the frontal cloud, however, the ice cloud concentration is centered at ~7 km to ~8 km and decreases rapidly above ~10 km (Hogan and Illingworth, 2000, Intrieri et al., 1993).

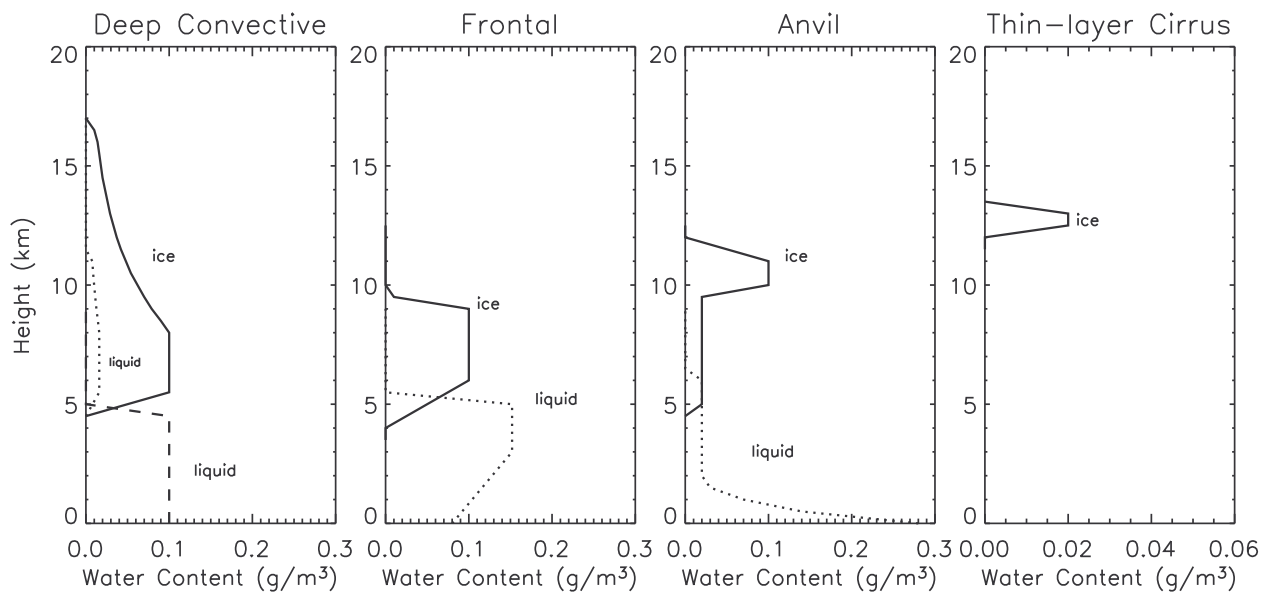


Figure 5.2 Four ideal cloud models with different liquid and ice water profiles.

#### 5.3.2 Particle Size Distributions

Size distributions of cloud hydrometeors vary greatly with cloud type and altitude. Such large variability makes it difficult to parameterize them in a simple form. However, great efforts have been made using in-situ data to provide useful formulations for remote sensing applications [e.g., Heymsfield and Platt, 1984; Mitchell et al., 1996; Platt, 1997; McFarquhar and Heymsfield, 1996; Liu and Curry, 1998; Ryan, 2000]. We choose the parameterization developed by McFarquhar and Heymsfield [1997] (MH here-after) as the default ice particle size distribution

for most of the sensitivity studies. Comparisons and discussions of other size distributions (e.g. McKague, et al. 1998, Evans and Stephen, 1995a, Liu and Curry, 1998, etc.) can be found in Appendix E. The uncertainties associated with the assumption about size distributions remain to be determined in the future research.

### 5.3.2.1 Ice Particle Size Distributions

The MH parameterization is based on observations made in cirrus anvils from outflows of tropical deep convection during the Central Equatorial Pacific Experiment (CEPEX), which is valid mainly for the tropical ocean region. The size distribution function is composed of a first-order gamma distribution function for small particles ( $D < 100 \mu m$ ) and log-normal distribution function for large particles ( $D > 100 \mu m$ ), given by:

$$n(D) = N_1 D \exp(-\alpha D) + N_2 D^{-1} \exp\left[-\frac{1}{2} \left(\frac{\log(D/D_0) - \mu}{\sigma}\right)^2\right] \quad (\text{Eq 5.3})$$

$$N_1 = \frac{IWC_{<100} \alpha^5}{4\pi\rho_{ice}} \quad \text{and} \quad N_2 = \frac{6 \cdot IWC_{>100}}{\sqrt{2\pi^3} \rho_{ice} D_0 \sigma \cdot e^{3\mu+4.5\sigma^2}}$$

where  $D_0 = 1 \mu m$ ,  $\rho_{ice} = 0.91 \text{ g/m}^3$ , and  $n(D)$  has units of  $\text{l}^{-1} \text{mm}^{-1}$ . Note that in the MH97 parameterization,  $n(D)$  is a function of  $IWC$  and  $T$ , and  $\rho_{ice}$  does not depend on  $D$ . The  $D$ -dependency in  $\rho_{ice}$  has been absorbed into the expression of  $n(D)$  as a result of the fitting in MH97.

The quantities  $IWC_{<100}$  and  $IWC_{>100}$  are the total ice content of particles with  $D <$  and  $> 100 \mu m$ , respectively. They can be calculated from parameters  $\alpha$ ,  $\mu$  and  $\sigma$  for a given  $IWC$ . These parameters are determined by the following expressions:

$$IWC_{<100} = \min[IWC, 0.252 \cdot (IWC/IWC_0)^{0.837}] \quad (\text{Eq 5.4})$$

$$IWC_{>100} = IWC - IWC_{<100} \quad (\text{Eq 5.5})$$

$$\alpha = -4.99 \times 10^{-3} + 0.0494 \log_{10}(IWC_{<100}/IWC_0) \quad (\text{Eq 5.6})$$

$$\mu = (5.2 + 0.0013T) + (0.026 - 1.2 \times 10^{-3}T) \log_{10}(IWC_{>100}/IWC_0) \quad (\text{Eq 5.7})$$

$$\sigma = (0.47 + 2.1 \times 10^{-3}T) + (0.018 - 2.1 \times 10^{-4}T) \log_{10}(IWC_{>100}/IWC_0) \quad (\text{Eq 5.8})$$

where  $T$  is the atmospheric temperature and  $IWC_0 = 1 \text{ gm}^{-3}$ .

At small ice particle sizes ( $D < 100 \mu m$ ) the MH size distribution depends mainly on  $IWC$ , whereas at large particle sizes ( $D > 100 \mu m$ ) it also depends on temperature (or altitude). As shown in Figure 5.3a for a fixed  $IWC$ , the ‘right-wing’ of the size distribution moves toward smaller size region as temperature decreases (or altitude increases). On the other hand, if the cloud altitude is fixed, the mean particle size increases with  $IWC$  (Figure 5.3b).

A parameter that is often used to characterize a size distribution is the *mass-mean-diameter*  $D_m$ , which is defined as:

$$D_m \equiv \int (2r)^4 n(r) dr / \int (2r)^3 n(r) dr$$

The physical meaning is:  $D_m$  is the size of the particles that contributed most to the overall masses. The MH distributions show that the higher the altitude, the smaller the mass-mean-diameter for a fixed IWC (see Figure 5.3 caption).

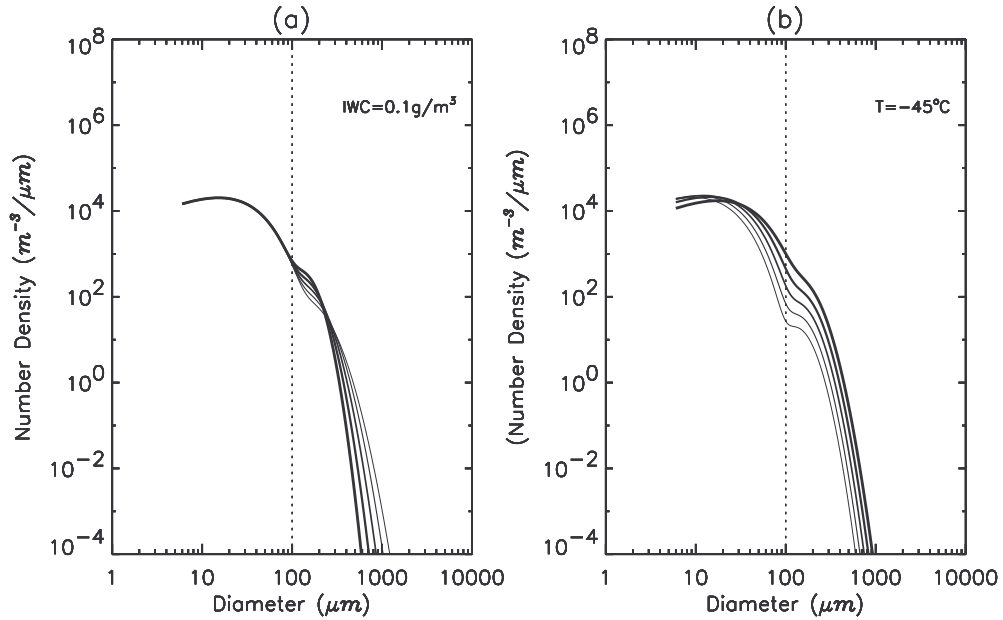


Figure 5.3 Characteristics of MH size distributions. (a) Temperature (altitude) dependence for IWC =  $0.1g/m^3$ . Curves from light to dark show the MH size-distribution at temperatures  $-15^\circ C$ ,  $-30^\circ C$ ,  $-45^\circ C$ ,  $-60^\circ C$  and  $-75^\circ C$ . The mass-mean-diameters are respectively 230, 203, 181, 162, and  $147\mu m$  for these temperatures. (b) IWC dependence for  $T = -45^\circ C$ . Curves from light to dark show the MH distribution for IWC equal to 0.01, 0.02, 0.04, 0.08, and  $0.16 g/m^3$ . The mass-mean-diameters at these IWCs are 118, 135, 153, 173, and  $196\mu m$ , respectively.

### 5.3.2.2 Water Droplet Size Distribution

For clouds composed of liquid water droplets, the gamma size distributions are widely used in modeling (e.g. Marshall and Palmer, 1948; Deirmendjian, 1963; Hansen, 1971; Eberhard, 1993). The analytic formula used by Deirmendjian [1963] is a modified gamma distribution, which yields:

$$n(r) = Ar^{c_1} e^{-Br^{c_2}} \quad (\text{Eq 5.9})$$

where  $r$  is the radii of the droplets (assumed to be spherical shaped) in  $\mu m$ , and parameters  $A$  and  $B$  can be computed from

$$A = \frac{3 \cdot \text{LWC} \cdot c_2 B^{\left(\frac{c_1+4}{c_2}\right)}}{4\pi\Gamma\left(\frac{c_1+4}{c_2}\right)} \times 10^{12} \quad (\text{Eq 5.10})$$

$$B = \frac{c_1}{c_2 r_c^{c_2}} \quad (\text{Eq 5.11})$$

where LWC is in  $g/m^3$ ,  $r_c$  is the characteristic radius in  $\mu m$ , and  $\Gamma$  is the Gamma function. The shape of the size distribution can be changed by parameters  $r_c$ ,  $c_1$  and  $c_2$  that varies from Stratus ( $r_c=10 \mu m$ ,  $c_1=6$ ,  $c_2=1$ ) to Cumulus Congestus ( $r_c=20 \mu m$ ,  $c_1=5$ ,  $c_2=0.5$ ).

For radiance simulations, cloud IWC and LWC profiles are supplied by the user. The particle size distributions are computed with 40 size-bins from 1-4000 $\mu m$  for ice clouds and 1-200 $\mu m$  for liquid water clouds (Figure 5.4).

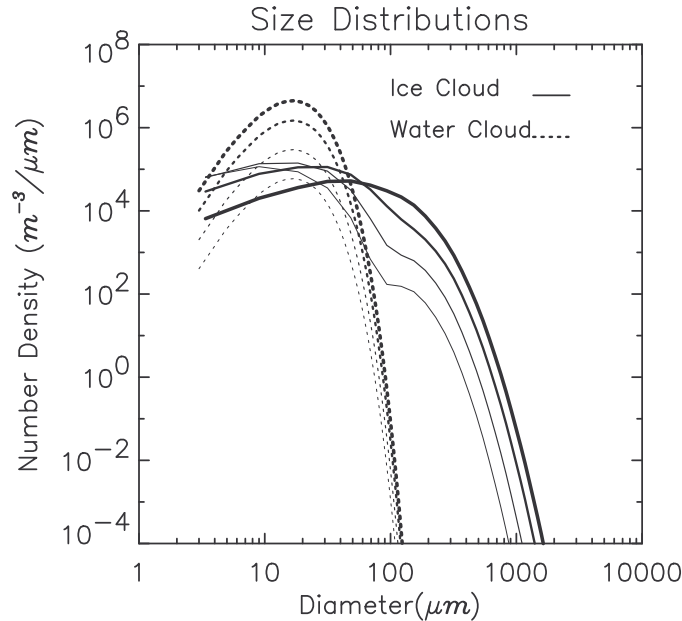


Figure 5.4 Modeled ice particle and water droplet size-distributions for a water cloud layer (cumulus-like) at 4 km and an ice-cloud layer at 8 km. Curves from light to dark indicate the IWC for ice cloud or LWC for water cloud to be: 0.01, 0.05, 0.25, and 0.75  $g/m^3$ .

### 5.3.2.3 Cloud Radiative Properties

Determination of cloud volume scattering properties requires knowledge of particle size distribution since clouds contain poly-dispersion of particles. An important parameter, that defines overall cloud radiative property, is the so-called *cloud single scattering albedo*  $\omega'_0$ . It is the ratio of cloud volume scattering  $\beta_{c-s}$  to volume extinction coefficients  $\beta_{c-e}$ , namely,

$$\omega'_0 = \frac{\beta_{c-s}}{\beta_{c-e}} \quad (\text{Eq 5.12})$$

Note that this single scattering albedo does not include any gas contribution. In reality, clouds are in the middle of the emitting atmosphere and effects of gas emission/absorption must be taken into account. This consideration leads to definition a parameter called *total single scattering albedo*, a quantity reflecting the relative importance of cloud scattering in a background atmosphere, i.e.,

$$\omega_0 = \frac{\beta_{c-s}}{\beta_e} \quad (\text{Eq 5.13})$$

where  $\beta_e$  is the total volume extinction coefficient including gas absorption and cloud extinction. If  $\omega_0 > 0.5$ , scattering processes dominate the radiative transfer.

Figure 5.5 shows the general behavior of cloud single scattering albedo (with and without air) as functions of IWC and mass-mean-diameter for various size distributions. Large variability is seen in these diagrams but realistic values are bounded by the curves that are calculated using the MH distributions at different IWCs and temperatures (i.e., altitudes). As shown in Figure 5.5(a), one cannot judge the relative importance of cloud scattering solely by IWC or cloud height (cloud height is indicated by temperature level). If MLS uses a scattering-based method to retrieve IWC, the sensitivity is limited to  $\text{IWC} > \sim 0.05 \text{ g/m}^3$ . If MLS uses an emission-based method, the sensitivity is mainly at  $\text{IWC} < \sim 0.03 \text{ g/m}^3$ . These estimates do not consider the instrument/model uncertainties that would set a minimum threshold for the sensitivity.

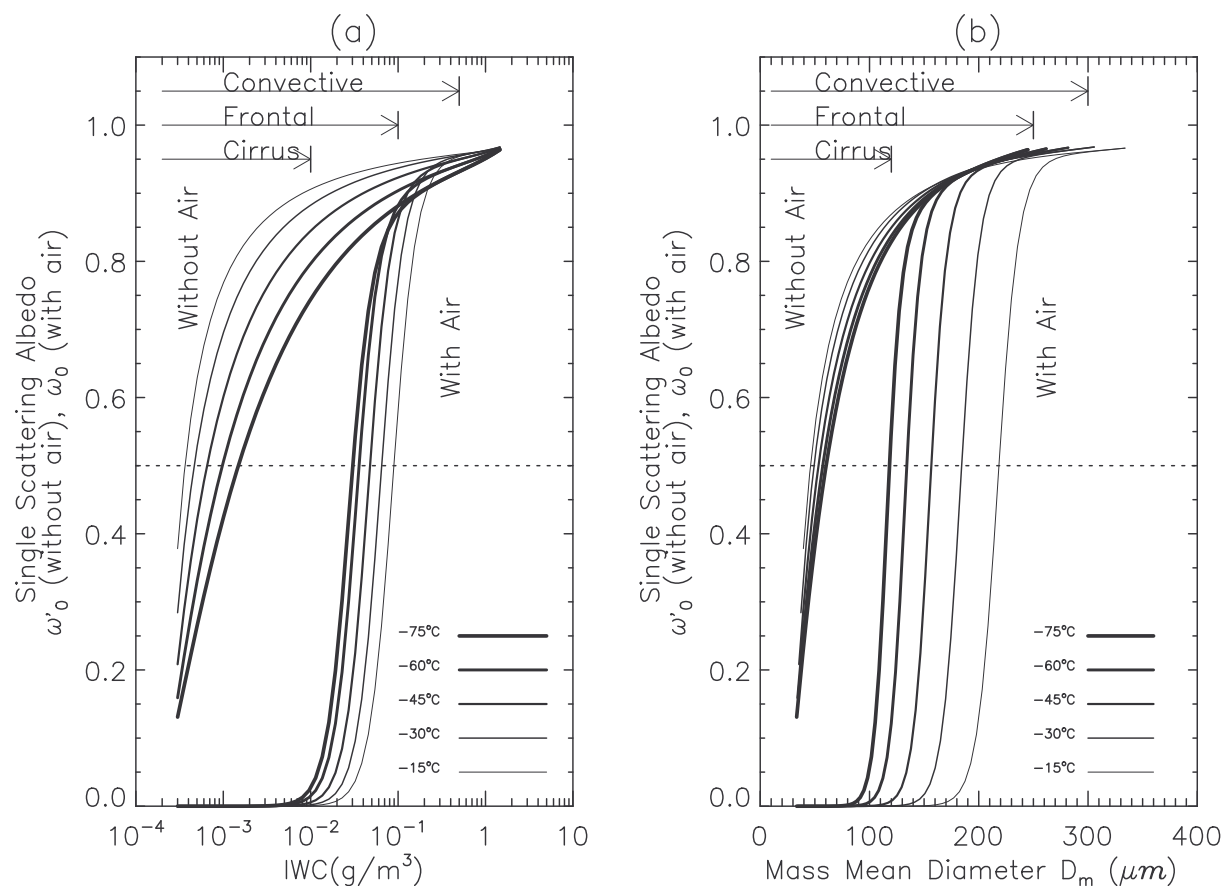


Figure 5.5 Single scattering albedos as a function of (a) IWC and (b) mass-mean-diameter  $D_m$  at 203 GHz. The MH size distributions are used to compute these relations and the cloud variability is given for different cloud types. Curves with different thickness indicate size distributions at different altitudes (measured by temperature). Note that the single scattering albedos with/without air are substantially different, and it is misleading to evaluate the relative importance of scattering when using the one without air. Generally speaking, for thin-layer cirrus the scattering process can be neglected in the radiative transfer at this frequency whereas in the case of frontal/convective clouds both emission and scattering processes are important.

Figure 5.6 shows the  $\beta_{e_c}$ -IWC relation at 203 GHz to be used in the IWC retrieval. The  $\beta_{e_c}$ -IWC relation depends on particle size distribution, and hence on cloud height or temperature. For the MH size distributions, the relation can be fit to a power law as follows,

$$\beta_{c-e} = \left( \frac{\text{IWC}}{\text{IWC}_0} \right)^\alpha \quad (\text{Eq 5.14})$$

where  $\alpha \sim 1.4$ , which is nearly same for all heights, and

$$\text{IWC}_0 = 10^{-2.64+0.0137T} \quad (\text{g/m}^3) \quad (\text{Eq 5.15})$$

Here,  $T$  is temperature in  $^\circ\text{C}$ . Unlike other size distributions (Appendix E), which yield  $\alpha=1$ , the MH size distributions suggest that  $\beta_{c-e}$  is not simply proportional to IWC. Similarly, the  $\beta_{c-e}$ -IWC relation at other frequencies can be modeled as a function of  $T$ .

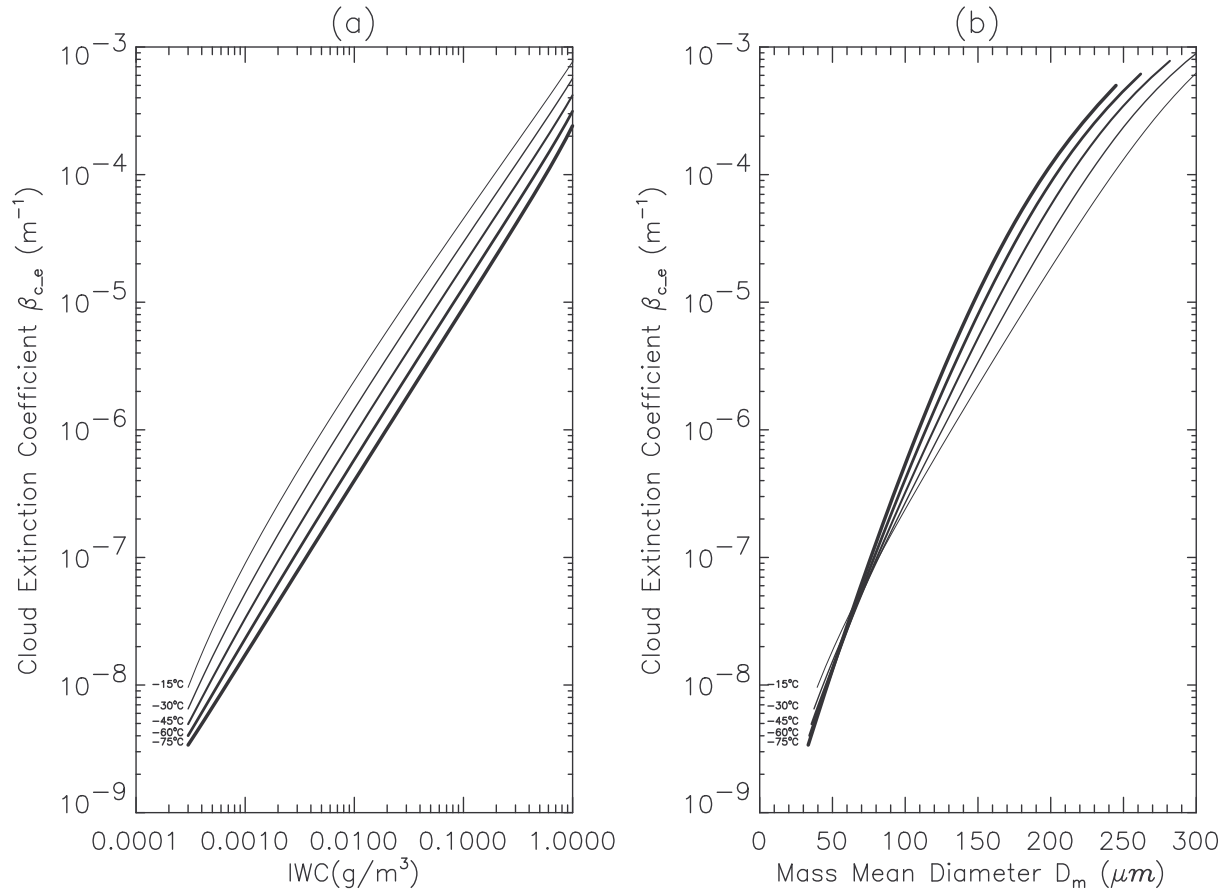


Figure 5.6 Cloud volume extinction coefficients  $\beta_{c-e}$  versus (a) IWC and (b) mass-mean-diameter  $D_m$  at 203 GHz for the MH size-distributions.

#### 5.3.2.4 Particle Size Dependence of Volume Extinction/Scattering Coefficients

In this section we discuss scattering contribution as a function particle size. We weigh Mie efficiencies with particle area and number density, which measure relative contributions at that size, namely,

$$\text{weighted scattering efficiency} = \frac{\pi r^2}{\beta_s} n(r) \xi_s(r) dr$$

$$\text{weighted extinction efficiency} = \frac{\pi r^2}{\beta_e} n(r) \xi_e(r) dr$$

For two typical ice clouds, a high thin-cirrus ( $IWC=0.01 \text{ g/m}^3$ ,  $T=-60 \text{ }^\circ\text{C}$ ) and a deep-convective or frontal cloud ( $IWC=0.1 \text{ g/m}^3$ ,  $T=-30^\circ\text{C}$ ), we calculate the Mie efficiencies weighted by the MH size distribution to highlight the sensitivity as a function of particle size with realistic size distributions. As shown in Figure 5.7, the sensitivity to cloud scattering peaks near  $190 \mu\text{m}$  at both 203 and 640 GHz for the thin cirrus. In other words, tripling frequency *does not* shift the sensitivity peak to a smaller particle size as generally expected. This is because at  $D < 300 \mu\text{m}$  the Mie efficiency is proportional to  $D^4$  for both frequencies, where shapes up the nearly same peak sensitivity. The 203-GHz extinction coefficient exhibits additional peak near  $40 \mu\text{m}$  due to cloud ice emission. This secondary peak increases for decreasing IWC, as expected for more important role of small particles in these cases.

The sensitivity peak has an important implication to the IWC measurement. As shown in Figure 5.8, the weighted IWC, defined as follows, has two modes peaking at  $\sim 40 \mu\text{m}$  and  $150 \mu\text{m}$  for the thin cirrus case, and at  $60 \mu\text{m}$  and  $210 \mu\text{m}$  for the convective/frontal case.

$$\text{weighted IWC} = \rho_{ice} \frac{4}{3} \pi n(r) r^3 \bigg/ \left[ \sum n(r) \frac{4}{3} \pi r^3 \right]$$

In the thin cirrus case, the large size mode, i.e., IWC from sizes  $> 100 \mu\text{m}$ , represents only 47% of the total IWC, whereas in the convective/frontal case, it increases to 63%. Hence, MLS scattering sensitivity is disproportional to IWC in terms of particle size. Because most of the MLS GHz sensitivity peaks around the large-size mode, it relies largely on model size distribution to determine IWC contributions from the small-size mode.

The sensitivity modes of 203 and 640 GHz remain close in the convective cloud case, showing peaks at  $\sim 320 \mu\text{m}$  and  $\sim 250 \mu\text{m}$  respectively. Again, the shift in the peak sensitivity is not large enough to resolve the IWC modes. Nevertheless, this pair is perhaps useful for studying the PSD tail at sizes  $> 200 \mu\text{m}$ .

A more useful frequency for resolving the IWC modes is 2.5 THz. As shown in Figure 5.7, the 2.5-THz sensitivity peaks at sizes  $< 100 \mu\text{m}$  for both ice cloud cases, providing an ideal means to measure IWC from the small-size mode. Therefore, the MLS duals, (203 GHz, 2.5 THz) and (640 GHz, 2.5 THz), will be very valuable for accurate cloud ice measurements.

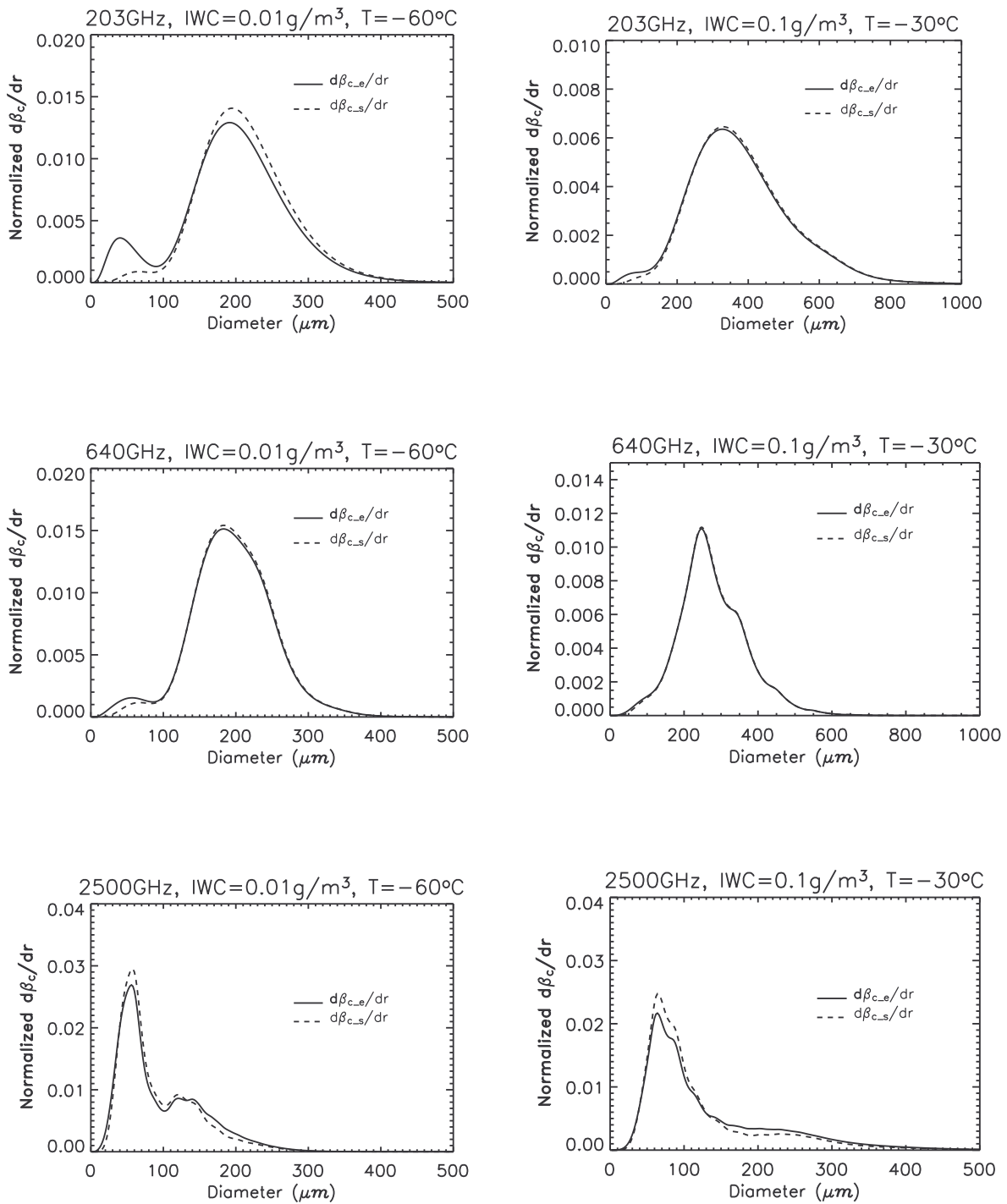


Figure 5.7 Weighted volume extinction (solid) and scattering (dashed) coefficients for two ice cloud conditions, (IWC=0.01g/m<sup>3</sup>, -60°C) and (IWC=0.1g/m<sup>3</sup>, -30°C), and three MLS frequencies, 203, 640 and 2500 GHz. The area under each curve is normalized to unity.

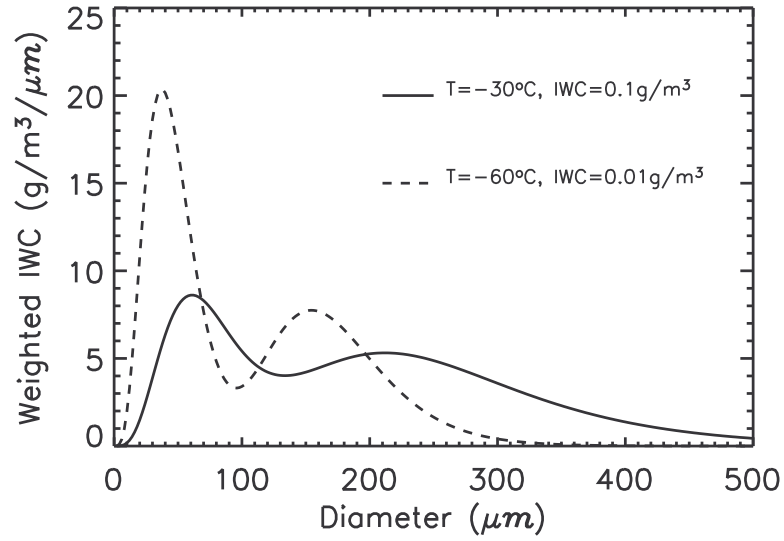


Figure 5.8 Weighted IWC for MH size distributions using IWC=0.01g/m<sup>3</sup>, -60°C or IWC=0.1g/m<sup>3</sup>, -30°C, at 203 and 640 GH.

## 6 Cloud Radiance Simulations and Fast Models

This chapter presents model simulations of MLS radiances needed to form fast (or physical) RT models that can characterize the sensitivities to cloud parameters without CPU-consuming calculations. These simulations reveal various aspects of complex cloud effects on the limb radiances and *fast models* are developed to, including the  $\Delta T_{cir}$ -IWC and  $\Delta T_{cir}$ -*hIWP* relations. A key concept, effective optical depth ( $\tau_{eff}$ ), is introduced to help the understanding of cloud-induced radiance.

### 6.1 Cloud-Induced Limb Radiance ( $\Delta T_{CIR}$ ) and its Sensitivity to IWC

Cloud-induced radiance, or cloud radiance, is defined as the difference between cloudy and clear sky brightness temperatures, namely,

$$\Delta T_{cir} = T_b(\text{cloudy} - \text{sky}) - T_b(\text{clear} - \text{sky}).$$

The simulated profiles shown in Figure 6.1 are consistent with the limb radiance characteristics observed by UARS MLS [Chapter 3].

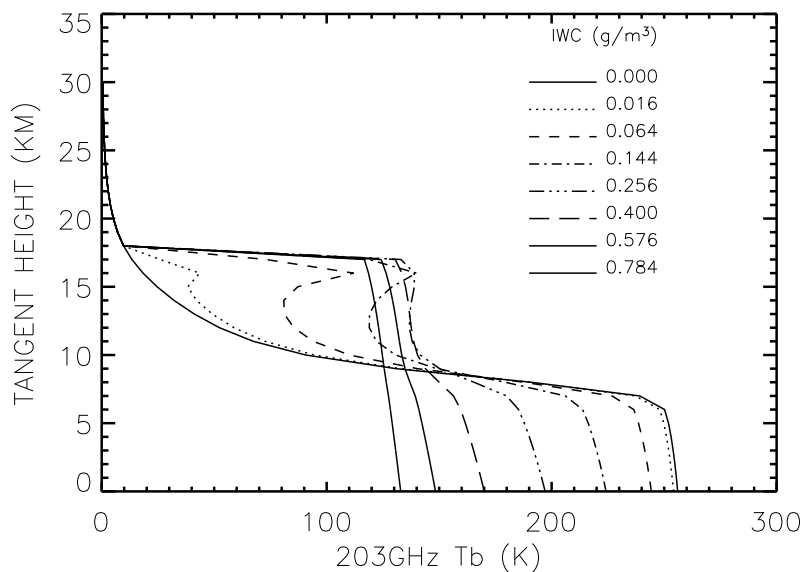


Figure 6.1 Calculated 203-GHz limb radiance profiles for a thin-layer cloud. The cloud layer is centered at 16.5 km with a constant IWC at 16-17 km that tails off linearly to zero in 0.5 km at top and bottom. The radiance profiles from different cloud IWCs are shown. For small IWCs, the cloudy radiance has a peak at 16.5 km and the  $\Delta T_{cir}$  is nearly linearly proportional to IWC (in  $\text{g/m}^3$ ). The  $\Delta T_{cir}$  at low tangent height decreases with IWC but become saturated to  $\sim 120$ - $140$ K for large ( $>0.5 \text{ g/m}^3$ ) IWC. In the saturated cases, the clouds are so opaque that radiation comes only from the uppermost cloud layer.

As shown in Figure 6.2, radiance sensitivity to IWC is tangent height dependent, especially at high tangent heights. High- $h_t$  cloud radiance increases linearly with IWC at small values but becomes saturated for large IWCs. The saturation is unlikely to occur in reality since most cloud IWC at 16 km are  $< 0.1 \text{ g/m}^3$ . At  $h_t < 8$  km the  $\Delta T_{cir}$ -IWC relation is almost same for all tangent heights, showing a linear trend at small values and saturation when IWC reaches  $\sim 0.8 \text{ g/m}^3$ . The saturation means that clouds are so thick that the cloud self-extinction prevents radiation from

penetrating deep into the cloud. In the presence of multiple cloud layers, the radiance sensitivity with respect to IWC may differ from the single-layer case due to modified radiation underneath. This is a secondary effect and will be investigated in the future studies.

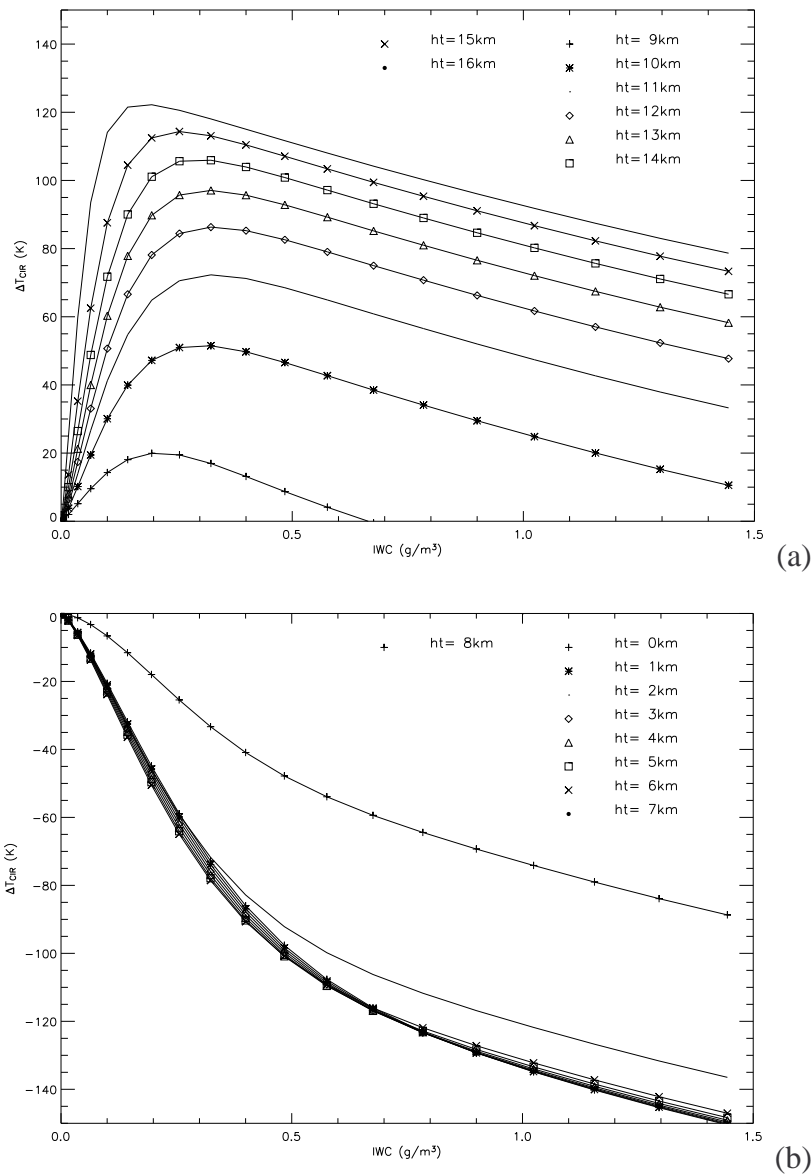


Figure 6.2 Calculated 203-GHz cloud limb radiances for a thin (1 km) layer cirrus centered at 16.5km versus IWC ( $\text{g/m}^3$ ) at (a) high  $h_t$  and (b) low  $h_t$ .

### 6.1.1 High- $h_t$ Radiances

As discussed in Chapter 3, emission and scattering of cloud ice particles can both contribute higher-than-normal radiances at high  $h_t$ . Different slopes in the  $\Delta T_{cir}$ -IWC relation at high  $h_t$  are mainly due to height-dependent PSD. As height decreases, scattering becomes more and more important than ice emission and reduces the slope of the  $\Delta T_{cir}$ -IWC relation. One of the advantages with high- $h_t$   $\Delta T_{cir}$  is their relative independence on emissions from low-altitude liquid

clouds or from the surface. Because most deep convective clouds top out at 100-200 hPa, the  $IWC$  may be obtained through an *ad-hoc*  $\Delta T_{cir}$ -to- $IWC$  conversion at top levels. Cloudy-sky RT calculations show that the  $\Delta T_{cir}$  high tangent height  $h_t$  is approximately proportional to  $IWC$  at the altitude equal to  $h_t$  when effects of cloud inhomogeneity are ignored. In other words,  $\Delta T_{cir}$  is proportional to the  $IWC$  averaged along MLS LOS.

### 6.1.2 Low- $h_t$ Radiances

Low- $h_t$  radiances are depressed in the presence of clouds due to large ice particles scattering. UARS 203-GHz measurements have shown that radiance depressions can be as large as  $-150$  K in the case of dense, thick clouds. Unlike the nadir-viewing cases, the limb radiances are often saturated at low  $h_t$  due to dry and wet continuum emissions over a long slant path length. The saturation makes these limb radiances depend little on surface conditions, greatly simplifying radiative transfer calculation and cloud detection.

Because of strong attenuation by gases at low altitudes, cloud location related to LOS transmission  $\tau$  becomes quite important. If a cloud is placed at  $\tau < 1$ , it would produce the same  $\Delta T_{cir}$  as if there were no attenuation between the cloud and the receiver. If the cloud is placed at  $\tau > 1$ ,  $\Delta T_{cir}$  could be reduced due gas emission and absorption of the air in between. Hence, it is important in low- $h_t$  cases to probe clouds with channels over a broad frequency range such that cloud inhomogeneity may be resolved by varying penetrating ability. The low  $h_t$  radiances have better sensitivity to middle-and-low level clouds but also can be affected by liquid clouds. Liquid cloud effects mainly reduce the radiance sensitivity to ice in scattering-based cases.

## 6.2 Effective Ice Water Path ( $hIWP$ )

We define effective ice water path as:

$$hIWP \equiv \int_{LOS} IWC(s) e^{-\tau_{ext}(s)} ds$$

where  $\tau_{ext} = \int_{MLS}^s \beta_{ext}(s') ds'$  is the total optical depth (cloud + air) between MLS and location  $s$  along LOS. The weight  $e^{-\tau_{ext}(s)}$  is called the transmission function, which determines the percentage of observable cloud ice. This definition of  $hIWP$  accounts only for the  $IWC$  within the MLS penetration and excludes the contributions beyond extinction. As shown in Figure 6.3, the  $\Delta T_{cir}$ - $hIWP$  relations are tangent height dependent and the slope can also vary if different PSDs are assumed. However, the slope varies only a little at  $h_t < 6$  km.

The  $\Delta T_{cir}$ -to- $hIWP$  conversion coefficients, or slopes in unit of  $K \cdot kg^{-1} \cdot m^2$ , are given in Table 6-1 through Table 6-5 for selected frequencies used by MLS radiometers. For comparisons, the overlapped UARS MLS frequencies are specially featured. All these coefficients are calculated assuming the convective cloud type defined in §5.3.1. As secondary effects, their variations of with respect to PSD, cloud height, and air/surface temperature are important for accurate  $hIWP$  retrieval and will be investigated in the future studies.

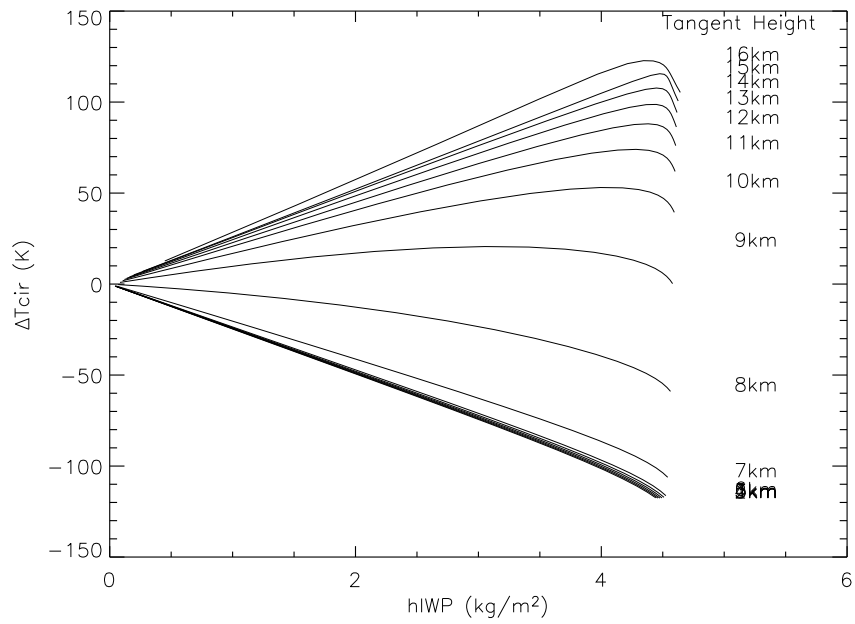


Figure 6.3 The  $\Delta T_{cir}$ -hIWP relation for 203 GHz. For the MH distribution, the maximum retrievable hIWP is  $\sim 4.5 \text{ Kkg}^{-1}\text{m}^2$ , limited by cloud self extinction. The deviation from the linearity near  $4.5 \text{ Kkg}^{-1}\text{m}^2$  (or thick clouds) is likely an artifact of numerical error in evaluating the integration.

Table 6-1 The  $\Delta T_{cir}$ -to-hIWP conversion coefficients near 118 GHz

Frequency (GHz)								
Tgt Ht (km)	112	113	114	116	115.3	117	118.175	118.253
1	-2.8	-2.7	-2.4	-1.2	-1.7	-0.4	-0.1	-0.1
2	-2.8	-2.7	-2.4	-1.1	-1.7	-0.4	-0.1	-0.3
3	-2.8	-2.6	-2.3	-1.1	-1.6	-0.4	-0.1	-0.1
4	-2.8	-2.6	-2.3	-1	-1.5	-0.3	0	0
5	-2.7	-2.6	-2.2	-0.9	-1.5	-0.3	0	-0.1
6	-2.6	-2.5	-2.2	-0.9	-1.4	-0.3	-0.1	0
7	-1.8	-2	-1.9	-0.8	-1.2	-0.3	0	0
8	-0.7	-1.1	-1.3	-0.7	-1.1	-0.3	-0.1	0
9	0	-0.4	-0.8	-0.6	-0.8	-0.2	0	0
10	0.4	0.1	-0.3	-0.5	-0.5	-0.2	-0.1	0
11	0.6	0.4	0.1	-0.3	-0.3	-0.2	0	0
12	0.7	0.5	0.3	-0.2	-0.1	-0.2	0	0
13	0.8	0.7	0.4	-0.1	0.1	-0.1	0	0
14	0.8	0.7	0.6	0	0.2	-0.1	0	0
15	0.8	0.8	0.7	0.2	0.4	-0.1	0	0
16	0.9	0.9	0.8	0.4	0.6	0	0	0

Table 6-2 The  $\Delta T_{cir}$ -to- $hIWP$  conversion coefficients near 190 GHz

Tgt $h_t$ (km)	Frequency (GHz)																
	200.5	177	179	181	182	182	182	182	183	183	183	183	183	183	183	183	183
						.735	.813	.927	.007	.071	.135	.191	.231	.259	.279	.293	.303
1	-21.5	-11.6	-10.5	-8.1	-6.2	-4.6	-4.4	-4.2	-4	-3.9	-3.8	-3.7	-3.6	-3.5	-3.4	-3.2	-3
2	-21.4	-11.5	-10.4	-8	-6.1	-4.5	-4.3	-4.1	-3.9	-3.8	-3.7	-3.6	-3.5	-3.4	-3.3	-3.2	-3
3	-21.3	-11.4	-10.3	-7.9	-6	-4.4	-4.2	-4	-3.9	-3.7	-3.6	-3.5	-3.4	-3.3	-3.2	-3.1	-2.9
4	-21.1	-11.3	-10.1	-7.8	-5.9	-4.3	-4.2	-3.9	-3.8	-3.7	-3.5	-3.4	-3.3	-3.3	-3.1	-3	-2.8
5	-20.9	-11.1	-10	-7.7	-5.8	-4.2	-4.1	-3.8	-3.7	-3.6	-3.5	-3.4	-3.3	-3.2	-3.1	-2.9	-2.7
6	-20.7	-10.9	-9.8	-7.5	-5.7	-4.1	-4	-3.7	-3.6	-3.5	-3.4	-3.3	-3.2	-3.1	-3	-2.8	-2.7
7	-16.7	-10.6	-9.5	-7.3	-5.5	-4	-3.8	-3.6	-3.5	-3.3	-3.2	-3.1	-3	-3	-2.9	-2.7	-2.5
8	-0.5	-5.6	-8.5	-7	-5.3	-3.8	-3.7	-3.5	-3.3	-3.2	-3.1	-3	-2.9	-2.8	-2.7	-2.6	-2.4
9	9.5	3.7	-0.8	-6	-5	-3.6	-3.5	-3.3	-3.1	-3	-2.9	-2.8	-2.8	-2.7	-2.6	-2.5	-2.3
10	10	6.2	4.7	-0.2	-3.7	-3.4	-3.2	-3	-2.9	-2.8	-2.7	-2.6	-2.6	-2.5	-2.4	-2.3	-2.1
11	9	6.1	5.7	3.7	0.3	-2.4	-2.5	-2.5	-2.5	-2.4	-2.4	-2.3	-2.2	-2.2	-2.1	-2	-1.8
12	7.4	5.2	5.1	4.4	2.7	-0.2	-0.5	-0.9	-1.1	-1.2	-1.3	-1.4	-1.4	-1.4	-1.4	-1.3	-1.3
13	6.3	4.4	4.5	4.2	3.5	1.5	1.1	0.6	0.3	0.1	-0.1	-0.3	-0.4	-0.5	-0.6	-0.7	-0.7
14	5.4	3.9	3.9	3.9	3.5	2.3	2	1.6	1.2	1	0.7	0.4	0.2	0.1	-0.1	-0.2	-0.3
15	4.9	3.5	3.6	3.6	3.4	2.6	2.4	2	1.7	1.4	1.1	0.8	0.6	0.4	0.2	0	-0.1
16	4.7	3.4	3.5	3.5	3.4	2.8	2.7	2.4	2.1	1.8	1.5	1.1	0.8	0.6	0.4	0.2	-0.1

Table 6-3 The  $\Delta T_{cir}$ -to- $hIWP$  conversion coefficients near 240 GHz

Tgt $h_t$ (km)	Frequency (GHz)																
	230.2	233	233	233	233	233	233	233	233	233	233	233	233	233	249	245	
			.325	.403	.517	.597	.661	.725	.781	.821	.849	.869	.883	.893	.2	.37	
1	-34.6	-35.4	-35.1	-35	-34.7	-34.4	-34.2	-33.8	-33.5	-33.2	-32.9	-32.7	-32.5	-32.4	-41.7	-41.9	
2	-34.4	-35.2	-34.9	-34.7	-34.4	-34.1	-33.9	-33.6	-33.2	-32.9	-32.6	-32.4	-32.2	-32.1	-41.3	-41.6	
3	-34.1	-34.9	-34.6	-34.4	-34.1	-33.8	-33.5	-33.2	-32.9	-32.6	-32.3	-32.1	-31.9	-31.8	-40.9	-41.3	
4	-33.8	-34.5	-34.2	-34	-33.7	-33.4	-33.2	-32.8	-32.5	-32.2	-31.9	-31.7	-31.5	-31.4	-40.4	-40.8	
5	-33.4	-34.1	-33.7	-33.6	-33.2	-33	-32.7	-32.3	-32	-31.7	-31.4	-31.2	-31	-30.9	-39.8	-40.3	
6	-33	-33.6	-33.2	-33	-32.6	-32.3	-32.1	-31.7	-31.4	-31	-30.8	-30.6	-30.4	-30.2	-39	-39.6	
7	-27.5	-28.9	-28.9	-28.9	-28.8	-28.7	-28.5	-28.4	-28.2	-28	-27.8	-27.7	-27.6	-27.5	-35.5	-34.8	
8	-6	-9	-10.6	-11.2	-12.1	-12.8	-13.4	-14	-14.5	-14.9	-15.2	-15.4	-15.6	-15.7	-17.4	-11.4	
9	9.3	6.8	4.4	3.6	2	0.8	-0.3	-1.5	-2.6	-3.4	-4.1	-4.5	-4.9	-5.2	-0.9	8.7	
10	11.8	10.6	8.8	8.1	6.8	5.7	4.7	3.6	2.5	1.7	1.1	0.6	0.2	0	5	13.4	
11	11.3	10.8	9.6	9	7.9	7	6.1	5.1	4.1	3.4	2.8	2.3	2	1.8	6.2	13.3	
12	9.4	9.3	8.5	8.1	7.3	6.6	5.9	5.1	4.2	3.6	3.1	2.8	2.5	2.3	5.7	11.3	
13	8.1	8.2	7.6	7.4	6.8	6.2	5.6	4.9	4.2	3.6	3.2	2.9	2.6	2.4	5.2	9.7	
14	7	7.2	6.9	6.7	6.3	5.8	5.4	4.8	4.1	3.6	3.2	2.9	2.6	2.5	4.8	8.4	
15	6.4	6.6	6.4	6.2	5.9	5.6	5.2	4.6	4.1	3.6	3.2	2.9	2.6	2.5	4.6	7.7	
16	6.2	6.5	6.3	6.2	6	5.7	5.4	4.9	4.4	3.9	3.5	3.1	2.9	2.7	4.9	7.4	

Table 6-4 The  $\Delta T_{cir}$ -to- $hIWP$  conversion coefficients near 640 GHz and 2.5 THz

Tgt Ht (km)	Frequency (GHz)							
	636.5	649.5	2514.8	2530.8	2513.8	2531.8	2510.5	2535.1
1	-593.2	-370.5	-2453.4	-2452.3	-2448.4	-2246	-2426.9	-2469
2	-589.5	-365.7	-2444.2	-2443.4	-2439.3	-2237	-2418	-2459.6
3	-585.3	-360.4	-2434.1	-2433.7	-2429.2	-2227.1	-2408.2	-2449.3
4	-580.6	-354.5	-2422.9	-2422.9	-2418.1	-2216.3	-2397.4	-2437.9
5	-575.2	-583.2	-2410.5	-2411	-2405.8	-2204.4	-2385.5	-2425.3
6	-569	-576.3	-2396.8	-2397.7	-2392.2	-2191.2	-2372.3	-2411.4
7	-561.7	-568.2	-2381.4	-2382.9	-2376.9	-2176.5	-2357.5	-2395.7
8	-552.7	-558.2	-2364.1	-2366.1	-2359.7	-2160.2	-2340.9	-2378.1
9	-541	-545.5	-2344.5	-2347.1	-2340.3	-2141.7	-2322.1	-2358.2
10	-516.6	-521.9	-2322.1	-2325.3	-2318	-2120.7	-2300.6	-2335.4
11	-444.9	-430.8	-2296.1	-2300	-2292.2	-2096.7	-2275.9	-2309
12	-343.4	-364.5	-2265.7	-2270.3	-2262	-2068.8	-2247	-2278.1
13	-253.2	-304.3	-2229.6	-2234.9	-2226.2	-2035.8	-2212.8	-2241.3
14	-174.5	-247.5	-2185.4	-2191.3	-2182.5	-1996.6	-2171.4	-2196.4
15	-102.8	-190	-2133.8	-2140.6	-2131.5	-1955.5	-2124.3	-2143.7
16	-29.1	15	-2020.3	-2028.9	-2019.9	-1904.9	-2023.8	-2027.4

Table 6-5 The  $\Delta T_{cir}$ -to- $hIWP$  conversion coefficients for UARS MLS 183 and 204 GHz channels

Tgt Ht (km)	Frequency (GHz)									
	183.309	183.308	183.306	183.299	183.287	183.263	183.218	183.125	186.2	203.5
1	-2.6	-2.7	-2.9	-3.1	-3.3	-3.4	-3.6	-3.8	-9.9	-22.5
2	-2.5	-2.7	-2.8	-3.1	-3.2	-3.4	-3.5	-3.7	-9.8	-22.4
3	-2.5	-2.6	-2.8	-3	-3.2	-3.3	-3.5	-3.6	-9.7	-22.3
4	-2.4	-2.5	-2.7	-2.9	-3.1	-3.2	-3.4	-3.6	-9.5	-22.1
5	-2.3	-2.5	-2.6	-2.8	-3	-3.1	-3.3	-3.5	-9.4	-21.9
6	-2.2	-2.4	-2.5	-2.7	-2.9	-3.1	-3.2	-3.4	-9.2	-21.7
7	-2.1	-2.3	-2.4	-2.6	-2.8	-2.9	-3.1	-3.3	-8.9	-17.8
8	-2	-2.2	-2.3	-2.5	-2.7	-2.8	-2.9	-3.1	-8.6	-1.7
9	-1.9	-2	-2.2	-2.4	-2.5	-2.7	-2.8	-3	-6.2	9
10	-1.8	-1.9	-2	-2.2	-2.3	-2.5	-2.6	-2.7	1.3	10
11	-1.5	-1.6	-1.7	-1.9	-2	-2.2	-2.3	-2.4	4.7	9.1
12	-1.1	-1.1	-1.2	-1.3	-1.3	-1.4	-1.4	-1.3	4.9	7.5
13	-0.6	-0.7	-0.7	-0.7	-0.6	-0.5	-0.4	-0.1	4.6	6.4
14	-0.4	-0.4	-0.4	-0.3	-0.1	0	0.3	0.7	4.1	5.5
15	-0.3	-0.3	-0.2	-0.1	0.1	0.3	0.7	1.2	3.8	5
16	-0.3	-0.2	-0.2	0	0.2	0.5	0.9	1.5	3.7	4.8

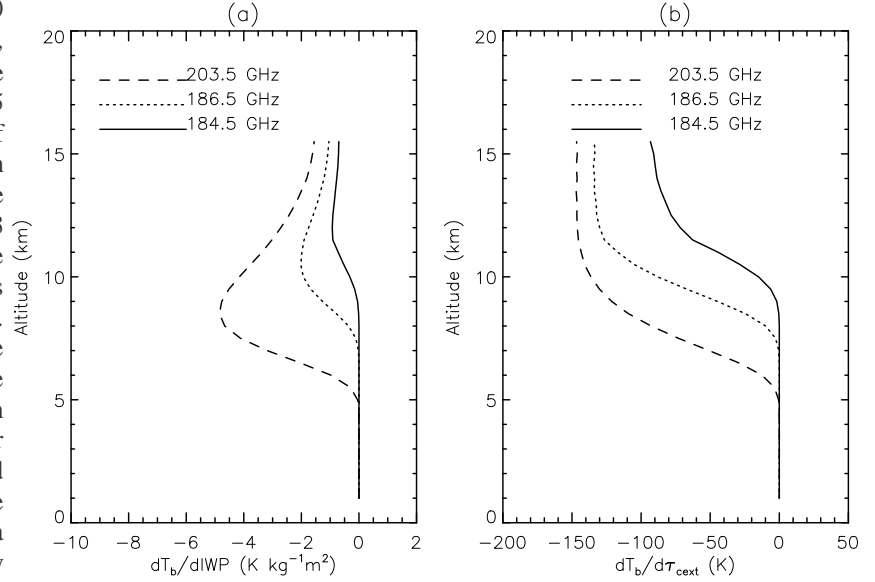
### 6.3 Effective Cloud Optical Depth ( $\tau_{eff}$ )

Similarly, we introduce effective cloud optical depth,  $\tau_{eff}$ , which is defined as:

$$\tau_{ceff} \equiv \int_{LOS} \beta_{c-e}(s) e^{-\tau_{ext}(s)} ds \quad (\text{Eq 6.1})$$

where  $\beta_{c-e}(z)$  is cloud volume extinction coefficient. The effective optical depth is a more fundamental variable affecting  $\Delta T_{cir}$  measured. This variable reflects the extinction within the MLS penetration depth, and hence is more directly related to  $\Delta T_{cir}$  measured. As a result, the  $\tau_{ceff}$ - $\Delta T_{cir}$  relation (called *sensitivity*), as a fundamental property in cloudy-sky RT, should depend little on cloud microphysics.

Figure 6.4 Weighting functions of cloud radiances on (a) IWC and (b) cloud optical depth  $\tau_{cext}$  at a low  $h_t$ , where  $d\tau_{cext} = \beta_{c-e} \cdot dz$ . The frequencies 203.5, 186.5, and 184.5 GHz are used to show the effect of atmospheric opacity differences on cloud radiance sensitivity. The channel farther away from the 183.3 GHz H<sub>2</sub>O emission, which can see deeper into the atmosphere, has better sensitivity at lower altitudes. The sensitivities to IWC are altitude dependent since the MH particle size distributions used in the simulation depends on altitude. On the other hand, the sensitivities to cloud optical depth do not depend on size distribution, and therefore have a uniform shape that reflects clear-sky transmission profiles at these frequencies.



The  $\tau_{ceff}$ - $\Delta T_{cir}$  relation is a key intermediate variable in MLS cloud retrieval, which we would like to model well under various situations (with the fast model if possible). It is required for the retrieval of from  $\Delta T_{cir}$  to  $\beta_{c-e}(z)$  and then  $\beta_{c-e}(z)$ -to-*IWC*. The introduction of  $\tau_{ceff}$  helps better characterize, estimate and diagnose the uncertainties associated with cloud products. As illustrated in Figure 6.4, the dependence of  $\Delta T_{cir}$  on *dIWP* varies with PSDs at each altitude, whereas the dependence on  $d\tau_{cext}$  mimics the transmission function, which leads to the definition of  $\tau_{ceff}$  in Eq. 6.1.

#### 6.4 Cloud Radiance Sensitivity

Cloud radiance sensitivity is defined as the cloud radiance change with respect to the effective optical depth, namely,

$$S_{CIR} \equiv \frac{\Delta T_{CIR}}{\tau_{ceff}} \quad (\text{Eq 6.2})$$

### 6.5 Low- $h_t$ $\Delta T_{cir}$ - $\tau_{eff}$ Relations

The calculated sensitivity is nearly constant, about -106 K, for all frequencies and all tangent height  $< 7$  km. This can be explained with a simple conceptual model (Appendix D) as a result of scattering-based radiative transfer. From the conceptual model, we have

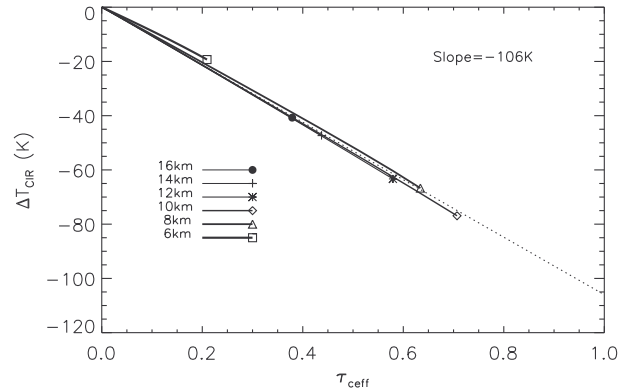
$$\frac{\Delta T_{cir}}{\tau_{eff}} \approx T_{scat} - T_{AB} \quad (\text{Eq 6.3})$$

where  $T_{scat}$  is the scattering radiance as in Chapter 4 and  $T_{AB}$  is the background clear-sky radiance behind the cloud. Assuming  $T_{scat}=150$  K for typical high clouds and  $T_{AB}=250$  K as the background air emission, we have the sensitivity equal to about -100 K. The following subsections describe various dependence of the sensitivity on cloud parameters.

#### 6.5.1 Effects of Cloud Height

The sensitivity depends only slightly on cloud top height, which can be neglected at present. Figure 6.5 shows that all the slopes are very close to -106 K for cloud heights between 6 to 16 km. As cloud height increases, the clear-sky attenuation to cloud radiance reduces from nearly opaque to nearly transparent. The clear-sky attenuation effect is evident in the simulations in Figure 6.5 where the maximum effective cloud depth increases with decreasing cloud height. In other words, the observed  $\Delta T_{cir}$  increases as the cloud layer rises from the air.

Figure 6.5 Sensitivity for different cloud heights. In these calculations a 1-km cloud layer is placed at various altitudes. As indicated by the legend, each line represents the sensitivity when the cloud height is used. Only clouds with IWC less than  $0.5 \text{ g/m}^3$  are shown



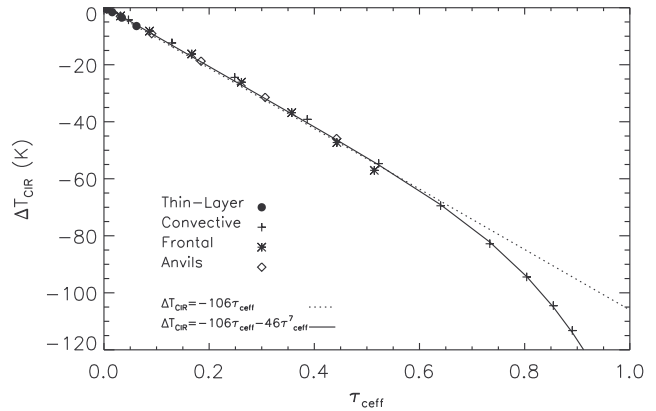
#### 6.5.2 Effects of Cloud Profile Type

The sensitivity depends little on cloud profile type, or cloud inhomogeneity, which is one of the most useful properties of microwave cloud measurements. Figure 6.6 shows that the sensitivity is nearly constant at -106 K for most clouds at small  $\tau_{eff}$ . The deviation from the -106 K slope exhibits only at large  $\tau_{eff}$ , where multiple scattering becomes important, like the cases of deep convective clouds in the tropics. As a fast model, the sensitivity can be fit to the following form

$$S_{CIR} = a(1 + b\tau_{eff}^n) \quad (\text{Eq 6.4})$$

where  $n=6$ ,  $a=-106$  K and  $b=0.46$ .

Figure 6.6 Sensitivities for different cloud profiles as described in chapter 5. The largest IWC in these calculations are 0.1, 0.5, 0.25, and 0.15  $\text{g/m}^3$ , respectively, for the four cloud types in chapter 5.



### 6.5.3 Effects of Tangent Height

Little dependence on tangent height is found for sensitivities at  $h_t < 7$  km [Figure 6.7] where the differences may be neglected for fast models. However, the difference becomes significant when  $h_t > 7$  km. An *ad hoc* correction for the sensitivity slope would be to use the saturated radiance ( $T_{b0}$ ) from the background air, i.e.

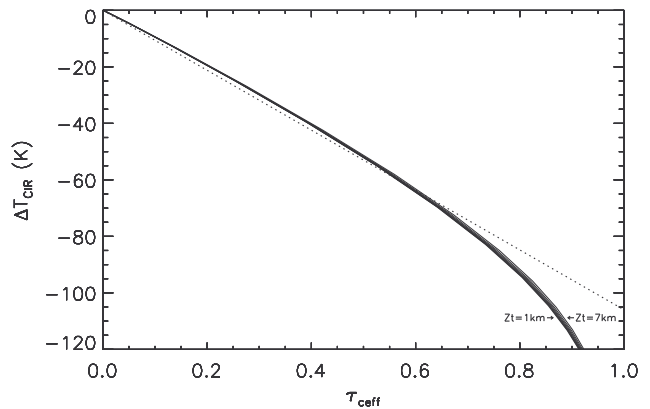


Figure 6.7 Sensitivity at different  $h_t$ . Convective cloud type is used in these calculations. The dotted line indicates the slope of -106 K.

$$a = 186 - 1.21T_{b0} \quad (\text{K}) \quad (\text{Eq 6.5})$$

where  $T_{b0}$  can be obtained from the clear sky radiances of nearby scans.

### 6.5.4 Effects of Frequency

The sensitivity varies a little but systematically with frequency for MLS channels near 190 GHz. As shown in The frequency-dependent sensitivity is not significant compared to uncertainty of cloud radiances, which is about 5-10 K at low- $h_t$ . We may therefore neglect this effect in the fast models.

Figure 6.8, the slope decreases slightly when frequency approaches the center of the 183.3 GHz water line. Two possible causes can explain this behavior. First, according to Eq.(6.3), the radiances near the  $\text{H}_2\text{O}$  line would have a colder brightness temperature ( $T_{AB}$ ) as they are saturated at a higher altitude in the troposphere. As a result, these radiances would have a lower sensitivity for the same  $T_{scat}$ . Second, in the MH modeled PSD, cloud emission contributes more

at higher altitudes so as to increase  $T_J$ . The  $T_{scat}$  in Eq.(6.3) is replaced by  $T_J$ , which is  $T_J \equiv (1 - \omega_0)T_A + \omega_0 T_{scat}$  and greater than  $T_{scat}$ . Thus, the sensitivity would be smaller than those from frequencies farther from the line center.

The frequency-dependent sensitivity is not significant compared to uncertainty of cloud radiances, which is about 5-10 K at low- $h_t$ . We may therefore neglect this effect in the fast models.

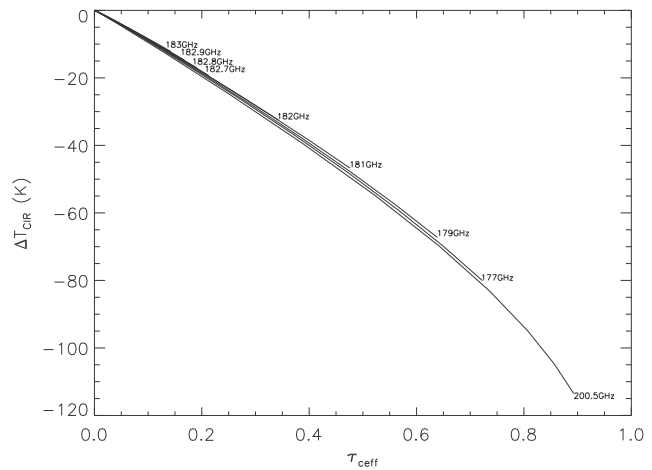


Figure 6.8 Sensitivity for different frequencies near 183.3 GHz. The cloud profile is the convective type and only calculations with IWC<0.5 g/m3 are shown.

### 6.5.5 Effects of Temperature Profile

Atmospheric temperature varies largely with latitude and time. As shown in Figure 6.9, the sensitivity slopes are mostly between -100 K and -106 K at latitudes 0-60°N. It becomes 10-20% steeper at higher latitudes due to low water vapor content and surface emission influence. The small sensitivity variation at 0-50°N latitudes, likely owe to different background clear-sky temperatures, can be corrected using the saturated air temperature as in Eq.(6.5),

$$a = 86 - 0.79T_{b0} \quad (\text{K}) \quad (\text{Eq. 6.6})$$

Figure 6.9 Strong latitude dependence of air temperature profiles. These are from the CIRA December climatology in the Northern Hemisphere.

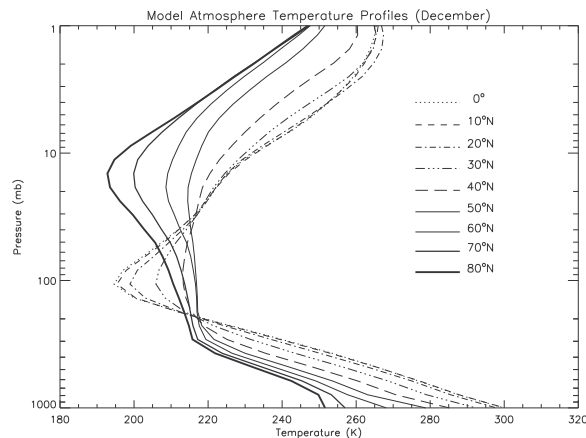
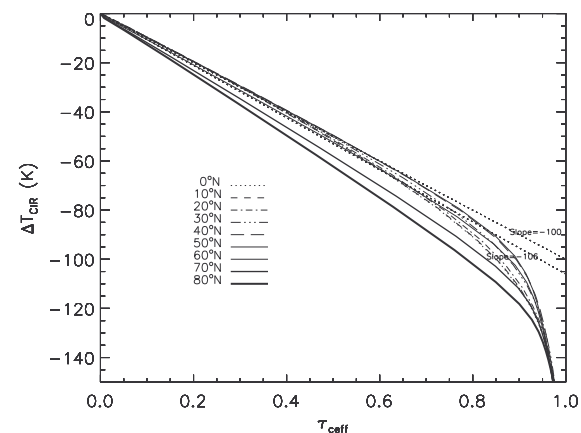


Figure 6.10 Latitude dependence of the sensitivity calculated from the temperature profiles in Figure 6.9. A convective cloud type is used with the same cloud top pressure, surface model, and relative humidity profile. The relative humidity within and below the cloud is set to 100%.



This empirical relation works reasonably well at mid- and low latitudes but does not apply to the cases at high latitudes. Due to low relative humidity, radiation from cloud scattering may have more contribution from the surface and a sophisticated surface model is needed for more accurate cloud radiance sensitivity at high latitudes.

### 6.5.6 Effects of Ice PSD and Habit

To study the sensitivity variation on PSD, we take a range of Knollenberg-like size distributions, which have been considered as some extreme cases. The results from five Knollenberg-like size distributions [Appendix E] are shown in

Figure 6.11, which have mass mean diameters ( $D_m$ ) of 21, 43, 89, 260, and 413  $\mu\text{m}$ . Each simulation assumes the same size distribution in the entire cloud profile, where only IWC is allowed to vary. As seen in

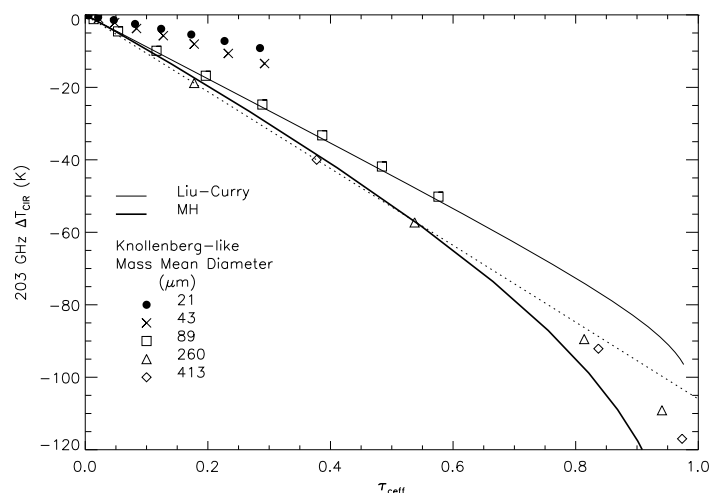
Figure 6.11, sensitivity differences due to size distribution are considerably large, where the slope is shallower for smaller  $D_m$ . They are respectively -36, -46, -80, -107, and -113 K for the five size distributions. Nevertheless, we can approximate the sensitivity variation in term of  $D_m$  as follows

$$a = 55.8 - 66.2 \log(D_m / D_0) \quad (\text{K}) \quad (\text{Eq 6.7})$$

where  $D_0 = 1 \mu\text{m}$ .

What is the significance of these different size distributions in reality? Observations repeatedly show that  $IWC$  is small when  $D_m$  is small [e.g., Knollenberg et al., 1993; McFarquhar and Heymsfield; 1996]. The size distributions of small  $D_m$  (21 or 43  $\mu\text{m}$ ) are generally unimportant to scattering radiances (since the cloud radiance contributions are usually less than 10 K for realistic IWCs). In the case of large IWC,  $D_m$  varies between 100 and 250  $\mu\text{m}$  [Appendix E], and the sensitivity slope does not vary largely with  $D_m$ . Given the 5-10 K uncertainty in cloud radiances, we might be able to tolerate the differences among various particle size distributions and consider the MH distribution as the representative form for most ice clouds. But we can readily incorporate the sensitivity change accordingly for any new PSD.

Figure 6.11 Sensitivity changes from different PSD. Five Knollenberg-like PSDs [see examples in Appendix E] are used for the extended calculations where their mass mean diameters are indicated with symbols. The MH and Liu-Curry PSDs are compared to the Knollenberg-like PSD calculations. The Liu-Curry PSD results are very similar to  $D_m = 80 \mu\text{m}$  with the Knollenberg case, which is not surprising since for the  $D_m$  in the former distributions mostly fall between 50 and 100  $\mu\text{m}$ . In these calculations, the convective cloud type is used with a vertical range between 5 and 16 km, and only results with IWC less than  $0.5 \text{ g/m}^3$  are shown. The dotted line is the slope of -102 K.

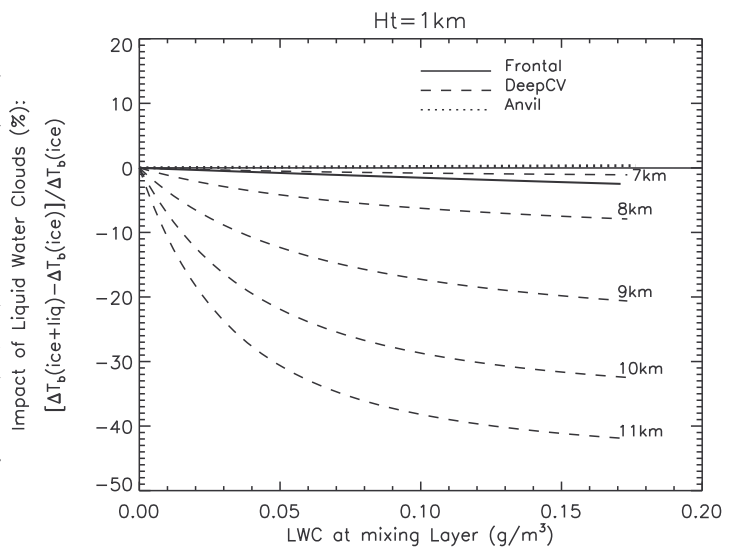


For ice clouds containing different particle shapes (habits), we expect that their impacts be similar to those due to PSD since particle habit variations can effectively change  $D_m$  and scattering efficiency. We will investigate these potential effects in the future studies, particularly on MLS radiance measurements at 118GHz (V,H), 2.5THz (V, H), and (200.5GHz-V, 245.4GHz-H) pairs.

### 6.5.7 Effects of Liquid Clouds

To evaluate liquid cloud effects on the scattering-based cloud radiances, we made a number of simulations for mixed-phase clouds. Water droplets inside ice clouds tend to enhance the percentage of emission contribution and therefore reduce the sensitivity at low  $h_t$ . Since most liquid droplets are near or below  $\sim 5$  km [Riedi, et al., 2001], their effects are often small and negligible for MLS measurements. Liquid droplets in deep convective clouds can cause degradation in the sensitivity by mixing water droplets with ice at a higher altitude (sometimes as high as 8-10 km).

Figure 6.12 Relative error of the sensitivity due to liquid clouds. For the frontal and anvil cloud models described in chapter 5, liquid cloud impacts are negligible since they reside mostly at low altitudes. In convective clouds, liquid droplets may be brought up to a higher altitude and significantly reduce the scattering-based sensitivity.



Several simulations are made, using a fixed ice cloud profiles but varying liquid content in the liquid clouds, to examine the percentage differences in cloud radiance. As shown in Figure 6.12, most liquid clouds have little ( $< 2\%$ ) impact on ice cloud radiances except for the convective core/eye cases. In the core/eye situations, water droplets can be brought up a much higher altitude, producing a thick mixed-phase layer. Depending on how high the droplets can reach, the impact of liquid clouds varies between 5% in weak mixing and 30-50% in strong mixing situations.

## 6.6 High- $h_t$ $\Delta T_{CIR} - \tau_{eff}$ Relations

At  $h_t > 12$  km, as we learn from the physical model of cloud scattering described in Appendix D, the sensitivity can be expressed as

$$\frac{\Delta T_{CIR}}{\tau_{eff}} \approx T_J - T_{AB} \quad (\text{Eq 6.8})$$

where the background emission would decrease with  $h_t$ . Hence, the sensitivity should depend on the pointing [Figure 6.13]. We can incorporate such dependence by letting coefficient  $a$  in Eq.(6.4) vary with  $h_t$ , i.e.,

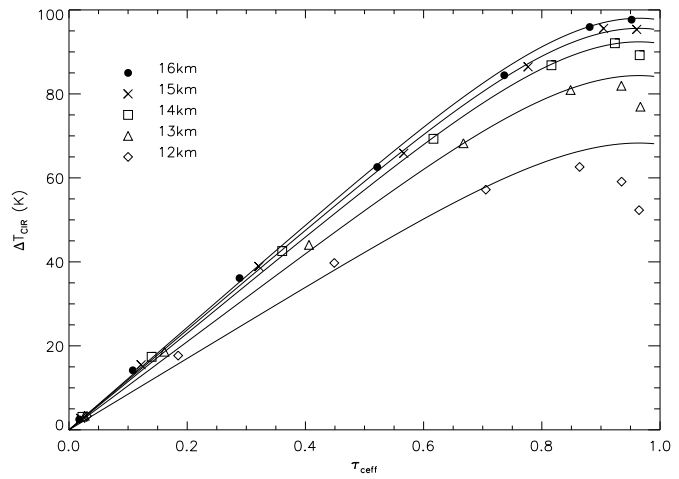
$$S_{CIR} = a(h_t)(1 - b\tau_{ceff}^n) \quad (\text{Eq 6.9})$$

If we choose  $b=0.2$  and  $n=5$  (note that the sign for  $b$  is changed here) from the best fit, coefficient  $a$  can be determined as a function of  $h_t$ . Instead of using the  $h_t$ -dependent expression, coefficient  $a$  can be written as a function of the background clear-sky radiance, namely,

$$a = 135 - 0.70T_{b0} \quad (\text{K}) \quad (\text{Eq 6.10})$$

This expression is a more generalized than that discussed in the above sections, and it is more robust in terms of  $T_{b0}$  since the  $h_t$ -dependence may vary with latitude as pressure changes for the same height.

Figure 6.13 High- $h_t$  cloud-induced radiances (203 GHz) simulated for the convective clouds (Chapter 5) with the 5-km IWC  $< 0.2 \text{ g/m}^3$ . Symbols denote the RT results whereas lines are the fits from the generalized form in Eq.6.10.



## 6.7 The Fast Model

### 6.7.1 The $\Delta T_{cir} - \tau_{ceff}$ Relation at Low- $h_t$

From the previous discussion, we have concluded that the sensitivity variation can be written as a generalized form like Eq. (6.9), called the fast model, where coefficient  $b$  is constant and  $a$  varies with other atmospheric and measurement parameters as follows

$$a = a_L(T_{b0}, h_t, f, D_m) \quad (\text{Eq 6.11})$$

where  $a$  is around -106 K,  $T_{b0}$  is the saturated brightness temperature,  $f$  is frequency, and  $D_m$  is mass mean diameter. If we use the more generic variable  $T_{b0}$  to replace  $h_t$  and  $f$ , the expression for  $a$  can be reduced to

$$a = a_L(T_{b0}, D_m) \quad (\text{Eq 6.12})$$

and  $T_{b0}$  is obtained from adjacent clear-sky measurements.

**6.7.2 The  $\Delta T_{cir} - \tau_{eff}$  Relation at High- $h_t$** 

At high  $h_t$ , the sensitivity slope may depend on  $h_t$ , frequency, and mass mean diameter, namely,

$$a = a_H(z_t, f, D_m) \quad (\text{Eq 6.13})$$

The coefficient can also be parameterized as in Eq.(6.12).

## 7 Cloud Retrievals

MLS cloud ice retrievals are normally divided into two steps: (i)  $\Delta T_{cir}$  to extinction/baseline, and (ii) extinction/baseline to IWC. The two-step retrieval allows better diagnosis of retrieval errors due to complex cloud effects, such as:

- a. Relative importance of scattering and emission/absorption,
- b. Mixture of ice and water clouds,
- c. Particle size and shape distributions,
- d. Inhomogeneity,

The extinction/baseline retrievals are sensitive mostly to (a) and (b), whereas the ice content retrieval is affected largely by (c).

With the fast models, such as the  $\Delta T_{cir}$ -IWC relation, the cloud ice retrievals are straightforward. This approach is likely used in early versions of Aura MLS Level 2 processing before more sophisticated schemes are implemented.

### 7.1 Overview of Cloud Retrieval Algorithm

Figure 7.1 shows the data files and modules that will be used in cloud retrieval. Following are brief descriptions of these files and modules.

#### Modules:

*Clear-Sky Forward Model* is described in a separate document [Read, 2004], which will provide clear-sky opacity for each  $h_t$  as a function of LOS distance. It can be replaced with the less accurate *Cloud Radiance Model* that does not use Voigt lineshape at frequencies near line centers.

*Cloud Radiance Model* is described in Chapter 4, which has a fast model version [Chapter 6] and a full calculation version. The main purpose of this model is to provide the  $\Delta T_{cir}$ - $\tau_{cs}$ ,  $\Delta T_{cir}$ -IWC and  $\Delta T_{cir}$ -*hIWP* relations and clear sky transmission functions.

*Optical Depth Calculation* module converts cloud radiances to cloud effective optical depth using the  $\Delta T_{cir}$ - $\tau_{eff}$  relation determined from the *Cloud Radiance Model*.

*Inversion along LOS* is a retrieval process for low-  $h_t$  cloud radiances to obtain cloud extinction profiles. It takes advantage of different absorption near a strong line (such as 183GHz H<sub>2</sub>O and 234GHz O<sup>18</sup>O) to profile cloud extinction structure along the LOS for each  $h_t$ . In this case, retrievals are independent among each  $h_t$ .

*2-D Tomographic Inversion* is used in high-  $h_t$  cases to produce extinction/baseline profiles along track. These extinction/baseline profiles represent radiances unexplained by the clear-sky RT model. If assumed due to clouds, they can be converted to IWC or *hIWP*.

*Ice Water Content Calculation* converts the retrieved cloud extinction/baseline to ice content for given particle size distributions.

#### Inputs:

*Cloud radiances* are obtained by calculating the difference between the measured radiance and expected clear-sky radiance.

*Ice Particle Size Distribution* can be either modeled or measured size distribution and will be used in the cloud ice retrieval to convert volume extinction coefficient to ice water content.

### Outputs:

*Cloud Ice Volume Extinction Coefficients* are the retrieval outputs with estimated uncertainties, and will be saved as a daily diagnostic file. The results from high and low  $h_t$  are kept separately because of different resolutions and observing principles. The low-  $h_t$  results usually have a finer horizontal resolution.

*Cloud IWC* files contain values and estimated uncertainties at the standard MLS pressure levels but on a finer horizontal resolution (i.e., a multiple of 240 profiles per orbit).

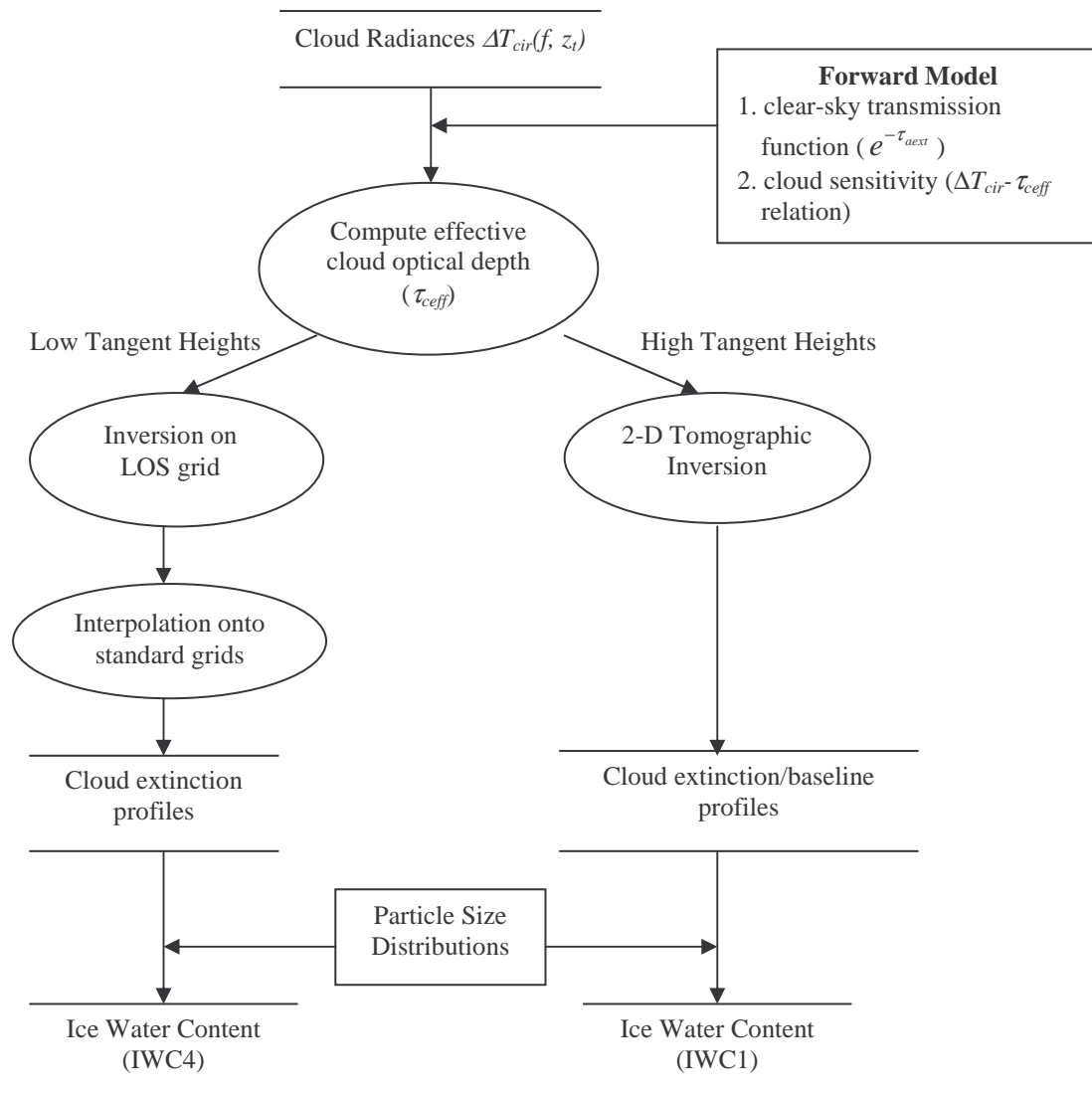


Figure 7.1 Data flow and components of cloud ice retrieval algorithm.

## 7.2 Determination of Cloud-Induced Radiances

Preliminary  $\Delta T_{cir}$  can be estimated after initial  $P_{tan}$  and  $T$  retrievals. A simple RT model method, as described in Chapter 3, is to compute the residuals between measured and modeled radiances (assuming 110%  $RHi$  in the troposphere). This calculation produces a rough estimate of  $\Delta T_{cir}$ , which are used initially to flag large  $\Delta T_{cir}$  for clear-sky retrievals. As clear-sky retrievals improve in the subsequent phases, more accurate  $\Delta T_{cir}$  are computed with various methods such as the *baseline* approach and the single-channel approach. These methods and their error were discussed in §3.4.

### 7.2.1 The $f^4$ Approximation for Splitting Double Sideband $\Delta T_{cir}$

Aura MLS receivers are double-sideband radiometers except for the 118-GHz. Ice particle scattering at the upper and lower sidebands can produce very different  $\Delta T_{cir}$  values due to frequency separation and LOS absorption differences. As a result, the sensitivity, the cloud effect optical depth, and  $\Delta T_{cir}$  need to be handled on a single sideband basis. Here, we apply the  $f^4$  approximation to the  $\Delta T_{cir}$  measured by the double sidebands and split it into  $\Delta T_{cir}$  with respect to two single sidebands.

At size parameter  $\chi < 1$ , Rayleigh scattering approximation is valid and yields the  $f^4$  dependence among volume scattering coefficients. As shown in Figure 5.7, most contributions to the  $\beta_{c,s}$  at 203 GHz come from particles with  $\chi < 1$ , suggesting that the  $f^4$  law is a good approximation at 203 GHz. Figure 7.2 shows that the  $f^4$  approximation works very well for MLS 190 and 240-GHz channels over a wide range of the MH PSDs. At large  $D_m$  the calculated ratios depart slightly from the  $f^4$  law, as expected for more contributions from scattering in the Mie regime.

Under the  $f^4$  approximation, the upper and lower sideband cloud-induced radiances,  $\Delta T_{cirU}$  and  $\Delta T_{cirL}$ , respectively, may be obtained from the double sideband  $\Delta T_{cir}$  as follows

$$\Delta T_{cirU} = \frac{f_U^4}{f_U^4 \gamma_U + f_L^4 \gamma_L} \Delta T_{cir}$$

$$\Delta T_{cirL} = \frac{f_L^4}{f_U^4 \gamma_U + f_L^4 \gamma_L} \Delta T_{cir}$$

if the radiances at both sidebands are optically thin, where  $\gamma_U$  and  $\gamma_L$  are the upper and lower sideband ratios, and  $f_U$  and  $f_L$  are their frequencies. The above splitting formulas will not work for the case where one of sideband is optically thick. A more sophisticated RT method is needed to accurately split  $\Delta T_{cir}$ . Such method is subject to future MLS algorithm developments.

The  $f^4$  approximation is not valid for the 640 GHz and 2.5 THz channels where cloud scattering occurs mostly in the Mie regime. For 190-240 GHz, the  $f^4$  approximation has error of  $< 5\%$  for PSDs of large  $D_m$ .

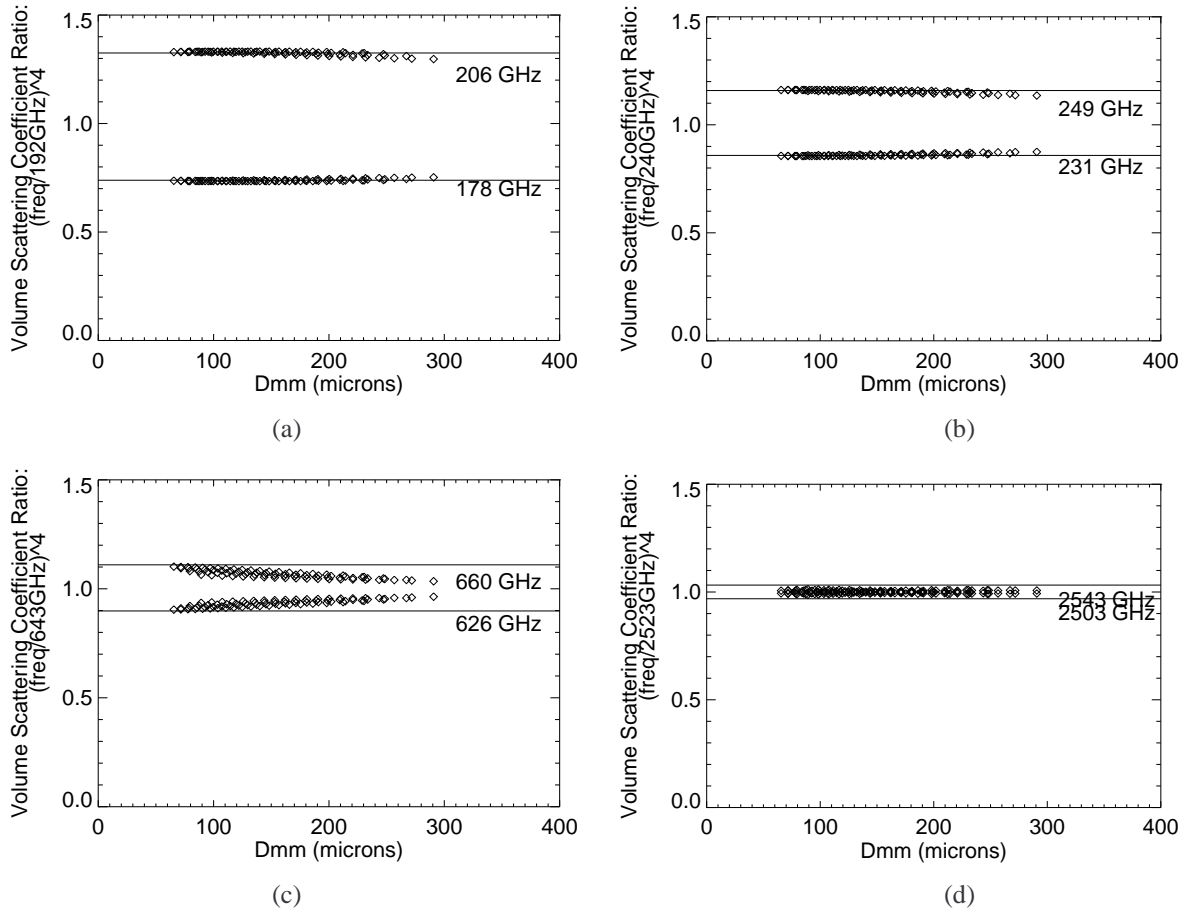


Figure 7.2 Comparisons of the  $f^4$  approximation and calculated volume scattering coefficients for the upper and lower sideband frequencies relative to the LO frequency. The solid lines are the  $f^4$  ratios of upper (lower) sideband frequency over the LO frequency, whereas symbols are the calculated ratios of corresponding volume scattering coefficients assuming the MH97 PSDs. The volume scattering is determined by modes of PSDs, and thus comparisons are made for different mass mean diameters. The MH PSDs used in the calculations cover a wide range of temperature ( $-15^\circ\text{C}$ ,  $-30^\circ\text{C}$ ,  $-45^\circ\text{C}$ ,  $-60^\circ\text{C}$  and  $-75^\circ\text{C}$ ) and IWC ( $0.004 - 1 \text{ g/m}^3$ ) values. The frequencies from four MLS double-sideband radiometers are studied and validation of the  $f^4$  law depends strongly on frequency.

### 7.3 Cloud Extinction Retrieval

Cloud extinction retrieval is quite different at high- and low- $h_t$  cases in terms of viewing geometry and sensitivity. At high  $h_t$ , useful radiances are usually limited to single frequency in a window channel that has a relatively cold clear-sky background. The clear-sky background must be cold enough to observe the contrast (warmer radiances) induced by clouds. The retrievals at high  $h_t$  have relatively poor horizontal resolution due to long path length. One way to improve the horizontal resolution is to use the so-called tomographic inversion that makes use of samplings from adjacent scans and  $h_t$ . The tomographic inversion is feasible since EOS MLS is viewing forward and all observations are made within the orbital plane. In fact, this cloud retrieval is a similar scheme to MLS clear-sky gas retrieval [Livesey, 2004].

The low- $h_t$  cloud retrievals are independent of  $h_t$  and the vertical distribution of IWC comes from penetration differences of various frequency channels. The bottom of penetration depth varies from  $\sim 20$  km to  $\sim 5$  km in altitude. As the unique sounding, the low- $h_t$  retrieval inverts cloud extinction profile as a function of distance along LOS. Thus, such result will affect both horizontal and vertical distributions of cloud field. The continuous MLS scan in the orbital plane may allow full 2-D coverage along track as the sampling at  $h_t < 8$  km overlaps between adjacent scans. The retrieved cloud variables (IWC or  $\beta_{ce}$ ) along LOS can be averaged onto the standard vertical and horizontal grids.

### 7.3.1 Cloud Extinction Retrieval from Low- $h_t$ Radiances

For low- $h_t$  cases, the cloud extinction is retrieved in two steps through multiple iterations. Because cloud self-extinction (i.e., radiation loss caused by cloud itself) is not negligible, we introduce a new quantity, called the derivative of cloud attenuation, to form linear retrieval systems

$$x(s) \equiv -\frac{d\Gamma_c(s)}{ds} \quad (\text{Eq 7.1})$$

where

$$\Gamma_c \equiv e^{-\tau_{cext}}$$

$$\tau_{cext} = \int_0^s \beta_{cext}(s') ds'$$

The first problem to solve is the linear system between  $x(s)$  and  $\tau_{ceff}$  (effective cloud optical depth), where  $s$  is the distance along LOS. The linear relation is simply the definition of  $\tau_{ceff}$  in Eq.(6.1) that can be rewritten as

$$\tau_{ceff}(f, z_t) = \int_{s(z_t)} x(s') \Gamma_a(f, s') ds' \quad (\text{Eq 7.2})$$

where  $\Gamma_a \equiv e^{-\tau_{aext}}$  is the clear-sky attenuation or the *weighting function* for  $x(s)$ .  $\Gamma_a$  can be obtained from the gas absorption model, i.e.,

$$\tau_{aext} = \int_0^s \beta_{aext}(s') ds'.$$

The second problem to solve is the relationship between  $\beta_{cext}(s)$  and  $x(s)$ . It is a straightforward calculation if we consider the facts:

$$\beta_{cext}(s) = x(s)/\Gamma_c(s) \quad (\text{Eq 7.3})$$

$$\Gamma_c(s) = 1 - \int_0^s x(s') ds' \quad (\text{Eq 7.4})$$

In Eq (7.4), we have used the fact  $\Gamma_c(s=0) = 1$ .

To solve the first problem, an inversion for  $x$  is carried out independently for each  $h_t$ . At each  $h_t$  (or MIF), multi-channel cloud radiances or effective optical depths are used, producing a set of Eq.(7.2), which can be written in a discrete form as follows

$$\begin{bmatrix} \tau_{eff}(f_1) \\ \tau_{eff}(f_2) \\ \vdots \\ \tau_{eff}(f_m) \end{bmatrix} = \begin{bmatrix} k_{11} & \cdots & k_{1n} \\ \vdots & \ddots & \vdots \\ k_{m1} & \cdots & k_{mn} \end{bmatrix} \begin{bmatrix} x(s_1) \\ x(s_2) \\ \vdots \\ x(s_n) \end{bmatrix} \quad (\text{Eq 7.5})$$

where  $m$  is the number of frequencies,  $n$  is the number of grids along LOS, and

$$k_{ij} = \Gamma_a(f_i, s_j) \Delta s \quad (\text{Eq 7.6})$$

Now in Eq.(7.5), the effective optical depths from multiple channels become the measurement vector while  $x(s_j)$  is the state vector. Once  $x(s_j)$  is inverted, we have solved the first problem in the retrieval. The second problem is then solved numerically by computing  $\Gamma_c(s_j)$  and  $\beta_{c-e}(s_j)$  as follows

$$\Gamma_c(s_j) = 1 - \sum_{k=1}^j x(s_k) \Delta s \quad (\text{Eq 7.7})$$

$$\beta_{c-e}(s_j) = x(s_j) / \Gamma_c(s_j) \quad (\text{Eq 7.8})$$

### 7.3.2 Cloud Ice Retrieval from High-ht Radiances

High- $h_t$  limb radiances are optically thin, i.e.,  $\Gamma_a \approx 1$ , and Eq. (7.2) can be re-written as

$$\tau_{eff}(z_t) \approx \int_{s(z_t)} x(s') ds' \quad (\text{Eq 7.9})$$

Note that  $\tau_{eff}$  does not depend on frequency here simply because cloud-sensitive radiances are only from the window channels. The high- $h_t$  cloud ice (extinction and IWC) retrievals are similar to the tomographic inversion, which is described as follows.

First, a 2D domain is defined, e.g., (-800 km, 800 km) along track and (12 km, 22 km) in height. Radiance measurements at  $h_t > 13$  km are used to assure reliable cloud detection. A discrete form of Eq.(7.9) set can be written as

$$\begin{bmatrix} \tau_{ceff}(z_1^1) \\ \vdots \\ \tau_{ceff}(z_{q_1}^1) \\ \vdots \\ \tau_{ceff}(z_1^i) \\ \vdots \\ \tau_{ceff}(z_{q_i}^i) \\ \vdots \\ \tau_{ceff}(z_1^p) \\ \vdots \\ \tau_{ceff}(z_{q_p}^p) \end{bmatrix} = \begin{bmatrix} k_{11} & \cdots & k_{1N} \\ \vdots & \ddots & \vdots \\ k_{M1} & \cdots & k_{MN} \end{bmatrix} \begin{bmatrix} x_{11} \\ \vdots \\ x_{1m} \\ \vdots \\ x_{j1} \\ \vdots \\ x_{jm} \\ \vdots \\ x_{n1} \\ \vdots \\ x_{nm} \end{bmatrix} \quad (\text{Eq 7.10})$$

where scan index  $i=1, \dots, p$ , and  $q_i$  is the number of  $h_t$  used. The state vector in the selected domain has  $n$  profiles and  $m$  vertical levels. We choose the coordinates of the state vector such that  $n$  is a multiple (1-2) of the number of scans in the domain. The vertical grids are on every other pressure surface (i.e., 6 levels per decade) of the MLS standard grid. Hence, the number of measurements and unknowns in Eq.(7.10) are respectively given by,

$$M = \sum_{i=1}^p q_i \quad (\text{Eq 7.11})$$

$$N = nm \quad (\text{Eq 7.12})$$

The weights ( $k_{uv}$ ) that link  $x$ 's and  $\tau_{ceff}$  's are simply the length of LOS inside each state vector element, i.e.,

$$k_{uv} = \Delta s_{uv} \quad (\text{Eq 7.13})$$

where  $u = 1, \dots, M$ , and  $v = 1, \dots, N$ . After  $\mathbf{x}$  is inverted from Eq.(7.10), the transmittance function  $\Gamma_c(z)$  is then computed for each profile as

$$\Gamma_c(j, z_k) = \sum_{k'=1}^k x_{jk'} \Delta z \quad (\text{Eq 7.14})$$

where the first index of  $k'$  corresponds to the top pressure surface of the profile. Subsequently,  $\beta_{c\_e}(s_j)$  can be found from

$$\beta_{c\_e}(j, z_k) = x_{jk} / \Gamma_c(j, z_k) \quad (\text{Eq 7.15})$$

#### 7.4 Retrieval of IWC from Baseline

As an alternative, IWC can be retrieved from the high- $h_t$   $\Delta T_{cir}$  directly, using the modeled  $\Delta T_{cir}$ -IWC relation in §6.6. Since the optically-thin limb radiances peel the topmost cloud layer, the  $\Delta T_{cir}$  is normally proportional to IWC at the same height where the instrument is pointing [Wu et al., 2004].

The *baseline*, the spectrally-flat  $h_t$ -dependent radiance component in each radiometer, is a good proxy for  $\Delta T_{cir}$ . This is the absolute radiance unexplained by the clear-sky forward model and is often caused by clouds. The retrieved *baseline* may come from sources other than clouds, such as excess dry/wet continuum emission, antenna thermal emission, spillover radiation, cosmic background. Therefore, the baseline method depends on the RT model accuracy and how well the other contributions are understood and modeled.

#### 7.5 Convective and Cirrus Cloud Classification

More advanced cloud ice retrievals need to take particle size variations into consideration. Classification of convective and cirrus clouds is a qualitative retrieval of ice PSD and can be made with MLS 190 GHz, 640 GHz, and 2.5 THz radiance measurements. Each of these measurements is sensitive to a unique part of PSD. Since Aura MLS is not designed for cloud measurements, it needs to be careful to co-locate cloud measurements (via averaging or smoothing) in both horizontal and vertical dimensions. As shown in Figure 7.3, the R5 (2.5 THz) channel has a matched transmission function to R1 (118 GHz) band32.c2, and the R4 (640 GHz) has a matched transmission function to R1 band32.c1. These matches are valuable for cloud classification and further particle size studies.

Figure 7.3 also suggests the poor vertical resolution at 10-20 km for the retrievals with R2/R3 channels, where no channel exhibits a sharp penetration bottom to peel out the vertical content. The R2 channels near the center of the water line are not saturated sufficiently by stratospheric water vapor to yield a penetration path ended at 10-20 km. On the other hand, the R3 channels near the O<sup>18</sup>O line are neither sufficiently saturated by the isotope abundance.

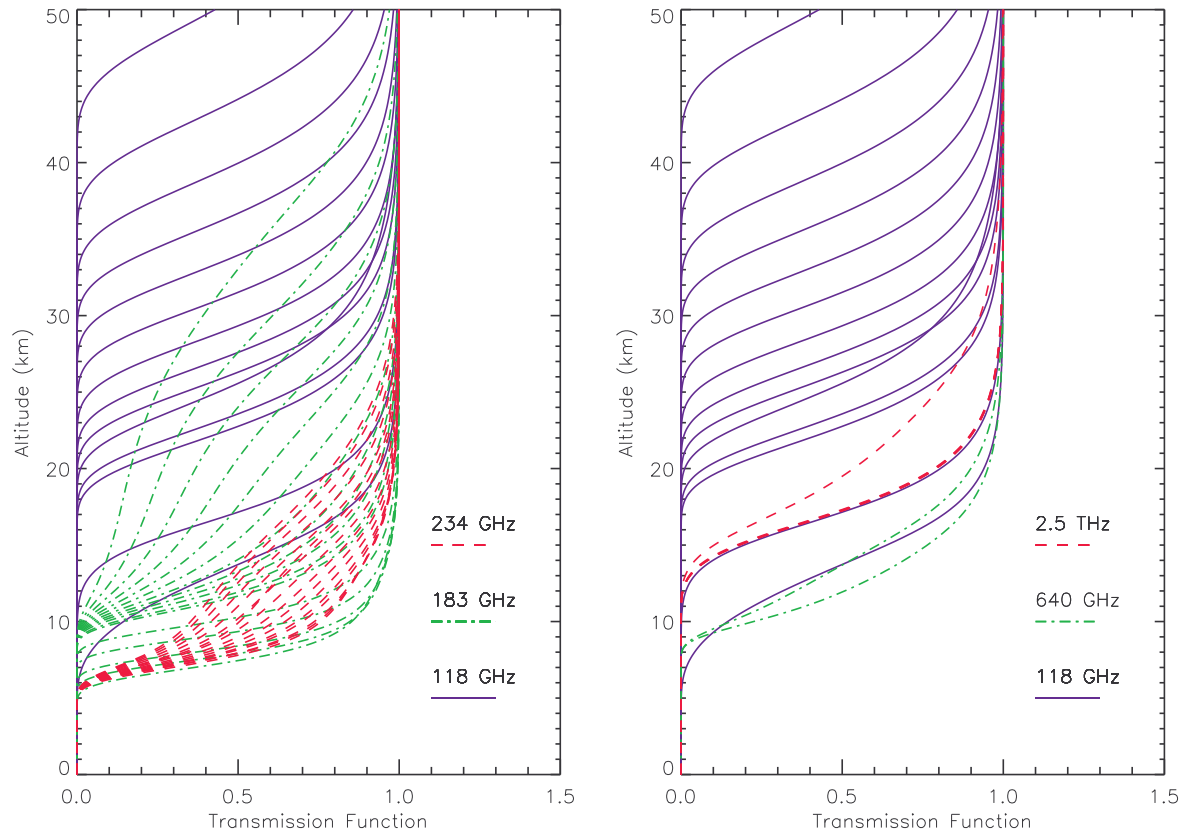


Figure 7.3 Transmission functions for Aura MLS frequency channels. Channels with matched penetration depths are useful for particles size studies. For the 640 GHz (Band10.C1) and 2.5 THz (Band15.C1) calculations, the transmission functions of the upper and lower sidebands are plotted.

## 7.6 Error in $\Delta T_{cir}$ -to- $IWC$ or $\Delta T_{cir}$ -to- $IWP$ conversion

Large uncertainty arises when converting MLS  $\Delta T_{cir}$  to  $IWC$  because MLS radiances are only sensitive to large ice particles. Assumptions about ice particle size and shape distributions are critical to relate ice scattering sensed by MLS to the total ice mass. As discussed in Appendix E, a bimodal PSD can complicate the  $IWC$  retrieval by having more degrees of freedom in the PSD.

MLS  $IWC$  uncertainty is dominated by scaling error from the  $\Delta T_{cir}$ -to- $IWC$  conversion, not bias. Table 7-1 lists the estimated scaling differences estimated for the 203-GHz radiance at 100 hPa using different PSDs. The derived  $IWC$  can differ by a factor of 2-3 depending on the PSD used. The MH97 PSD parameterization was developed from aircraft observations of deep convective outflows during the Central Equatorial Pacific Experiment (CEPEX). The MH97 work incorporates effects of size-dependent bulk density of ice particles in their parameterization in terms of mass-equivalent spheres. It produces clear bimodal distributions for large  $IWC$  near the tropopause. However, the dataset lack measurements inside convective cores. In the case of strong turbulence/mixing during convective updraft, the PSD inside convective cores may differ substantially from those measured in the outflows. Strong overshooting cases can yield updraft

velocities as high as  $20 \text{ ms}^{-1}$  (e.g., Geerts et al., 2000), with which ice particles can be readily mixed over several km. As a result, deep convective clouds at 100 hPa may have a PSD similar to those at lower altitudes. Such PSD mixing between vertical cloud layers, as shown in Table 7-1 for the  $-60^\circ\text{C}$  and  $-75^\circ\text{C}$  cases, would result 30% differences in *IWC* from, which is relatively small compared to the differences from using different PSD parameterizations.

Table 7-1 100-hPa *IWC* converted from the same  $\Delta T_{cir}$  at 203 GHz using different PSDs. The differences reflect uncertainties caused by assumptions about PSDs in the upper troposphere.  $D_{mm}$  is mass-mean diameter associated with each PSD.

PSD parameterization	T ( $^\circ\text{C}$ )	$D_{mm}$ ( $\mu\text{m}$ )	<i>IWC</i> ( $\text{mg}/\text{m}^3$ )
McFarquhar and Heymsfield [1997]	-60	114	5.6
	-75	103	<b>7.5</b>
Heymsfield et al., [2002]	-60	143	5.6
	-75	73	20.1
Liu and Curry [1998]	-60	64	12.3
	-75	56	17.1

PSD can be height-dependent and sometimes *IWC*-dependent as suggested by MH97. Liu and Curry (1998) studied essentially the same CEPEX dataset but came up with a slightly different PSD parameterization. The primary difference between MH97 and Liu-Curry parameterizations is the assumption about particles with diameter  $< 100 \mu\text{m}$ , which turns out to be critical for *IWC* retrievals at 203 GHz. The Liu-Curry parameterization produces a smaller mass-mean diameter for the same temperature and hence a would-be larger MLS *IWC*. Heymsfield et al. (2002) compiled a parameterization by fitting height-dependent gamma distributions to in-situ measurements in the tropics and subtropics at  $T > -55^\circ\text{C}$ . The MLS *IWC* from this parameterization at  $-60^\circ\text{C}$  yields the same result as one from the MH97 PSD despite different mass-mean diameters. The Heymsfield (2002) result at  $-75^\circ\text{C}$  may be negligible because it is extrapolated from the measurements at lower altitudes. Lack of reliable PSD information renders large scaling error as high as 100-200% for the *IWC* at 100 hPa.

In addition to the PSD uncertainties, Evans and Stephens (1995a) argued that assumptions about ice particle shape and density could be equally important as PSD under extreme conditions. Czekala (1998) showed that horizontally aligned non-spherical ice particles would have a significantly large effect on microwave limb sounding measurements. However, it remains to be seen how much in reality such an effect is detectable by Aura MLS. Polarized radiances from the R5H and R5V will be the best measurement to provide such information.

## 8 Implementation and Future Work

MLS V1.4 algorithm is a launch-ready software where some cloud flag and retrieval schemes discussed in the previous chapters are implemented. A more comprehensive overview of the V1.4 Level 2 retrieval can be found in Livesey [2004]. The cloud-related implementation in V1.4 is detailed in this chapter.

### 8.1 The V1.4 Implement for Cloudy Radiance Handling

Here, the discussion is focused on the methods for  $\Delta T_{cir}$  calculations in each retrieval phase, the handling of the flagged radiances, and the IWC retrieval. Figure 8.1 outlines the cloud flag schemes in the V1.4 retrieval processing, along with the caveats in implementing these cloud schemes.

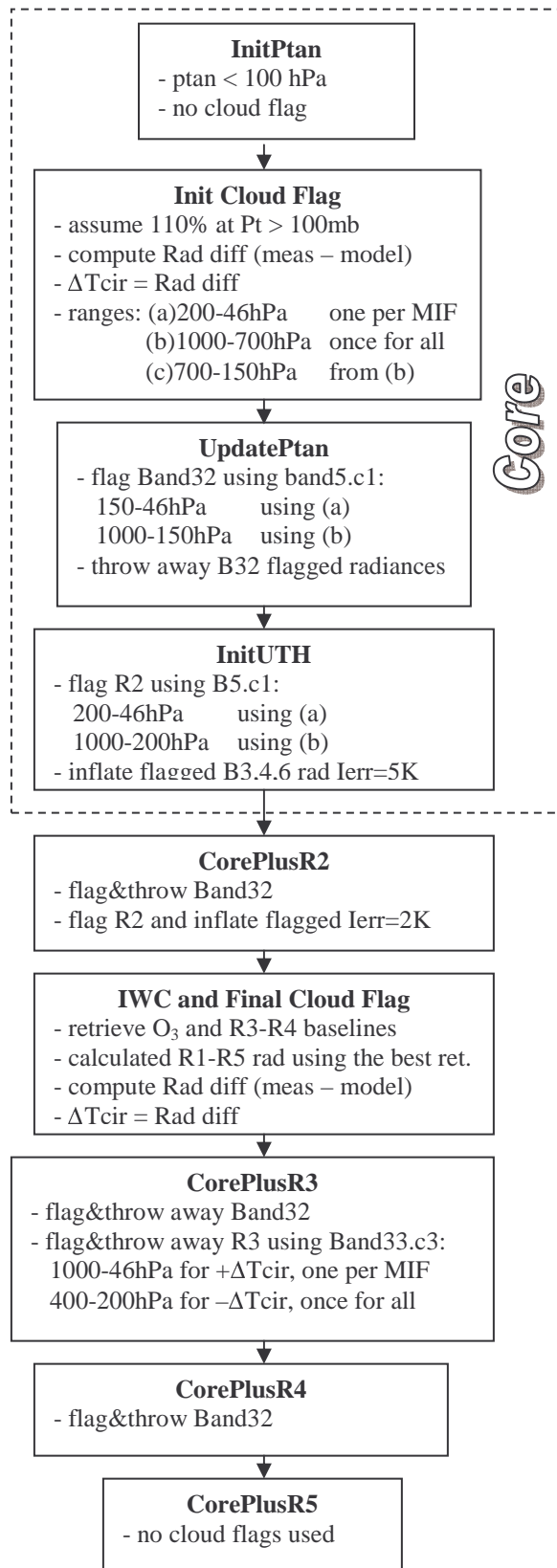
#### 8.1.1 Cloud flag thresholds

The parameters for flagging cloudy radiances in V1.4 are listed in Table 8-1, where methods for  $\Delta T_{cir}$  calculations, as shown in Figure 8.1, may be different in each retrieval phase.

Table 8-1 V1.4 cloud flag thresholds, ranges and actions

RETRIEVAL PHASE	RADIANCE TO OBTAIN FLAG	$\Delta T_{cir}$ THRESHOLDS FOR CLOUD FLAG		PRESSURE RANGE	ACTIONS ON FLAGGED RADIANCES
InitPtan	None	None		None	None
UpdatePtan	Band5.C1	R1.B32	> 5 K < -10 K	150-46 hPa 1000-150 hPa	Excluded
InitUTH	Band5.C1	R2	> 5 K < -10 K	200-46 hPa 1000-200 hPa	Ierr = 5 K
CorePlusR2	Band5.C1	R1.B32	> 5 K < -10 K	150-46 hPa 1000-150 hPa	Excluded
		R2	> 5 K < -10 K	200-46 hPa 1000-200 hPa	Ierr = 2 K
CorePlusR3	Band5.C1	R1.B32	> 5 K < -10 K	150-46 hPa 1000-150 hPa	Excluded
	Band33.C3	R3	> 5 K < -20 K	1000-46 hPa 400-200 hPa	Excluded
CorePlusR4	Band5.C1	R1.B32	> 5 K < -10 K	150-46 hPa 1000-150 hPa	Excluded
	Band10.C1	R4	None	None	None
CorePlusR5	Band5.C1	R1.B32	> 5 K < -10 K	150-46 hPa 1000-150 hPa	Excluded
	Band15.C1	None	None	None	None

## 8. Implementation and Future Work



### Caveats:

For **Init Cloud Flag**, **UpdatePtan**, & **InitUTH**, the cloud flag is generated using the RT model method described in §3.4.1.1 in which  $RH_i$  is assumed 110% in the troposphere. R2 radiances at 200-46 hPa (over all bands) are flagged on a MIF basis if  $R2.B5.C1 \Delta T_{cir} > 5$  K. At 1000-700 hPa, R2 radiances are flagged if the  $\Delta T_{cir} < -10$  K in any MIF. At 700-150 hPa, since the  $\Delta T_{cir}$  calculations are not reliable, the cloud flag from 1000-700hPa is used instead. R1.B32 radiances are flagged in a similar manner using the R2.B5.C1 radiances but in slightly different P<sub>tan</sub> ranges. R1.B1 is not flagged at all. The flagged B32 radiances are excluded in all the retrieval phases. The flagged R2 radiances are used for T, P<sub>tan</sub>, H<sub>2</sub>O, and O<sub>3</sub> retrievals with radiance noise inflated to 5 K.

In **CorePlusR2**, the flagged R2 radiances are used in the retrieval with noise inflated to 2 K. In this case, a more accurate and hence slower RT model is used to retrieve multiple species simultaneously. The best tropospheric H<sub>2</sub>O retrieval is expected in this phase.

In **IWC and Final Cloud Flag**, IWC is retrieved using the baseline method described in §7.4. R2 IWC is from the baseline retrieved in **CorePlusR2**. R3 and R4 baselines along with O<sub>3</sub> are retrieved specially in this phase, using Band33.C3-4 and B10.C1. T, P<sub>tan</sub> and H<sub>2</sub>O and other species are constrained to the **CorePlusR2** results. Together, B33.C3-4 allows the simultaneous retrievals of baseline and O<sub>3</sub>. The joint O<sub>3</sub>-baseline retrieval produces better accuracy for R3 baseline than using a single channel. As a result, O<sub>3</sub> is slightly improved from the **CorePlusR2** result. With the updated O<sub>3</sub> and the species retrieved in **CorePlusR2**, we compute the finalized R1-R5  $\Delta T_{cir}$ , the (measured-modeled) radiance differences, using the methods discussed in §3.4.1.2.

In **CorePlusR3**, R3 radiances (over all bands) are flagged if  $R3.B33.C2 \Delta T_{cir} > 5$  K at 1000-46 hPa on a MIF basis. The radiance is also flagged if the  $\Delta T_{cir} < -20$  K at 400-200 hPa. The flagged R3 radiances are excluded in the retrieval. A R3 baseline is still used in the gas retrievals to deal with less-severe cloudy radiances that are not flagged. This baseline is not used for any cloud ice measurements.

In **CorePlusR4 and CorePlusR5**, only B32 radiances are flagged. Baseline is retrieved along with other species to deal with minor cloud-induced radiances, but it is not used by cloud ice measurements.

Figure 8.1 V1.4 Processing flow with cloud flag and ice retrieval.

### 8.1.2 The $\Delta T_{cir}$ -IWC conversion coefficients

The V1.4 IWC is obtained from the retrieved R3 and R4 baselines (as the proxy for  $\Delta T_{cir}$ ) using the modeled  $\Delta T_{cir}$ -to-IWC coefficients for R1-R4  $\Delta T_{cir}$  at high tangent heights. Table 8-2 lists these conversion coefficients for the R1-R4 radiances, as described in §7.4.

Table 8-2 The  $\Delta T_{cir}$ -IWC conversion coefficients ( $\text{g}/\text{m}^3/\text{K}$ )

hPa	R1	R2	R3	R4
68	0.001	0.001	0.002	0.0002
83	0.001	0.001	0.002	0.00022
100	0.001	0.0015	0.0022	0.00045
121	-	0.002	0.0026	0.0019
147	-	0.003	0.004	-
178	-	0.005	0.004	-
215	-	0.005	0.004	-

## 8.2 Performance of V1.4 on Simulated Data

### 8.2.1 $\Delta T_{cir}$ calculations

The final  $\Delta T_{cir}$  calculations in V1.4 are made after the CorePlusR2 retrieval where the best  $\text{H}_2\text{O}$  retrieval is expected. At this stage, using the retrieved CorePlusR2 state vector and the full clear-sky forward model, we compute the radiance residuals (measured – modeled) for one cloud-sensitive channel in each radiometer, i.e., R1A.Band32.C1, R2.Band5.C1, R3.Band33.C3, R4.Band10.C1, and R5.Band15.C1. These radiance residuals are called  $\Delta T_{cir}$  in the end, and are archived for further cloud ice retrievals and diagnosis (i.e., §7.3 and §7.5).

Figure 8.2 and Figure 8.3 show the performance of the calculated V1.4  $\Delta T_{cir}$  at tangent pressures of  $\sim 100$  and  $\sim 1000$  hPa, respectively. The clear-sky residuals are mostly scattered around zero whereas cloudy radiances exhibits as the values significantly greater and smaller than zero. Estimated  $\Delta T_{cir}$  bias and  $3\sigma$  precision from the V1.4 calculations are plotted in Figure 8.4, where the best height regions for  $\Delta T_{cir}$  measurements appear to be at  $P_{tan} < 200$  hPa and  $P_{tan} > 700$  hPa as expected.

## 8. Implementation and Future Work

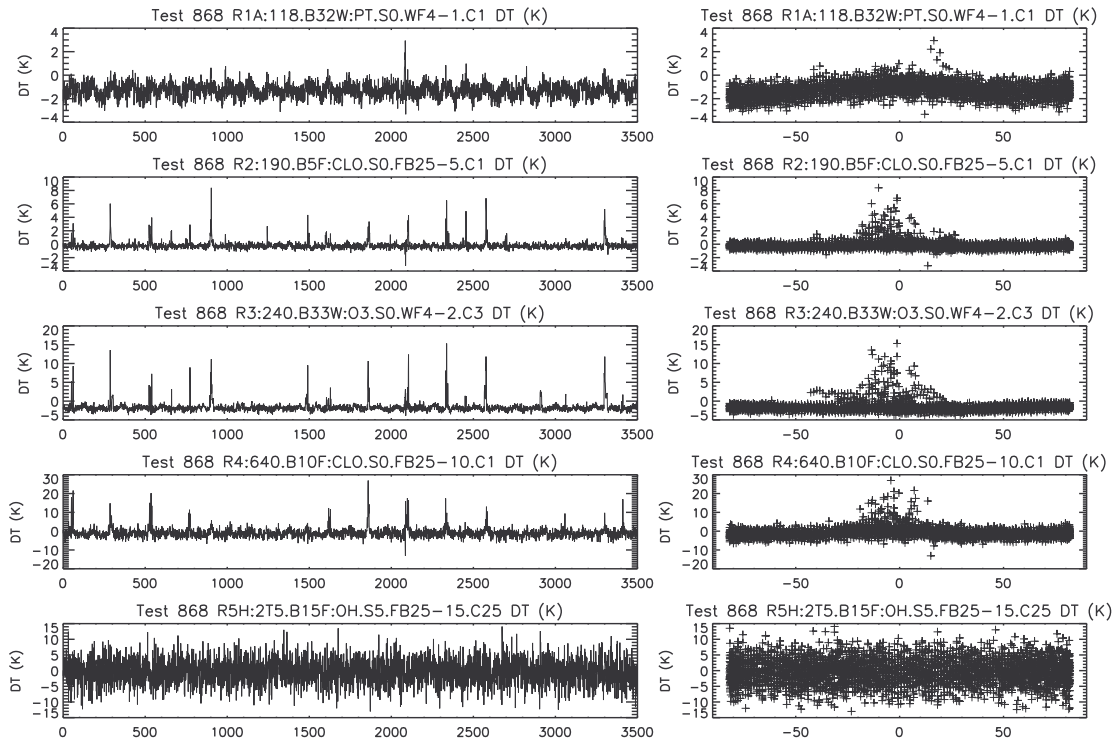


Figure 8.2 Retrieved cloud-induced R1-R5 radiances at 100 hPa.

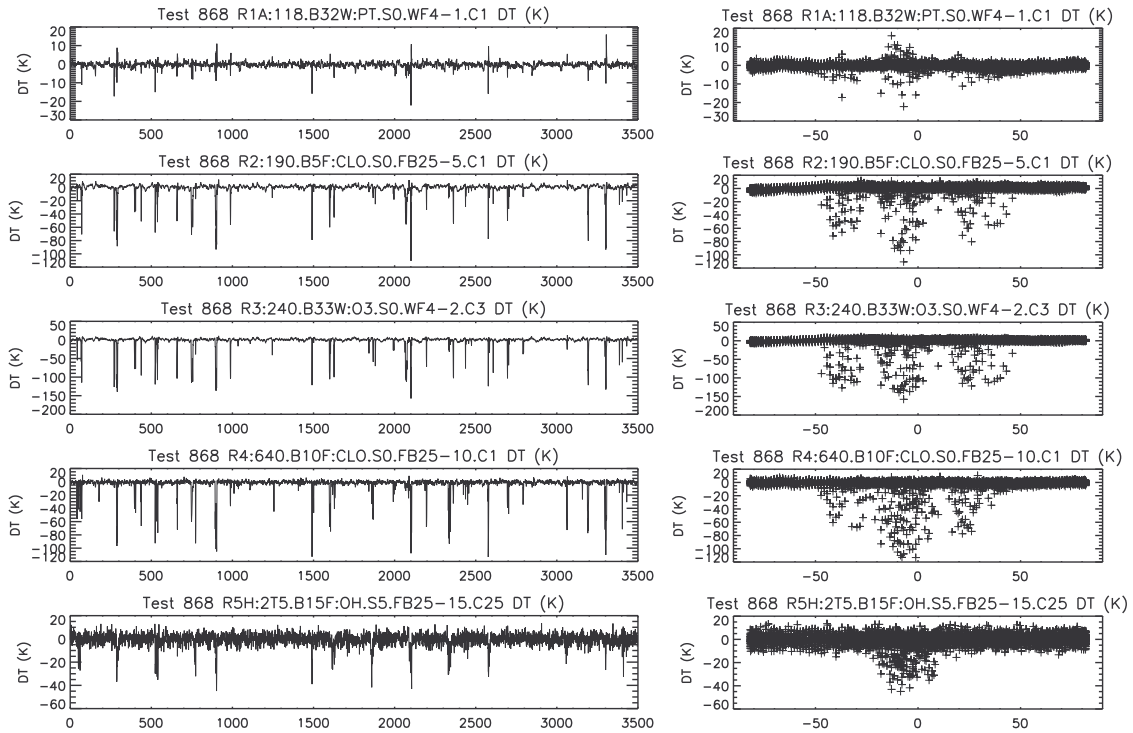


Figure 8.3 Retrieved cloud-induced R1-R5 radiances at 1000 hPa.

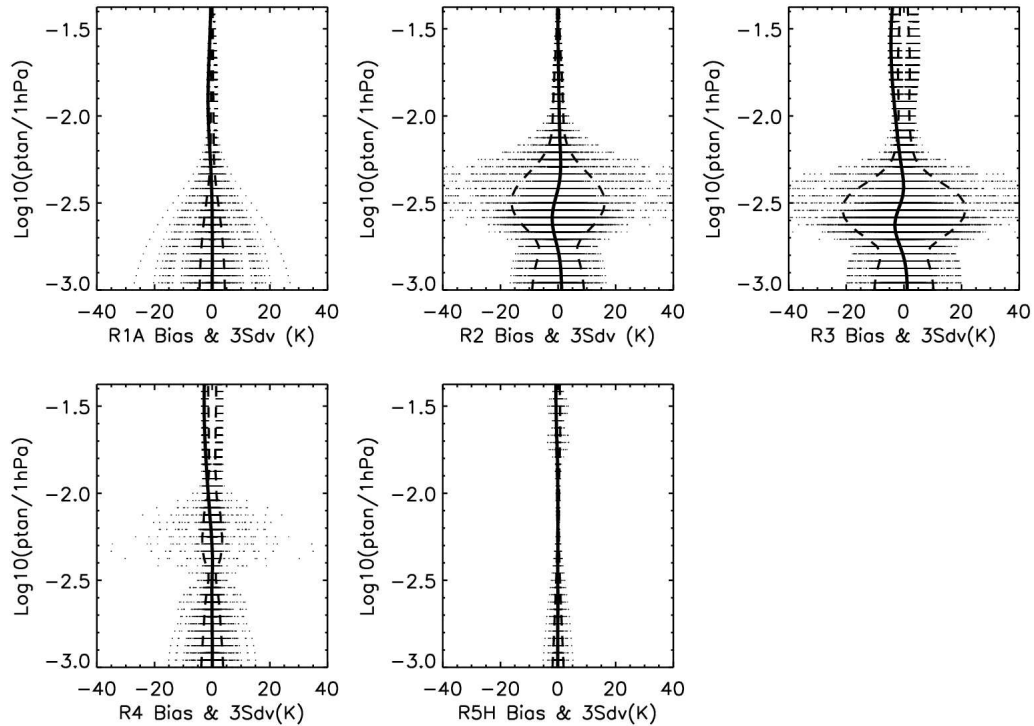


Figure 8.4 Error of R1-R5  $\Delta T_{cir}$  retrievals estimated from the simulated data. Scattered points are the  $\Delta T_{cir}$  residuals (retrieved – truth) in the simulated data. Vertical solid and dashed lines represent bias and the  $3\sigma$  standard deviation around the bias, respectively. About 3400 profiles are simulated, including many clear and cloudy (5-10%) situations.

### 8.2.2 IWC Retrievals

Despite several mismatches between the simulated and retrieved profiles, the IWC retrievals with the baseline approach have produced some promising results. As shown in Figure 8.5 from the simulated data, the 100-hPa IWC retrieved from R4 and R3 has precision of 1 and 2  $\text{mg}/\text{m}^3$ , respectively. The IWC error with the baseline method increases with tangent pressure as sensitivity decreases. Table 8-3 lists the IWC error estimated from the simulated data, where the bias and precision are directly associated with errors in the  $\Delta T_{cir}$  calculations. The scaling error is mostly related to modeled cloud microphysical properties (i.e., particle size, habit and ice density), which needs to be evaluated further with other independent measurements.

In addition to the IWC retrieval with high- $h_t$ , a retrieval using low- $h_t$  as described in Chapter 7 is also implemented in V1.4. The fast model for the radiance sensitivity, as described in Chapter 6, is not used. Instead, the sensitivity is calculated on flight

## 8. Implementation and Future Work

assuming the convective cloud type. The performance of this retrieval remains to be evaluated.

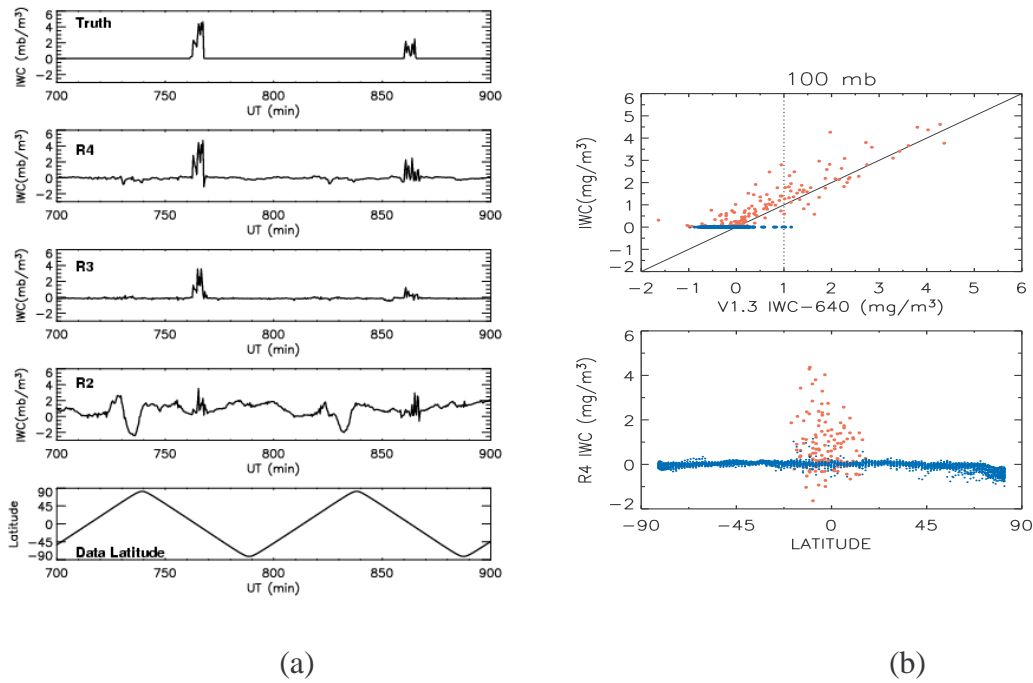


Figure 8.5 (a) Examples of 100-hPa IWC retrieval from simulated radiances where cloudy-induced radiances are calculated using the 1D cloudy-sky radiance model and added to selected clear-sky profiles. Since V1.4 retrieves 2D baseline profiles along orbital track [Livesey 2004], the IWCs converted from the 2D baselines are not expected to exactly match the truth (1D) profiles. As shown in the time series, the quality of these IWC retrievals depends directly on how well the baselines are retrieved. The R2 baseline seems to have the largest error. (b) Retrieved 100-hPa R4 IWC. Blue (red) points are cloud-free (cloudy) profiles in the truth file. In the IWC-Latitude plot, the clear-sky floor is mostly below 0.5 mg/m<sup>3</sup> except in the tropics where some positive blue points are likely due to the 1D-2D mismatches in the simulations. Also shown is that the blue points are bound tightly within  $\sim 1$  mg/m<sup>3</sup>, suggesting good reliability of the baseline retrieval scheme in the 2D retrieval.

Table 8-3 Estimated IWC biases and precisions

Pressure	Radiometer	Bias	Precision	Scaling
100 hPa	R4	$\pm 1$ mg/m <sup>3</sup>	1 mg/m <sup>3</sup>	TBD
	R3	$\pm 2$ mg/m <sup>3</sup>	2 mg/m <sup>3</sup>	TBD
147 hPa	R3	$\pm 2$ mg/m <sup>3</sup>	2 mg/m <sup>3</sup>	TBD
215 hPa	R3	$\pm 20$ mg/m <sup>3</sup>	20 mg/m <sup>3</sup>	TBD

### 8.3 Plans for Future Algorithm Improvements

#### 8.3.1 Refine Post-Launch $\Delta T_{cir}$ Calculations

The V1.4 cloud flag and  $\Delta T_{cir}$  calculation algorithms are sensitive to MLS forward model bias, which can be caused by error in the spectroscopy. Some *ad-hoc* corrections (such as in continuum coefficients) to the algorithm are planned shortly after launch.

In addition, improving gas retrievals in Core and CorePlusR2 will essentially help to improve the final  $\Delta T_{cir}$  calculations. Configuration changes are likely needed to reduce the number of oscillatory retrieved profiles, to reduce false cloud flag, and to increase cloud flag success rate.

Accurate  $\Delta T_{cir}$  calculations are also desired by the cloud ice retrieval. The algorithms used to determine  $\Delta T_{cir}$  and to split double-sideband  $\Delta T_{cir}$  need further improvements with trade-off against CPU effectiveness. Affordable and accurate  $\Delta T_{cir}$  calculations remain as a challenge in the future algorithm changes.

#### 8.3.2 Implement and Improve the *IWC* and *hIWP* Retrievals

The *hIWP* retrieval depends directly on accuracy of the  $\Delta T_{cir}$  calculations at low tangent heights. The range of useful tangent heights and reliability of the algorithm at high latitudes remain to be tested. Once the  $\Delta T_{cir}$  calculations are robust and reliable, we will apply the conversion coefficients tabulated in Table 6-1 through Table 6-5 for the *hIWP* retrieval.

Both  $\Delta T_{cir}$  -*IWC* and  $\Delta T_{cir}$  -*hIWP* coefficients are calculated using 1D RT model on ideal cloud water content profiles. They are expected to vary somewhat with PSD, cloud height, and air/surface temperature. These variations remain to be quantified in the future algorithm development.

#### 8.3.3 Enhance MLS RT Model for 2D Cloudy-Sky Atmospheres

Effects of MLS FOV averaging need to be explored in detail in order to relate MLS cloud ice to other measurements due to great cloud inhomogeneity. For this purpose, a 2D cloudy-sky RT model has been developed and will be tested for cases where ice particle size distributions, fine cloud structures, and multi-frequency observations are of interest. An important application of MLS 2D RT model will be directed towards investigations of nearly coincident cloud ice measurements from CloudSat/CPR, which produce *IWC* profiles ~7 min before MLS measurements.

#### 8.3.4 Develop a Physical Retrieval for Cloud-Induced *Baseline*

The current baseline retrieval in V1.4 has demonstrated the ability of handling cloud-induced radiances by taking care of the first-order (spectrally-flat) effect. However, it is not accurate since the cloud-induced radiances are not spectrally-flat. For example, the CorePlusR3 O<sub>3</sub> and CO retrievals have not been satisfactory in the presence of clouds when the radiances in the mid-troposphere are used. A better alternative will be direct

retrievals of the quantities related to clouds (e.g.,  $T_{\text{scat}}$ ,  $\beta_{\text{cs}}$ ,  $\beta_{\text{ca}}$ ) in conjunction with gas retrievals. Such retrievals will be studied and tested in the future algorithm development.

### **8.3.5 Algorithms to Infer Ice Microphysical Properties**

MLS multi-frequency and polarimetric measurements of cloud-induced radiances contain information on particle size and habit. Modeling and analysis of the sensitivity of MLS radiances to these properties remain to be accomplished.

## Appendices (A-F)

### Appendix A: Determining Upper/Lower Sideband Radiances

Except for the 118-GHz radiometers, all MLS measurements are double-sideband radiances. This appendix describes a technique to split single-sideband radiances from double-sideband measurements at  $h_t < 20$  km. This method is applicable to the double sideband measurements of one optically-thick sideband and one optically-thin sideband.

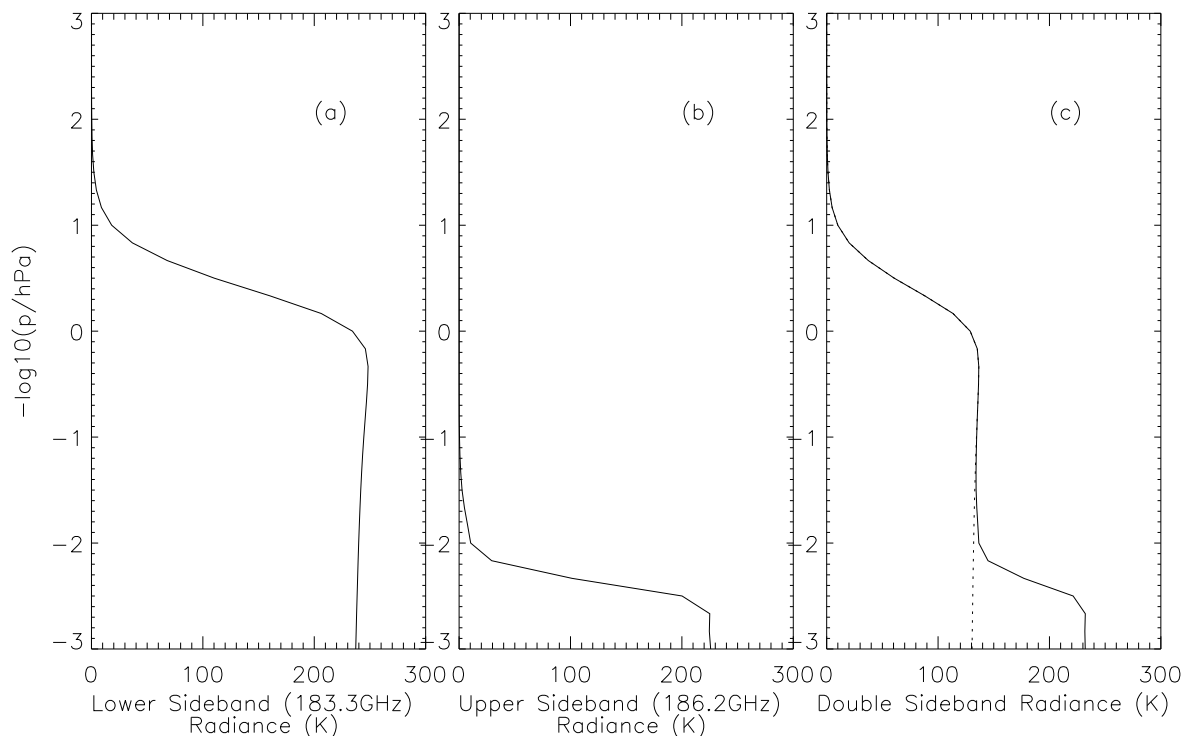


Fig A-1 Calculated MLS radiances for (a) lower sideband (183.3 GHz), (b) upper sideband (186.2 GHz), and (c) double sideband as would be measured by the radiometer. Although the lower sideband radiance is saturated below  $\sim 50$  km, it still has weak dependence on tangent height due to slight differences in path length. Such dependence is nearly linear at heights below  $\sim 50$  km and can be modeled relatively easily. A realistic sideband ratio ( $L/U=1.22$ ) is used to calculate the double sideband radiances. There are a quite number of samples between 50 km and 20 km which is a good height range to estimate the lower-sideband contribution. After the lower-sideband radiance is determined at this height, one may extrapolate it to lower  $h_t$ , and remove it from the double-sideband radiance to obtain the upper-sideband radiance.

Accurate single-sideband radiances are of special interest to cloud studies since each sideband may have very different LOS absorption. The following example is the UARS MLS 183-GHz measurement where the lower sideband of this channel is at 183.31-GHz, the center of a  $H_2O$  line, and the upper sideband is at 186.2 GHz. This channel has a bandwidth of 2 MHz and the lower-sideband radiance is nearly saturated at  $h_t < \sim 50$  km as a result of the strong absorption of stratospheric and mesospheric water vapor [Figure A.1(a)]. Its upper-sideband radiance is affected little by the stratospheric water vapor at these tangent heights. However, the upper sideband radiance is affected by tropospheric water vapor due to its continuum emission. As

shown in Figure A.1(b), the radiance increases due to water vapor below ~20km. The measured double-sideband radiances are a sum of (a) and (b) weighted by the sideband ratios [Figure A.1(c)].

As shown in Figure A.1(c), the rapid radiance increases occur at two well-separated height ranges (above 50km and below 20km). There is a broad height range (20-50km) where the radiance is relatively constant, which can be used to estimate the lower sideband radiances. Since the saturated lower-sideband radiance varies slightly and linearly with  $h_t$ , one may extrapolate it to the tropospheric  $h_t$  as the modeled lower sideband radiances there [dotted line in Figure A.1(c)]. The differences between the measured radiances and the modeled lower sideband radiances yield the upper-sideband radiances.

More accurate RT models can be employed to compute the lower sideband radiances, which may be CPU time consuming, and the essential idea is same. Such radiance splitting can be implemented together with the retrieval so that the single-sideband radiances are calculated based on the current atmospheric state.

## Appendix B: Cloud-Induced Radiances in Emission-Dominated Situations

Emission-dominated cloud radiances represent an ideal case, which is of special interest because of the  $\beta_{c\_e}$ - $IWC$  or  $\Delta T_{cir}$ - $IWC$  relation is independent of model PSD. Under the Rayleigh approximation, the Mie coefficients  $\xi_e$  and  $\xi_s$  can be written as

$$\begin{aligned}\xi_e &= 4\chi \text{Im}(-K) + \frac{8}{3}\chi^4 |K|^2 + \dots, \\ \xi_s &= \frac{8}{3}\chi^4 |K|^2 + \dots,\end{aligned}\tag{Eq B.1}$$

where  $\chi$  is the size parameter and  $K = \frac{n_i^2 - 1}{n_i^2 + 2}$ , a function of the complex refractive index of ice

( $n_i$ ). Substituting  $n_i^2 = \varepsilon' - j\varepsilon''$ , we have  $\text{Im}(-K) = \frac{3\varepsilon''}{(\varepsilon' + 2)^2 + \varepsilon''^2}$ , where  $\varepsilon'$  and  $\varepsilon''$  are the real and imaginary parts of ice permittivity. The volume extinction coefficients ( $\beta_{c\_e}$  and  $\beta_{c\_s}$ ) are related to  $\xi_e$  and  $\xi_s$ , respectively, by

$$\begin{aligned}\beta_{c\_e} &= \int_0^\infty \pi r^2 N(r) \xi_e dr \\ \beta_{c\_s} &= \int_0^\infty \pi r^2 N(r) \xi_s dr\end{aligned}\tag{Eq. B.2}$$

If cloud induced radiation is dominated by emission, i.e.,  $\beta_{c\_e} \gg \beta_{c\_s}$ , then

$$\begin{aligned}\beta_{c\_e} &\approx \beta_{c\_a} = \int_0^\infty \pi r^2 N(r) (\xi_e - \xi_s) dr \\ &= \frac{6\pi \text{Im}(-K)}{\lambda} \int_0^\infty N(r) \frac{4}{3} \pi r^3 dr\end{aligned}\tag{Eq B.3}$$

Using the definition for  $IWC$ ,  $IWC \equiv \rho_i \int_0^\infty N(r) \frac{4}{3} \pi r^3 dr$ , we have

$$\begin{aligned}\beta_{c\_e} &\approx 6\pi \frac{\text{Im}(-K)}{\lambda} \frac{IWC}{\rho_i} \\ &= 2.1 \frac{IWC}{\lambda} \frac{3\varepsilon''}{(\varepsilon' + 2)^2 + \varepsilon''^2} \quad (\text{km}^{-1})\end{aligned}\tag{Eq B.4}$$

where  $IWC$  is in  $g/m^3$  and  $\varepsilon$  is in  $cm$ .  $\rho_i$  is the density of ice and a value is  $0.9 g/m^3$  in Eq.(B.4). As implied by Eq.(B.4), the  $\beta_{c\_e}$ - $IWC$  relation is independent of particle size distribution and depends only on wavelength of radiation and ice dielectric property. For  $\varepsilon = 3.15 - j0.0068$ , which is the value from our empirical model at  $-75^\circ\text{C}$  and 203 GHz [Appendix C], we obtain  $\text{Im}(-K) = 0.00077$  and the  $\beta_{c\_e}$ - $IWC$  expression becomes

$$\beta_{c\_e} \approx 0.011 \bullet IWC \quad (\text{km}^{-1}) \quad (\text{Eq. B5})$$

Now we can further estimate the  $\Delta T_{cir}$ - $hIWP$  relation using Eq.(B.5) by assuming an isothermal atmosphere near 100 hPa. For isothermal atmospheres, the limb brightness temperature radiation can be written as

$$T_b = T(1 - e^{-\tau}) \quad (\text{Eq. B.6})$$

where  $T$  is air temperature and  $\tau$  is the optical depth along LOS. For 203-GHz radiation, the limb radiance is  $\sim 20$  K at 100 hPa. If air temperature is assumed around 200 K, which yields  $\tau=0.22$  according to Eq.(B.6), we may apply the perturbation theory to relate  $\Delta T_{cir}$  to cloud-induced optical depth  $\Delta\tau_{cir}$ , i.e.,

$$\Delta T_{cir} = \frac{\partial T_b}{\partial \tau} \Delta\tau_{cir} = T e^{-\tau} \Delta\tau_{cir} \quad (\text{Eq. B.7})$$

For a ice cloud with horizontal extent  $\Delta s$ , the perturbation  $\tau_{cir}$  is given by

$$\begin{aligned} \Delta\tau_{cir} &= \beta_{c\_e} \Delta s \\ &= 0.011 \bullet IWC \bullet \Delta s \\ &= 0.011 \bullet hIWP \end{aligned} \quad (\text{Eq. B.8})$$

where  $hIWP$  is ice water path along LOS in unit of  $\text{kg}/\text{m}^2$ . Substituting Eq. (B.8) and the values of  $T$  and  $\tau$  into Eq.(B.7), we have

$$\Delta T_{cir} = 1.76 \bullet hIWP \quad (\text{Eq.B.9})$$

where  $hIWP$  has unit of  $\text{kg}/\text{m}^2$ . Note that this coefficient,  $1.76 \text{ Kkg}^{-1}\text{m}^2$ , is much smaller than the calculated values ( $7 \text{ Kkg}^{-1}\text{m}^2$  at 15 km and  $11 \text{ Kkg}^{-1}\text{m}^2$  at 11 km) using the MH97 PSDs, implying scattering plays a dominated role at 203 GHz for the MH97 PSDs.

## Appendix C: Refractive Indices and Dielectric Constants of Ice and Water

The cloudy-sky radiative transfer calculations (Chapter 4) require knowledge of the relative refractive index  $m = m_1/m_0$  of ice and water, where  $m_1 = n' - in''$  is a complex refractive number and  $m_0$  is the index of the surrounding medium. For the Earth atmosphere,  $m_0 = 1$ , and  $m$  is simply equal to the particle refractive index, which is the square root of the complex dielectric constant  $\varepsilon$ ,

$$m = \sqrt{\varepsilon} \quad (\text{Eq. C-1})$$

where  $\varepsilon$  is composed of a real part,  $\varepsilon'$  and an imaginary part,  $\varepsilon''$ ,

$$\varepsilon = \varepsilon' - i\varepsilon'' \quad (\text{Eq. C-2})$$

This appendix describes the real and imaginary parts of dielectric constant ( $\varepsilon'$ ,  $\varepsilon''$ ) used in our model, which is based on the empirical model developed by Liebe et al. [1989, 1993] and Hufford [1991] (hereafter LH) at frequencies <1000GHz.

### C1 The LH formulae

For pure-water ice particles, the LH model gives

$$\begin{aligned} \varepsilon'_{ice} &= 3.15 \\ \varepsilon''_{ice} &= \alpha(T)/\nu + \beta(T)\nu \end{aligned} \quad (\text{Eq. C-3})$$

where  $\nu$  is frequency in GHz, and the temperature dependent parameters  $\alpha(T)$  and  $\beta(T)$  are given by

$$\begin{aligned} \alpha(T) &= [50.4 + 62 \cdot (300/T - 1)] \cdot 10^{-4} e^{-22.1 \cdot (300/T - 1)} \\ \beta(T) &= (-0.14 + 0.00211T) \cdot 10^{-4} + 0.585 \times 10^{-4} / [1 - (T - 273.15) / 29.1]^2 \end{aligned}$$

For pure liquid water droplets, these constants are:

$$\begin{aligned} \varepsilon'_{water} &= (\varepsilon_0 - 5.48) / [1 + (\nu/\nu_p)^2] + 1.97 / [1 + (\nu/\nu_s)^2] + 3.51 \\ \varepsilon''_{water} &= (\varepsilon_0 - 5.48)(\nu/\nu_p) / [1 + (\nu/\nu_p)^2] + 1.97(\nu/\nu_p) / [1 + (\nu/\nu_p)^2] \end{aligned} \quad (\text{Eq. C-4})$$

where

$$\begin{aligned} \varepsilon_0 &= 77.66 + 103.3 \left( \frac{300}{T} - 1 \right) \\ \nu_p &= 20.09 - 142.4 \left( \frac{300}{T} - 1 \right) + 294 \left( \frac{300}{T} - 1 \right)^2 \\ \nu_s &= 590 - 1500 \left( \frac{300}{T} - 1 \right) \end{aligned}$$

Since the super cooled water droplets can hardly exist below 233 K (−40°C), the LH formulae for liquid water is valid for  $T > 233 K$ .

### C2 Modified LH formula

To extend LH formulae to frequencies >1000GHz, we modified it by including a  $\nu^3$  term to equation (C-3) [Mishima *et al.* 1983], such that

$$\epsilon''_{ice} = \alpha(T)/\nu + \beta(T)\nu + \gamma\nu^3 \quad (\text{Eq. C-5})$$

where  $\gamma(=1.16 \times 10^{-11})$  is calculated from the  $B$  factor in equation (16) in Mishima *et al.* [1983]. Selected dielectric constants from the modified LH formulae for pure-water ice and pure liquid water at MLS frequencies are listed in Table. C-1.

Table. C-1 Complex dielectric constants at different temperatures computed using the modified LH Formulae.

Temperature	Ice		Water	
	$\epsilon'_{ice}$	$\epsilon''_{ice}$	$\epsilon'_{water}$	$\epsilon''_{water}$
<b>63GHz</b>				
+15°C			9.41	17.17
0°C			7.06	11.72
−15°C	3.15	0.0042	5.92	6.99
−30°C	3.15	0.0033	5.55	4.86
−45°C	3.15	0.0028		
−60°C	3.15	0.0024		
−75°C	3.15	0.0021		
<b>118GHz</b>				
+15°C			6.56	9.81
0°C			5.82	6.68
−15°C	3.15	0.0079	5.42	4.16
−30°C	3.15	0.0062	5.15	3.12
−45°C	3.15	0.0052		
−60°C	3.15	0.0045		
−75°C	3.15	0.0039		
<b>190GHz</b>				
+15°C			5.71	6.52
0°C			5.35	4.58
−15°C	3.15	0.0128	5.08	3.04
−30°C	3.15	0.0100	4.74	2.41
−45°C	3.15	0.0084		
−60°C	3.15	0.0073		
−75°C	3.15	0.0064		

Table. C-1 continues...

<i>203GHz</i>				
+15°C			5.62	6.18
0°C			5.29	4.36
-15°C	3.15	0.0137	5.02	2.93
-30°C	3.15	0.0107	4.67	2.33
-45°C	3.15	0.0090		
-60°C	3.15	0.0078		
-75°C	3.15	0.0068		
<i>240GHz</i>				
+15°C			5.42	5.41
0°C			5.15	3.89
-15°C	3.15	0.0162	4.87	2.67
-30°C	3.15	0.0127	4.50	2.13
-45°C	3.15	0.0107		
-60°C	3.15	0.0093		
-75°C	3.15	0.0081		
<i>640GHz</i>				
+15°C			4.35	2.73
0°C			4.16	2.07
-15°C	3.15	0.0458	3.96	1.48
-30°C	3.15	0.0366	3.75	1.08
-45°C	3.15	0.0312		
-60°C	3.15	0.0274		
-75°C	3.15	0.0243		
<i>2500GHz</i>				
+15°C			3.60	0.849
0°C			3.57	0.632
-15°C	3.15	0.4906	3.54	0.436
-30°C	3.15	0.4544	3.52	0.297
-45°C	3.15	0.4336		
-60°C	3.15	0.4187		
-75°C	3.15	0.4066		
-90°C	3.15	0.3960		

### C3 Comparisons with measurements

There are a few published measurements of the refractive indices or dielectric constants for ice and liquid water in the MLS frequency range. They are compared to the calculations of the modified LH model, and the results are summarized in Table. C-2 through Table. C-4, as well as in Fig C-1 through Fig C-3.

#### (1) The imaginary part of refractive indices or dielectric constants for ice

As shown in Table. C-2 and Fig C-1, the differences between the modified LH formulae and the measurements are generally less than ~12% for frequencies ~30-800GHz and about 50% at frequencies ≥ 3.0THz.

Table. C-2 The measured imaginary refractive indices or dielectric constants for pure water ice\*\*.

Measurements	GHz	T	$n''$	$n''_{LH}$	diff(%)	$\epsilon''$	$\epsilon''_{LH}$	diff(%)
<sup>1</sup> Mishima et al. 1983	240	-71°C	0.0026	0.0024	8			
	270	-71°C	0.0028	0.0027	4			
	300	-71°C	0.0032	0.0030	7			
	330	-71°C	0.0034	0.0033	3			
	360	-71°C	0.0039	0.0036	8			
	390	-71°C	0.0042	0.0040	5			
	420	-71°C	0.0045	0.0043	5			
	449	-71°C	0.0048	0.0046	4			
	480	-71°C	0.0049	0.0050	2			
<sup>2</sup> Matzler & Wegmuller 1987	95	-3°C				0.0085	0.0088	3
	35	-10°C				0.0025	0.0026	4
<sup>3</sup> Perry & Straiton 1973	95	-28°C				0.0045	0.0051	12
<sup>4</sup> Whalley & Labbe 1969	500	-73°C	0.0055	0.0052	6			
	600	-73°C	0.0065	0.0064	2			
	666	-73°C	0.0075	0.0073	3			
	750	-73°C	0.0080	0.0085	6			
<sup>5</sup> Bertie et al. 1969	*900	-173°C	0.00797	0.00471	69	0.0285	0.0167	71
	*1200	-173°C	0.0179	0.00876	104	0.0650	0.0311	109
	*1800	-173°C	0.0463	0.0237	95	0.168	0.0842	99
	*2400	-173°C	0.107	0.0514	108	0.388	0.182	113
	3000	-173°C	0.122	0.0959	27	0.447	0.341	31
	3600	-173°C	0.173	0.161	7	0.661	0.574	15
	4200	-173°C	0.352	0.251	40	1.35	0.898	50
	4800	-173°C	0.523	0.366	43	1.84	1.33	38

Notes:

<sup>1</sup>Mishima, Klug and Whalley (1983) measured the absorption spectrum from 8-25  $cm^{-1}$  (or 400-1250 $\mu m$  wavelength) for single crystals of ice at four temperatures (80, 100, 150, 202K). The values of imaginary refractive indices  $n''$  from their measurements at 202K are estimated from their figure 1.

<sup>2</sup>Matzler and Wegmuller (1987)'s values of  $\epsilon''$  are calculated from measurements of coefficient  $\beta$  (of the equation (C-1)) at temperatures between 0 to -30°C. The values of their  $\epsilon''$  listed here are estimated from Hufford (1991)'s figure 1 and 2.

<sup>3</sup>Perry and Straiton (1973) obtained values of  $\epsilon'$  and  $\epsilon''$  from measurements at -28°C. Their  $\epsilon''$  can be found in a number of sources, e.g., Ulaby *et al.* (1986), Warren (1984) and Hufford (1991).

<sup>4</sup>Whalley and Labbe (1969) measured the absorption spectrum from 17-42  $cm^{-1}$  (or 238-588 $\mu m$  wavelength) for blocks of ice at 100 and 200K. Their values of  $n''$  are estimated from their figure 1 and also from Warren (1984)'s figure 6.

<sup>5</sup>Berte, Labbe and Whalley (1969)'s measurements are made for thin films of ice (<1 $\mu m$  thick) at 100K from 100-8000  $cm^{-1}$  (3THz-240THz) wave-numbers. The listed values of  $n''$  and  $\epsilon''$  are taken from their table III.

\*Bertie et al (1969) also obtained some "preliminary and not very accurate" measurements of a 1-mm sample for 30-60  $cm^{-1}$  (900GHz-1.8THz) and estimated value at 80  $cm^{-1}$  (2.4THz). These measurements may have large error.

\*\*Some sources give only measured data for  $\epsilon''$  while others provide only  $n''$ . We did not convert between these two data because doing so needs knowledge of  $\epsilon'$  or  $n'$ . Also note that in comparing with Bertie et al's data, the percentage differences of  $n''$  and  $\epsilon''$  are different due to the different  $\epsilon'$  values that used by Bertie and in our LH model.

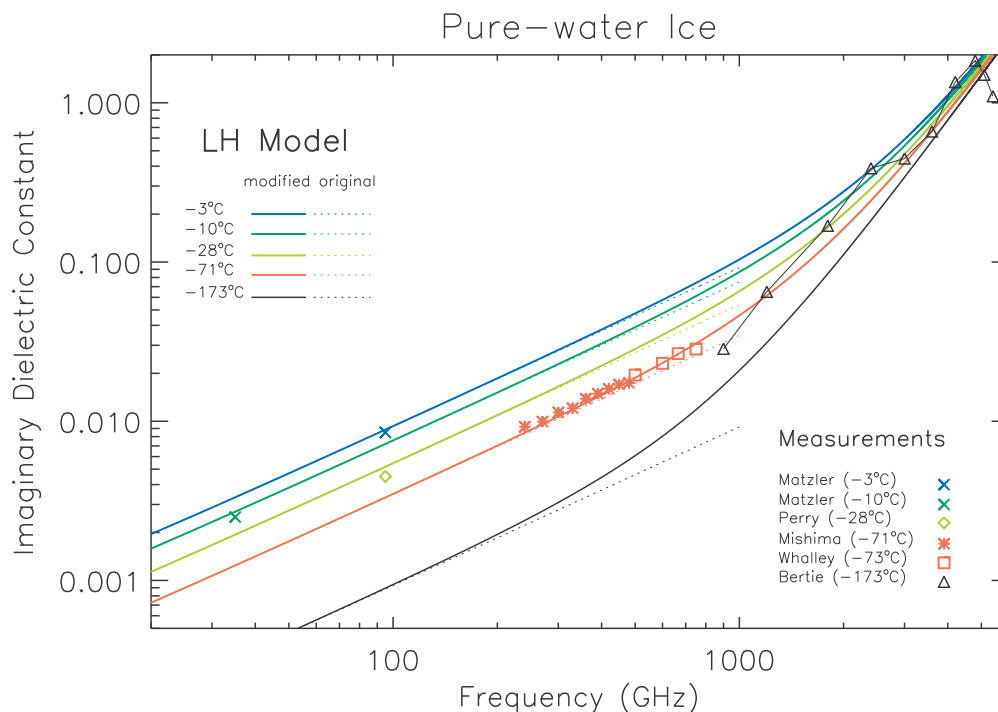


Fig C-1 Computed and measured imaginary part of ice dielectric constants. The solid lines are  $\epsilon''$  computed using the modified LH formula (C-6), the dash lines using the original LH formula (C-3).

\*Note the last two measurements by Bertie et al (1969) at the high frequency end (5100, 5400GHz) are not listed in Table. C-2.

## (2) Real part of dielectric constants for ice

Measurements of real part of the ice dielectric constants are summarized in Table. C-3 and Fig C-2. The measured values of  $\epsilon'$  are fairly constant over microwave spectrum, the differences with the LH model at frequencies <1000 GHz are generally less than 5%. At higher frequencies (~2.5 THz) the differences may be as high as ~15%.

Table. C-3 The measured real part of dielectric constants for pure-water ice.

Measurements	GHz	T	$\epsilon'$	$\epsilon'_{LH}$	diff (%)
<sup>1</sup> Cumming 1952	9.375	0 to -18°C	3.15	3.15	0
<sup>1</sup> von Hippel 1945	10	-12°C	3.17	3.15	0.6
<sup>1</sup> Vant et al. 1974	10	0 to -35°C	3.14	3.15	0.3
<sup>1</sup> Lamb 1946	10	-1 to -49°C	3.17	3.15	0.6
<sup>1</sup> Lamb & Turney	24	0 to -185°C	3.18	3.15	1
<sup>1</sup> Perry & Straiton	95	-28°C	3.08	3.15	2
<sup>2</sup> Bertie et al. 1969	900	-173°C	3.20	3.15	2
	1200	-173°C	3.30	3.15	5
	1800	-173°C	3.31	3.15	5
	2500	-173°C	3.37	3.15	7
	3000	-173°C	3.64	3.15	15
	4200	-173°C	3.57	3.15	13
	4800	-173°C	2.82	3.15	10

<sup>1</sup>Data obtained from the table E.3 in Ulaby, Moore and Fung (1986)

<sup>2</sup>Data from the table III in Bertie, Labbe and Whalley (1969)

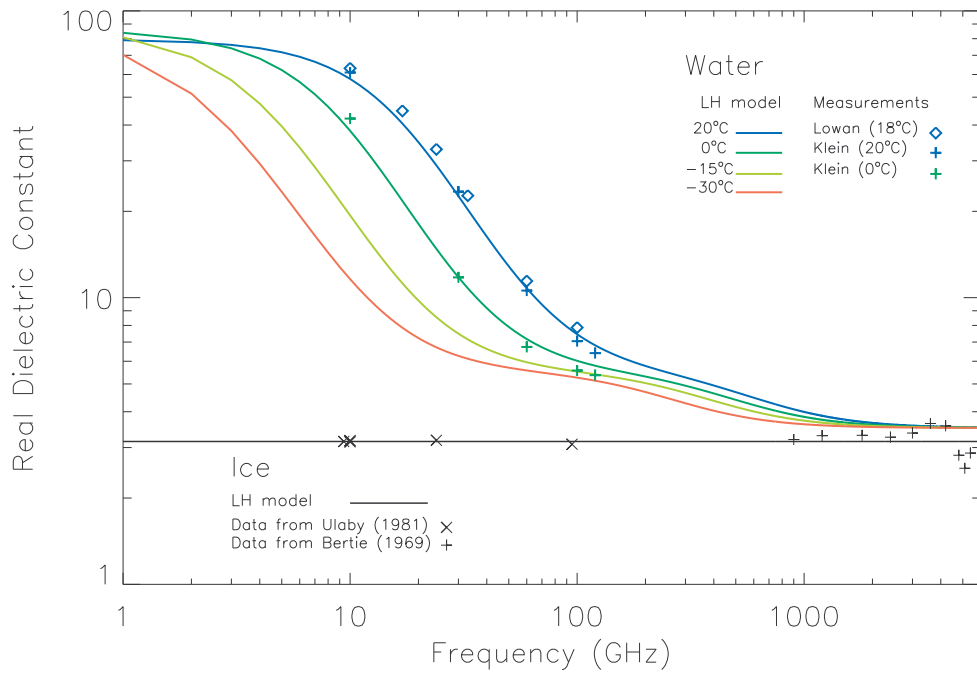


Fig C-2 Computed and measured real part of dielectric constants for ice (black-line) and liquid water (colored-lines). The measured data for ice are listed in Table. C-3, and the measured data for liquid water are given in Table. C-4.

### (3) The real and imaginary parts of dielectric constants for liquid water

For liquid water, the difference between measurements and the LH model is generally less than ~8% (Table. C-4). However, very few measurements are made below 0°C. Values of the dielectric constant of super-cooled pure liquid water (<0°C) are mostly computed from models (e.g. Ulaby *et al.* 1986, p2020-2025, Hulst 1981, p281-284). Measurements of the real part of the liquid water refractive index are shown in Fig C-2, and the imaginary part data are shown in Fig C-3.

Table. C-4 Refractive indices and dielectric constants for pure liquid water.

Measurements	GHz	T	$\epsilon'$	$\epsilon'_{LH}$	diff (%)	$\epsilon''$	$\epsilon''_{LH}$	diff(%)
Klein and Swift 1977	120	0°C	5.365	5.800	7	6.202	6.593	6
	100	0°C	5.568	6.036	8	7.424	7.720	4
	60	0°C	6.730	7.230	7	12.200	12.255	0.4
	30	0°C	11.768	12.177	3	22.888	22.653	1
	10	0°C	42.116	42.021	0.2	41.344	40.951	1
(Source: Ulaby, Moore & Fung 1981. Values of $\epsilon''$ computed from K&S's curve fits to lab measurements)	120	20°C	6.405	6.847	6	10.528	10.721	2
	100	20°C	7.049	7.495	6	12.524	12.616	0.7
	60	20°C	10.580	10.954	3	19.863	19.699	0.8
	30	20°C	23.420	23.481	0.3	32.383	32.027	1
	10	20°C	60.990	60.768	0.4	32.691	32.706	0.04

Table. C-4 continues...

Measurements	GHz	T	$\epsilon'$	$\epsilon'_{LH}$	diff (%)	$\epsilon''$	$\epsilon''_{LH}$	diff(%)
Lowan 1949  (Source: van Hulst 1981)	100	18°C	7.864	7.696	2	13.231	13.104	1
	60	18°C	11.424	11.452	0.2	21.134	20.379	4
	33	18°C	22.680	22.166	2	31.635	31.011	2
	24	18°C	32.908	31.749	4	36.665	35.449	3
	17	18°C	44.817	44.175	1	38.160	36.956	3
	10	18°C	63.071	61.678	2	32.066	31.555	2

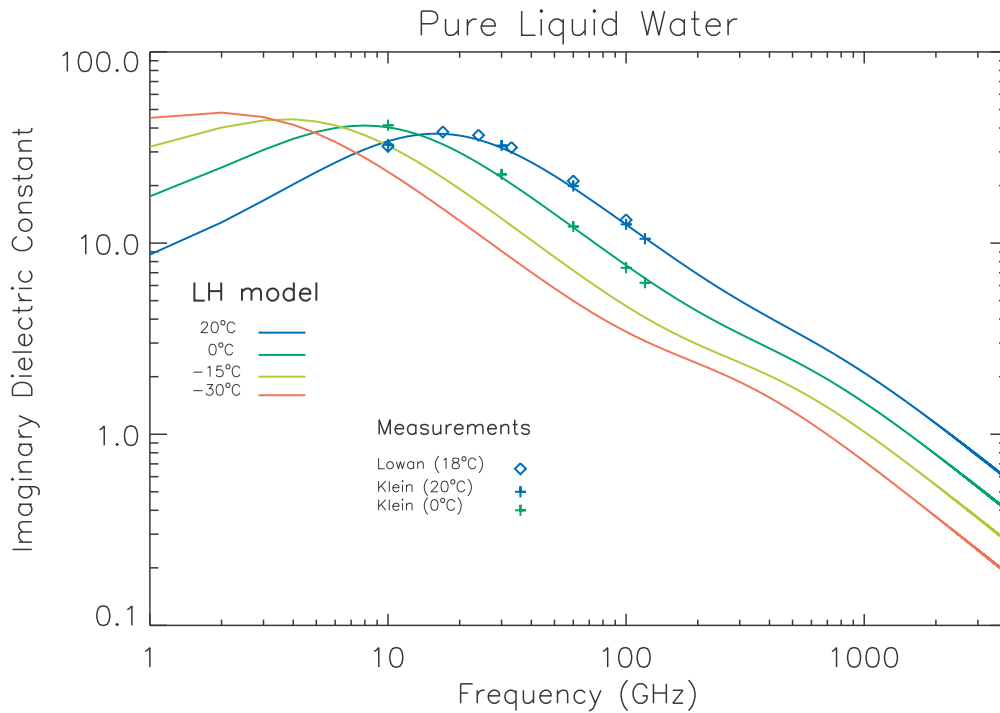


Fig C-3 Computed and measured imaginary part of dielectric constants for pure liquid water. The measured data are listed in Table. C-4.

### C4 Summary

Compared to the measurements, the modified LH formulae adopted in our model may have uncertainties of ~12% in the imaginary part and ~5% in the real part of ice dielectric constants at 63-640GHz. At 2.5THz, the uncertainties may be as high as ~50% in the imaginary part and ~15% in the real part. For liquid water, the uncertainties are less than 8% in both imaginary and real parts of dielectric constants.

## Appendix D: A Conceptual Cloud Radiance Model

### D1 Simple Radiative Transfer (RT) Equation

We will simplify the radiative transfer equation in a cloudy sky to introduce some key components in interpreting cloud radiances. As a result, a useful expression will be derived on the cloud-extinction dependence of limb radiances. As illustrated in Fig D-1, the limb radiance ( $T_b$ ) can be written as the sum of the following components:

$$T_b = (1 - e^{-\tau_{aext}})T_{AF} + e^{-\tau_{aext}} (T_{CSin} + T_{CE} + e^{-\tau_{cext}}T_{AB}) \quad (\text{Eq. D-1})$$

where

- $\tau_{cext}$  - LOS cloud optical depth
- $\tau_{aext}$  - LOS air optical depth in front of cloud
- $T_{CSin}$  - radiance scattered into FOV
- $T_{CSout}$  - radiance scattered out of FOV
- $T_{AF}$  - air radiance in front of cloud
- $T_{AB}$  - air radiance behind cloud
- $T_{CE}$  - radiance due to cloud emission

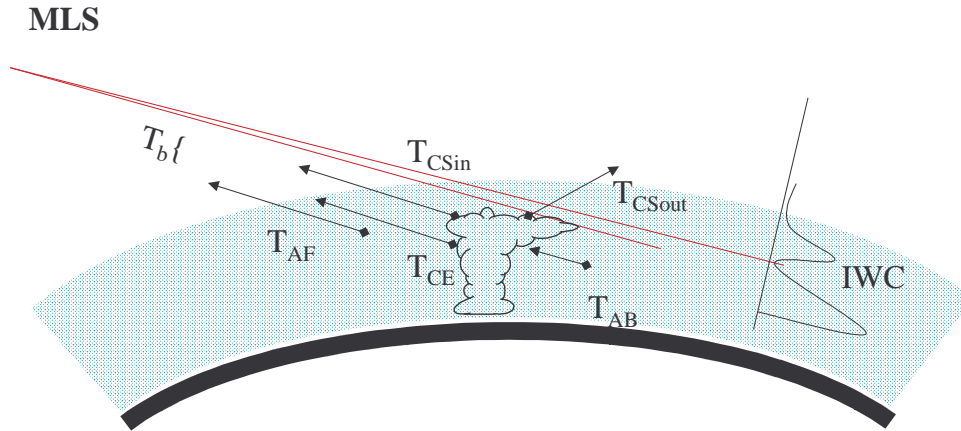


Fig D-1 Schematic to show the radiative components of MLS optically-thick radiances at low  $h_t$ . The important radiation components are indicated by arrows: clear-sky radiation in the front/back of clouds ( $T_{AF}/T_{AB}$ ), radiation of cloud emission ( $T_{CE}$ ), and radiation scattered into/out of FOV by clouds ( $T_{CSin}/T_{CSout}$ ).

In the case of clear sky,  $T_{CSin}$ ,  $T_{CE}$  and  $\tau_{cext}$  vanish, which yields the clear-sky radiance, or  $T_0$ ,

$$T_0 \equiv (1 - e^{-\tau_{aext}})T_{AF} + e^{-\tau_{aext}}T_{AB} \quad (\text{Eq. D-2})$$

Subtracting it from cloudy-sky radiance, we obtain the cloud-induced radiance ( $\Delta T_{cir}$ ), namely,

$$\begin{aligned}\Delta T_{cir} &= T_b - T_0 \\ &= e^{-\tau_{aext}} (T_{SCin} + T_{CE} - (1 - e^{-\tau_{cext}}) T_{AB})\end{aligned}\quad (\text{Eq. D-3})$$

where  $T_{SCin} + T_{CE}$  is the source function from clouds, and

$$T_{SCin} + T_{CE} = (1 - e^{-\tau_{cext}}) T_J \quad (\text{Eq. D-4})$$

From Chapter 4 we have

$$T_J \equiv (1 - \omega_0) T_A + \omega_0 T_{scat} \quad (\text{Eq. D-5})$$

where  $T_{scat}$  is the scattering radiance and  $T_A$  is the cloud emission at local air temperature. Thus, Eq.(D3) reduces to

$$\Delta T_{cir} \approx e^{-\tau_{aext}} (1 - e^{-\tau_{cext}}) (T_J - T_{AB}) \quad (\text{Eq. D-6})$$

Note that  $e^{-\tau_{aext}} (1 - e^{-\tau_{cext}})$  is the effective cloud optical depth because

$$\begin{aligned}\tau_{ceff} &= \int_{LOS} \beta_{cext} e^{-\tau_{ext}} ds \\ &= \int_{LOS} \beta_{cext} e^{-(\tau_{aext} + \tau_{cext})} ds \\ &= \int_{LOS} e^{-(\tau_{aext} + \tau_{cext})} d\tau_{cext} \\ &= e^{-\tau_{aext}} \int_{LOS} e^{-\tau_{cext}} d\tau_{cext} \\ &= e^{-\tau_{aext}} (1 - e^{-\tau_{cext}})\end{aligned}$$

Rewriting Eq.(D6), we have

$$\frac{\Delta T_{cir}}{\tau_{ceff}} \approx T_J - T_{AB} \quad (\text{Eq. D-7})$$

For scattering dominated cases,  $T_J \approx T_{scat}$ . Since  $T_{AB}$  and  $T_{scat}$  are roughly constant at low  $h_t$  (optically-thick cases), and  $T_{AB} > T_{scat}$ , which yields a negative  $\Delta T_{cir}$ , or brightness temperature depression.

$$\frac{\Delta T_{cir}}{\tau_{ceff}} \approx T_{scat} - T_{AB} \quad (\text{Eq. D-8})$$

In optically-thin situations,  $T_{AB}$  and  $\tau_{ext}$  are small and negligible. Hence, Eq.(D7) reduces to

$$\frac{\Delta T_{cir}}{\tau_{ceff}} \approx T_{scat} \quad (\text{Eq. D-9})$$

where the sensitivity is positive.

For the cases where cloud emission dominates, Eq.(D7) reduces to

$$\frac{\Delta T_{cir}}{\tau_{ceff}} \approx T_A - T_{AB} \quad (\text{Eq. D-10})$$

In optically-thick conditions,  $T_A \approx T_{AB}$ , which means that  $\Delta T_{cir}$  are very small and difficult to detect from space. In optically-thin conditions,  $T_{AB}$  and  $\tau_{ext}$  are negligible, which yields

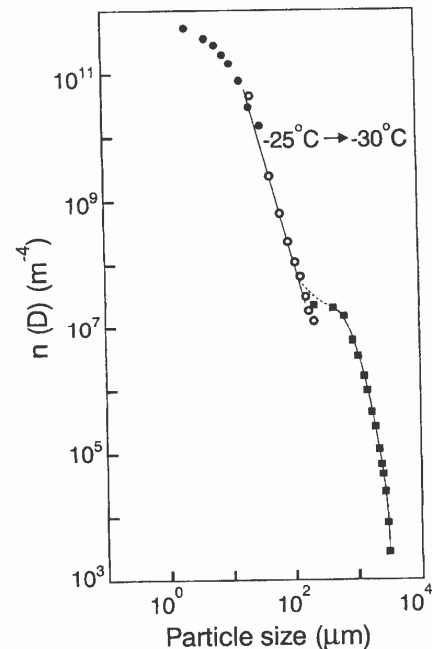
$$\frac{\Delta T_{cir}}{\tau_{ceff}} \approx T_A \quad (\text{Eq. D-11})$$

Note that  $\Delta T_{cir}$  are also positive and make the situations similar to the scattering-based signals. Therefore, at high  $h_t$ , both emission and scattering can produce significant cloud radiances.

## Appendix E: Ice Particle Size Distributions

Cloud optical depth and other radiative properties can vary substantially with particle size distribution as well as the ice water content (IWC). Therefore, the concept of equivalent, or effective, particle size is not sufficient for characterizing all clouds. There is plenty of evidence now against the single-parameter or simple-function characterization. The bimodal size distribution of ice crystals, as shown in Figure E.1, has been observed in a large number of studies [e.g., Mitchell et al., 1996; Platt, 1997]. Since microwave remote sensors are only sensitive to scattering of large particles, it is essential to accurately know the shape of the size distribution in order to derive total ice/liquid water content.

Fig E-1 Observations of cloud particle number density  $n(D)$  as a function of the long dimension of the particles at the temperature range of  $-25^{\circ}\text{C}$  and  $-30^{\circ}\text{C}$  [from Platt, 1997]. It shows a bimodal structure in the ice crystal distribution with the second peak at  $\sim 500\ \mu\text{m}$ . The bimodal distribution of ice particle spectra is not fully understood although it has been speculated as a result of balancing between the nucleation of ice particles and the removal of ice particles by aggregation and enhanced diffusion growth via ventilation [Mitchell, 1994].



Heymsfield and Platt (1984) found that the size distributions observed by airborne probes were fitted quite well to a simple power law at sizes less than  $100\ \mu\text{m}$ , shedding some light on the size distribution parameterization. To parameterize the bimodal size distribution, Platt [1997] presents a model for temperatures of  $-5^{\circ}\text{C}$  to  $-50^{\circ}\text{C}$  with two functions for sizes greater and less than  $100\ \mu\text{m}$ . Over the range of  $20\text{-}100\ \mu\text{m}$ , the observed number size distributions can be fitted by a power law, i.e.,  $n(D) = aD^b$ , where  $D$  is the maximum crystal dimension and  $a$  and  $b$  are the fitted parameters. Beyond  $100\ \mu\text{m}$ , the measurements fit well the so-called Marshall-Palmer distribution [Marshall and Palmer, 1948], i.e.,  $n(D) = N_0 e^{-\lambda D}$ , where  $N_0$  and  $\lambda$  are the fitted parameters. More size distribution parameterizations have been used in ice cloud studies recently and we will compare them in the following sections.

### E1 Modeled Size Distributions

#### *McFarquhar-Heymsfield (MH) Distribution*

This parameterization is based on observations made in outflows of deep convection during Central Equatorial Pacific Experiment (CEPEX) [McFarquhar and Heymsfield, 1997]. It is valid for most tropical clouds with ice water content (IWC) between  $10^{-4}$  and  $1\ \text{g/m}^3$  at temperatures between  $-70^{\circ}\text{C}$  and  $-20^{\circ}\text{C}$ , where temperature is often used to replace height. The number distribution function is composed of a first-order gamma distribution function for small particles ( $D < 100\ \mu\text{m}$ ) and lognormal distribution function for large particles ( $D > 100\ \mu\text{m}$ ), which are given by

$$n_{MH}(D) = N_1 D \exp(-\alpha D) \quad \text{for } D < 100 \mu\text{m} \quad (\text{Eq. E-1})$$

$$n_{MH}(D) = N_2 D^{-1} \exp\left[-\frac{1}{2}\left(\frac{\log D - \mu}{\sigma}\right)^2\right] \quad \text{for } D > 100 \mu\text{m} \quad (\text{Eq. E-2})$$

where coefficients  $\alpha, \mu$ , and  $\sigma$  are functions of IWC and height, but  $N_1$  and  $N_2$  are functions of IWC.  $n_{MH}(D)$  has unit of  $L^{-1}\mu\text{m}^{-1}$ . For each IWC, the model automatically creates partitions for the small and large particles using

$$IWC_{<100} = \min [ IWC, a(IWC/IWC_0)^b ] \quad (\text{Eq. E-3})$$

where  $a = 0.252 \text{ g/m}^3$ ,  $b = 0.837$ , and  $IWC_0 = 1 \text{ g/m}^3$ .

The MH distribution can reproduce many bimodal distributions seen in dense-and-thick clouds. Examples of the MH size distribution are shown in Figure 5.3. The ability of reproducing the bimodal distributions is believed very important for the IWC measurement with 100-600 GHz techniques because these frequencies are sensitive mostly to particles of the larger size mode. As we will find, the IWC derived from large particle scattering can vary substantially with the size distribution.

### Gamma Size Distribution

The Gamma size distributions have been frequently used in studying rain droplets [e.g. Ulbrich, 1983; McKague, et al., 1998] and cloud ice particles [Evans and Stephens, 1998; Matrosov et al., 1994]. It is a three-parameter function

$$n_G(D) = N_0 D^{-\alpha} \exp\left[-(\alpha + 3.67) \frac{D}{D_m}\right] \quad (\text{Eq. E-4})$$

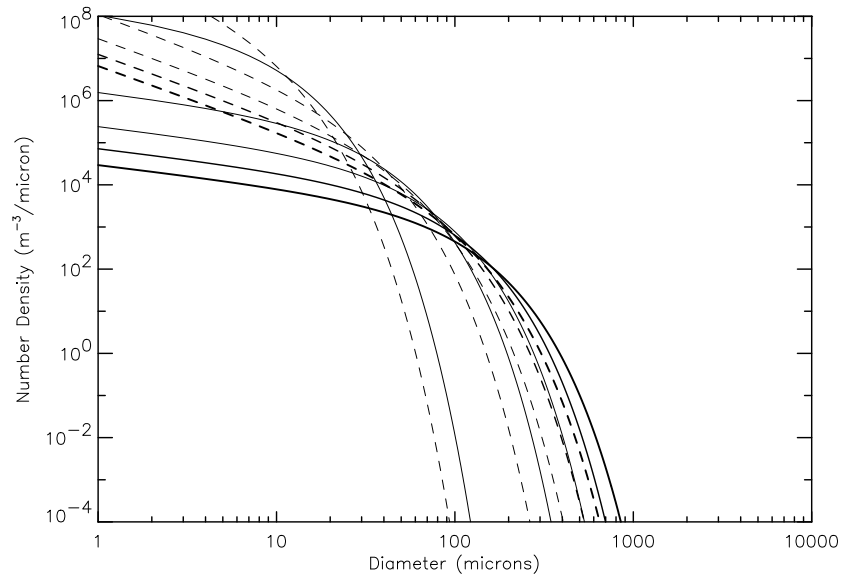


Fig E-2 Gamma size distributions for  $IWC=0.01\text{g/m}^3$  and  $\alpha=0.5$  (solid lines) and  $\alpha=1.5$  (dashed lines). Thickness of the lines represents different  $D_m$  at 20, 70, 120, 170, 220, and  $270\mu\text{m}$  (from thin to thick).

where the width parameter  $\alpha$  usually ranges from 0 to 2 and is equal to 1 in the following comparisons.  $D_m$  is the mass (third power) mean diameter of the distribution and  $N_0$  can be determined from  $IWC$ . Note that a single Gamma distribution can not reproduce the bimodal size distributions seen in real ice clouds. Therefore, we include it only for comparison purposes. Examples of the Gamma size distributions are shown in Fig E-2.

**Liu-Curry Distribution**

Based on the CEPEX observations, Liu and Curry [1998] also derived a parameterization as follows:

$$n_{LC}(D) = N_0 \left( \frac{100}{D} \right)^{3.5} \quad \text{for } D < 100 \mu\text{m} \quad (\text{Eq. E-5})$$

$$n_{LC}(D) = N_0 \exp \left( -5 \left( \frac{D-100}{D_e + 500} \right)^{0.75} \right) \quad \text{for } D > 100 \mu\text{m} \quad (\text{Eq. E-6})$$

where  $D_e = 750 + 10t$  is a parameter to adjust the distribution shape and  $t$  is temperature in Celsius. Note that the shape of the modeled distribution is independent of  $IWC$ , which is the major difference to McFarquhar-Heysfield distribution. Examples of the Liu-Curry size distributions are shown in Fig E-3.

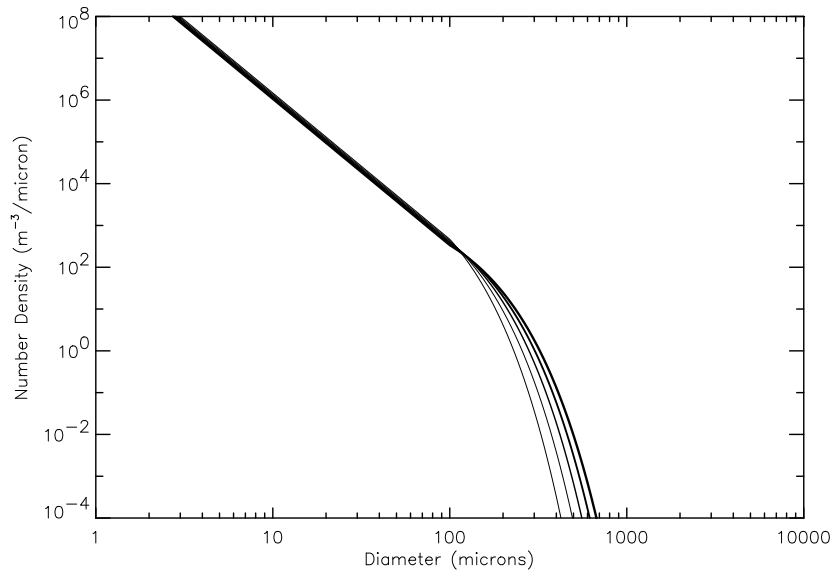


Fig E-3 Liu-Curry size distributions for  $IWC=0.01\text{g/m}^3$  and temperature  $-15^\circ\text{C}$ ,  $-30^\circ\text{C}$ ,  $-45^\circ\text{C}$ ,  $-60^\circ\text{C}$ , and  $-75^\circ\text{C}$  (from thick to thin).

### Knollenberg Distributions

Knollenberg et al. [1993] reported several size distributions (0.1-1000 $\mu m$ ) measured from the anvils in tropical and extratropical cumulonimbus complexes during a number of aircraft flights. They found IWC up to 0.07 g/m<sup>3</sup> at 15-17.5 km altitudes in tropical anvils, which is thought towards the high end among all the observations. With rare exceptions, particles large than 100  $\mu m$  were not observed near the cloud tops. The bimodal feature is not as prominent in Knollenberg et al [1993] as in McFarquhar and Heymsfield [1997]. We choose the following parameterization to mimic the shape of the size distributions observed in Knollenberg et al. [1993],

$$n_K(D) = N_0(10^{-5} + D^{-1.9})e^{-\alpha D} \quad (\text{Eq. E-7})$$

where  $D$  is particle diameter in  $\mu m$ , and  $\alpha$  is an adjustable parameter varying from 0.002 (more large particles) to 0.1 (more small particles).  $N_0$  can be determined from IWC. Examples of the Knollenberg-like size distributions are shown in Fig E-4.

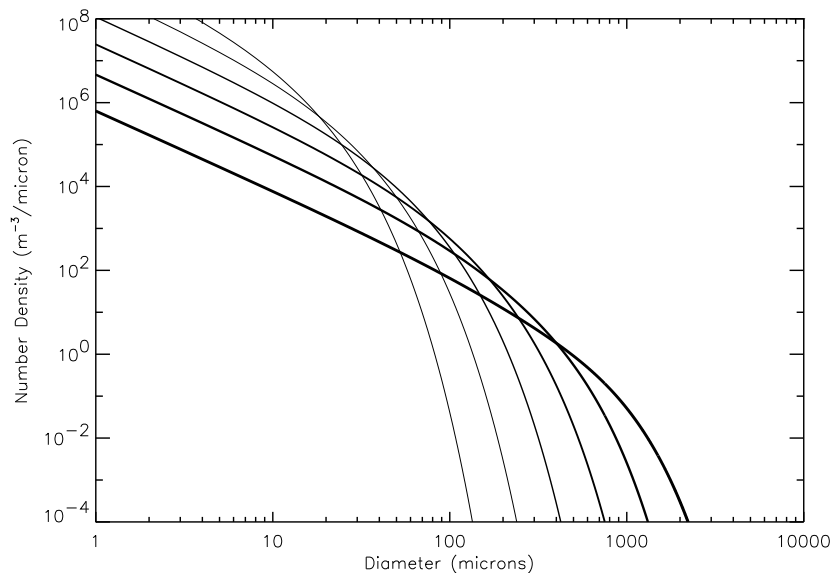


Fig E-4 Knollenberg-like size distributions for IWC=0.01g/m<sup>3</sup> and  $\alpha = 0.005, 0.01, 0.02, 0.04, 0.08,$  and 0.16 (from thick to thin).

### E2 Discussions

Since particle size distribution varies largely with cloud type, altitude, and latitude, a parameterization can be very general to cover all the variability but become less useful. A unique property about the MH parameterization is that it provides size distributions with realistic constraints from cloud IWC and altitude. Down in the list, the Liu-Curry parameterization is constrained to cloud altitude but IWC is unbounded. The parameterization like Gamma distribution is very general and can be applied to any cloud at any altitude. In the following we will compare characteristics of the other parameterizations to those of the MH parameterization in terms of single scattering albedo, ice water content, mass mean diameter, and volume extinction coefficient.

Fig E-5 shows the dependence of volume extinction coefficient on IWC and mass mean diameter for different size distribution parameterizations. We compare the results of these parameterizations for  $IWC \in (0.001, 0.6) \text{ g/m}^3$  and temperature  $\in (-75^\circ\text{C}, -15^\circ\text{C})$ . Shown in Fig E-5(a), the MH and Liu-Curry distributions provide a unique  $\beta_{c,e}$ -IWC relation for each temperature but with different slope whereas it requires more specific parameterization to relate  $\beta_{c,e}$  to IWC if one would like to use the Gamma or Knollenberg-like distributions. The  $\beta_{c,e}$ -IWC relation can be formulated as follows

$$\beta_{c,e} = \left( \frac{IWC}{IWC_0} \right)^\alpha \quad (\text{Eq. E-8})$$

where  $\alpha=1.4$  for the MH distribution and  $\alpha=1$  for the others. This is a major difference, or uncertainty, among various size distributions. Another uncertainty is associated with  $IWC_0$  that is a function of temperature or height. For the MH distribution, it is given by

$$IWC_0 = 10^{-2.77+0.01T} \quad (\text{g/m}^3)$$

The coefficient is somewhat different for the Liu-Curry distribution, which gives

$$IWC_0 = 10^{-3.91+0.01T} \quad (\text{g/m}^3)$$

where  $T$  is in  $^\circ\text{C}$ .

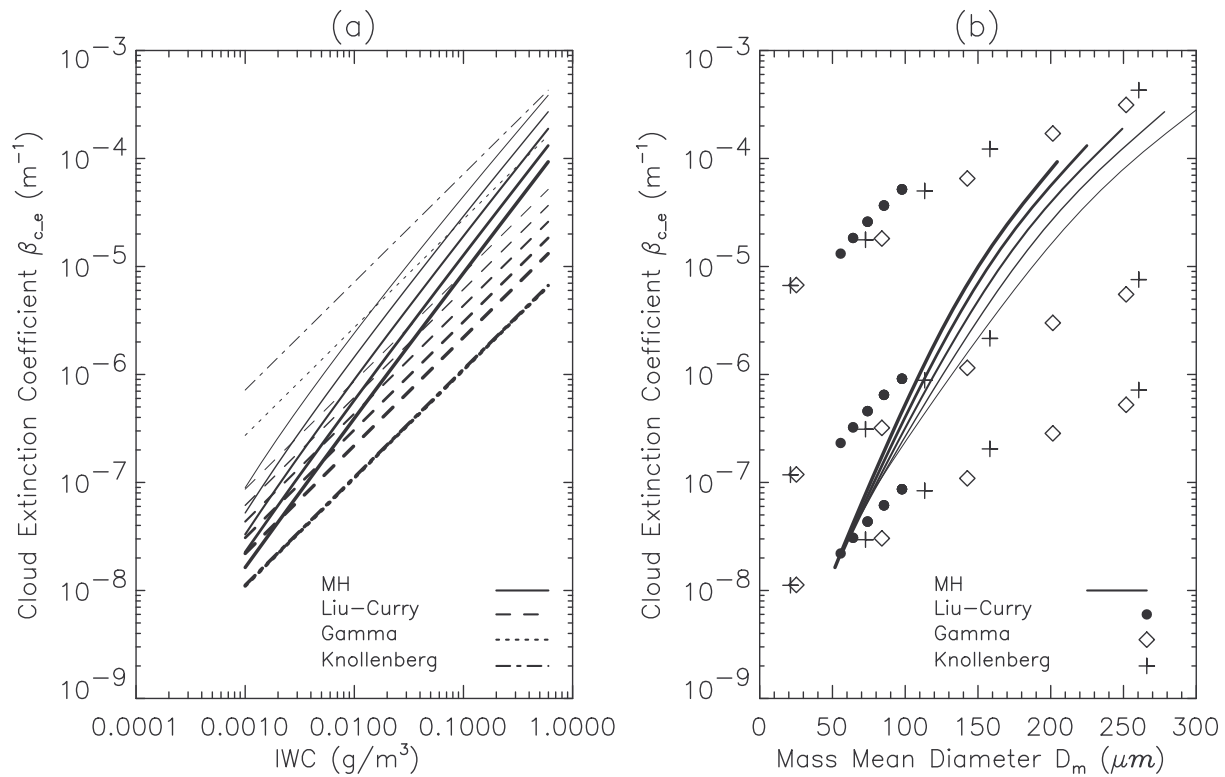


Fig E-5 Volume extinction coefficient  $\beta_{c,e}$  vs. (a) IWC and (b) mass mean diameter. In (a), for the MH and Liu-Curry distributions, the line thickness represents temperature of  $-15^\circ\text{C}$ ,  $-30^\circ\text{C}$ ,  $-45^\circ\text{C}$ ,  $-60^\circ\text{C}$ , and  $-75^\circ\text{C}$

(from thin to thick); for the Gamma distribution ( $\alpha=1$ ), the lower/upper line is respectively for  $D_m = 30 \mu m$  at  $-75^\circ C$  and  $D_m = 300 \mu m$  at  $-15^\circ C$ ; for the Knollenberg-like distribution, the lower/upper line is respectively for  $\alpha=0.1$  at  $-75^\circ C$  and  $\alpha=0.01$  at  $-15^\circ C$ . In (b), the same ranges are applied for these distributions but only IWC=0.001 (the lower set), 0.1 (the middle set), 0.6 (the upper set)  $g/m^3$  are plotted.

The results in Fig E-5(b) show that one may obtain a different mass mean diameter for the same volume extinction coefficient if a different size distribution is used. If most clouds obey the MH distribution, many parameters in the Liu-Curry and Gamma distributions would be unrealistic. For instance, the mass mean diameters of Liu-Curry distributions would be too small in most cases.

Fig E-6 and Fig E-7 show IWC- and  $D_m$ -dependence of volume scattering and absorption, respectively. There is a great similarity in the behaviors between volume extinction coefficient and scattering coefficient. But for absorption, the coefficients from the Gamma and Knollenberg-like distributions are independent of  $D_m$  and only proportional to IWC in logarithm scale. The IWC-dependence in Fig E-7 for the Gamma and Knollenberg-like distributions collapse into a single line, suggesting the retrieval of IWC from absorption coefficient is independent of the shape of particle size distribution. However, such independency is not quite valid for the MH and Liu-Curry distributions.

Fig E-8 shows cloud single scattering albedo as a function of mass mean diameter for different size distributions. The  $\omega_0$ -  $D_m$  relation is similar for all the size distributions but the span in  $D_m$  shows slight differences. For instance, all the Liu-Curry distributions have small  $D_m$  between 50 and 110  $\mu m$ , which may not represent some ice clouds in reality.

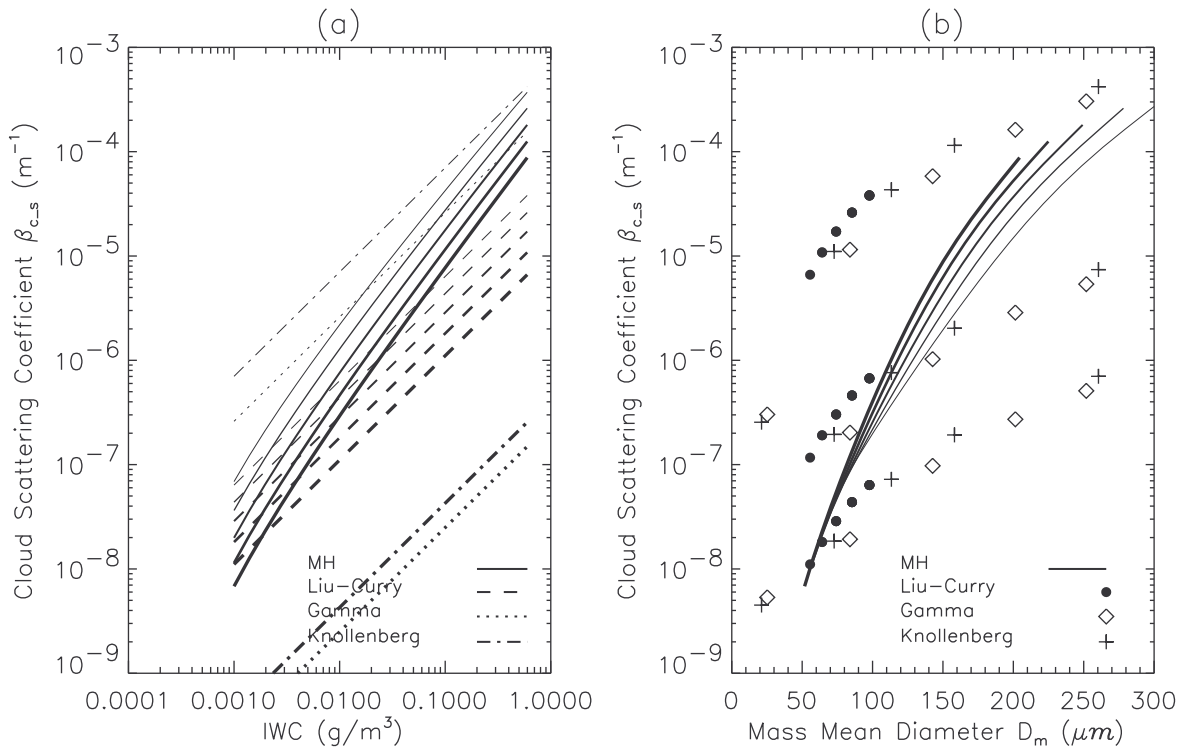


Fig E-6 As in Fig E-5 but for volume scattering coefficients.

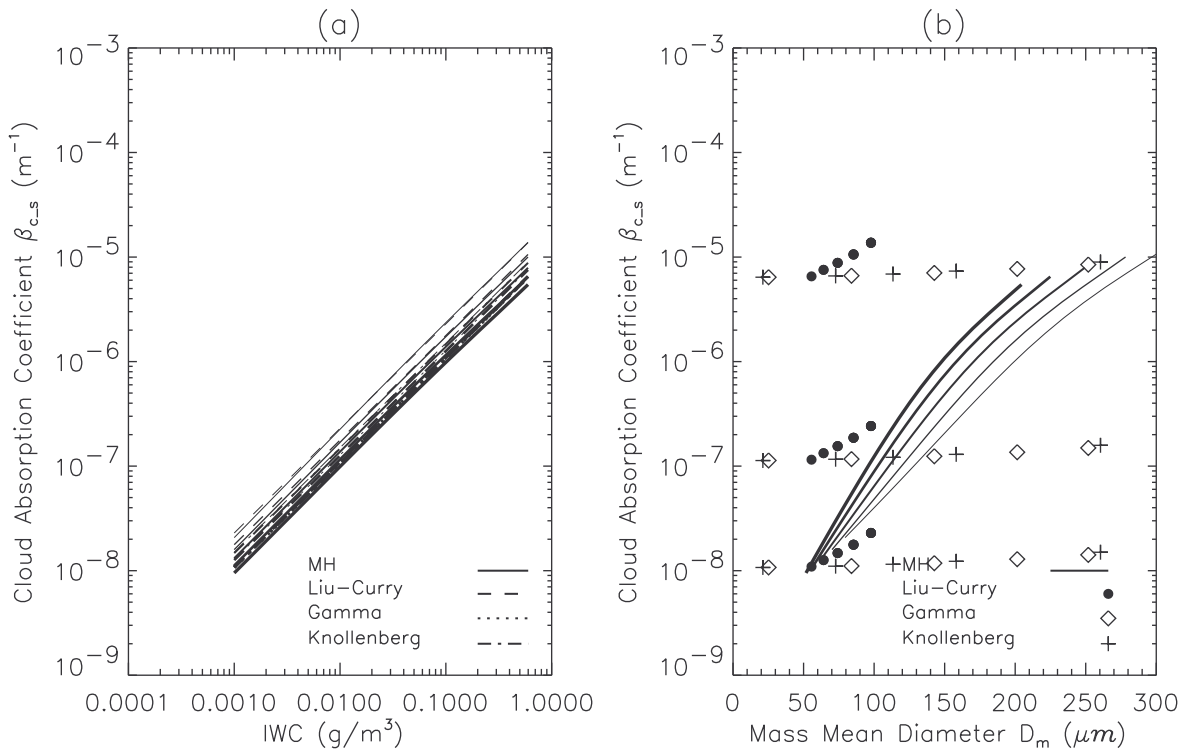


Fig E-7 As in Fig E-5 but for volume absorption coefficients.

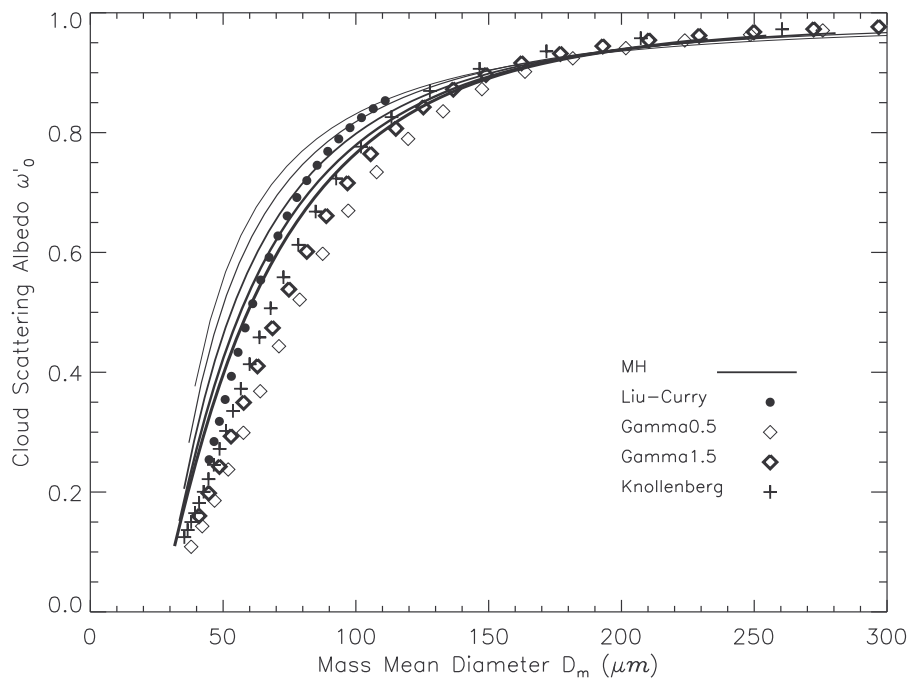


Fig E-8 Cloud single scattering albedo without air  $\omega'_0$  vs. mass mean diameter  $D_m$  for different size distributions.

## Appendix F: Dry Continuum Absorption

### F1 What is the dry continuum absorption?

The dry continuum absorption at 100-3000 GHz from the Earth atmosphere is believed mostly due to collision-induced absorption of  $N_2$  and  $O_2$  molecules, which includes  $N_2-N_2$ ,  $N_2-O_2$ , and  $O_2-O_2$  pairs. A number of experimental and theoretical studies have been dedicated to the  $N_2-N_2$  collision-induced absorption at 1-250  $\text{cm}^{-1}$  (30-7500 GHz) frequencies [e.g., Dagg et al., 1978; Stone et al., 1984; Dagg et al., 1985; Joslin et al., 1984; Borysow and Frommhold, 1986] but little discussion was on  $N_2-O_2$ , and  $O_2-O_2$  pairs at these frequencies.

In a comparison to the atmospheric transmission measured above Mauna Kea, Pardo et al. [2000] found the calculated  $N_2-N_2$  collision-induced absorption, after scaled up by 1.29, agrees very well with the dry continuum derived from the data at 350-1100 GHz. The additional absorption was interpreted due to the contributions of other molecule pairs.

In this appendix, we aim to develop an empirical model that calculates the  $N_2-N_2$  collision-induced absorption at frequencies up to 3 THz for EOS MLS. By multiplying the  $N_2-N_2$  spectrum with the scaling factor 1.29 as used by Pardo et al. [2000], we can obtain the dry continuum absorption for the Earth atmosphere at these frequencies.

### F2 The $N_2-N_2$ collision-induced absorption

A lineshape function  $I(\nu)$  is used to describe the spectrum of collision-induced absorption, which is defined as,

$$I(\nu) \propto \frac{A_{N_2-N_2}(\nu)}{\rho_{N_2}^2 \nu^2} \quad (\text{Eq. F-1})$$

where  $A_{N_2-N_2}(\nu)$  is absorption coefficient in unit length at frequency  $\nu$ , and  $\rho_{N_2}$  is  $N_2$  density.

Two mechanisms can cause a weak absorption in the far infrared as  $N_2$  molecules encounter each other: translational and rotational mechanisms. The first one refers to two molecules colliding with each other while the second one refers to rotation of the  $N_2$  molecules themselves. The translational spectral lineshape has the appearance as in Fig F-1(a), with a width of 50  $\text{cm}^{-1}$  at 300K. On the other hand, the rotational lineshape has the appearance shown in Figure F1(b). A simple theory to model the  $N_2-N_2$  collision-induced absorption spectrum is based on the convolved spectrum of Fig F-1(a) and (b), which is shown in Fig F-1(c) [Joslin et al., 1984]. Such model produces an excellent agreement with experimental observations of the far infrared spectrum of  $N_2$  over a wide range of temperatures.

To reduce computation time, we develop the following empirical function to calculate the lineshape like Fig F-1(c) that may vary with frequency and temperature,

$$\alpha_{N_2-N_2}(\nu) \equiv \frac{A_{N_2-N_2}(\nu)}{\rho_a^2 \nu^2} = (a_1 e^{-c_1 \theta \nu^2} + a_2 e^{-c_2 \theta \nu^2} (d^2 + \nu^2)) \theta^b \quad (\text{Eq. F-2})$$

where  $\alpha_{N_2-N_2}(\nu)$  in  $\text{cm}^{-1}/\text{cm}^{-2}/\text{amagat}^2$ ,  $A_{N_2-N_2}(\nu)$  is absorptivity in  $\text{cm}^{-1}$ ,  $\nu$  is frequency in  $\text{cm}^{-1}$ ,  $\theta=300/T$  is a normalized temperature, and  $\rho_a$  is  $N_2$  density in amagat (as often used in laboratory). Amagat Number is defined as the ratio of gas density relative to its density at the standard atmosphere, namely,

$$\rho_a \equiv \frac{\rho_{N_2}}{\rho_{N_2}^0} \quad (\text{Eq. F-3})$$

where  $\rho_{N_2}$  is  $N_2$  density and  $\rho_{N_2}^0$  is  $N_2$  density in the standard atmosphere. By definition,  $\rho_{N_2}^0$  is 1 amagat. Other constants in Eq.(F.2) are given in the following:

$$\begin{aligned} a_1 &= 7.7 \times 10^{-10} & a_2 &= 1.0 \times 10^{-13} \\ b &= 1.7 & c_2 &= 1.0 \times 10^{-4} \\ c_1 &= 1.5 \times 10^{-3} & d &= 60 \end{aligned}$$

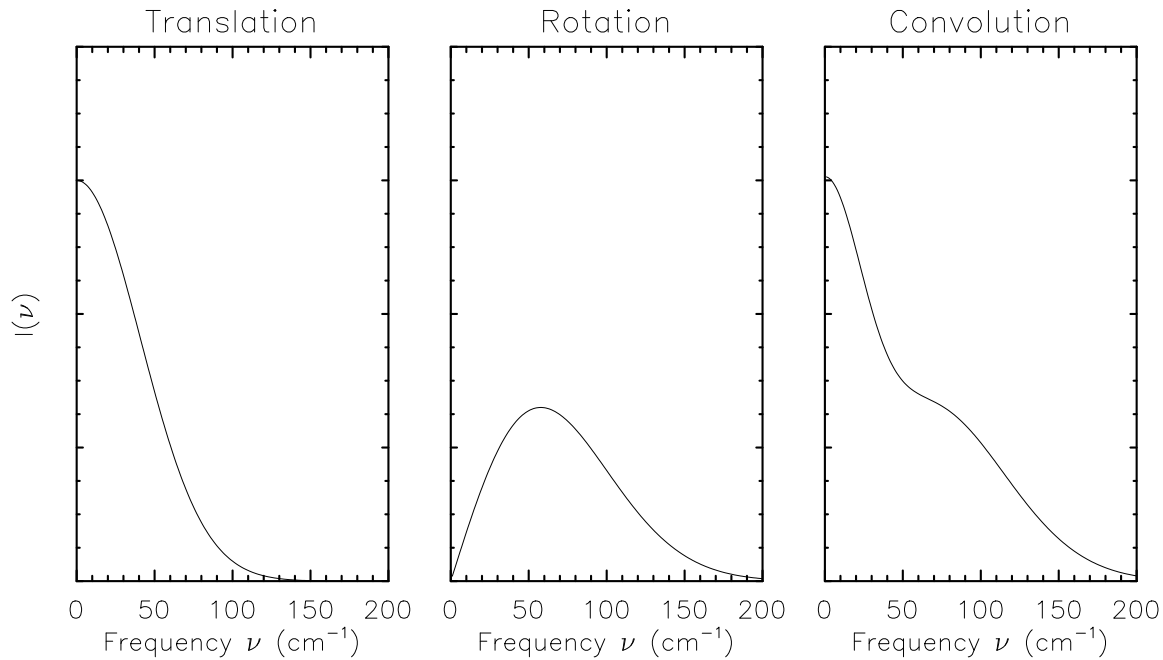


Fig F-1 The components of the  $N_2$  collision-induced absorption spectrum. (a) The translational spectrum. (b) The rotational spectrum. (c) The resulting profile is the convolution of (a) and (b).

### F3 Atmosphere dry-air continuum

Pardo et al. [2000] argued that the collision-induced absorption from  $O_2-O_2$  pairs is much weaker than that of  $N_2-N_2$  and the absorption from  $N_2-N_2$  and  $N_2-O_2$  are similar, i.e.,

$$\alpha_{N_2-N_2}(\nu) \approx \alpha_{N_2-O_2}(\nu) \quad (\text{Eq. F-4})$$

$$\alpha_{N_2-N_2}(\nu) \gg \alpha_{O_2-O_2}(\nu) \quad (\text{Eq. F-5})$$

If so, the atmospheric dry continuum can be expressed in terms of  $\alpha_{N_2-N_2}(\nu)$  as follows,

$$\begin{aligned} A_{dry}(\nu) &= \rho_{N_2}^2 \nu^2 \alpha_{N_2-N_2}(\nu) + \rho_{N_2} \rho_{O_2} \nu^2 \alpha_{N_2-O_2}(\nu) \\ &= \rho_{N_2} \rho_{air} \nu^2 \alpha_{N_2-N_2}(\nu) \\ &= \frac{1}{0.78} \rho_{N_2}^2 \nu^2 \alpha_{N_2-N_2}(\nu) \end{aligned} \quad (\text{Eq. F-6})$$

Converting  $\rho_{N_2}$  to amagat unit, we have

$$\begin{aligned} A_{dry}(\nu) &= \frac{1}{0.78} 10^{-2z} \theta^2 \nu^2 \alpha_{N_2-N_2}(\nu) \\ &= 0.78 \times 10^{-2z} \left( \frac{T_0}{300} \right)^2 \theta^2 \nu^2 \alpha_{N_2-N_2}(\nu) \\ &= 0.65 \times 10^{-2z} \theta^2 \nu^2 \alpha_{N_2-N_2}(\nu) \end{aligned} \quad (\text{Eq. F-7})$$

where we have used the relations

$$\begin{aligned} \frac{p_{N_2}}{p_0} &= \frac{0.78p}{p_0} = \frac{\rho_{N_2}}{1 \text{ amagat}} \frac{T}{T_0} \\ z &\equiv -\log_{10}(p/p_0) \end{aligned}$$

and  $p_0 = 1013$  hPa is the standard atmospheric pressure,  $T_0=273.15$  K is the standard temperature, and  $A_{dry}(\nu)$  in  $cm^{-1}$ . The factor 1.28 or  $0.78^{-1}$  is claimed by Pardo et al. [2000] in order to agree with their measurements. We find that this factor can be derived if the assumptions in Eqs. (F4-F5) hold.

#### F4 Comparisons to experimental data

The coefficients in Eq.(F.2) are determined by minimizing differences to the laboratory measurements. As shown in Table. F-1, the empirical function agrees with the measurements at temperatures between 200-300 K within 10%. There is slightly larger error for 2526 GHz at low temperatures, which is out of the range of most atmospheric temperatures. Plotted in Fig F-2 is the percentage error of the empirical function when compared to the experimental data.

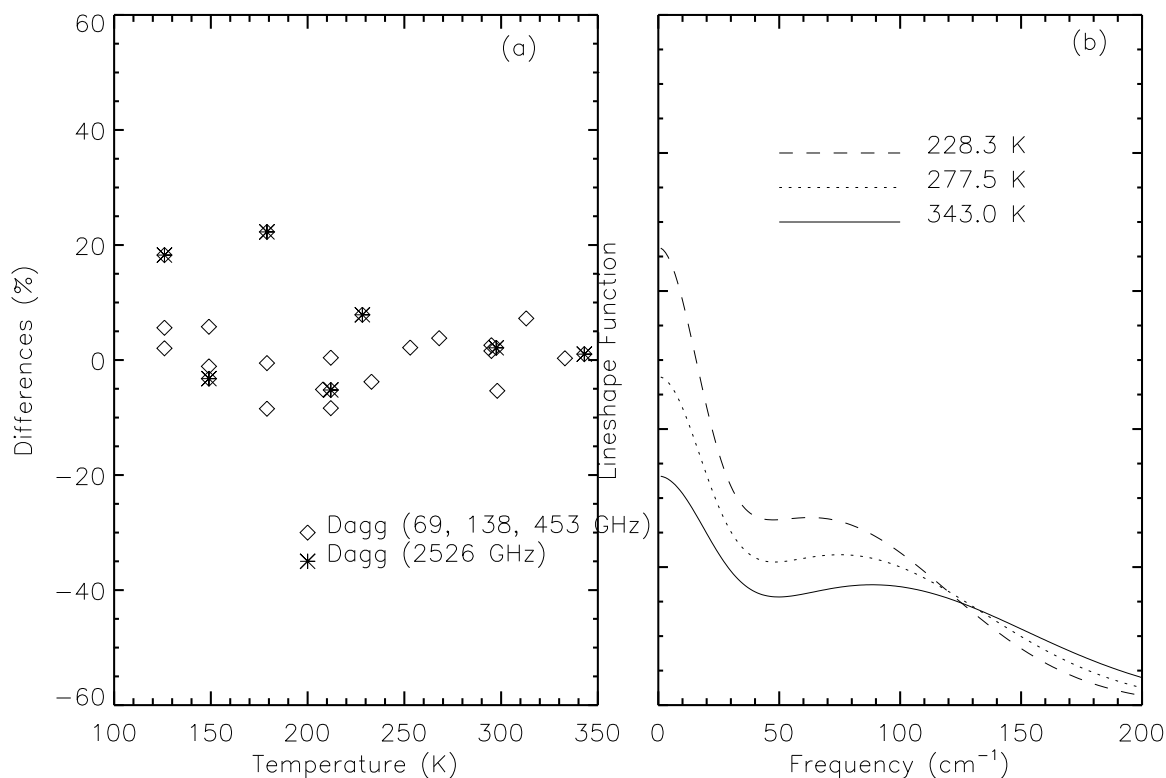


Fig F-2 Comparisons between the calculations from the empirical function and the experimental data. (a) The relative error vs. temperature. (b) The calculated lineshape function at different temperatures.

Table. F-1 Comparisons to some laboratory measurements. Measured and calculated N<sub>2</sub>-N<sub>2</sub> absorption has a unit of  $cm^{-1}/cm^2/amagat^2$ .

69 GHz	Temp (K)	208	233	253	268	295	313	333
	Meas. <sup>(a)</sup>	2.01	1.68	1.55	1.43	1.20	1.14	0.96
	Cal.	2.11	1.74	1.52	1.38	1.17	1.06	0.95
	Diff. (%)	-5.1%	-3.8%	2.2%	3.8%	2.6%	7.2%	0.3%
138 GHz	Temp (K)	126	149	179	212	295		
	Meas. <sup>(b)</sup>	5.03	3.82	2.64	2.01	1.17		
	Cal.	4.75	3.60	2.65	2.00	1.15		
	Diff. (%)	5.6%	5.8%	-0.5%	0.4%	1.6%		
453 GHz	Temp (K)	126	149	179	212	298		
	Meas. <sup>(c)</sup>	3.20	2.49	1.81	1.43	0.90		
	Cal.	3.13	2.52	1.96	1.55	0.94		
	Diff. (%)	2.0%	-1.1%	-8.5%	-8.4%	-5.3%		
2526 GHz	Temp (K)	126	149	179	212	228.3	297.5	343
	Meas. <sup>(d)</sup>	1.10	0.85	1.05	0.70	0.76	0.56	0.48
	Cal.	0.90	0.88	0.82	0.74	0.70	0.55	0.48
	Diff. (%)	18.3%	-3.2%	22.3%	-5.2%	7.9%	2.1%	1.0%

Note:

(a) from Dagg et al. [1975];

(b) measurements at 126-212K from Dagg et al. [1985] and measurement at 295K from Dagg et al. [1978];

- (c) measurements at 126-212K from Dagg et al. [1985] and measurements at 298K from Stone et al. [1984];
- (d) measurements at 126-212K from Dagg et al. [1985] and measurements at 228-340K from Stone et al. [1984].

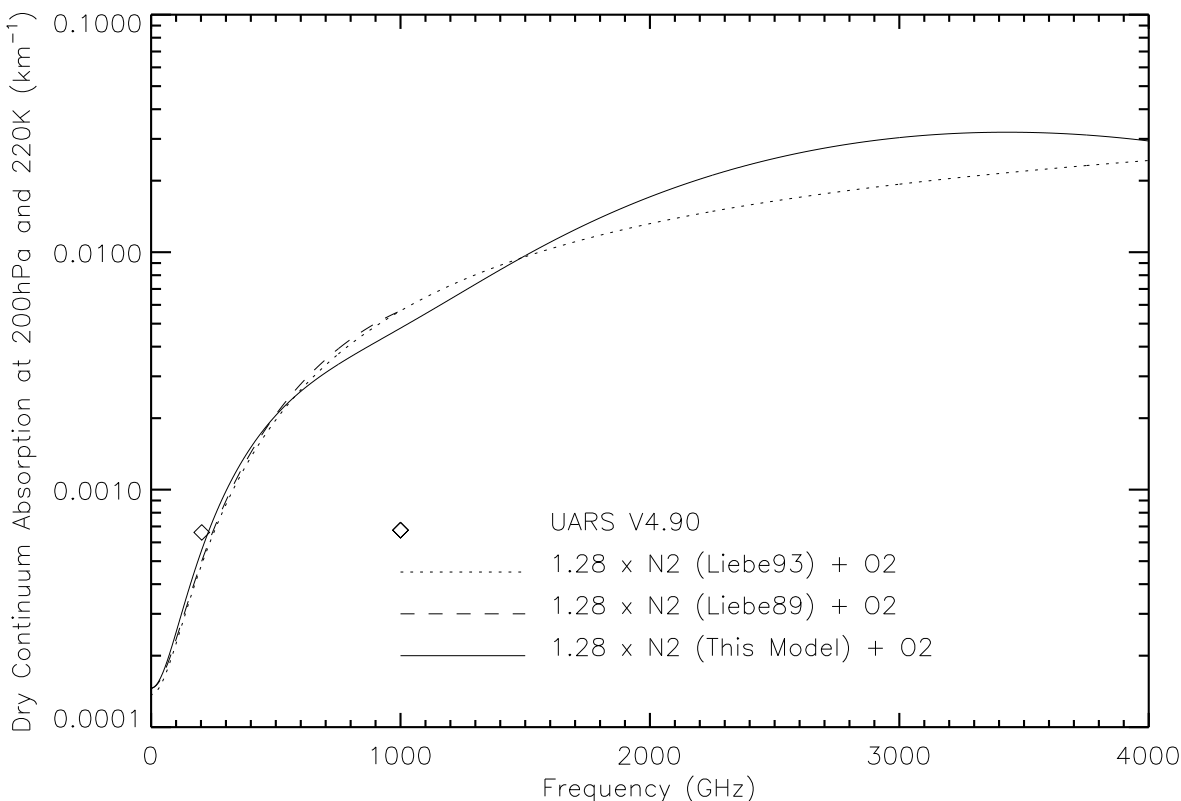


Fig F-3 Comparisons of dry continuum absorption calculated from different models. The Debye term, important at low frequencies, is included in the calculations.

Table. F-2 Dry continuum absorption estimated from different models for  $f=203\text{GHz}$ ,  $P_{air} = 200 \text{ hPa}$  and  $T=220\text{K}$

Model	Volume Absorption Coefficients ( $10^{-4} \text{ km}^{-1}$ )
UARS 4.90	6.6
1.28 x N <sub>2</sub> (Liebe'93) + O <sub>2</sub> (Debye)	4.8 (3.3 + 1.5)
1.28 x N <sub>2</sub> (Liebe'89) + O <sub>2</sub> (Debye)	5.0 (3.5 + 1.5)
1.28 x N <sub>2</sub> (This Model) + O <sub>2</sub> (Debye)	5.6 (4.1 + 1.5)

In Fig F-3 are the comparisons among different dry-continuum models where the UARS 203-GHz value is indicated by symbol. A factor of 1.28 is used for the  $N_2$ - $N_2$  contribution whereas the  $O_2$  contribution is same for all the models, which is the Debye term used in Liebe et al.

[1989]. The Debye spectrum is only important at low frequencies but remains significant near 200 GHz. Table. F-2 lists the dry continuum absorption coefficients calculated by these models at the UARS MLS frequency (203 GHz). The relative importance of the  $N_2-N_2$  and  $O_2$  contributions are given with the numbers in the parentheses. Liebe et al. [1989, 1993] model calculations are slightly lower than our model at frequencies  $< \sim 500$  GHz or  $> \sim 1500$  GHz, but all the models are lower than the value estimated in UARS MLS V4.90. At temperature 220K, our model is closest to the V4.90 value at 203GHz but remains  $\sim 15\%$  smaller. It should be noted that the factor of 1.28 does make these models agree better with the UARS estimate.

**Acronyms**

AFGL	Air Force Geophysics Laboratory
AMSU	Advanced Microwave Sounding Unit
CEPEX	Central Equatorial Pacific Experiment
CIR	Cloud-Induced Radiance
CIRA	COSPAR International Reference Atmosphere
CPR	Cloud Profiling Radar
DMSP	Defense Meteorological Satellite Project
DSB	Double-Sideband
EOS	Earth Observing System
FOV	Field of View
IWC	Ice Water Content
IWP	Ice Water Path
ITCZ	Inter-tropical Convergence Zone
JPL	Jet Propulsion Laboratory
LH	Liebe et al.[1989] and Hufford [1991]
LO	Local Oscillator
LOS	Line of Sight
LWC	Liquid Water Content
MAF	Major Frame
MH	McFarquhar and Heymsfield (1997)
MIF	Minor Frame
MIR	Millimeter-wave Imaging Radiometer
MLS	Microwave Limb Sounder
PSC	Polar Stratospheric Cloud
PSD	Particle Size Distribution
$RH_i$	Relative Humidity with respect to Ice
RT	Radiative Transfer
SAGE	Stratospheric Aerosol and Gas Experiment
SSM/T2	Special Sensor Microwave/Temperature 2
UARS	Upper Atmosphere Research Satellite
UTH	Upper Tropospheric Humidity

## References

- Arfken, G., *Mathematical Methods for Physicists* (3<sup>rd</sup> edition), Academic Press, 1985.
- Bauer, A. and M. Godon, Temperature dependence of water-vapor absorption in line wings at 190GHz. *J. Quant. Spectrosc. Radiat. Trans.*, **46**, 211-220, 1991.
- Bauer, A., M. Godon, J. Carlier, Q. Ma, and R. H. Tipping, Absorption by H<sub>2</sub>O and H<sub>2</sub>O-N<sub>2</sub> mixtures at 153GHz. *J. Quant. Spectrosc. Radiat. Trans.*, **50**, 463-475, 1993.
- Bauer, A., M., Godon, J. Carlier, and Q. Ma, Water vapor absorption in the atmospheric window at 239GHz. *J. Quant. Spectrosc. Radiat. Trans.*, **53**, 411-423, 1995.
- Baumgardt, Dan, Wintertime Cloud Microphysics Review, National Weather Service, La Cross WI, 2000.
- Bertie, J.E., H.J. Labbe, and E. Whalley, Absorptivity of Ice I in the Range 4000-30 cm<sup>-1</sup>, *J. Chem. Phys.*, **50**, 4501-4520, 1969.
- Blanchet, J.-P., N. McFarlane, Cloud Treatment in the GCM, *Description of the Radiative Scheme in the CCC Spectral General Circulation Model*, AES/CCC, Doc-GCMII-87, 1987.
- Bond, S. T., The potential effect of cirrus on MLS retrievals. Ph.D. Dissertation, The University of Edinburgh, UK, pp. 199, 1996.
- Borysow, A., and L. Frommhold, Collision-induced rototranslational absorption spectra of N<sub>2</sub>-N<sub>2</sub> pairs for temperatures from 50 to 300K. *Astrophys. J.* **311**, 1043-1057, 1986.
- Buck, A. L. New equations for computing vapor pressure and enhancement factor. *J. Appl. Meteorol.*, **20**, 1527-1532, 1981.
- Cumming, W.A., *J. Appl. Phys.*, **23**, 768, 1952.
- Czekala, H., Effect of ice particle shape and orientation on polarized microwave radiation for off-nadir problems. *Geophys. Res., Lett.*, **20**(10): 1669-1672, 1998.
- Dagg, I. R., G. E. Reesor, and J. L. Urbaniak, Collision induced absorption in N<sub>2</sub>, CO<sub>2</sub>, and H<sub>2</sub> at 2.3 cm<sup>-1</sup>. *Can. J. Phys.*, **53**, 1764, 1975.
- Dagg, I. R., G. E. Reesor, and M. Wong, A microwave cavity measurement of collision-induced absorption in N<sub>2</sub> and CO<sub>2</sub> at 4.6 cm<sup>-1</sup>. *Can. J. Phys.*, **56**, 1037-1045, 1978.
- Dagg, I. R., et al., Collision-induced absorption in Nitrogen at low temperatures. *Can. J. Phys.*, **63**, 625-631, 1985.
- Deirmendjian, D., Complete microwave scattering and extinction properties of polydispersed cloud and rain elements. Rand Corporation, Santa Monica, Calif., Report R-422-PR, 1963.
- Dowling, D.R. and L.F. Radke, A summary of the physical properties of cirrus clouds, *J. App. Meteor.*, **29**, p970, 1990.
- Evans, K. F., and G. L. Stephens, Microwave radiative transfer through clouds composed of realistically shaped ice crystals. Part I: Single scattering properties. *J. Atmos. Sci.*, **52**, 2041-2057, 1995a.
- Evans, K. F., and G. L. Stephens, Microwave radiative transfer through clouds composed of realistically shaped ice crystals. Part II: Remote sensing of ice clouds. *J. Atmos. Sci.*, **52**, 2058-2072, 1995b.
- Evans, K. F., et al., Modeling of submillimeter passive remote sensing of cirrus clouds. *J. Appl. Meteor.*, **37**, 184-205, 1998.
- Fleming, E. L., S. Chandra, M.R. Shoeberl, and J.J. Barnett, Monthly mean global climatology of temperature, wind, geopotential height and pressure for 0-120 km, *National Aeronautics and Space Administration*, Technical Memorandum 100697, Washington, D.C., 1988.
- Gasiewski, A. J., Numerical sensitivity analysis of passive EHF and SMMW channels to

- tropospheric water vapor, clouds, and precipitation. *IEEE Trans. Geosci. Remote Sens.*, **30**, 859-870, 1992.
- Gaut, N.E., and E. C. Reifstein III, *Interaction model of microwave energy and atmospheric variables*, Technical Report #13, Environmental Research and technology, Inc., Waltham, Mass, 1971.
- Geerts, B., G.M. Heymsfield, L. Tian, J.B. Halverson, A. Guillory and M.I. Mejia, Hurricane Georges's Landfall in the Dominican Republic: Detailed Airborne Doppler Radar Imagery, *Bulletin of the American Meteorological Society*, **81**, 999-1018, 2000.
- Godon, M., J. Carlier, and A. Bauer, Laboratory studies of water vapor absorption in the atmospheric window at 213GHz. *J. Quant. Spectrosc. Radiat. Trans.*, **47**, 275-285, 1992.
- Hansen, J.E., Multiple scattering of polarized light in planetary atmospheres. Part II. Sunlight reflected by terrestrial water clouds, *J. Atmos. Sci.*, **28**, p1400, 1971.
- Heymsfield, A., and C. M. R. Platt, A parameterization of the particle size spectrum of ice clouds in terms of the ambient temperature and the ice water content. *J. Atmos. Sci.*, **41**, 864-855, 1984.
- Heymsfield, A. J., A. Bansemer, P. R. Field, S. L. Durden, J. L. Stith, J. E. Dye, W. Hall, and C. A. Grainger: Observations and parameterizations of particle size distributions in deep tropical cirrus and stratiform precipitating clouds: Results from in situ observations in TRMM field campaigns. *J. Atmos. Sci.*, **59**, 3457-3491, 2002.
- von Hippel, A., *Tables of Dielectric Materials*, MIT Press, Cambridge, 1945.
- van de Hulst, H. C., *Light Scattering by Small Particles*. pp 470, New York, Dover, 1981.
- Hufford, G., A model for the complex permittivity of ice at frequencies below 1 THz. *Int. J. Infrared Millimeter Waves*, **12**, 677-682, 1991.
- Hogan, R. J., and A. J. Illingworth, Measuring Crystal Size in Cirrus Using 35- and 94-GHz Radars, *J. Atmos. Oceanic Tech.*, **27**, 27-37, 2000.
- Intrieri, J. M., G. L. Stephens, W. L. Eberhard, and T. Uttal, A Method for Determining Cirrus Cloud Particle Sizes Using Lidar and Radar Backscatter Technique, *J. Appl., Meteor.*, **36**, No. 6, pp1074-1082, 1993.
- Jarnot, R. F., et al., EOS MLS Level 1 Data Processing Algorithm Theoretical Basis. Jet Propulsion Laboratory Document *D-15210*, 2004.
- Jones, P., Shuttle Views the Earth: Clouds from Space, *NASA Johnson Space Center Publication*, <http://cass.jsc.nasa.gov/publications/slidesets/clouds.html>, 1986.
- Klein, L.A., and C.T. Swift, An Improved Model for the Dielectric Constant of Sea Water at Microwave Frequencies, *IEEE Transactions on Antennas and Propagation*, **25**, 1977.
- Knollenberg, R. G., K. Kelly, and J. C. Wilson, Measurements of high number densities of ice crystals in the tops of tropical cumulonimbus. *J. Geophys. Res.*, **98**, 8639-8664, 1993.
- Lamb, J., Measurements of the Dielectric Properties of Ice, *Discuss. Faraday Soc.*, **42A**, p238, 1946.
- Lamb, J., and A. Turney, *Proc. Phys. Soc. London Sect., B* **62**, p272, 1949.
- Lenoble, J., Radiative transfer in scattering and absorbing atmospheres: Standard computational procedures, A. Deepak, 1985.
- Liebe, H. J., MPM-An atmospheric millimeter wave propagation model. *Int. J. Infrared Millimeter Waves*, **10**, 631-650, 1982.
- Liebe, H. J., T. Manabe, and G. A. Hufford, Millimeter-wave attenuation and delay rates due to fog/cloud conditions. *IEEE Trans. Ant. Prop.*, **37**, 1617-1623, 1989.
- Liebe, H. J., Hufford, G. A., and Cotton M. G., Proceedings of AGARD 52<sup>nd</sup> Specialists Meeting

- of the Electromagnetic Wave Propagation Panel, Palma de Mallorca (Spain), 1993.
- List, R. J., Smithsonian meteorological tables, *Smithson. Misc. Collect.* **114**, Smithson. Inst., Washington, D. C., 1951.
- Livesey, N. J., EOS MLS Retrieval Processes Algorithm Theoretical Basis. Jet Propulsion Laboratory Document D-16159, 2004.
- Liou, K. N., and N. Rao, Radiative transfer in cirrus clouds. Part IV: On cloud geometry, inhomogeneity, and absorption. *J. Atmos. Sciences*, **53**, No. 21, 3046–3065, 1996.
- Liu, G., and J. A. Curry, Topical ice water amount and its relations to other atmospheric hydrological parameters as inferred from satellite data. *J. Appl. Meteor.*, **38**, 1182-1194, 1998.
- London, J., A Study of the Atmospheric Heat Balance, Research Division, College of Engineering, New York University, AFCEC-TR-57-287, Astria No. 117227, 1957.
- Lowan, A.N., Tables of Scattering Functions for Spherical Particles, *U.S. National Bureau of Standards*, Applied Mathematics Series 4, 1949.
- Ma, Q., and R.H. Tipping, Water vapor continuum in the millimeter spectral region, *J. Geophys. Res.*, **93**, p6127, 1990
- Marshall, J. S., and W. McK. Palmer, The distribution of raindrops with size. *J. Meteor.*, **5**, 165-166, 1948.
- Matrosov, S. Y., et al., Retrieval of vertical profiles of cirrus cloud microphysical parameters from Doppler radar and infrared radiometer measurements. *J. Appl. Meteor.*, **33**, 617-626, 1994.
- Matzler, C., and U. Wegmuller, *J. Phys. D: Appl. Phys.*, **20**, p1623, 1987.
- McCormick, M.P. SAGE Aerosol Measurement: Vol. III –January 1, 1981 to November 1981, *NASA Ref. Publ.* 1173, 2/87, NASA, Langley Research Center, Hampton, Virginia, 1987.
- McFarquhar, G. M., and A. J. Heymsfield, Microphysical characteristics of three anvils sampled during the central equatorial pacific experiment. *J. Atmos. Sci.*, **53**, 2401-2423, 1996.
- McFarquhar, G. M., and A. J. Heymsfield, Parameterization of tropical cirrus ice crystal size distributions and implications for radiative transfer: Results from CEPEX. *J. Atmos. Sci.*, **54**, 2187-2200, 1997.
- McKague, D, K. F. Evans, and S. Avery, Assessment of the effects of drop size distribution variations retrieved from UHF radar on passive microwave remote sensing of precipitation. *J. Appl. Meteor.*, **37**, 155-165, 1998.
- Mishima, O., D. D. Klug, and E. Whalley, The far-infrared spectrum of ice Ih in the range 8-25  $\text{cm}^{-1}$ . Sound waves and difference bands, with application to Saturn's rings. *J. Chem. Phys.*, **78**, 6399-6404, 1983.
- Mitchell, D. C., et al., Modeling cirrus clouds. Part I: Treatment of bimodal size spectra and case study analysis. *J. Atmos. Sci.*, **53**, 2952-2966, 1996.
- Pardo, J. R., E. Serabyn, and J. Cernicharo, Submillimeter atmospheric transmission measurements on Mauna Kea during extremely dry El Nino conditions: Implications for broadband opacity contributions. *J.Q.S.R.T.*, **67**, 169-180, 2000.
- Perry, J., and A.W. Straiton, *J. Appl. Phys.*, **44**, p5180, 1973.
- Platt, C. M. R., A parameterization of the visible extinction coefficient in terms of the ice/water content. *J. Atmos. Sci.*, **48**, 2083-2098, 1997.
- Pruppacher, H.R., and J.D. Klett, *Microphysics of Clouds and Precipitation*, *D. Reidel Publishing Company*, Boston, 1990.
- Ramanathan, V., R. D. Cess, E. F. Harrison, et al., Cloud-radiative forcing and climate - results

- from the Earth radiation budget experiment. *Science* **243**, 57-63, 1989.
- Ryan, B. F., A bulk parameterization of the ice particle size distribution and the optical properties of ice clouds. *J. Atmos. Sci.*, **57**, 1436-1451, 2000.
- Read, W.G, J.W. Waters, D.L. Wu, E.M. Stone, Z. Shippony, A.C. Smedley, C.C. Smallcomb, S. Oltmans, D. Kley, H.G.J. Smit, J.L. Mergenthaler, M.K. Karki, "UARS Microwave Limb Sounder Upper Tropospheric Humidity Measurement: Method and Validation," *J. Geophys. Res.* **106**, 32,207-32,258, 2001.
- Read, W. G., EOS MLS Forward Model Algorithm Theoretical Basis, *JPL D-18130*, 2004.
- Riedi J, Goloub P, Marchand RT, Comparison of POLDER cloud phase retrievals to active remote sensors measurements at the ARM SGP site. *Geophys. Res. Lett.*, **28**, 2185-2188, 2001.
- Rosenkranz, P. W., Chapter 2 in *Atmospheric Remote Sensing by Microwave Radiometry*, (M. A. Janssen, ed.), Wiley-Interscience, N.Y., 1989.
- Skofronick-Jackson, G. M., and J. R. Wang, The estimation of hydrometeor profiles from wideband microwave observations. *J. Appl. Meteor.*, **39**, 1645-1656, 2000.
- Sprichtinger, P., K. Gierens, and W. G. Read, The statistical distribution law of relative humidity in global tropopause region. *Meteorol. Z.*, **11**(2), 83-88, 2002.
- Stephens, G.L., S.C. Tsay, P.W. Stackhouse., P.J. Flatau, The relevance of the microphysical and radiative properties of cirrus clouds to climate and climatic feedback, *J. Atmos. Sci.*, **47**, p1742., 1990.
- Stone, N. W. B., et al., Temperature dependent collision-induced absorption in nitrogen. *Can. J. Phys.*, **62**, 338-347, 1984.
- Ulaby, F. T., Moore, R. K., and Fung, A. K., *Microwave Remote Sensing: Active and Passive, Volume I*, Artech House, Inc., 1981.
- Ulaby, F. T., Moore, R. K., and Fung, A. K., *Microwave Remote Sensing: Active and Passive, Volume III*, Artech House, Inc., 1986.
- Ulbrich, C. W., Natural variations in the analytical form of the raindrop size distribution. *J. Climate Appl. Meteor.*, **22**, 1764-1775, 1983.
- Vant, M.R., R.B. Gray, R.O. Ramseier, and V. Makios, *J. Appl. Phys.*, **45**, p4712, 1974.
- Vivekanandan, J., J. Turk, and V. N. Bringi, Ice water path estimation and characterization using passive microwave radiometry. *J. Appl. Meteor.*, **30**, 1407-1421, 1991.
- Waters, J. W., Microwave limb sounding. *Atmospheric Remote Sensing by Microwave Radiometry*. M. A. Janssen, Ed., John Wiley and Sons, Inc., 572 pp., 1993.
- Waters, J. W., An overview of the EOS MLS experiment. Jet Propulsion Laboratory Document D-15745, 2004.
- Weng, F., and N. C. Grody, Retrieval of ice cloud parameters using a microwave imaging radiometer. *J. Atmos. Sci.*, **57**, 1069-1081, 2000.
- Whalley, E., and H.J. Labbe, Optical Spectra of Orientationally Disordered Crystals. III. Infrared Spectra of the Sound Waves, *J. Chem. Phys.*, **51**, 3120-3127, 1969.
- Wilheit, T. T., et al., Microwave radiometric observations near 19.35, 95 and 183 GHz of precipitation in tropical storm Cora, *J. Appl. Meteorol.*, **21**, 1137-1145, 1982.
- Wu, D. L., et al., UARS MLS Cloud Ice Measurements and Implications for H<sub>2</sub>O Transport near the Tropopause. *J. Atmos. Sci.*, in review, 2004.
- Wylie DP, et al., 4 Years of global cirrus cloud statistics using HIRS. *J CLIMATE* **7**: (12) 1972-1986, 1994.